University of Stuttgart
Institute of Mechanical Handling
and Logistics

8th International Stuttgart Ropedays 2025

Conference Proceedings

21-22 May 2025
Stuttgart, Germany

Univ.-Prof. Dr.-Ing. Robert Schulz
Institute of Mechanical Handling and Logistics
University of Stuttgart, Germany

Conference Proceedings
of
8th International Stuttgart Ropedays 2025

21- 22 May 2025
Stuttgart, Germany

LEGAL NOTICE

Conference Proceedings of 8th International Stuttgart Ropedays 2025

Published by:

Univ.-Prof. Dr.-Ing. Robert Schulz

Institute of Mechanical Handling and Logistics, University of Stuttgart, Germany

Compiled by:

Dennis Kurrle, M.Sc.

Institute of Mechanical Handling and Logistics, University of Stuttgart, Germany

Printed by: DS.Printmedien GmbH, Murkenbachweg 21, 71032 Böblingen, Germany

ISBN: 978-3-00-081732-8

University of Stuttgart
Institute of Mechanical Handling and Logistics
Holzgartenstr. 15B
70174 Stuttgart, Germany
Phone number: +49 711 685-83770
Mail address: institut@ift.uni-stuttgart.de
https://www.ift.uni-stuttgart.de/en/

TABLE OF CONTENTS

DAY 2 - 22. MAY 2025

FOREWORD

Dear Readers,

It is my great pleasure to present to you the proceedings of the „8th International Stuttgart Ropedays 2025," which, for the first time, include contributions in English, thereby underscoring the consistent international orientation of our conference.

The contributions collected here from science and industry reflect the multifaceted nature of the rope industry and highlight the close collaboration between academic institutions and practical applications. This diversity is also evident in the broad spectrum of topics covered: from fiber ropes to hybrid and wire ropes, from material testing at the wire and yarn level to destructive and non-destructive testing of fiber, hybrid and wire ropes. Particularly innovative measurement techniques and new testing methods for wire and fiber ropes emphasize the innovative strength of this field.

A key focus of this conference is the exchange with internationally recognized experts from both science and industry. The conference contributions provide deep insights into the latest findings and illustrate how bringing together an international professional audience promotes knowledge transfer and the development of innovative solutions. Noteworthy are also research projects funded by the DFG and the EU. In the past, these have led to the development of novel hybrid ropes, which have already resulted in the successful production of prototypes.

My sincere thanks go to all authors for their valuable contributions and to the organizers of the conference for their dedicated work. Without the commitment of all involved, this successful event would not have been possible.

I wish you an inspiring read and hope that the presented works will provide new impulses for your own research and practice as well.

Stuttgart, May 2025

Univ.-Prof. Dr.-Ing. Robert Schulz

New approach to identify wire breakage location in cross-section of steel wire ropes

Masatoshi Ogata

National Institute of Occupational Safety and Health, Japan

Atsushi Yamaguchi

National Institute of Occupational Safety and Health, Japan

Kenta Yamagiwa

National Institute of Occupational Safety and Health, Japan

Naoya Kurahashi

Kobe Material Testing Laboratory Co., Ltd., Japan

Summary

Wire ropes are major components of cranes and elevators. However, their wires gradually break with long-term use, eventually leading to rope fracture, which may cause serious accidents. Thus, the rope damage mechanism should be clarified to prevent such accidents. Previous studies have found wire breakage inside independent wire rope core (IWRC) ropes. Therefore, rope damage is difficult to identify through visual observation, and a method for determining the wire breakage state in the rope cross section, including the inner wires, is required. This study proposes a method for identifying wire breakage locations in an IWRC rope cross section based on a geometric formulation of the wire shape. A damaged rope with wire breakage was produced for wire rope fatigue tests, and the wire breakage locations were estimated using the proposed method. Estimation results suggested that the wire breakage locations were concentrated in a specific area in the cross section. This study enables further analysis of the fatigue mechanism of wire ropes through an evaluation of the relationship between the fatigue test conditions and wire breakage locations in the cross section.

Keywords: steel wire rope, wire breakage location, fatigue life, bending over sheave

1 Introduction

A wire rope consists of multiple wires twisted together, providing high flexibility and tensile strength. Wire ropes in cranes undergo repeated bending over sheaves (BOS). These repeated loads gradually cause wire breakage, causing wire ropes to weaken and eventually fail. The relationship between repeated loads and wire breakage should thus be clarified to prevent wire rope failure.

Researchers have conducted numerous fatigue tests by applying repeated BOS loads to wire ropes [1-3]. The effects of rope tension and sheave diameter on fatigue life have also been demonstrated [2, 3]. Additionally, studies have highlighted the susceptibility of the internal wires of independent wire rope core (IWRC) ropes to breakage [3].

The stress and contact force of wires should be evaluated to predict wire fatigue life under BOS. Finite element analysis (FEA) is an effective method for stress evaluation [4-6]. We previously developed an FEA model for single strand to reproduce wire stress under BOS and confirmed that the model can accurately predict the fatigue life of wires under BOS [6]. Currently, we are developing an FEA model for multistrand wire ropes.

Wire breakage locations should be identified to assess the fatigue life of wire ropes. Previous studies have revealed that wire breakage occurs inside ropes [3]. However, the wire breakage locations within the rope cross section and the relationship between the sheave and wire breakage locations have not been detailed. Wire breakage locations are difficult to identify because wire positions within the rope cross section change along the rope axial direction. Nonetheless, identifying wire breakage locations is crucial for the verification and validation (V&V) of the finite element modeling of wire ropes.

In this study, we propose a method for identifying wire positions in cross sections perpendicular to the rope axis by geometrically formulating the wire shape [7]. We apply this method to wire ropes after fatigue testing and report our results on wire breakage locations.

2 Identification of wire breakage locations in rope cross section

2.1 Geometric formulation of wire shape

This study focused on IWRC 6×Fi(29) wire ropes. **Figure 1** shows a cross-sectional view of the wire rope. This wire rope consists of an IWRC, which is composed of I_{in} and I_{out} strands, and Fi(29) strands. In this paper, the central wire of each strand is called core wire, and the outer-layer wires are called outer wires. Each Fi(29) strand has a core wire, inner wires, outer wires, and filler wires between the core and outer wires.

In terms of shape, the wires in this wire rope can be classified as straight, helical, or double helical. Researchers have proposed geometric formulations of these shapes [8, 9]. With the axial direction of the wire rope defined as the *z* axis, the straight shape $\boldsymbol{C_0}$, helical shape $\boldsymbol{C_1}$, and double helical shape $\boldsymbol{C_2}$ are defined as follows [9]:

$$\boldsymbol{C}_0 = [0 \quad 0 \quad z], \tag{1}$$

$$\boldsymbol{C}_1 = [r_0 \cos\varphi_0 \quad r_0 \sin\varphi_0 \quad r_0 A_1(\varphi_0 - \varphi_{00})], \tag{2}$$

$$\boldsymbol{C}_2 = \begin{bmatrix} -r_1 \cos\varphi_0 \cos\varphi_1 + r_1 \cos\varphi_1 \sin\varphi_0 \sin\varphi_1 \\ -r_1 \sin\varphi_0 \cos\varphi_1 - r_1 \cos\varphi_1 \cos\varphi_0 \sin\varphi_1 \\ r_1 \sin\varphi_1 \sin\varphi_1 \end{bmatrix} + \begin{bmatrix} r_0 \cos\varphi_0 \\ r_0 \sin\varphi_0 \\ r_0 A_1(\varphi_0 - \varphi_{00}) \end{bmatrix}. \tag{3}$$

Figure 2 shows curves drawn in *xyz* coordinates using Equations (1) to (3). Here, r_0 and r_1 are the helix radii, φ_0 and φ_1 are the angles formed by these radii, φ_{00} and φ_{10} are the initial phases, and A_1 and A_2 are the pitch coefficients. The pitch coefficients have the following relationship with the pitch length *p* and the lay angle ψ:

$$p = 2\pi r A = 2\pi r / \tan\psi. \tag{4}$$

The wire shape parameters (r_0, r_1, A_0, A_1, ϕ_{00}, and ϕ_{01}) are obtained by measuring the wire rope. These parameters are then substituted into Equations (1) to (3) to identify each wire position (x, y, z) in the *xy* cross section perpendicular to the rope axial direction *z*.

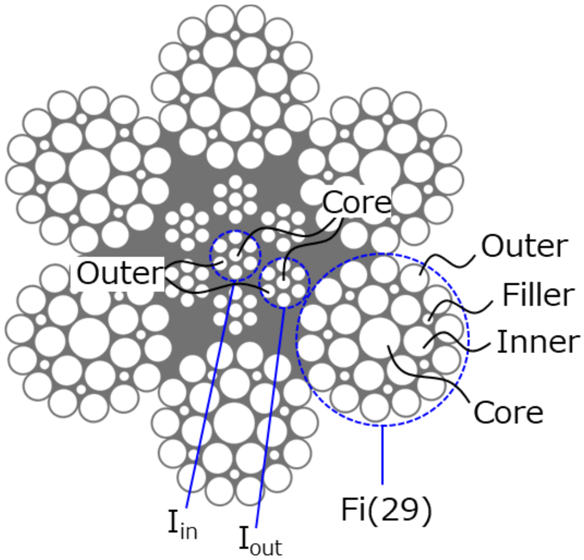

Figure 1: Cross section of IWRC 6×Fi(29)

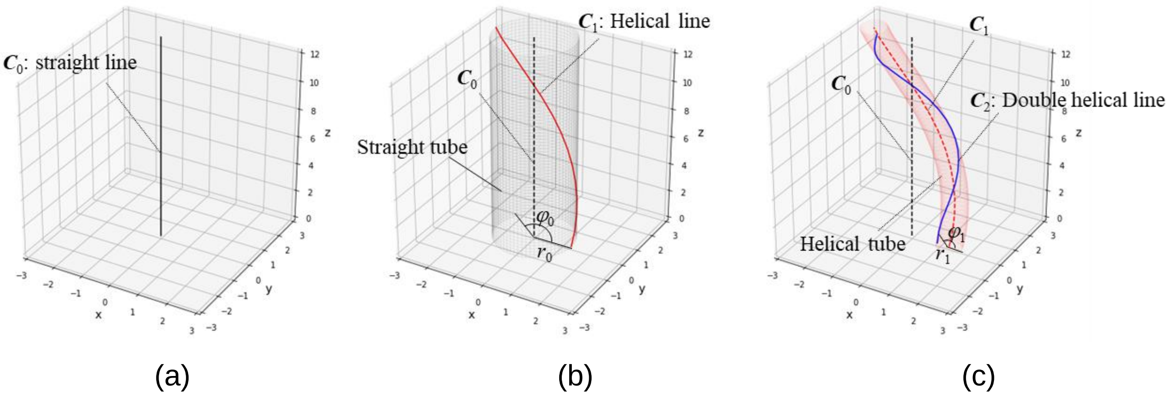

Figure 2: Geometric modeling of wire shapes: straight (a), helical (b), double helical (c)

2.2 Identification of wire breakage location using geometric model

The wire locations (x, y, z) in the xy cross section perpendicular to the rope axis direction z are calculated using Equations (1) to (3) (Section 2.1). Therefore, the wire breakage location (x_b, y_b, z_b) in the cross section perpendicular to the rope axial position z_b can be identified by measuring the rope axial position z_b of the wire breakage. **Figure 3** shows the measurement of z_b. A strand was separated from the wire rope, and the z_b at the wire breakage was measured using calipers. The wire breakage location (x_b, y_b, z_b) was identified using z_b and Equations (1) to (3).

In this study, the wire breakage locations (x_b, y_b) obtained from the geometric wire model were converted into parameters (α, β) to represent the positional relationships between the wires within the rope cross section and the sheaves. Figure 4 shows a schematic diagram of the wire locations in the xy cross section perpendicular to the rope axis direction z. First, the polar coordinates (r_1, θ_1) were defined as shown in Figure 4, and the angular coordinate θ_1 was used to define α ($0 \leq \alpha \leq 2\pi$). Next, as shown in Figure 4, the polar coordinates (r_2, θ_2) were defined, where the radial coordinate r_2 is the vector from the rope center to the strand center (x_1, y_1). The origin of the polar coordinates (r_2, θ_2) was set to (x_1, y_1). The angular coordinate θ_2 of these polar coordinates (r_2, θ_2) was then used to define β ($-\pi \le \beta \le \pi$).

As shown in **Figure 4**, α quantifies the rotational position of the wire relative to the rope center, and β quantifies the rotational position of the wire relative to the strand center. Specifically, a wire with $\beta = 0$ is on the surface of the rope, and a wire with $\beta = \pm\pi$ is closer to the rope center.

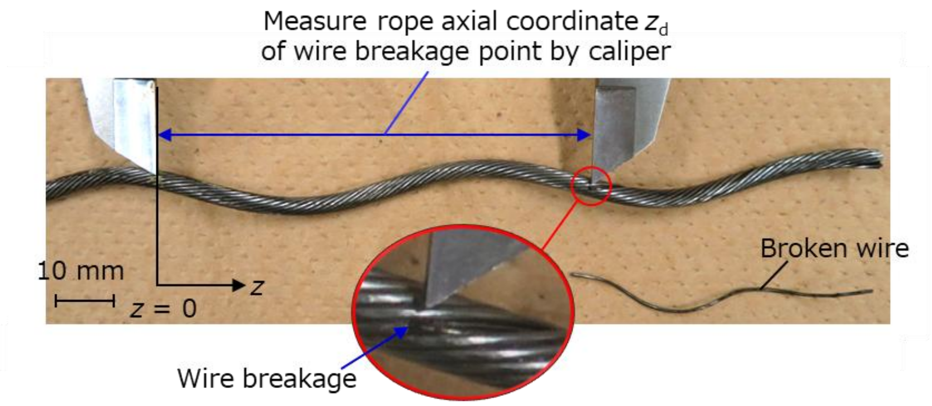

Figure 3: Measuring the rope axial position of the wire breakage

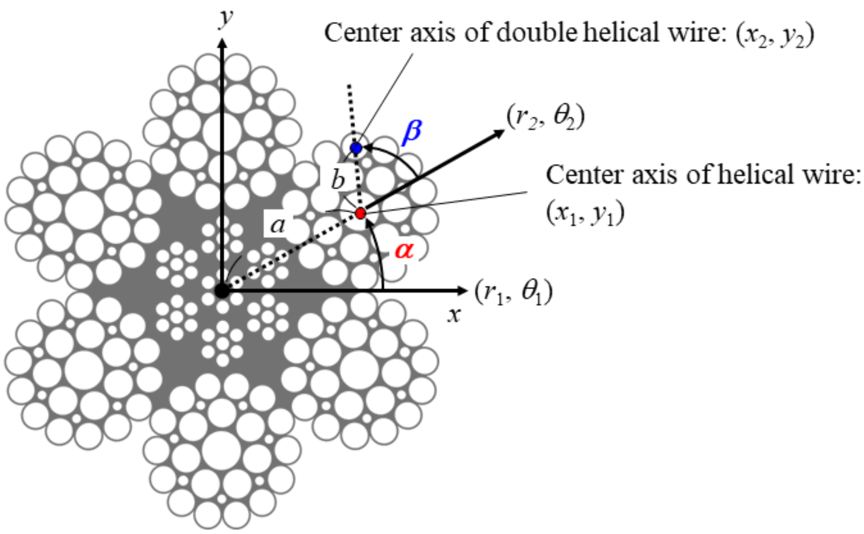

Figure 4: Conversion of wire position (x_2, y_2) into (α, β)

3 Wire rope fatigue test

Wire ropes with broken wires were created for wire rope fatigue tests. The wire breakage positions in these damaged ropes were identified using the method described in Section 2. The tested IWRC 6×Fi(29) wire rope had a diameter of d = 16 mm and a nominal breaking force of 173 kN.

Two types of fatigue tests were conducted, namely, double- and single-bending tests, where the wire rope passed over two sheaves and one sheave, respectively. **Figure 5** shows the fatigue testing machine used in the double-bending fatigue test. This machine was also used in the single-bending fatigue test. A hydraulic actuator applied a specified tension to the wire rope. A servo motor reciprocated the wire rope over the test sheaves. The effective diameter of the test sheave was D = 256 mm (D/d = 16). The rope tension was set to 34.6 kN, which was 20% of the nominal breaking force of 173 kN. The fatigue test was stopped before wire rope failure. The rope in the region subjected to bending loads over the sheaves was cut to a length of 12 d.

Figure 6 shows the positional relationship between the wires in the rope cross section and the sheaves during the fatigue tests. Before the wire rope was removed from the fatigue testing machine, the rope surface was marked at $\alpha = \pi/2$. Therefore, in the single-bending test, the wires at $\alpha = 3\pi/2$ were at the bottom of the sheave groove; in the double-bending test, the wires at $\alpha = \pi/2$ and $3\pi/2$ were at the bottom of the sheave groove. At α close to 0 or π, the wires were on the side of the rope, away from the bottom of the sheave groove.

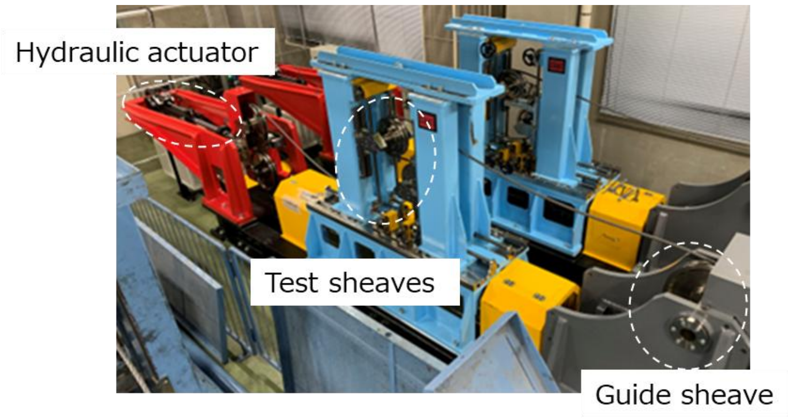

Figure 5: Wire rope fatigue testing machine for double-bending test

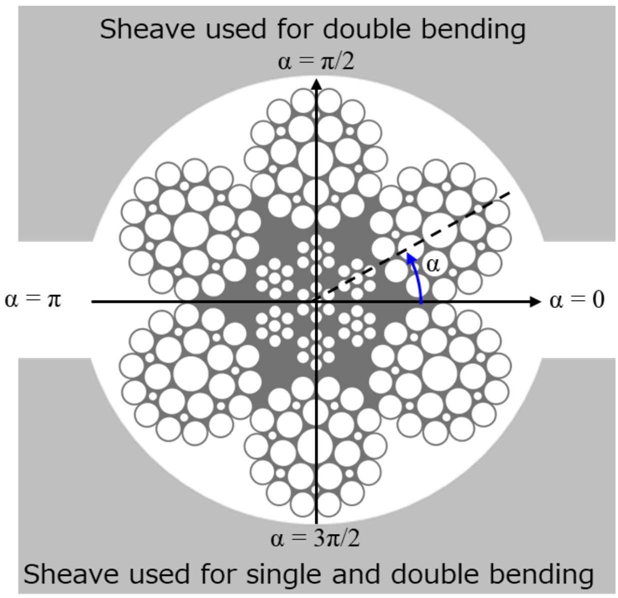

Figure 6: Positional relationship between wires in rope cross section and sheaves

4 Results and discussion of wire breakage locations

Figure 7 and **Figure 8** show the identified wire breakage locations in the double- and single-bending tests, respectively. Figures (a) to (c) present the results for different numbers of repetition cycles. One cycle is one round trip of the wire rope during the fatigue test. The upper figures show the results for the outer, inner, and core wires of the Fi(29) strands. The lower figures show the results for the outer and core wires of the I_{in} and I_{out} strands. The average fatigue life of the wire rope, obtained using the same fatigue test, was 5924 cycles for the double-bending test and 25704 cycles for the single-bending test.

According to the double-bending test results (Figure 7), the breakage locations of the outer and core wires of the Fi(29) strand were at approximately $\alpha = \pi$. Thus, the wire breakage locations were on the side of the rope as shown in Figure 6. Additionally, the breakage location of the outer wire was at $\beta = \pm\pi$, indicating that the outer wire breakage was concentrated toward the inner part of the rope. In Figure 7(c), close to the fatigue life, the inner wire broke at the same location as the outer wire.

As for the IWRC wires, the breakage locations were more widely distributed than those in the Fi(29) strand. The outer and core wires of I_{out} tended to break at the rope sides, at $\alpha = 0, \pi, 2\pi$. The outer wires of I_{out} tended to be distributed on the surface side of the IWRC at $-\pi/2 \leqq \beta \leqq \pi/2$. The theoretical value of bending stress over a sheave is higher for wires on the sides of a rope [1]. Thus, the identified wire breakage locations in Figure 7 qualitatively agree with previously published results.

In the single-bending test (Figure 8), the breakage of the outer and core wires of the Fi(29) strand was concentrated on the rope sides, at $\alpha = 0, \pi, 2\pi$. The outer wires broke at $\beta = \pm\pi$, on the center side of the rope. These wire breakage locations were similar to those in the double-bending test. As shown in Figure 8(c), the outer wires near the fatigue life broke at approximately $\alpha = 3\pi/2$ and $\beta = 0$. This breakage was due to the contact of the rope with the sheave groove. For the IWRC wires, the outer and core wires of the I_{out} strand tended to break at $\alpha = 3\pi/2$ at the sheave groove. Additionally, the outer wires were distributed on the surface side of the IWRC at $-\pi/2 \leqq \beta \leqq \pi/2$. Therefore, the fatigue life of the IWRC wires in the single-bending test depended more on the rope contact with the sheave.

The proposed method quantitatively demonstrates that the wire breakage locations in IWRC 6×Fi(29) are concentrated in specific regions within the rope cross section (Figure 7 and Figure 8). This method can be applied to various types of wire ropes to study wire breakage mechanisms and fatigue phenomena in wire ropes. In addition, it can be used for the V&V of FEA models designed to calculate the stress distribution and contact stress of wire ropes under BOS.

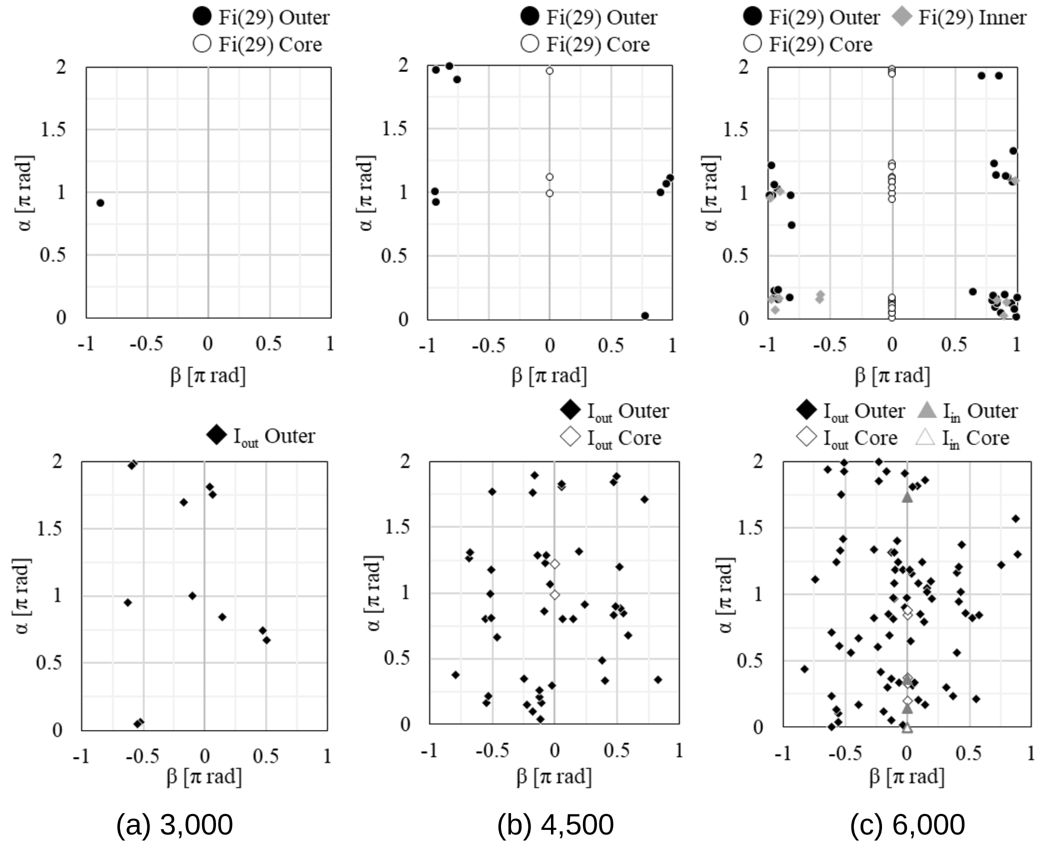

Figure 7: Wire breakage locations in double-bending test: 3,000 cycles (a), 4,500 cycles (b), 6,000 cycles (c)

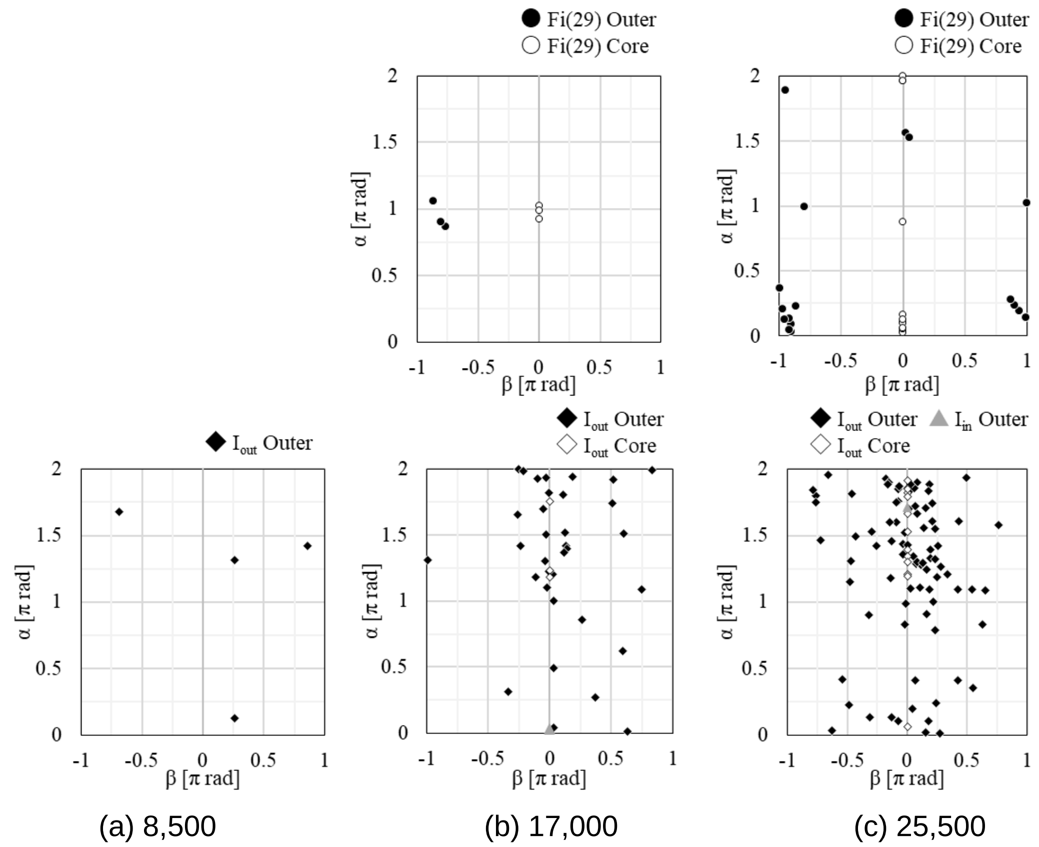

Figure 8: Wire breakage locations in single-bending test: 8,500 cycles (a), 17,000 cycles (b), 25,500 cycles (c)

5 Conclusions

We propose a method for quantitatively identifying the wire breakage locations within a rope cross section. This method involves formulating geometric models of the wire shape. Double- and single-BOS fatigue tests were conducted on an IWRC 6×Fi(29) wire rope with a diameter of 16 mm. After these fatigue tests, the wire breakage locations in the wire rope were analyzed using the proposed method. In the double-bending test, the breakage locations of the outer, inner, and core wires of the Fi(29) strand were concentrated on the rope sides. Furthermore, the outer and inner wires tended to break more easily on the center side of the rope. For the IWRC wires, the outer wires of the I_{out} strand had the most breakages. These wires tended to break on the surface side of the IWRC. In the single-bending test, the outer wires of the Fi(29) strand near the fatigue life broke at the rope contact points with the sheave groove. Additionally, the wire breakages of the IWRC tended to be distributed near the contact points with the sheave. These breakages were significantly influenced by the contact between the sheave and the rope.

Currently, we are developing a finite element model for bending fatigue tests of wire ropes. Future work includes validating the results using the distribution of the wire breakage locations obtained in this study and elucidating the breakage mechanisms considering wire stress and contact conditions.

6 References

[1] Feyrer, K., Wire ropes, elements and definitions, Wire Ropes: Tension, Endurance, Reliability, Springer GmbH (2007).

[2] Editorial Board of Wire Rope Handbook, Wire rope handbook (1995), pp. 387–394 (in Japanese).

[3] Honda, T., Yamagiwa, K., Yamaguchi, A. and Sasaki, T., Evaluation of damage of conventional and new material ropes used for cranes and reconsideration of discard codes for wire ropes, JNIOSH-SRR-No. 44-1 (2014) (in Japanese).

[4] Erdonmez, C. and Imrak, C. E., A finite element model for independent wire rope core with double helical geometry subjected to axial loads, Sādhanā, Vol. 36, No. 6 (2011), pp. 995–1008.

[5] Kastratović, G. and Vidanović, N., 3D finite element modeling of sling wire rope in lifting and transport processes, Transport, Vol. 30, No. 2 (2013), pp. 129–134.

[6] Ogata M., Yamaguchi, A., Yamagiwa, K., Kurahashi, N. and Izumi, S., Finite element modeling for single-twisted Fi(29) strand that reproduces strand stiffness and wire stress, Mechanical Engineering Journal, Vol. 11, No. 6 (2024), p. 24–00299.

[7] Ogata M., Yamaguchi, A., Yamagiwa, K., Sasaki, T. and Izumi, S., Estimation of breakage position in wire rope cross-section by geometrical formulation of wire shape, Transactions of the JSME, Vol. 88, No. 908 (2022), p. 22–00038 (in Japanese).

[8] Costello, G. A., Theory of wire rope, Mechanical Engineering Series, Springer New York (1997).

[9] Ono, S., Approach to differential geometry in wire rope, Transactions of the Japan Society for Industrial and Applied Mathematics, Vol. 3, No. 4 (1993), pp. 387–424 (in Japanese).

7 Authors' Introductions

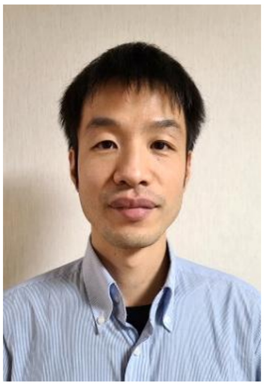

Dr.Eng. Masatoshi Ogata received his Doctorate degree in Mechanical Engineering from the University of Tokyo in Japan. He started his professional career as a research and development of strength reliability at Hitachi, Ltd. in Japan for 8 years. Then he changed his job as a member of Mechanical System Safety Research Group at National Institute of Occupational Safety and Health, Japan (JNIOSH) in 2020. He has been engaged in research contributing to the prevention of occupational accidents in JNIOSH for 5 years. His research interests are in rope fatigue life estimation and a development of a finite element model to simulate the stress condition of wires.

Dr.Eng. Atsushi Yamaguchi received his Doctorate degree in Mechanical System Engineering from Tokyo Denki University in Japan. He started his professional career as a member of Mechanical System Safety Research Group at National Institute of Occupational Safety and Health, Japan (JNIOSH). He has been engaged in research contributing to the prevention of occupational accidents in JNIOSH for 16 years. His research interests are a prediction of replacement time for wire ropes and estimation of burst pressure of pressure equipment with local thin area based on experimental mechanics.

Dr.Eng. Kenta Yamagiwa received his Doctorate degree in Mechanical Engineering from the University of Tokyo in Japan. He started his professional career as a member of Mechanical System Safety Research Group at National Institute of Occupational Safety and Health, Japan (JNIOSH). He has been engaged in research contributing to the prevention of occupational accidents in JNIOSH for 21 years. His research interests are mainly in Image Analysis of Fractography, especially Application of Machine Learning to it. His state-of-the-art outcome is shown in https://www.frad-tech.com/en/.

Mr Naoya Kurahashi received his Bachelor's degree in Mechanical Engineering from Oita University in Japan. He started his professional career as a material testing specialist at Kobe Material Testing Laboratory Group in Japan for 7 years. In this year, he also started to study his doctoral course of Engineering in Aoyama Gakuin University. His research interests are evaluate of fatigue strength for wire rope and evaluate of fatigue crack growth threshold in metallic materials.

Rope mesh as structural substitute for lightweight footbridge structures

Fabian Graber

Jakob Rope Systems, Switzerland

University of Applied Science Berne BFH, Switzerland

Summary

Rope meshes, composed of individual wire ropes, woven together or interconnected by sleeves, are characterised by their mesh diamond geometry, rope diameter, knot type and steel grade and are mainly made of stainless steel, less frequently of galvanised steel or fibre ropes. Due to their favourable mechanical properties of high strength and flexibility, rope meshes are typically used in applications for fall protection, spatial lightweight structures as well as bridge constructions.

In bridge construction, rope meshes classically act as infill elements for vertical and horizontal fall protection.

The case studies Pedestrian bridge – Himmelhausmattesteg (span 26m) and Suspension bridge – La Pendenta (span 270m) illustrate how mesh can be integrated into the primary structural system, serving as a combined substitute for classic hanger cables as well as fall protections. The design of the mesh with its resistance and stiffness is determined by semi-empirical methods to calibrate the FEM analysis. The meshes are tested as a system in uniaxial and biaxial tests to determine their stiffness, but also as individual nodes to evaluate their resistance from the resulting loss factors of the ropes.

These case studies provide valuable insight into the design process including structural calculations, design details, method statements and basic behaviour.

Keywords: lightweight structure; new structural component; rope mesh; cable; suspension bridge; design method

1 Rope mesh

The characteristics of a rope mesh are defined by the following parameters, which define the behavior of the mesh in terms of its stiffness and resistance:

- **Knot types:** either by sleeves [(2);Fig.1] or by wooven rope conncetions [(3);Fig.1]
- **Mesh diamond geometry:** Mesh diamond width W; mesh diamond length H; mesh diamond aperture α (usually $\rightarrow 60°$)
- **Steel grade of ropes:** Mainly made out of stainless steel (EN1.4401) circular wire strand ropes (6x7+WC; 6x19+WC) with nominal tensile strength $f_u = 1'570\, {}^{N}/_{mm^2}$

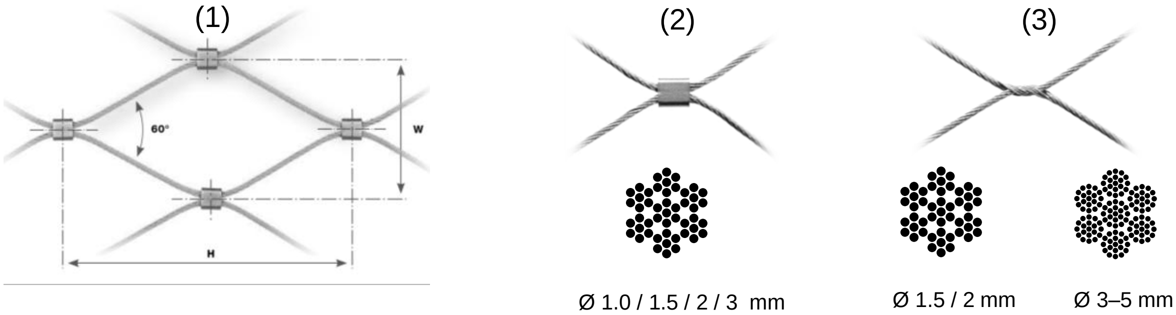

Figure 1: Definition of a rope mesh, knot types with its rope constructions and diameters

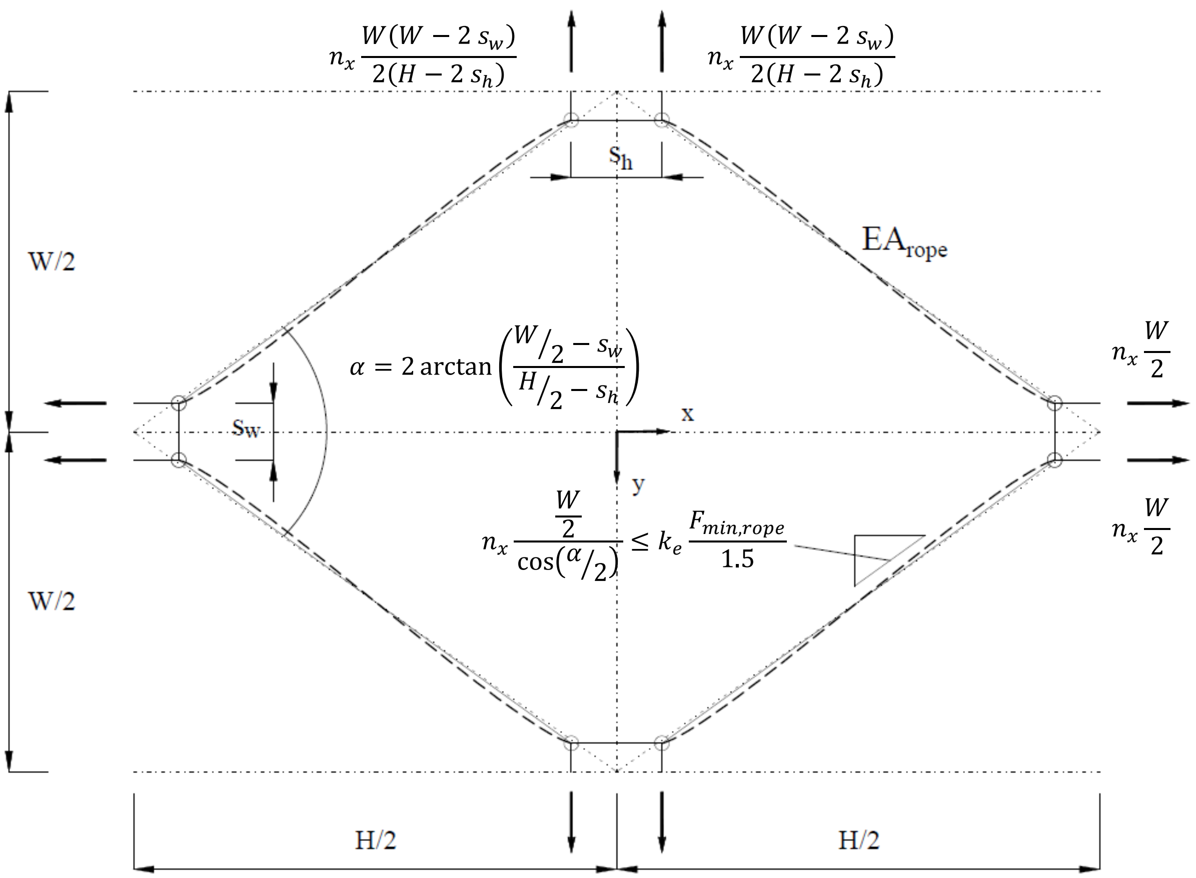

Figure 2: Single mesh diamond for meshes with sleeves, dashed-bolt: initial S-shape of the mesh rope

1.1.1 Stiffness

The diamond-shaped mesh geometry, along with the orientation of the knots, defines the stiffness in the major direction E_x and the minor direction E_y. The mesh has a nonlinear behavior, with increasing stiffness under higher loads. This behavior results from the combination of the initial rope alignment, which forms an S-shape at the knots [Fig.2, red lines], and the nonlinear characteristics of the circular wire ropes.

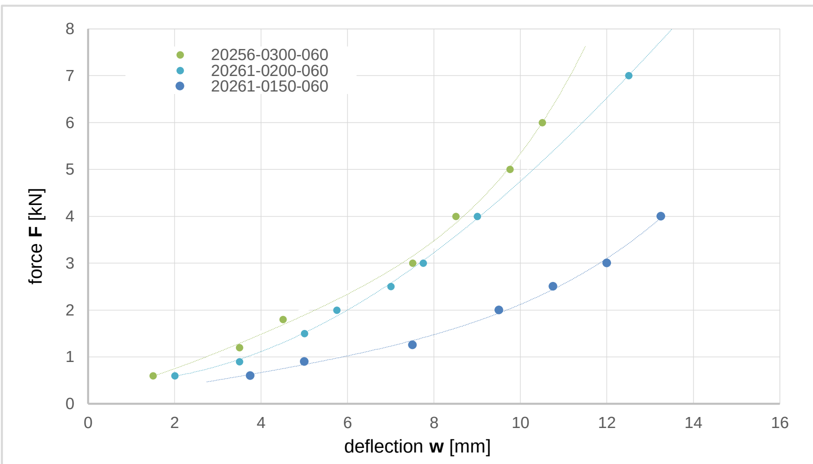

Figure 3: Uniaxial test – different rope mesh types for determination of mesh stiffness

The effective stiffness values and the ratio ${E_x}/{E_y}$ are empirically determined through uniaxial and biaxial tests. These test results serve as the basis for calibrating FEM simulations, which are used to determine the stiffness of individual structural elements. Since footbridge applications primarily involve uniaxial loading, the results from uniaxial tests are considered most relevant for the presented case studies in this document.

1.1.2 Resistance

The resistance of rope meshes under quasi-static loads is constrained by the empirically determined loss factors k_e of the ropes (vary for mesh ropes $\emptyset \leq 2mm \rightarrow k_e = 0.6 \dots 0.9$), which result from swaging the mesh sleeves. Additionally, the resistance at the mesh perimeters is influenced by the rope eye-endsand the configuration of the lacing cable (where lacing cable $\emptyset \geq \emptyset_{mesh\ rope}$), as well as the geometry of the adjacent structural elements. These include connections to suspension ropes, railings of steel structures, and other boundary components.

The failure of individual mesh sleeves or mesh ropes due to external impact does not lead to a complete failure of the mesh system. This structural redundancy has been demonstrated through pull tests [1], confirming the mesh's ability to maintain load-bearing capacity despite localiced damage.

Figure 4: left: single mesh sleeve test; right: test of single failed mesh sleeve in y-direction

2 Design method

Depending on the mesh application (planar or 3D-freeform structures), the type of applied loads and the purpose of the calculations, different mesh modelling and calculation methods, as illustrated in Fig.5, can be considered.

Method 1: **“Real” ropes**	**Method 2:** **“Ideal” ropes**	**Method 3:** **Orthotropic Membranes**
Beam elements with a real, representative bending stiffness Rope deviation at the sleeve or tensioning process is taken into account	Ideal, straight rope elements Simplified geometry in the tensioned stage (shown figure for mesh width 60 mm, scale factor 1)	Orthotropic membrane with linear-elastic material model; definition on major (X-axis) and minor (Y-axis) mesh alignment
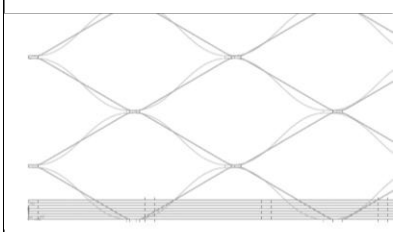	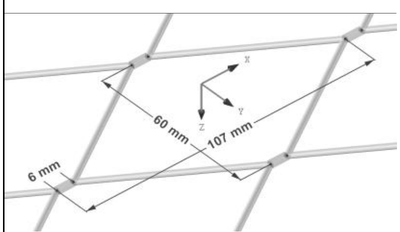	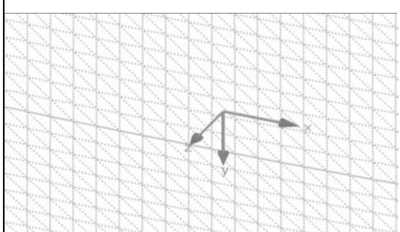

Exact determination non-linearity of the single mesh-diamond	Simplification of the single mesh-diamond with linear-elastic material model; can be applied with scale factors for the mesh and mesh ropes	For efficient FEM-modelling (fromfinding, displacement, strength and patterning) of freeform mesh shapes; not applicable for point loads analysis
Detailed investigations: Initial stressing in the tensioned mesh stage, local stress analysis around sleeves	Loads in plane or perpendicular to the network plane	Structural system modeling of large-scale spatial free-forms, basis for patterning

Figure 5: Comparison of modelling and design methods; [2]

For footbridge applications or rope mesh structures, Method 3 is commonly used to limit deflection and enhance structural stiffness, thereby improving dynamic behavior. If localiced stress concentrations are anticipated, Method 2 or a combination of both approaches may be more appropriate.

2.1.1 Dimensioning Method

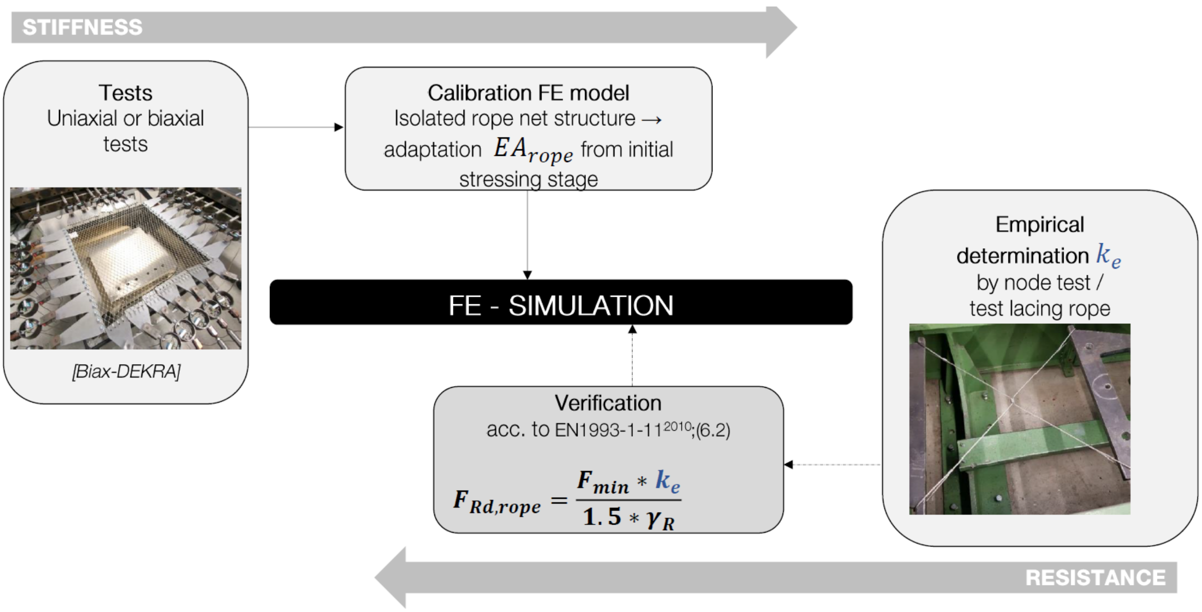

Figure 6: Design Method; [3]

Experimental investigations are carried out to assess the stiffness of cable nets under varying load levels. Furthermore, the resistance of the rope mesh is validated through isolated node tests, incorporating the corresponding loss factors k_e, which directly correlate with the ultimate tensile strength of the wire rope.

3 Applied Loads

The loads listed are typically applied to meshes in footbridge applications. However, additional load cases may need to be considered in the design process.

Initial stressing forces: A defined initial stressing force must be applied during mesh installation to achieve the intended geometric configuration. These forces vary depending on the required stiffness. For example, in Case Study 1 – Himmelhausmattesteg, an initial pre-stressing force of $p_{0,x} \approx 3.5\, {}^{kN}/_{m}$ was applied, whereas in Case Study 2 – La Pendenta, a force of $p_{0,x} \approx 0.9\, {}^{kN}/_{m}$ was used. These forces are also taken into account during the mesh patterning process to compensate for elongation effects alongside constructive deductions.

For aperture angles of $\alpha \approx 60°$::

$$p_{0,y} \approx {}^{1}\!/_{3}\, p_{0,x}$$

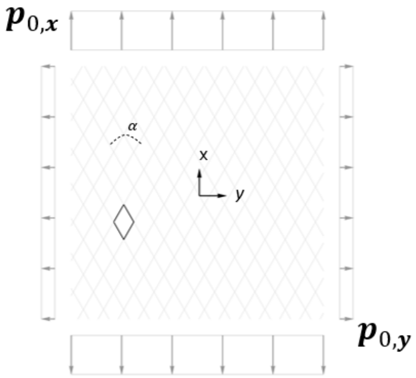

Figure 7: ratio of initial stressing force

Wind: Although the force coefficient of the meshes c_f is relatively low, as determined by wind tunnel tests, the large surface area of the mesh makes wind a critical load case.

	mesh width W $[mm]$	rope diameter Ø $[mm]$	permeab. $[\%]$	$c_{f,v}$ nearly vertical position of mesh $[-]$	$c_{f,h}$ nearly horizontal position of mesh $[-]$
1	60	3	84.0	0.18 → **0.20**	0.06 → **0.10**
2	100	3	91.4	0.10 → **0.15**	0.03 → **0.05**
3	30	1.5	86.0	0.21 → **0.25**	0.06 → **0.10**
4	60	1.5	92.8	0.09 → **0.15**	0.03 → **0.05**
5	100	1.5	96.0	0.05 → **0.10**	0.02 → **0.05**
6	30	1.0	89.3	0.14 → **0.15**	0.05 → **0.05**

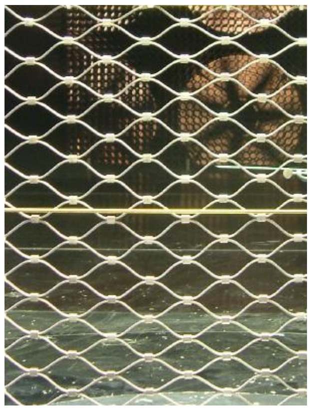

Figure 8: force coefficient for different mesh types, bolt recommended values [3]

Ice / snow: Depending on the location, the combination of ice and wind or snow can result in critical load cases. In the absence of specific building code guidelines for snow loads, Jakob Rope Systems has established a test setup to compare different mesh types and alignments with closed surfaces.

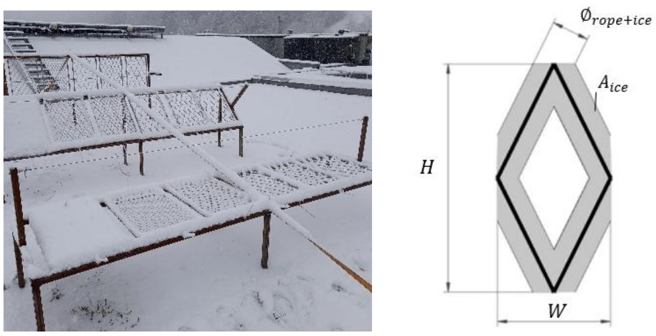

Figure 9: left: snow test setup; right: Wind with ice model

Fall protection: A general technical approval (Z-14.7-557) has been granted for the Jakob Rope Systems rope mesh Webnet, with a European Technical Assessment (ETA) currently in progress. This approval encompasses its function as both vertical and horizontal fall protection.

4 Case Study 1: Cycle and footbridge – Himmelhausmattesteg, Trubschachen – Switzerland

The Himmelhausmatt Bridge, constructed in 2019, serves as a case study illustrating the application of rope meshes (Webnet, rope ø 3 mm, W 80 mm, with sleeves, vertically oriented) as a structural load-bearing element.

The bridge, with an overall length of 25.8 meters, features a structure tensioned by a rope mesh system composed of suspension cables and bridge deck beams. It has a maximum incline of 5% and a sag of 280 mm. This mutual tensioning enhances the overall system stiffness, reduces susceptibility to significant deformations, and improves dynamic performance. The incorporation of rope meshes as a replacement for traditional hanger cables further eliminates the need for additional fall protection.

The free span of the bridge beam between the pylons is 21.4 meters. With a bridge width of 2.2 meters, it accommodates the passage of a 5-ton municipal snowplow. The bridge is designed to support a live load of 4 kN/m².

The suspension cables exhibit a sag of 2.4 meters over a span of 23.7 meters, yielding an f/l ratio of 1/10. These suspension cables (*Jakob Forte* – OSS, 1x37, ø 26 mm) are connected to the pylon head blocks, alongside the guy rods (Jakob Forte – M36) and the net retention cables (*Jakob Forte* – OSS,1x19 ø 12 mm).

The 12-ton bridge structure (whereas 8.5-ton for pylons, bridge deck and 2.8-ton for gratings) is supported and anchored on a heavyweight solution, consisting of a steel-reinforced concrete basin filled with excavated material.

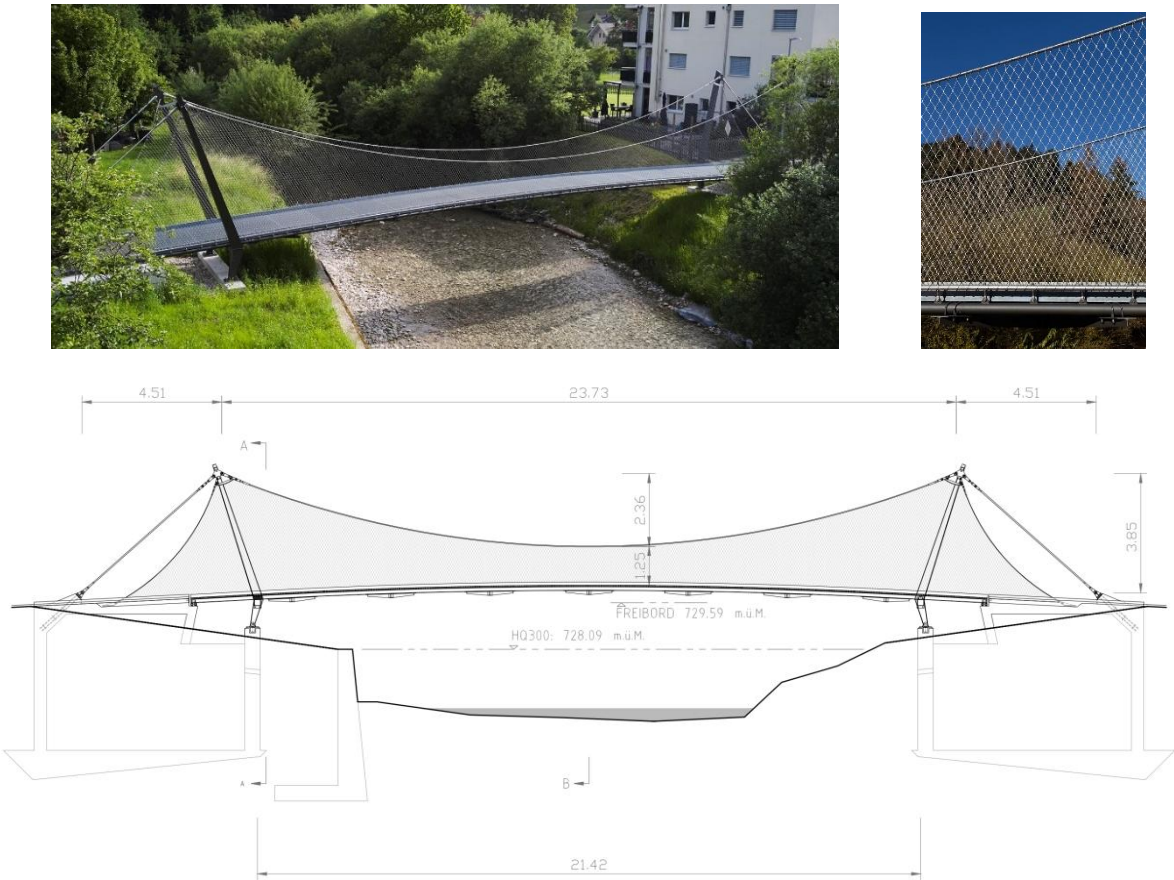

Figure 10: Suspension Bridge – Himmelhausmattesteg, Trubschachen – Switzerland, span 26m

The mesh was calculated according to Method 2: “Ideal” ropes with a scale factor of 4 and with the modelling simplification with consecutive rope members without geometrical interruptions by sleeves. Resulting from calibrations by a uniaxial test the mesh ropes have been considered with an average elastic modulus of E=20’000 N/mm^2 (-5’000 / +10’000 N/mm^2 for limit state analysis).

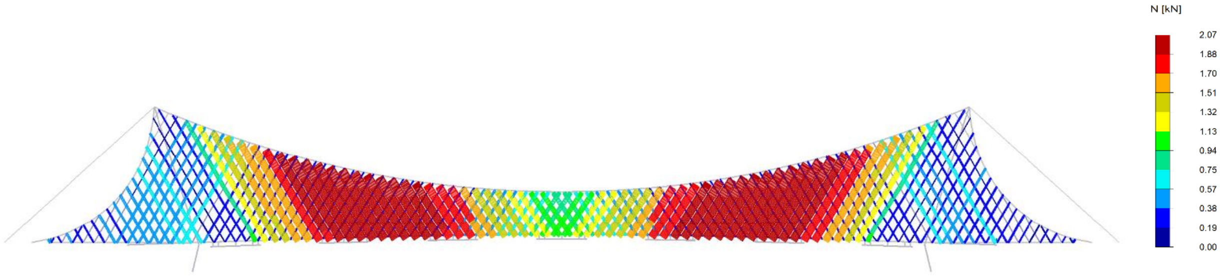

Figure 11: Tension forces for $G + P + Q$; mesh modelling acc. to Method 2: “Ideal” ropes

Advanced measurements of bridge deck deflection conducted during the workshop, combined with continuous monitoring throughout the installation process—primarily through the controlled tensioning of the bridge deck and suspension cables using chain hoists—enabled an optimal alignment of the pre-patterned rope mesh to its final fabricated shape.

In-situ measurements with 10 persons walking on the bridge revealed vertical vibrations with a frequency of 2.9 Hz and an acceleration of 1.0 m/s². These values were assessed according to Hivoss [4] and classified as non-critical.

Post-completion continuous monitoring indicated a decrease in tension force of approximately 5%, following a load test, after which a stable condition was monitored.

Figure 12: left: alignment of suspension cable and bridge deck using chain hoists
right: preparation for lacing the rope mesh to the suspension cable at the top and the railing at the bottom

It is noteworthy that the cables and meshes used for this bridge accounted for approximately a quarter of the total costs, with another quarter attributed to the steel components, and a half allocated to ground and foundation work. A comparison with a traditional suspension bridge, incorporating separate fall protection integrated into the balustrade alongside hanger cables from the bridge deck to the suspension cables, demonstrates a cost optimization of approximately 5 to 10%. Furthermore, this design not only enhances the transparency of the structure, contributing to its harmonic integration into the landscape, but also reduces the amount of required construction material, thereby yielding a positive environmental impact.

5 Case Study 2: Suspension footbridge - La Pendenta, Disentis – Switzerland

The suspension bridge, spanning the Vorderrhein, is supported by six fully locked cables (FLC, Ø 45 mm, Galfan) and was realized in 2024. The 1-meter-wide walkway is suspended from the four lower main cables and consists of grating panels supported by longitudinal beams made of bent steel plates (t 6, S355), which are in turn positioned on transverse beams. The two upper main cables function additionally as handrails at chest height.

A significant technical challenge was the 15-meter height difference between the abutments, combined with the structure’s low sag, only 8 meters over a span of 270 meters (f/l = 1/35; maximum incline approximately 15%). While a pylon could have mitigated the horizontal forces, its implementation was not compatible with the landscape constraints.

Lateral stabilization is achieved through wind bracing cables made of galvanized open spiral strands (OSS, ∅ 30.9 mm), which are connected to the main cables via coupling cables (∅ 12–19 mm). The transverse A-frames to which these cables are attached gradually decrease their spacing from 29 meters at the ends to 12 meters at the bridge center, thereby enhancing structural stiffness in this critical region.

The rope mesh system (Webnet, rope ∅ 2 mm, W 60 mm, with sleeves, vertically oriented) is installed laterally along the walkway. This mesh serves as both a transparent fall protection barrier and an active load-bearing element. It transfers vertical loads from the walkway to the upper main cables, thereby reinforcing the walkway structure in accommodating variable loads and reducing longitudinal bending by approximately 50% for a given spacing of the cross beams.

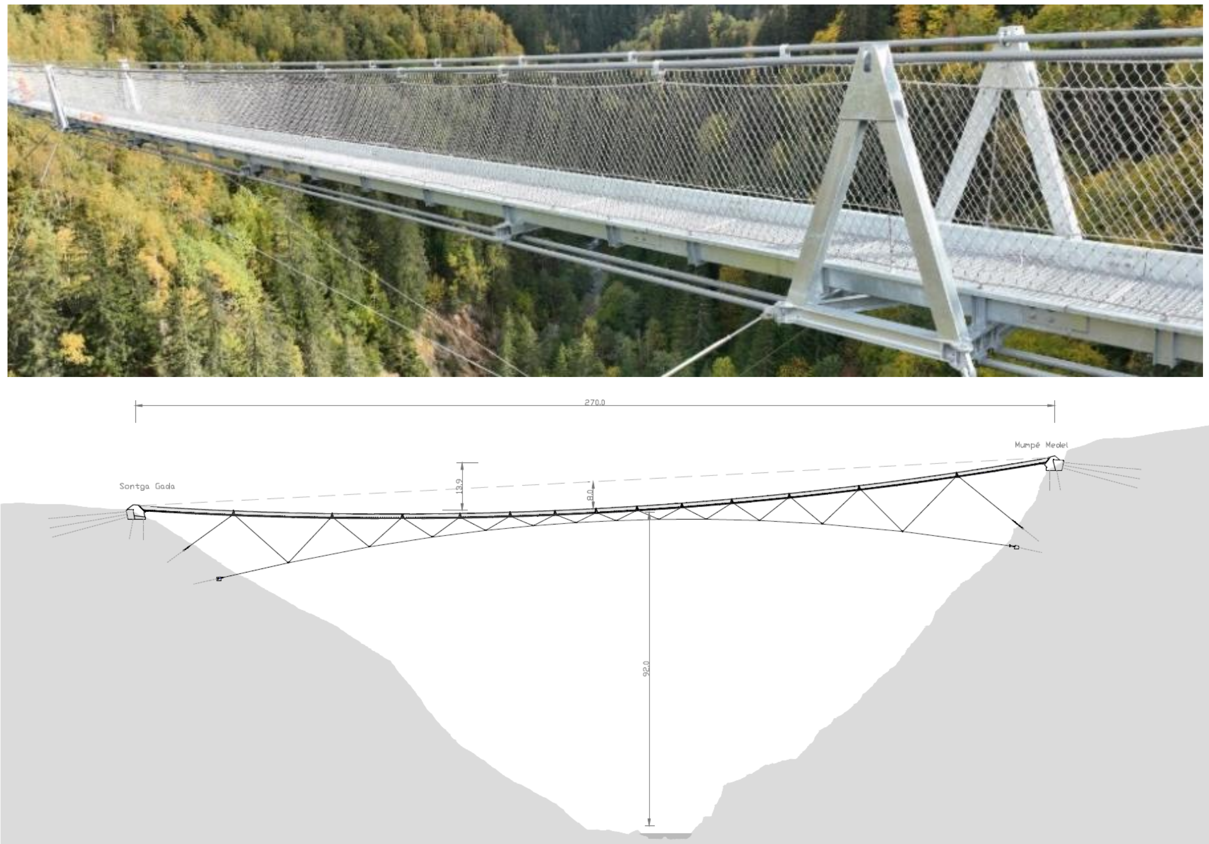

Figure 13: Suspension Bridge – LaPendenta, Disentis – Switzerland, span 270m

The mesh was intergrated in the modelling by Method 3: Orthotropic membranes. Due to the long spans form A-frame to A-frame especially close to the abutments, the initial stressing force of the mesh had to be limited to restrict the deflecton of the upper main cables and to allow the required height of the fall protection everywhere.

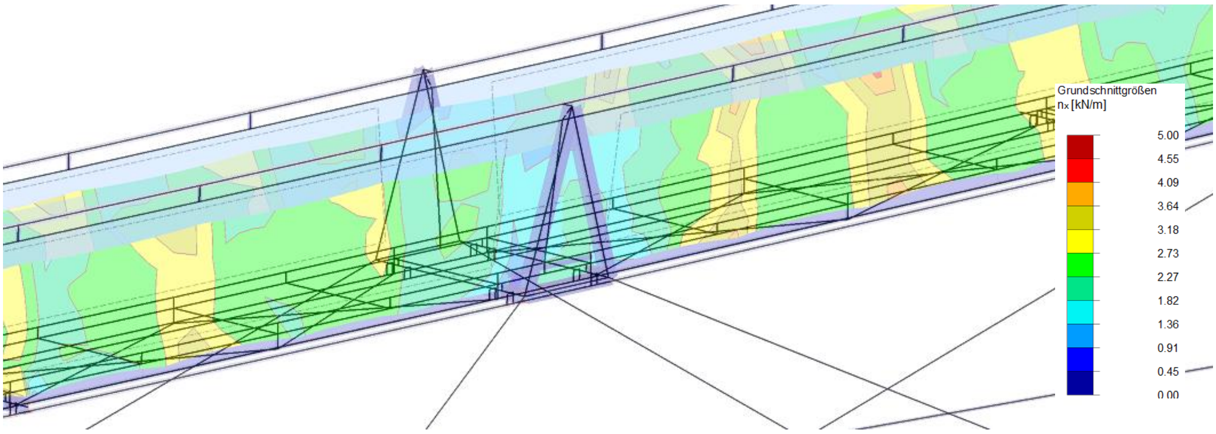

Figure 14: membrane forces n_x of critical load case, modelling acc. to Method 3: Orthotropic membranes

To validate structural calculations, the bridge underwent a load test before opening. 23 tons were evenly distributed, simulating 0.9 kN/m^2, one-seventh of the maximum design load.

With the local Fire Department, 35 pallet frames were filled with up to 530 liters of water. The load was applied in stages, from 30 cm to 60 cm to simulate the load scenarios.

Real-time monitoring confirmed structural stability, with deflections deviating by a maximum of 4%. However, a clamping effect caused a residual deformation of 130 mm (2% of f) at the bridge center.

Figure 15: Load test to validat structural calculations

To assess dynamic behavior and walking comfort, a test simulated various traffic loads. Only intentional torsional vibrations affected the structure, while free walking and marching caused no critical excitation. Initial findings confirmed stable oscillatory behavior under wind loads.

6 Learnings

In considering climbability, dense meshes were selected, with the rope diameter primarily determined by the required stiffness and robustness rather than resistance.

Measurements of the suspension bridge in Trubschachen confirm that the long-term behavior of the mesh results in negligible displacements.

A critical external factor could arise from snow removal equipment. Therefore, guide elements should be incorporated into the design. However, if a defect occurs, it can be repaired locally without resulting in a complete failure of the mesh.

The torsional vibrations observed in the walkway of the suspension bridge in Disentis suggest the need to shorten the span of the A-frames, particularly near the abutments. Alternatively, the initial mesh stressing force could be increased, and compression members should be added to ensure the fall protection height of the upper main cables.

Another key consideration during the design process is the constructive detailing, following the principles of design-for-disassembly. This approach allows also for easy replacement in case of external impacts or vandalism. Additionally, the impact of bird strikes on the mesh was evaluated and found to be non-critical.

7 Conslusions

Using a rope mesh as a primary load-bearing structural element for footbridges, in addition to its role as fall protection, effectively reduces the need for additional materials and structural components. This approach can be advantageous due to its initial stress application, which can positively influences dynamic behavior, decrease loading on longitudinal deck elements and enhances integration with the landscape through its transparency.

The semi-empirically developed design methods, along with their calibrations, have been validated through load tests and measurements of constructed structures. Ongoing monitoring of the completed projects has provided no evidence against the applicability of this approach.

8 Acknowledgements

I would like to sincerely thank the engineering team at Jakob Rope Systems for their outstanding work in developing the design methods and structural details of rope mesh systems. A special thanks goes to Dr. Konstantin Kühner for his expertise in rope applications and his leadership in advancing the development of rope mesh systems, including their integration into ETA. I would also like to thank Ms. Dorothea Drayer for her invaluable work in the analytical development of various design methods.

9 References

[1] Graber, F.: Load carrying behaviour of cable mesh structures with rep-sleeves, Jakob Rope Systems, March 2020

[2] Drayer, D.: Webnet – Membrane Stiffness and Resistance, Jakob Rope Systems, Rev.03

[3] Buselmeier, M., Wacker Ingenieure:Wind tunnel tests for determination of the force coefficient a wire grating; 2008

[4] Hivoss, RFS2-CT-2007-00033: Human induced vibrations of steel structures; Guide for design if pedestrian bridges; 10.9.2008

[5] Wagner, R. : Bauen mit Seilen und Membranen, chapter 3.3; Beuth Verlag GmbH, 2016

[6] Jakob Rope Systems: Webnet Catalogue; 11/2024

10 Author Introduction

Fabian Graber obtained his MSc degree in Civil Engineering from ETH Zurich, following his initial studies in Architecture at the University of Applied Sciences in Berne. He gained professional experience while working for consultancies in Switzerland before joining the technical center of VSL International in Singapore, where he specialised in bridge and post-tensioning design. Since 2016, he has served as Head of Engineering and member of the executive board at Jakob Rope Systems and began teaching at the University of Applied Sciences in Berne, where he also leads the Group of Construction & Structure.

Integrating automated wire rope condition monitoring in information environment of industrial facilities

Selsarev D.

INTRON PLUS, Moscow

Summary

Integration of rope monitoring into the comprehensive enterprise information system not only increase safety of industrial facility but also reduce operation costs, so it is important to find out key data parameters and describe procedures that give decisive information about rope condition for technical and administrative staff. A detailed presentation of practical experience in the implementation of Intros-Auto rope monitoring system at different mining and drilling facilities and its integration into appropriate information systems can give a useful example of such a solution. Depending on hoist type and construction different types of magnetic head are applied. MH delivers information to controlling computer unit, which can be connected to external workstation or interact directly with operator smartphone. Resulting information flows into enterprise information system. This paper gives an overview and case study of practical implementation of rope monitoring at high intensity industrial facilities.

Keywords: steel wire ropes, magnetic rope testing, rope monitoring, digital enterprise

1 Introduction

Diagnostics of technical condition of wire ropes plays a key role in ensuring the safety of industrial facilities such as mine hoists, factory cranes, aerial rope-ways and drilling rigs. Transition from conventional non-destructive testing to automated quasi-continuous rope monitoring corresponds to a wide trend for the latter's implementation in various industries. It is particularly important for enterprises with intensively used ropes of high importance to the production cycle allowing them to increase the safety of their operations and plan maintenance operations such as cutting and replacement, biased to the rope's actual condition. Implementation of such rope monitoring systems is possible when they are integrated with the enterprise's information and management system PIMS.

Conventional wire rope non-destructive testing technique is based on magnetic flux leakage method [1] which can be combined with partial visual inspection. The presence of rope deterioration due to corrosion, abrasion, wire breaks, geometrical distortions may be detected, evaluated, graded to determine safety of the rope's further operation and, ultimately, it's residual lifetime may be forecast. Rope discard criteria is stated in different international standards, such as the ISO 4309:2017 and EN 12927:2019 [2, 3]. The Automated rope monitoring systems, in their majority, also employ the said method of Magnetic Rope Testing (MRT) [4, 5], which will be examined in greater detail in this paper.

2 The rope monitoring system hardware

INTROS-AUTO is an automated condition monitoring system (ACMS) rope monitoring system based on magneto-inductive method for different industrial applications: drilling lines on rigs, mining hoists, factory cranes. The system consists of a compact magnetic head (MH), installed on the rope (**Figure 1** a), connected to a control and display unit (CDU), placed near an operator's workstation (Fig. 1b). CDU can be then be connected by cable or wireless to external PC or network. The inspection is done typically once per shift. The MH design can be tailored different applications, for example, for drilling rigs it's design can incorporate stabilisation rollers for high speed travel of the rope, and foresee frequent removal for re-cutting. In contrast the MH for mining hoists (Fig. 1a) and ladle crane are installed permanently on the rope [6], with a reinforced casing for arduous environments. CDU indicates rope condition in a traffic light manner, while additional information is displayed on the LED. Results may also be viewed on a PC in real time. Accuracy of LMA measurement is 2% and sensitivity to wire breaks is about 0.5% of metallic cross-sectional area. Fig. 1b shows installation of two CDU's at the double drum mine hoist.

a b

Figure 1: Magnetic head (at mine hoist) and 2 control and display units of INTROS-AUTO at the double drum hoist

2.1 Integration of rope monitoring into the enterprise information system

For a modern digital enterprise it is important that all manufacturing processes are controlled from one center and all processed data is fed into an appropriate database for further decision making. A rope monitoring system must thus allow local and remote centralised operation (access to control monitoring of all ropes in the hoist – one, two or four, from one console).

Inspection data should be processed automatically and the results loaded into the enterprise's information system. These results should be available for different level of staff: a detailed inspection report for engineers and foremen, and an aggregated report for managers and supervisors. Raw inspection data should be stored in the memory of monitoring system, but be readily available for downloading to verify inspections results by authorized experts. This increases reliability by allowing to fine-tune the system during comissioning and re-calibration (after the rope has been replaced).

Figure 2 depicts a generic information exchange between the monitoring and the enterprise information systems. MH acquires inspection signals from the sensors on the rope, these signals are processed and logged in the CDU; results can then transmitted to the operator console in real-time mode or downloaded later. Inspection result reports can be sent automatically to any appointed persons, for example the chief maintenance officer. If qualified staff wishes to review the inspection results, they call them from the data stored on enterprise servers.

Special software allows to estimate the residual rope lifetime based on inspection results and rope operation conditions. It is also important that accumulated inspection data can be represented in aform of an incremental report accessible from PC, tablet or smartphone, which reflects deterioration of the rope in dynamics to facilitate rope maintenance planing.

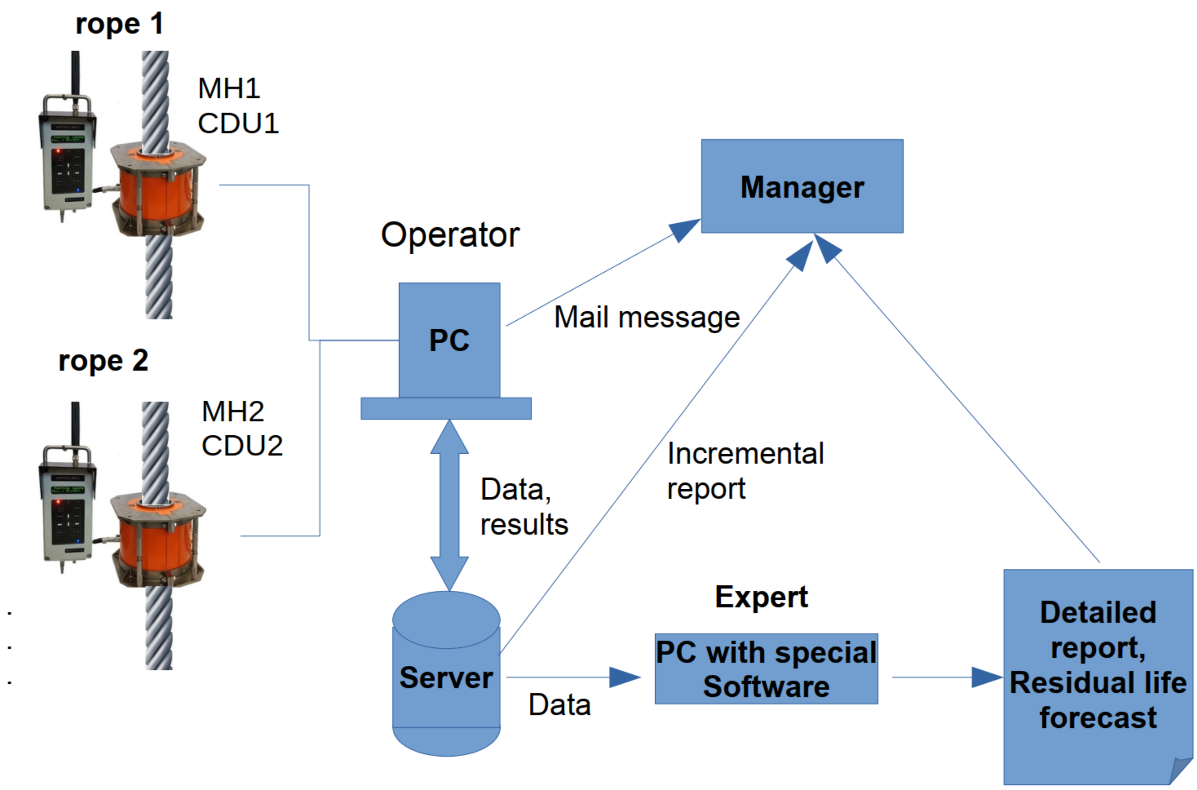

Figure 2: Data flow diagram for rope monitoring system

3 Drilling rig case study

Implementing the rope ACMSs on drilling rigs carries an additional challenge that these facilities are usually remotely situated in remote wilderness or open seas. Their manning personnel work in shifts, are subject to regular shuffles, with few holding any qualification in non-destructive testing. In addition, there is no regular time window for installation and maintenance at such facilities. Rope inspection should thus take a minimum of time and not require any special training.

The magnetic head must be positioned such that the most stressed segment of rope, prone to deterioration and be accessible to personnel, will be inspected. Usually this is near the drum. Due to the rope experiencing lateral travel as the drum unwinds, the MH is in constant mechanical contact with the rope (by means of special rollers). To minimise wear, its is removed when data collection is not required (**Figure 3** shows the MH INTROS-AUTO on a calf line). Installation and removal of MH from the rope takes no more than 15 minutes in total, which is acceptable for a daily inspection.

The drilling rig may not have a common local network and a single-unit server, so the monitoring system stores all the necessary data to forward the foreman or supervisor the results of ongoing monitoring and the ability to create an incremental report over a cable or wireless connection.

Rope maintenance on drilling rigs is planned in accordance to the mass-distance (tonne-kilometer, ton-mile etc.) that the rope carries, which is counted in the rig's controlling system. The INTROS-AUTO can receive this or calculate itself by taking raw data from the tension meter on the hook and an external odometer. **Figure 4** shows an incremental inspection report with reference to the current operating time of the rope. This allows to schedule rope maintenance operations and extend the service life by combining current mass-distance rope life and the found damage, should the operating company incorporate such a system into its management chart.

Figure 3: MH INTROS-AUTO at the rope of drilling rig hoist

Report on rope technical condition

Inspected item: Drilling rig NNN

Rope certificate: № 4134856006.

Rope construction: СТО 71915393

Rope lengtht, diameter: 0 м, 64 мм.

		Inspection date and time	Rope run , (tkm)	Length of inspected section, (м)	Found defects			Increment against previous inspection	Assessment of rope condition
					LF, (at the whole rope)	Maximum LF density (for 6D)	LMA, (%)		
1	2	3	4	5	6	7	8	9	10
		21.01.2021 18:36	125	748	5.0	1	1	0.0	Usable
		22.01.2020 18:55	305	769	6.0	2	0	1.0	Usable
		23.01.2020 18:36	562	758	8.0	2	1	2.0	Usable
		24.01.2020 18:36	794	748	12.0	2	1	4.0	Usable
		25.01.2020 18:32	1131	756	18.0	5	1	6.0	Limited-usable

Figure 4: An incremental report of rope testing according to rope run in ton-milage

The INTRO-AUTO system has been implemented on more than 20 drilling rigs of various oilfield service companies and has been successfully used for more than 8 years. It has also been delivered to a range of mining and metalurgy companies. Appraisals have been carried out on many other applications including ropeways, heave compensation systems, skip loaders and many other high value applications, where the ropes can face rapid subjective deterioration patterns

4 Conclusions

The best implementation of a wire rope automated condition monitoring system is when it is integrated into the general information environment of the enterprise. This ensures increased safety and accelerates management decision-making process. Full economic benefit will be possible if the reports are integrated into the relevant operating regulations.

5 References

[1] Sukhorukov V., Slesarev D., Vorontsov A. Electromagnetic Inspection and Diagnostics of Steal Ropes: Technology, Cost-Effectiveness, Problems. – Materials Evaluation, 2014, №8, pp. 1019- 1027.

[2] ISO 4309:2017 International standard. Cranes – Wire ropes – Care and maintenance, inspection and discard.

[3] EN 12927:2019. Safety Requirements for Cable Way Installation Designed to Carry Persons Ropes. Part 8. Magnetic Rope Testing (MRT).

[4] Marais J., Bester N. A holistic approach to continuous rope monitoring. Proceedings of the OIPEEC Conference 2011, Texas, p. 85.

[5] Slesarev D., Sukhorukov D., Shpakov I. Automated magnetic rope condition monitoring: concept and practical experience. - Proceedings of the OIPEEC Conference 2017, La Rochelle, France 2017, pp.295-300.

[6] Sukhorukov V., Slesarev D, Shpakov I., Volokhovsky V., Vorontsov A., Shalashilin A. Automated condition monitoring with remaining life time assessment for wire ropes in ladle cranes. Materials Evaluation, 2021 (Vol.79), №11, pp. 1050-1060

Challenges and opportunities of Permanent Magnetic Testing with Automated Evaluation on Running Ropes

Dipl.-Ing. Ralf Eisinger

University of Stuttgart, IFT, Germany

Johannes Keller, M.Sc.

University of Stuttgart, IFT, Germany

Johannes Guter, M.Sc.

University of Stuttgart, IFT, Germany

Franziska Stegmaier, M.Sc.

University of Stuttgart, IFT, Germany

Summary

Magnetic rope testing (MRT) of steel wire ropes has different limitations on ropes with a high amount of small diameter wires. The metalic cross section of one broken wire is very small compared to the metallic cross section of the complete rope. This leads to a very small change of the base signal of the rope. So the detection of single wire breaks is challenging. The paper presents two methods, which deal with that situation and lead to a significantly improved quality of measurement results.

Keywords: Steel rope, permanent rope monitoring, discard detection, MRT

1 Introduction

1.1 History of magnetic wire rope testing

The origins of magnetic wire rope testing go back to the use of wire ropes in mining. At the beginning, simple circuits were used to detect protruding wires. In the early 20th century, magneto-inductive testing methods were used to check gun barrels, and this measuring method was first used to test wire ropes from 1906. Due to the high level of personal injury in the event of a failure, this testing technology was used early on in the ropeway sector. In addition, the prices for new ropes and their installation are high here. Richard Woernle began to research into magnetic rope testing at the University of Stuttgart in 1931. This resulted in the patent for the separable measuring coil in 1937, which significantly simplified the practical use of magnetic rope testing. Building on this, magnetic rope testing was continuously developed at the Institute of Mechanical Handling and Logistics (IFT) of the University of Stuttgart, Germany, with the next important step being the introduction and use of Hall sensors. Over the next few years, an important focus will be on the miniaturization and automation of the test methods and the associated evaluation. [1]

1.2 MRT – coil sensor and hall sensor

The variation in the magnetic field around the rope caused by wire defects can be recorded using various sensors. The two most commonly used types are Hall sensors (shown in green in **Figure 1**) and measuring coils (shown in orange in **Figure 1**). Basically, the sensors can be used in two orientations, axial (parallel) to the rope, or radial (perpendicular) to the surface, depending on the fault, one orientation is preferred. [1][2]

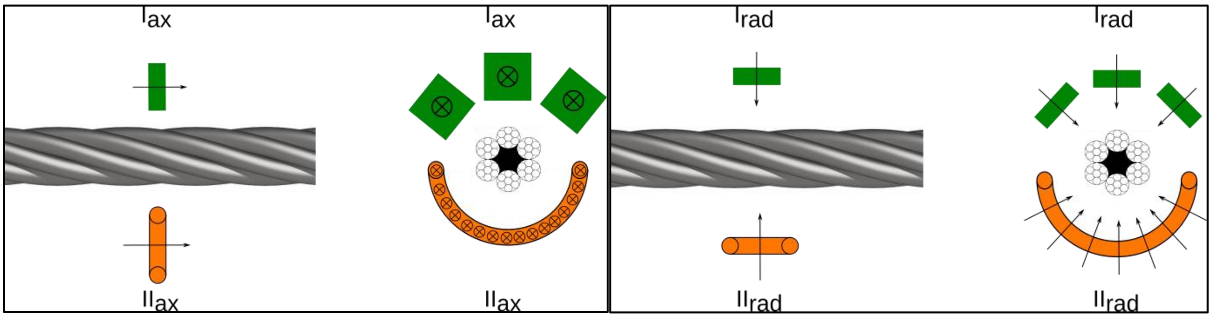

Figure 1: Most common sensor types of MRT

1.3 Hall sensor

A Hall sensor in general consists of a Hall element, a constant current source, an amplifier circuit and (if required) digitaliization. Due to the size of the Hall element installed in the Hall sensor, the measurement can be regarded as almost point-shaped. This makes it possible to precisely resolve local defects. This is particularly useful for wires with small diameters.

Furthermore, it is possible to make statements about the wire condition by forming sums or partial sums if individual wire break signals would otherwise be lost in the total sum of the measuring coil or the sum of all Hall sensors.

One challenge with measuring systems with many Hall sensors is the amount of data that has to be processed and stored. In addition, the power consumption of the Hall sensors and the evaluation electronics should not be underestimated.

1.4 Coil sensor

One advantage of a measuring system with coils is the simple design, which consists of the coil and a single channel for analog-digital conversion. Furthermore, there are no component-specific deviations (e.g. due to tolerances in production), which means that the sensor does not need to be calibrated. In addition, a coil forms an almost perfect integral over the magnetic field emerging vertically from the magnet; in contrast, the sum of individual Hall sensors is only a sum of individual points.

2 MRT and physical limits

A limiting factor in MRT is the size of the metallic cross-section area caused by the damage. When measuring using coils, this is evident from the law of induction, which states that the measurable voltage difference at the coil depends on the change in the magnetic field over time. With Hall sensors, the magnetic field is measured directly, which means that measurements can also be taken at low speeds or at standstill. In both cases, the change in the magnetic field depends on the magnitude of the change in the magnetic field and therefore on the change in the metallic cross-section area.

3 Permanent rope monitoring

There are several new challenges with permanent MRT, one of which is length measurement and position determination. Many MRT systems use an encoder in combination with a running wheel that rolls over the rope to determine the position. This is not possible for applications that are operated 24/7, as the wheels and encoders would otherwise have to be replaced regularly due to wear. If measurements are compared that were taken at two different points in time, slippage between the cable and the wheel can impact the evaluation, as the recorded position of defects in the measurement record can change. Another point that must be taken into account is the elongation of the rope. This is particularly important at the beginning of use, as the rope is still elongating. The elongation can also change the position of wire breaks, or the position no longer matches a subsequent measurement. A solution must therefore be found for combining several measurements with different rope elongations. To estimate the remaining service life, it is also important to have precise information about the rope drive and the moving load. This makes it possible to calculate the number of bending cycles per rope section and, in combination with the load, to estimate the remaining service life. In order to avoid special measurement runs, it is also necessary to combine partial measurements of the rope, for example those that occur during the usual travel movements of an S/R maschine, into an overall measurement. This generates large amounts of data that need to be processed and stored. The challenge here is to decide which data can be saved for comparison with a new measurement and which can be deleted. This requires the development of efficient data formats and algorithms.

4 Methods for automated evaluation of permanent data acquisition

In permanent measuring systems, coils, Hall sensors or a combination of both can be used as sensors. If the measuring system is used with a multi-strand cable construction, neither of the two typical evaluation methods can be used.

However, the two evaluation methods presented below fulfill the necessary conditions for use with a permanent measuring system.

4.1 Envelope-Method

The envelope curve method considers the changes between a reference measurement and the current measurement.

After a new rope has been applied, a reference measurement is carried out first. This is then stored in the evaluation system. The latest measurement is then compared with the reference measurement for each movement. Changes in shape between the envelope curve of the reference measurement are then evaluated as wire breaks. The reference measurement is then replaced by the current measurement. **Figure 2** shows a reference measurement (black curve). The actual measurement is shown in red and shows changes at two positions compared to the reference measurement. These two changes are then added to the list of wire breaks at the corresponding positions and the current measurement is used as the new reference measurement.

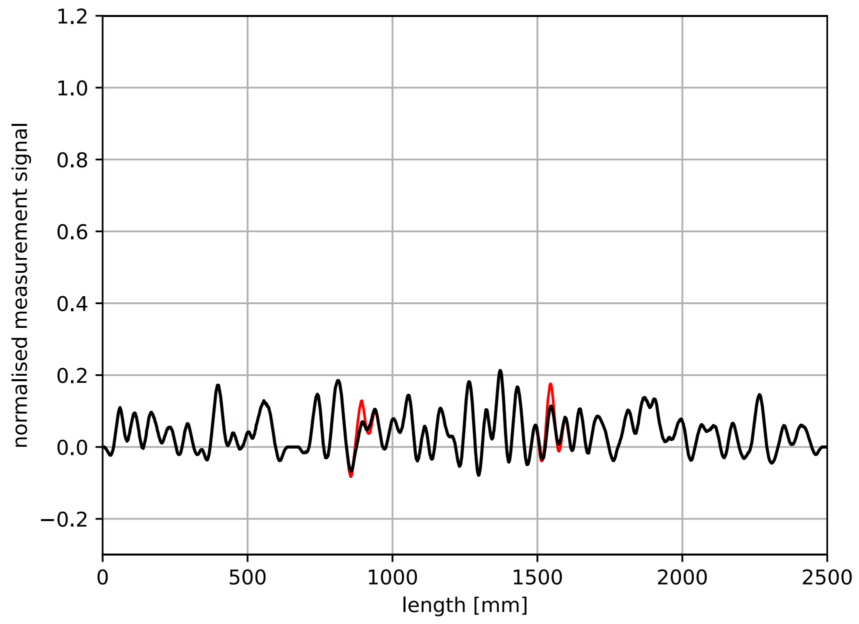

Figure 2: Reference measurement (black) and actual measurement with two changes (red)

This method does not enable the detection of multiple wire breaks at one position between two measurement points. However, since a permanent measuring system can be measured during every movement, it is statistically very unlikely that multiple wire breaks will occur in a very localized area.

4.2 Complementary method for single signals

When using Hall sensors, there are several possibilities compared to a coil sensor. On the one hand, the sum of all Hall sensors can be formed, so that an evaluation option with the envelope curve method is also available here.

Figure 3 shows a typical Hall signal of a stranded rope:

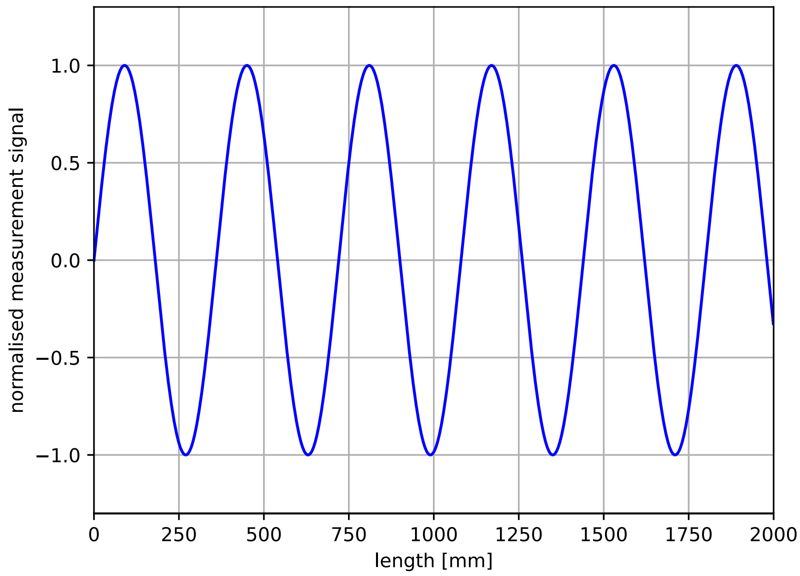

Figure 3: Typical Hall signal of a stranded rope

On the other hand, individual Hall sensor signals can also be analyzed.

It shows that the basic signal of a single Hall sensor is strongly dominated by the strand crests (high points) and strand troughs (low points). When wire breaks are superimposed on this basic signal, they are only recognizable if the signal of the Hall sensor is strongly influenced by the wire break. This means that the wire break should ideally be located directly under the Hall sensor and the broken wire should have the largest possible diameter.

The following method is intended to eliminate the disturbing influence of the background signal on the measurement in order to improve the detectability of wire breaks.

4.2.1 Basic method

If a signal has a pattern, then interference can be detected in this signal by comparing an undisturbed signal with a disturbed signal. This also makes it very easy to determine the type and form of the interference. In order to keep the computational effort low and the process fast, the undisturbed signal is converted into a complementary signal. Both signals are then added together. It is then very easy to detect interference in the sum signal.

Figure 4 shows the basic procedure using the example of a sine function. The blue curve represents the undisturbed signal. The black curve corresponds to the complementary signal. The green curve then represents the sum, which results in zero for all positions.

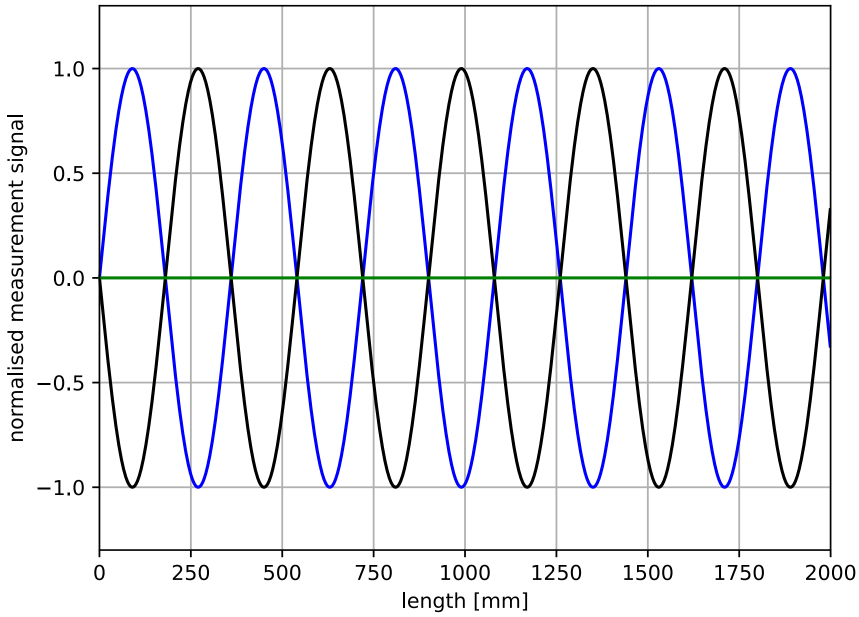

Figure 4: Basic prodcedure - undisturbed signal (blue), complementary signal (black), sum (green)

Figure 5 shows the same signal, but a disturbance in the form of a wire break signal has been added at one point. The blue curve again corresponds to the undisturbed signal, the red curve is then the signal with the disturbance: this would correspond to the measurement in reality. Here, the wire break signal is also very clearly recognizable in the sum curve. This can be detected automatically using very simple methods due to its clear highlighting in the sum curve.

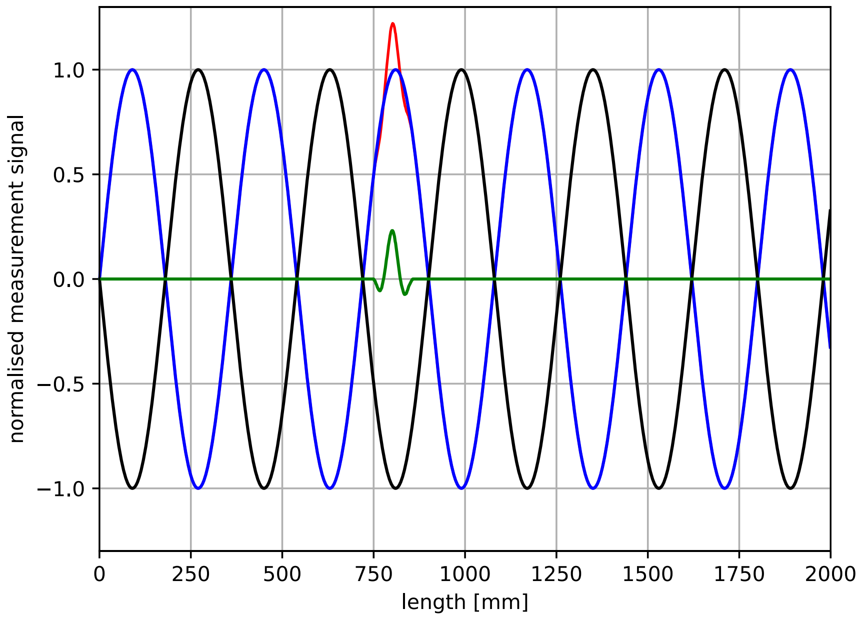

Figure 5: Disturbance in the form of a wire break signal has been added at one point

Figure 6 shows a similar situation: the blue curve again represents the undisturbed signal, the red curve the signal with the disturbance. The wire break is added here at a point that changes the signal only very slightly. Detecting this interference automatically and reliably is only possible - if at all - with very high computing effort. However, if the complementary method is also used here, the wire break in the sum signal is very easy to detect.

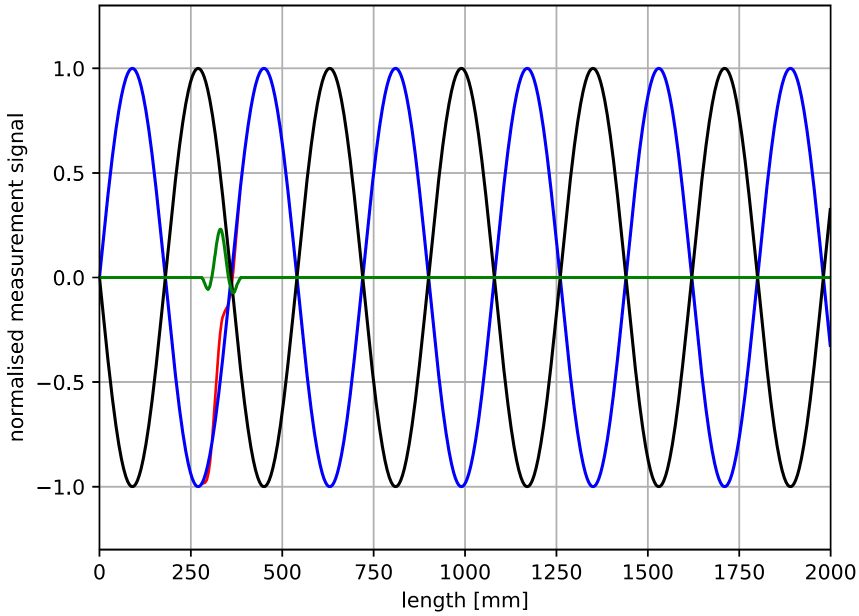

Figure 6: Wire break is added at a point that changes the signal only very slightly

4.2.2 Evaluation of permanent MRT in application

There are several points to consider when transferring this method, including the determination of the complementary signal, into the application. In principle, it is possible to record the signal of the rope in the unused state and generate the complementary signal from this. However, this method has two decisive disadvantages: Firstly, the method does not take into account the elongation of the rope over its service life and would have to be permanently adjusted. Secondly, the basic signal changes significantly over the service life of the rope. This means that the amplitude and signal shape would also have to be adjusted.

The method used here takes a different approach: the signal from a Hall sensor, which is offset by 360°/(number of strands) around the circumference, is used. This ensures that the complementary signal has the same lay length at this point and that the influence of the service life is the same.

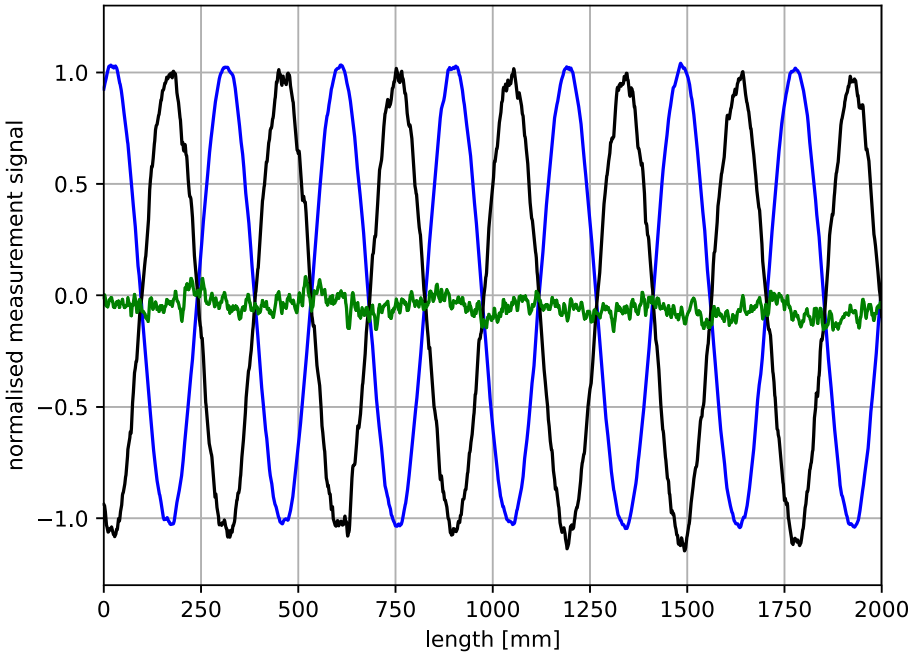

Figure 7: Signals of two Hall sensors that are in a complementary position

Figure 7 shows the signals of two Hall sensors that are in a complementary position. The blue curve shows the signal of the Hall sensor under investigation, the black curve shows the complementary signal. The green sum curve is not exactly zero, as in theory, but shows only slight fluctuations.

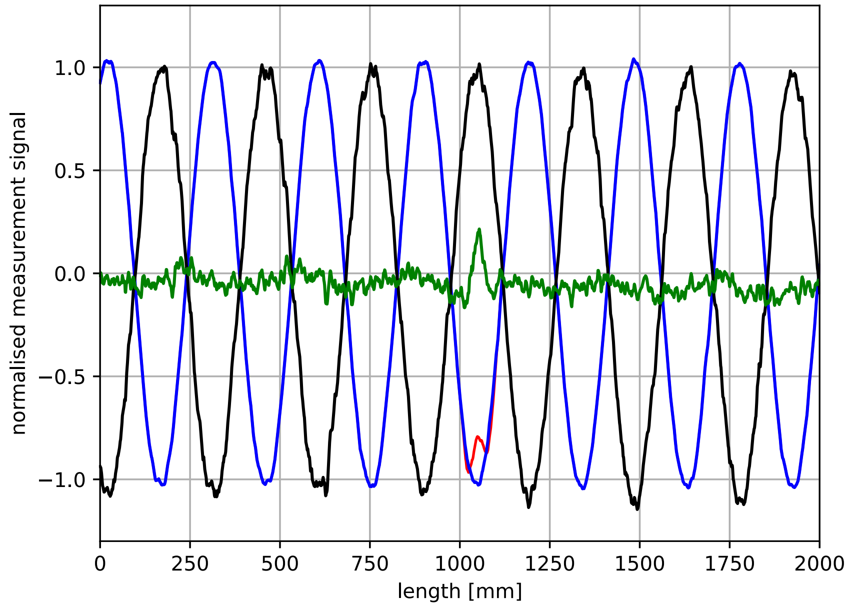

Figure 8: Signal with a wire break

Figure 8 shows the blue curve of the undisturbed signal. The red curve, on the other hand, was superimposed with a wire break. In the red measurement signal curve, you can safely assume that there is a fault at position 1100. However, it is not possible to recognise the nature of the fault. But in the green sum curve the wire break is clearly detectable.

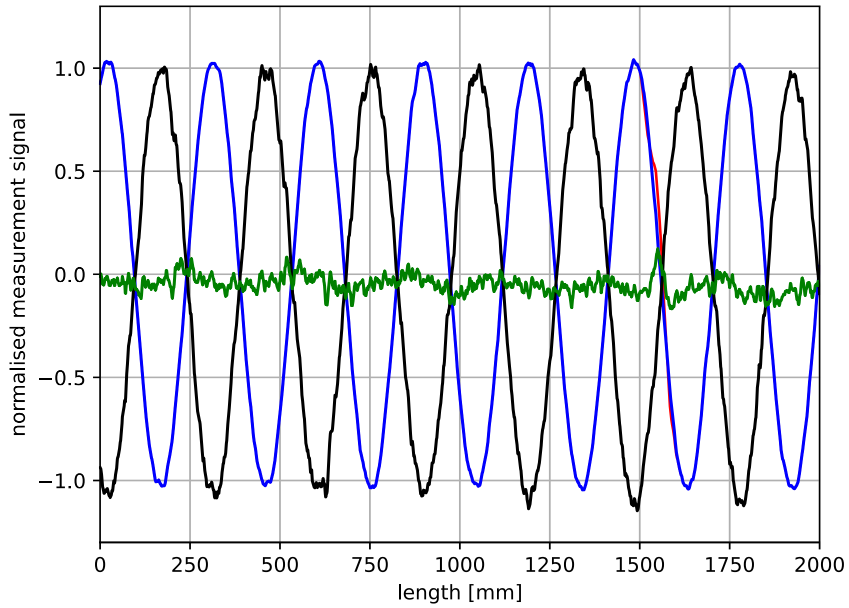

Figure 9: Another example with a more hidden wire break in the measurement

Figure 9 shows a similar case as Figure 8. However, no interference is recognisable in the red measurement curve. The comparison between the undisturbed blue signal curve and the red one also suggests that there is no interference. However, the wire break is clearly recognisable at position 1600 in the green summation curve.

Of course, with this method it cannot be ruled out that there is also a wire break in the complementary signal at exactly the same position, which is then mirror-inverted due to the complementation. In this case, the two signals would cancel each other out during summation and the two wire breaks would not be visible in the summation curve. However, this can be easily avoided by comparing the signal to be examined with different complementary signals or by combining several complementary signals into an averaged complementary signal. This makes it very unlikely that a wire break will not be detected.

5 Conclusions

Ropes that consist of many wires and therefore the metallic cross-sectional area of the individual wires is very small in relation to the total metallic cross-section still pose a challenge to the interpretation of signals that are recorded using magnetic measurement methods. Two methods were presented, both of which have been developed with this problem in mind. Initial tests have shown significantly better results than previously used methods.

Different test series are currently planned, which will be recorded using a permanent measuring method and analysed using these two methods.

However, the method with the complementary signals is also suitable for individual measurements in which the rope was measured using Hall sensors.

6 References

[1] Feyrer, K.: FEYRER: Drahtseile – Bemessung, Betrieb, Sicherheit. Heidelberg: Springer-Verlag, 2018.

[2] R. Eisinger, J. Görres, J. Keller, J.Guter: New ways of evaluation of damage to wire ropes by combining different non-desctructive rope testing methods, OIPEEC Conference 2024.

7 Authors' Introductions

Mr Dipl.-Ing. Ralf Eisinger received his degree in Mechanical Engineering from University of Stuttgart, Germany. He is working since 2006 at IFT as a scientific assistant. His main interest is in non-destructive rope tests and also in ropeways. Actually, he is the group leader of the no destructive rope test department.

Mr Johannes Keller, M.Sc. is a member of the team "Non-destructive Rope Testing" of the department “Rope Technology” of the Institute of Mechanical Handling and Logistics (IFT) of the University of Stuttgart, Germany. He is active in magnetic inductive and visual rope testing as well as in the development of rope testing methods and rope testing devices.

Mr Johannes Guter, M.Sc. received his M.Sc. degree in Mechanical Engineering from University of Stuttgart in 2023. He began his professional career at the Institute of Materials Handling and Logistics (IFT) at the University of Stuttgart, Germany, where he works in the field of non-destructive rope testing. His work focuses on the development of new rope testing methods, the supervision of students and research into non-destructive rope testing. He is active in the field of visual and magnetic rope testing.

Ms Franziska Stegmaier, M.Sc. is a member of the team “Destructive Rope Testing” of the department “Rope Technology” of the Institute of Mechanical Handling and Logistics (IFT) of the University of Stuttgart, Germany. She ist active in testing and research of fibre ropes, steel wire ropes and PPE against fall from heights.

Effect of load and twist on filament packing in three-strand aramid fibre ropes: a micro-CT study

Oday Allan, M.Sc.

University of Twente, The Netherlands

Dr. Tanmaya Mishra

University of Twente, The Netherlands

Prof. dr. ir. Matthijn de Rooij

University of Twente, The Netherlands

Summary

This study investigates how varying rope and strand twists influence the filament packing fraction in three-strand Aramid fibre ropes. Micro-computed tomography (micro-CT) scanning was used to visualize and quantify filament arrangements under different twist configurations and loads. High-resolution CT-scan image segmentation enabled the calculation of local filament packing fractions. Results indicate that twist parameters strongly affect how tightly filaments pack inside strands, particularly when a tensile load is applied. Higher twist levels often lead to a more compact internal structure, whereas lower twist levels introduce voids and an uneven arrangement. Under tensile loading, additional compaction is observed, especially at strand-to-strand interfaces. The findings help in understanding how twist geometry and applied tensile load redistribute filaments in a three-strand configuration, providing insights into load sharing, potential filament slip, and internal damage – all critical factors in assessing rope performance and service life.

Keywords: Rope mechanics, Packing fraction, Twist configuration, Micro-CT, Filament distribution, Internal wear

1 Introduction

Ropes are constructed at multiple hierarchical levels, starting with individual filaments that are twisted into strands and eventually into a final helical rope structure [1, 2]. The packing fraction of the filaments in a strand represents the proportion of the cross-sectional area (or volume) of the strand that is filled by filaments as a fraction of its total 'apparent' cross-sectional area (or volume), which also includes voids [3, 4]. This structural parameter of the rope is known to influence its performance significantly. Studies have indicated that a high packing fraction can reduce local stress concentrations, distribute loads more uniformly among filaments, and increase rope stiffness [5-7]. However, excessively tight packing of filaments can increase inter-filament friction, generating heat and promoting internal abrasion or fretting under cyclic loading. Conversely, a rope structure with loosely packed filaments can not only reduce internal friction but also increase filament slip/migration, allowing certain filaments to carry more load than others, causing stress localization. An optimal filament packing is, therefore, required to maximize rope strength and lifetime [8].

The twist introduced at the strand level (by twisting a bundle of filaments to form a strand) and at the rope level (by twisting multiple strands around a central axis of the rope) affects the internal arrangement of filaments. The overall twist configuration, which includes both strand and rope-level twisting, modifies the position and orientation of the filaments, changing the contact forces among them, which in turn can increase or decrease the local packing fraction. Excessive twist may cause severe contact pressure, resulting in non-uniform stress distribution and high frictional heating. Insufficient twist can allow filaments to splay outward, leading to low packing fractions and high filament slip or localized load sharing [3, 8-10]. It is therefore critical to understand how these twist combinations and loading conditions affect structural properties of the rope at the filament level, such as packing fraction, in order to fully understand the damage mechanisms at the rope level.

Recent developments in X-ray micro-computed tomography (micro-CT) have made it possible to image and characterize internal rope structures in detail [11]. Micro-CT provides a high-resolution, three-dimensional view of the placement and distribution of filaments and voids inside the rope, which are not directly observable in an intact, twisted rope. Several authors have leveraged micro-CT to analyse filament orientation and spatial distribution in twisted yarns and ropes [11, 12].

For instance, prior studies have focused on natural fibre ropes, where micro-CT was used to model fibre migration and measure fibre packing density across concentric rings of a rope's cross-section rather than segmenting individual strands [11]. This approach provided insights into staple fibre migration and tension distribution but had limitations in measurement precision and applicability to synthetic fibre ropes. Additionally, micro-CT has been employed to examine single continuous-filament yarns, analysing overall fibre packing density as a function of applied tensile load [12]. However, this study did not investigate variations in packing fraction within individual strands under the same applied load, nor did it address ropes with multiple twisted strands, such as three-strand aramid ropes.

In this paper, internal filament arrangements are examined to compute filament packing fractions in three-strand laid ropes with multiple twist configurations, under tensile loading and in a relaxed state, using micro-CT. The aim of this study is to determine how twist geometry and loads interact to influence the distribution and compaction of filaments across different regions of each strand, particularly near strand interfaces. Using micro-CT segmentation, we analyse how the filament packing fraction varies from the strand interface outward, distinguishing between the outer surface and inner core regions. This allows us to assess how these regions press against each other under load and how local filament compaction changes with applied tension. Our understanding of the filament packing fraction will inform practical rope engineering guidelines, such as the selection of strand twist levels and rope lay direction, to optimize rope designs for controlling frictional wear, managing filament slip, and extending service life. Materials and Methods

1.1 Rope Specimen

Specimens comprised three-strand synthetic ropes made from continuous aramid filaments. Each strand consisted of approximately 1000 filaments with a total linear density of 1620 $dtex$. The rope was developed by first applying a specific twist in each direction (Z) to gather the bundle of filaments into a strand, defined as strand twist (turns/m), followed by a twist in the opposite (S) direction to assemble the three strands into the rope, defined as rope twist (turns/m). Different specimens were produced, each with unique strand and rope twist parameters, as listed in **Table 1**. By controlling the twist geometry with a fixed fibre material, it was possible to isolate and study the effects of twist on the internal arrangement of filaments.

Table 1: Overview of the used rope specimens and the applied loads in the study.

Rope name	Z: Strand twist [turns/m]	S: Rope twist [turns/m]	Pre-tension [N/tex]	Tension [N/tex]
Z100S50	100	50	0.06	0.37
Z200S50	200	50	0.035	0.37
Z150S100	150	100	0.06	0.33
Z200S100	200	100	0.06	0.24

1.2 In-Situ Loading and Micro-CT Scanning

A micro-CT system (Zeiss Xradia 610 Versa) was used to scan rope sections placed under varying tensile loads, as shown schematically in Figure 1a. Samples were mounted on a small load frame that fits inside the micro-CT chamber, as shown schematically in Figure 1b. A low initial preload was applied, followed by either a near-zero tensile load (relaxed state, e.g., 0.06 N/tex) or a moderate working load (e.g., 0.37 N/tex). After holding the rope at the chosen tensile load for at least two hours to allow thermal equilibration and internal filament rearrangement, CT scanning was conducted at ~ 0.9 µm spatial resolution. The scanned length typically covered 3 – 4 mm of rope length and the entire rope diameter (~ 0.9 mm). A reconstruction from more than 3,200 projections of the CT-scanned images of cross-sections at different heights yielded a 3D image stack showing a clear contrast between solid filaments and the empty void space.

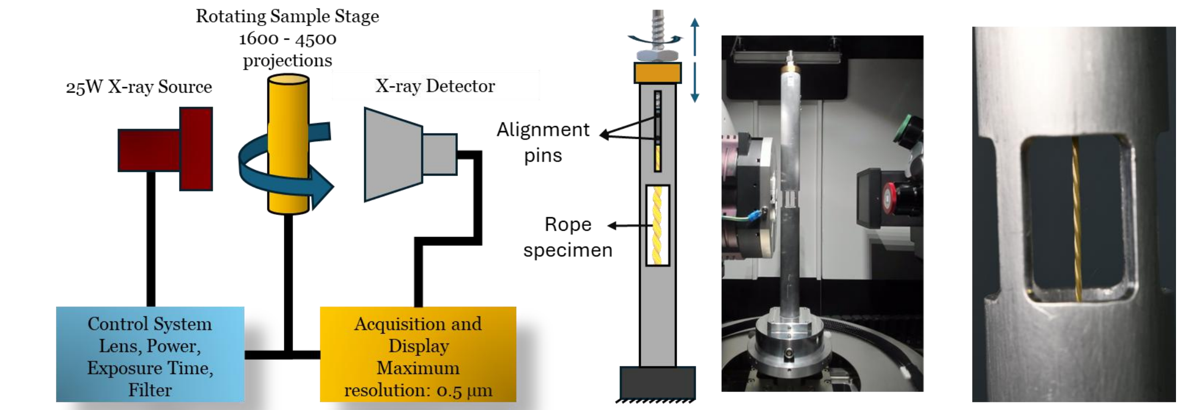

Figure 1: (a) Schematic illustration of the micro-CT system, showing the X-ray source, rotating sample stage, and detector. (b) Diagram of the in-situ tensile loading device used for rope testing within the micro-CT chamber. (c) Photograph of the setup installed inside the micro-CT scanner, with the rope specimen mounted for imaging. (d) Close-up image of a three-strand rope under applied tensile load.

1.3 Image Segmentation and Analysis

Micro-CT scans of fibrous strands were visualized and analysed in ORS Dragonfly [13]. To automate filament segmentation, two UNet++ [14] deep learning models were trained on manually processed images, each targeting a distinct segmentation task. The first model was trained on five carefully segmented slices to generate the filament region of interest (ROI_{fila}), distinguishing filaments from voids based on X-ray attenuation contrast. The second model was trained on five semi-manually labelled images, where small circular markers were placed at the centre of each filament to serve as seeds for individual filament identification. Once trained, both models were applied to the entire dataset, successfully generating ROI_{fila} (filament segmentation) and ROI_{seeds} (filament centre markers) across all scanned cross-sections.

This automated process worked efficiently across all rope constructions tested in this study, demonstrating its robustness. It suggests that the same approach can be applied to any fibrous material with filaments of similar diameter (~12 µm) and roundness.

The watershed technique [15, 16] was then applied to segment individual filaments within the rope structure. Each seed in ROI_{seeds} acted as a starting point, expanding into a unique region that defined a single filament. As a result, this process produced a multi-region segmentation, referred to as $mROI_{fila}$, where each filament is now distinctly separated and assigned an individual region within the dataset. Unlike ROI_{fila}, which only identified filaments collectively, $mROI_{fila}$ ensures that each filament is individually isolated. The step-by-step process of generating $mROI_{fila}$ is illustrated in **Figure 2**.

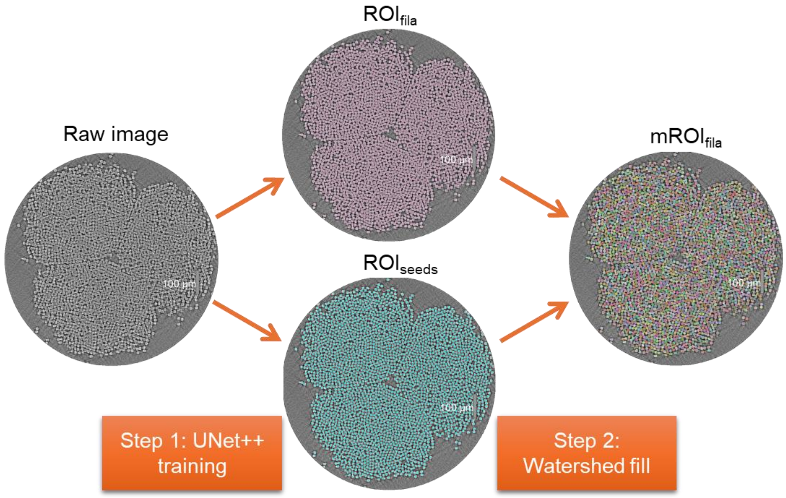

Figure 2: Workflow for Generating Multi-Region Filament Segmentation ($mROI_{fila}$)

To analyse the packing fraction of individual strands, filaments were further separated into three distinct strand-specific regions of interest (ROI_{filaN}). This was achieved by manually selecting a strand in a randomly chosen 2D slice (x, y image) to define a strand mask (ROI_{maskN}). The "Keep Intersected" algorithm was then applied between ROI_{maskN} and $mROI_{fila}$, automatically extracting any filaments touching the selected strand mask. This process enabled the efficient separation of filaments into ROI_{fila1}, ROI_{fila2}, and ROI_{fila3}, each corresponding to filaments of a different strand within the rope.

Small intra-strand gaps in the cross-sectional images were filled using the 3D Close Fill algorithm within ORS Dragonfly, with a fill value of 17 pixels, slightly exceeding the filament diameter, corresponding to an approximate volumetric size of ~15 µm in each spatial dimension. This step produced three continuous "filled strands" regions of interest ($ROI_{strand1}$, $ROI_{strand2}$, and $ROI_{strand3}$), which were segregated from the original filament-only segmentation. **Figure 3** provides a step-by-step illustration of this process.

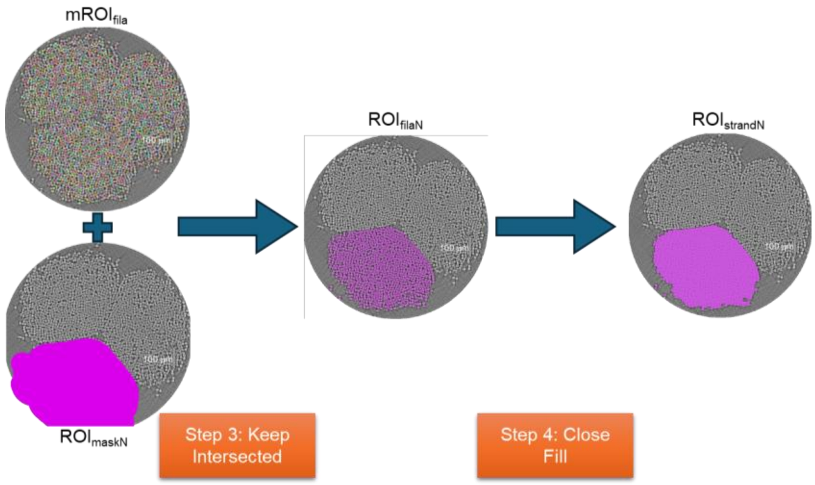

Figure 3: Strand-Specific Filament Extraction Using ROI Masking and Close Fill.

For clarity, the filament-only segmentation is referred to as ROI_{fila}, the multi-region segmentation (after watershed) is $mROI_{fila}$, and the continuous, filled segmentations are referred to as $ROI_{strandN}$. Both ROI_{filaN} and $ROI_{strandN}$ were exported as binary data (.raw files) on a slice-by-slice (cross-section) basis for subsequent analysis in MATLAB.
The packing fraction at any slice, ϕ, was then calculated by comparing the number of filament pixels to the total number of filled-strand pixels, as expressed in Equation (1). The ratio thus indicates the portion of the cross-section occupied by filament material.

$$\phi = \frac{(\text{Number of filament pixels in } ROI_{\text{strand}})}{(\text{Number of pixels in } ROI_{\text{filled}})} . \quad (1)$$

1.4 Rectangular Cross-Sectional Slicing

To analyse how the filament packing fraction varies within each strand, each strand's cross-section was further divided into discrete shells (rectangular bands) perpendicular to the strand's major axis, as shown in **Figure 4**. This slicing process allows for a detailed spatial analysis of filament distribution within strands, particularly how the filament packing fraction varies from the strand's interface to its core.

The MATLAB code first computes the 2D orientation (in degrees) and centroid for each strand cross-section using the *regionprops* function. A rotated coordinate system is then defined, ensuring that the primary axis of the strand aligns with the horizontal direction and that the perpendicular axis (cross-coordinate) follows the orthogonal direction to this orientation. This transformation standardizes the slicing approach across all strand sections.

Once the rotated coordinate system is established, the strand's cross-sectional width is measured along the cross-coordinate direction (i.e., perpendicular to the strand's primary axis). This range, from the minimum to the maximum cross-coordinate value, is divided into n equal-width intervals, creating n rectangular bands (shells) within each strand. In this study, n = 4, as illustrated in Figure 4.

For each shell, the number of filament pixels ($\text{ROI}_{\text{filaN}}$) and total strand pixels ($\text{ROI}_{\text{strandN}}$) are computed. The local packing fraction, ϕ_L, is then obtained for each shell as:

$$\phi_L = \frac{\sum \text{ROI}_{\text{filaN}} \text{ shell pixels}}{\sum \text{ROI}_{\text{strandN}} \text{ shell pixels}} \quad (2)$$

This process is repeated for every cross-sectional slice across the entire 3D dataset. The individual packing fraction values for each shell are then aggregated across all slices and averaged, yielding an overall packing fraction value for each shell.

Additionally, the centroid of each shell is used to calculate its distance from the global rope centre (defined at a reference slice). This measurement allows for an assessment of how filament compaction varies relative to the strand interface.

2 Results and Discussion

Figure 5 presents the aggregated packing fraction profiles for each shell within the strands, plotted against the distance from the strand interface. The y-axis represents the mean packing fraction of each shell, while the x-axis denotes the distance of the shell from the interface towards the strand's core. Different rope configurations and tensile loads are shown, allowing for comparison of packing fraction trends across various conditions. Across all rope specimens, a radial gradient in packing fraction was observed, with lower values near the strand's outer boundary and higher values towards the core (see Figure 5). This gradient indicates that filaments in the outer regions experience lower compaction, while those closer to the core are more densely packed. Under tensile loading, the packing fraction increased at all radial positions, but this effect was most pronounced at the strand-strand interfaces, where packing fractions frequently reached values as high as $\phi \approx 0.75$

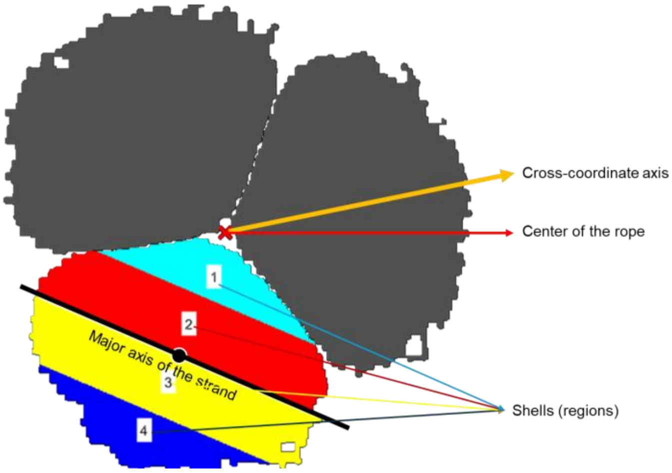

Figure 4: Schematic showing how one strand cross-section is subdivided into rectangular "shells" based on the strand's major axis. Each differently coloured band denotes a distinct shell, enabling the calculation of local filament packing fraction across the strand width.

Such high compaction in the interface regions suggests that tensile loading forces adjacent strands into tighter contact, increasing normal contact forces and consolidating filaments at these strand-strand interfaces. This mechanism could have significant implications for frictional interactions and load transfer efficiency in twisted rope structures.

For reference, the maximum theoretical packing fraction for 1,000 circles arranged in a hexagonal close-packed (HCP) structure is $\phi \approx 0.87$. The observed values near 0.75 suggest that while substantial compaction occurs under load, some voids and filament misalignment prevent perfect HCP arrangement. Additionally, natural variations in filament diameter, with a distribution around the average of $12\ \mu m$, also contribute to deviations from ideal HCP packing.

From a structural perspective, rope twist (S-turns/m, applied at the rope level) primarily controls the helix angle of strands around the rope's axis. A higher rope twist (S100 vs. S50) steepens the helical pitch of each strand, thereby increasing the contact between strands under load due to increased surface flattening [17]. Conversely, the strand twist (Z-turns/m inside each strand) dictates how filaments pack together within strands, thereby governing inter-filament friction and intra-strand consolidation. Together, these two twist parameters determine the overall rope geometry, which influences load sharing between strands (via rope twist) and filament compaction within strands (via strand twist).

Figure 5 illustrates the radial variation of packing fraction for each strand as a function of distance from the strand interface. The y-axis represents the mean packing fraction of each shell, while the x-axis denotes the distance from the interface (region 1) to the outer periphery (region 4). Different rope configurations and tensile loads are shown, allowing for comparison of packing fraction trends and radial compaction behaviours under different twist conditions.

Across all rope specimens, a gradual decrease in packing fraction was observed from region 1 (interface) to region 4 (outer periphery), but the extent of this variation depended on the twist configuration. The slope of the linear fits in Figure 5 quantifies how the packing fraction decreases radially, providing a mathematical comparison of compaction trends. Additionally, the total increase in packing fraction from unloaded to loaded conditions varied across configurations, indicating that the strand twist plays a primary role in increasing the overall packing fraction within strands under load.

The Z100S50 configuration exhibited the greatest variation in packing fraction among the three strands, as shown by the larger standard deviation (error bars) in Figure 5 (a). This suggests that the packing fraction is highly strand-dependent in this configuration, indicating non-uniform filament consolidation across strands. Interestingly, despite this high strand-to-strand variability, Z100S50 has the lowest slope of all configurations (-2.79×10^{-4} and -3.16×10^{-4}), meaning the packing fraction remains relatively consistent across radial positions (regions 1–4) within each strand. This suggests that the moderate rope twist (S50) does not strongly enforce inter-strand compaction, and the loose strand twist (Z100) allows more filament freedom, resulting in less radial compaction variation within strands.

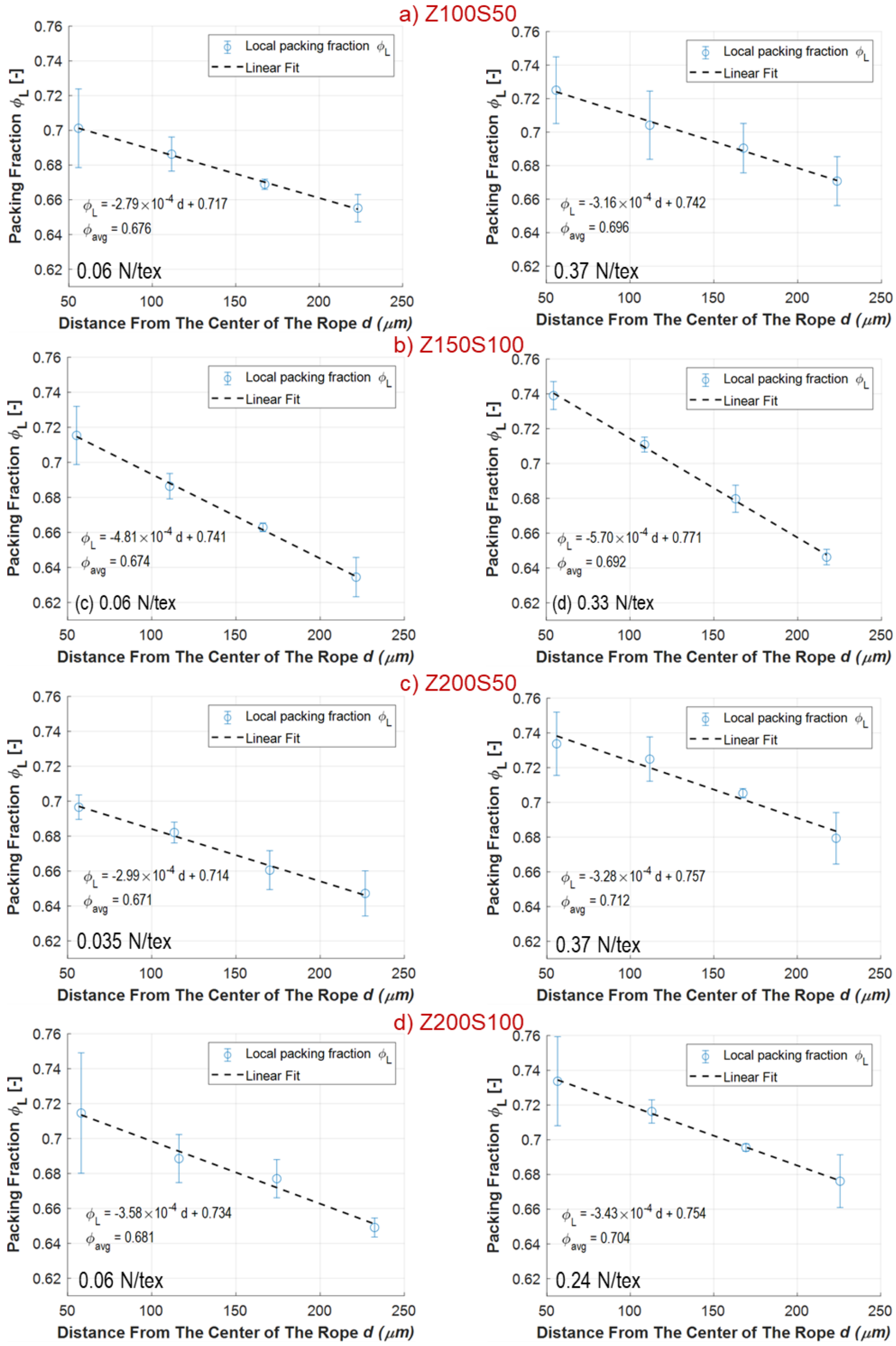

Figure 5: Radial packing fraction profiles for each strand in four three-strand rope specimens (a) Z100S50, (b) Z150S100, (c) Z200S50, and (d) Z200S100) under two tensile load levels. The packing fraction is plotted as a function of the distance from the strand interface. Φ_{avg} is given for each specimen based on the three strands.

Furthermore, Z100S50 exhibited the smallest increase in total packing fraction from unloaded to loaded states, meaning that applying a tensile load had the least impact on densification compared to other configurations. This indicates that a lower strand twist (Z100) limits the ability of filaments to compact under tension, leaving more void space even under load.

The Z150S100 specimen exhibited the most uniform packing fraction across all strands, as seen in Figure 5 (b). The packing fraction remained within ± 0.01 across strands, even at different loads, indicating a balanced interaction between strand twist (Z150) and rope twist

(S100). This combination effectively consolidated filaments while avoiding excessive inter-strand variation, leading to a more homogeneous compaction profile from the interface to the periphery.

The Z150S100 specimen exhibited the steepest decrease in packing fraction from interface (region 1) to the outer periphery (region 4), as shown in Figure 5 (b). The slopes of the linear fits -4.8×10^{-4} and -5.7×10^{-4}, meaning that the packing fraction declines most sharply from the strand interface to the outer periphery. Despite this steep radial shift, the packing fraction remains highly consistent across strands, suggesting that the balanced interaction between strand twist (Z150) and rope twist (S100) ensures a uniform filament consolidation. At lower loads ($0.060\ N/tex$), the interface region had $\phi \approx 0.74$, while the outer periphery dropped to $\phi \approx 0.63$. At higher loads ($0.33\ N/tex$), the difference was even more pronounced, with ϕ dropping from ≈ 0.77 to ≈ 0.69.

For ropes with a high strand twist (Z200) but lower rope twist (S50), such as Z200S50, the packing fraction exhibited the smallest radial variation, as seen in Figure 5(e, f). The linear fit slopes of -2.99×10^{-4} and -3.28×10^{-4} are the lowest among all configurations, meaning that packing fraction remains relatively stable across regions 1–4. At low loads (0.035 N/tex), the interface region packed to $\phi \approx 0.72$, but the outer periphery remained at $\phi \approx 0.69$, showing only a slight decline. Even under higher loads (0.370 N/tex), the total packing fraction remained stable ($\phi \approx 0.76$ at the interface and $\phi \approx 0.71$ at the periphery). Importantly, Z200S50 showed one of the largest increases in total packing fraction from unloaded to loaded states, reinforcing the idea that the strand twist is the dominant factor in increasing the packing fraction within strands. The high Z-twist (Z200) compresses filaments more effectively, even without strong rope twist enforcement (S50).

The Z200S100 configuration, which combines high rope twist (S100) with high strand twist (Z200), exhibited elevated strand-strand contact forces even at low loads, leading to high packing fractions at the interface (region 1), reaching $\phi \approx 0.75$ at just 0.060 N/tex (see Figure 5 (d)). The slopes of the linear fits -3.58×10^{-4} and -3.43×10^{-4}) indicate a moderate radial packing fraction gradient, showing more radial variation than Z200S50 but less than Z150S100. Additionally, Z200S100 showed a large increase in total packing fraction from unloaded to loaded states, further confirming that the strand twist plays a dominant role in increasing the filament packing within strands. However, the rope twist (S100) enhances inter-strand contact, ensuring stronger strand-to-strand compaction at lower loads compared to Z200S50.

Collectively, these findings demonstrate that twist parameters can be tuned to regulate how filaments pack under load at both the strand-strand interface (rope twist) and within each strand (strand twist). A higher strand twist results in a more densely packed cross-section, enhancing uniform load sharing but also raising inter-filament friction, which could lead to increased abrasion and internal damage over time. Conversely, a lower strand twist provides greater freedom for filament slip and reorientation, reducing localized overstress across the strand, but particularly leaving the periphery (region 4) less compacted unless a higher tensile load is applied. Additionally, the rope twist determines the extent of strand-to-strand contact, directly influencing the inter-strand packing and overall rope stability

Under identical load conditions, Z100S50 displayed the largest strand-to-strand variation in the packing fraction, whereas Z150S100 exhibited minimal differences among strands, suggesting that a moderate effective twist promotes a more uniform strand compaction. These observations align with previous works [3, 18], which emphasize the need for an intermediate twist level to maintain the rope geometry while avoiding excessive friction. Over-twisting increases inter-filament rubbing and accelerates internal wear, whereas under-twisting reduces the load sharing and increases the likelihood of excessive filament mobility, leading to fibre separation or filament migration. Furthermore, in most twist configurations, applying a tensile load primarily increased the packing fraction at the interface (region 1) rather than at the strand periphery (region 4). This is evident from the increase in slope between the lower and higher load states, indicating that loading drives more significant compaction at strand-

strand contact zones than in the outermost filament regions. By integrating micro-CT imaging with in-situ loading, these effects can now be directly visualized and quantified, offering a data-driven approach for optimizing the rope twist design based on service conditions (e.g., bending cycles, tensile fatigue, and exposure to environmental abrasives).

3 Conclusions

A methodology combining micro-CT imaging and image-based rectangular slicing was used to analyse the packing fraction of filaments within the strands of three-strand ropes. Different twist configurations and tensile loads were tested to evaluate their effects on filament compaction. The results demonstrate that:

1. Radial Variation: the packing fraction is generally lower at the strand's outer perimeter (region 4) and increases toward the rope's core (region 1).
2. Load-Induced Compaction: the tensile load increases the packing fraction throughout the strand, particularly at inter-strand contact interfaces, where neighbouring strands press together more tightly.
3. Influence of Twist:

- A higher strand twist results in a more uniform and overall higher packing fraction within each strand.
- A higher rope twist increases the contact forces between strands under tensile loading, causing earlier compaction at the strand-strand interface.

Thus, both twist parameters interact to regulate filament consolidation inside strands (strand twist) and strand-to-strand compression (rope twist). These findings highlight the importance of twist configuration in determining the internal geometry of strands. Both the applied load and effective twist levels dictate whether the cross-section is loosely packed or highly compacted, which in turn affects the internal stress distribution, friction, and long-term abrasion resistance. By carefully selecting strand and rope twist levels, rope designs can be optimized to maximize filament engagement and enhance durability in accordance with operational conditions.

4 Acknowledgements

This research was carried out under project number 17981 in the framework of the Partnership Program of the High Tech Systemen en Materialen (HTSM) 2019 TTW, Netherlands Organization for Scientific Research (www.nwo.nl). The authors would like to thank and acknowledge Vincent van Bommel and Dr. Bo Cornelissen from Teijin Aramid for their support with timely preparation and supply of aramid rope specimens.

5 References

[1] L. Treloar, 25—The Geometry of Multi-Ply Yarns, J Text Inst Trans 47(6) (1956) T348-T368.

[2] W. Morton, K. Yen, 5—The arrangement of fibres in fibro yarns, J Text Inst Trans 43(2) (1952) T60-T66.

[3] H.A. McKenna, J.W.S. Hearle, N. O'Hear, Handbook of fibre rope technology, Woodhead publishing2004.

[4] B.S. Jeon, J.Y. Lee, A new orientation density function of ideally migrating fibers to predict yarn mechanical behavior, Text Res J 70(3) (2000) 210-216.

[5] A. Kumar, S.M. Ishtiaque, A. Das, Impact of yarn extension on packing density of ring spun yarn, Fibers Polym 13(8) (2012) 1071-1078.

[6] T. Komori, K. Makishima, M. Itoh, Mechanics of Large Deformation of Twisted-Filament Yarns, Text Res J 50(9) (1980) 548-555.

[7] J. Hearle, T. Sakai, On the extended theory of mechanics of twisted yarns, J Text Mach Soc Jpn 25(3) (1979) 68-72.

[8] P.T. Hsu, Fracture mechanisms of synthetic fiber ropes, Massachusetts Institute of Technology, 1984.

[9] C. Leech, The Modelling and Analysis of the Mechanics of Ropes, Springer2014.

[10] J .-G. Lee, T.-J. Gang, I.-G. Park, A study on the geometrical structure of ring spun yarns, JTESE 26(4) (1989) 42-49.

[11] M. Toda, K.E. Grabowska, I.L. Ciesielska-Wrobel, Micro-CT supporting structural analysis and modelling of ropes made of natural fibers, Text Res J 86(12) (2016) 1280-1293.

[12] A. Sibellas, M. Rusinowicz, J. Adrien, D. Durville, E. Maire, The importance of a variable fibre packing density in modelling the tensile behaviour of single filament yarns, Text Inst 112(5) (2021) 733-741.

[13] M. Dragonfly 2024.1 [Computer software]. Comet Technologies Canada Inc., Canada; software available at https://dragonfly.comet.tech/.

[14] Z. Zhou, M.M. Rahman Siddiquee, N. Tajbakhsh, J. Liang, Unet++: A nested u-net architecture for medical image segmentation, Deep learning in medical image analysis and multimodal learning for clinical decision support: 4th international workshop, DLMIA 2018, and 8th international workshop, ML-CDS 2018, held in conjunction with MICCAI 2018, Granada, Spain, September 20, 2018, proceedings 4, Springer, 2018, pp. 3-11.

[15] A.S. Kornilov, I.V. Safonov, An overview of watershed algorithm implementations in open source libraries, J Imaging 4(10) (2018) 123.

[16] A. Kornilov, I. Safonov, I. Yakimchuk, A Review of Watershed Implementations for Segmentation of Volumetric Images, J Imaging 8(5) (2022) 127.

[17] O. Allan, T. Mishra, M. De Rooij, Effect of rope twist and strand twist on the contact pressure between strands in Aramid fibre three-strand ropes, in: P. Wang (Ed.) International Organization for the Study of Rope (OIPEEC) Conference, Bardolino, Italy, 2024.

[18] G.P. Foster, Advantages of fiber rope over wire rope, J Ind Text 32(1) (2002) 67-75.

6 Authors' Introductions

Oday Allan received his MSc degree in Mechanical Engineering through the Erasmus Mundus TRIBOS programme,. Since 2021, he has been pursuing a PhD at the University of Twente, focusing on the mechanics of fibre ropes, particularly the effects of twist configurations and loading using micro-CT imaging, experimental studies, analytical modelling, and characterisation techniques. His research interests include tribology, contact mechanics, and the experimental characterisation of wear, with expertise in image segmentation, numerical modelling, and image processing methodologies.

Dr. Tanmaya Mishra received his PhD degree in Mechanical Engineering from University of Twente in December 2019. He started his professional career as a post-doctoral researcher at Utrecht University in the Netherlands. Since August 2021, he has been working as an Assistant Professor at University of Twente. His research interests are in Tribology of interfaces which transition between stick and slip, numerical modelling and experimental characterisation of friction and wear, with applications in machine elements, rope mechanics, accurate positioning systems, metal forming, coatings and geomechanics.

Prof. dr. Matthijn de Rooij received his PhD degree in Mechanical Engineering from University of Twente in November 1998. He started his professional career as an Assistant Professor at the University of Twente. Since 2019 he is heading the Surface Technology and Tribology group, and was appointed as full professor in April 2023. The research group focusses on engineering interfaces, in particular degradation, friction, adhesion and lubrication phenomena. Fiber and rope mechanics, in particular frictional and degradation effects is one of his main research interests. Over the last 15 years, he has supervised several PhD students in the topic area.

Dynamic Climbing Rope Resilience: Advancements in Sharp Edge Resistance

Adriana Stöhr, M.Sc.

Mammut Sports Group AG, Switzerland

DI Arno Reiter, M.Sc.

Teufelberger Fiber Rope GmbH, Austria

Summary

The sport of climbing, whether for recreation or professional pursuits, demands equipment that is not only durable but also capable of ensuring the highest possible levels of safety. A fundamental component of this safety apparatus is the dynamic climbing rope, designed to endure the forces occurring during climbs and falls. In recent years, rope manufacturers have increasingly focused on enhancing sharp edge resistance, a critical factor in preventing rope failure when subjected to abrasive or sharp surfaces.

This research paper explores the novel “Core Protect” technology designed to improve the cut resistance of climbing ropes while maintaining their dynamic performance. Additionally, it highlights the current lack of a holistic test method to accurately evaluate a rope’s ability to withstand sharp edge impacts under real-world conditions. By assessing advancements in rope materials, protective technologies, and testing methodologies, this study provides a comprehensive overview of improvements in climbing rope safety and durability.

Keywords: Dynamic climbing rope, Cut resistance, Aramid, Intermediate sheath construction

1 Introduction

1.1 Climbing Ropes

A dynamic climbing rope is a crucial safety tool that protects climbers by absorbing and dispersing energy during a fall. When a climber falls, the rope stretches to absorb dynamic energy into deformation energy. This reduces impact forces on the climber, lowering the risk of injury and increasing safety. The rope’s elasticity also distributes the load across its length and the belay system, decreasing peak forces on anchors and reducing the probability of failure. [1]

To ensure reliability, dynamic ropes are tested under standards like EN 892, set by the committee of European standardizations (CEN), and UIAA 101, set by the International Climbing and Mountaineering Federation (UIAA).

Despite their high performance and safety, climbing ropes remain vulnerable to cuts and abrasion, especially when the loaded rope gets in contact with sharp rock edges or sharp metal devices such as worn carabiners. Unlike gradual wear, a single sharp edge can create a stress concentration, leading to instantaneous failure. High localized tensile forces combined with shear stress can exceed the rope’s strength, causing it to sever. [2] This highlights the need for rigorous testing, advanced sheath technology, and proper rope management to minimize risk.

Currently, no standardized test method exists for evaluating the cut resistance of climbing ropes, despite multiple attempts to establish one. Over the years, various laboratory tests and field simulations have been proposed, including the now-suspended UIAA 108 standard (2002), Energy absorbed before rupture test UIAA101 (2014), the Edelrid static cutting test, and the Elmenzwick method. While these tests provide valuable insights into rope behaviour under sharp edge loading, none fully replicates the complex failure mechanisms observed in real climbing fall scenarios. [3] The lack of a universally accepted test highlights the need for further research and methodological refinement to develop a reliable and reproducible test setup for assessing cut resistance in dynamic climbing ropes.

1.2 Cut failure mechanisms

1.2.1 Cutting stress on ropes

Cutting occurs when a sharp edge, such as a rock or carabiner, applies high localized compressive stress to the rope's sheath and core. This concentrated force causes the fibres to rupture, leading to material separation through fracture. The type of failure, ductile or brittle, depends on the rope's polymer properties, tension, and the sharpness of the edge.

1.2.2 Shearing stress on ropes

Shearing, on the other hand, happens when parallel opposing forces act along the rope's cross-section, generating shear stress that deforms fibres laterally. This process weakens the material over time, often leading to plastic deformation before complete failure.

Cutting and shearing are two distinct failure mechanisms that affect climbing rope integrity, each describing how the material responds to applied forces. While cutting leads to sudden structural failure due to localized severing, shearing progressively weakens fibre integrity, increasing the risk of delayed failure. Both mechanisms are critical considerations in rope safety and durability. [2]

1.3 Textile Fibres in Climbing Rope Designs

Modern climbing ropes use a kernmantle design, consisting of two key components: the kern (core) and the mantle (sheath).

1.3.1 Textile fibres for dynamic behaviour

The inner core, which provides the rope's primary tensile strength, elasticity, and energy absorption, is made of twisted or braided high-tenacity polyamide (e.g., HT PA6, HT PA6.6) fibres. High-tenacity polyamide offers an increased tensile strength of 70 – 100 MPa, an elongation at break of approximately 20 – 40 %, and an excellent suitability for material shrinking processes such as autoclaving. This allows the rope to stretch and absorb fall forces effectively, reducing the impact on the climber while maintaining durability under dynamic loads.
The outer sheath is tightly braided around the core, protecting against abrasion, dirt, and moisture while also adding structural stability. Besides a finely tuned interaction between core and sheath to ensure excellent fall absorption, the sheath enhances durability by resisting mechanical wear, UV degradation, and surface friction, all of which are essential for rope longevity.

This combination of a strong, elastic core and a protective sheath makes kernmantle ropes highly effective for climbing, balancing strength, flexibility, and impact resistance to ensure safety under dynamic loads. [1], [4]

1.3.2 Textile fibres for cut resistance

The most effective fibres for cut resistance under high strain are those with high strength, surface hardness, and the ability to maintain structural integrity under stress. Aramid fibres, such as Technora®, Kevlar®, Twaron®, are known for their exceptional cut resistance due to their highly oriented and crystallized polyamide chains. [5] This high crystallinity (~80 – 85 %) enhances tensile strength (up to 3.6 GPa) and modulus (~ 90 GPa), allowing aramid fibres to

withstand extreme mechanical stress without breaking. Above all Aramid fibres have excellent resistance against high temperatures.
This combination of high tensile strength, low elongation (~ 2.5 – 4 %), and exceptional toughness significantly reduces the risk of cuts, making aramid textiles ideal for protective gear, ballistic armour, and industrial applications. [4]

Table 1: Mechanical Properties PA6, Aramid [4]

Property	**HT PA 6**	**Aramid**
Tensile Strength [MPa]	70 – 100	Up to 3,600
Elongation at Break [%]	~ 20 – 40 %	2.5 – 4
Modulus [GPa]	8	60 – 96
Density [g/cm³]	1.14	~ 1.45
Abrasion Resistance	High	Very High
Cut Resistance	Moderate	Exceptional
Shear Strength	Moderate	High
Thermal Stability [°C]	~ 215 - 225 (melting point)	~ 500 (decomposes)

While aramid fibres provide superior cut resistance, their low elasticity and limited elongation present challenges in dynamic climbing ropes, where energy absorption and controlled elongation are crucial.
One major drawback is that aramid fibres lack elasticity, reducing their ability to absorb and dissipate energy during a fall. Dynamic climbing ropes rely on elasticity to elongate under load, helping to mitigate the forces experienced by the climber. In contrast, static fibres like aramid fail to provide this necessary requirement, potentially leading to higher impact forces and increased injury risk.
Additionally, reduced shock absorption increases the risk of shock loading. When a climber falls, a static fibre-based rope cannot stretch, leading to sudden, high-impact forces that may exceed the strength of climbing gear or anchors, raising the likelihood of catastrophic failure.
Because of these limitations, aramid fibres are rarely used in dynamic climbing ropes.

2 Core Protect Construction

The inherent trade-off between strength and elasticity in climbing rope materials presents a significant challenge. While polyamide 6 provides essential elasticity and energy absorption, it lacks the desired cut resistance. Conversely, aramid fibres offer exceptional tensile strength and cut resistance, but their low elongation makes them unsuitable for dynamic load applications. [4]

To address this challenge, the patented Core Protect Construction featuring an aramid-reinforced intermediate sheath was developed, see **Figure 1**. However, a sheath composed entirely of aramid fibres would lack the mechanical elongation necessary to accommodate dynamic loading. Instead, the patented design utilizes an intermediate sheath made of a hybrid yarn, combining polyamide and aramid filaments. [6]

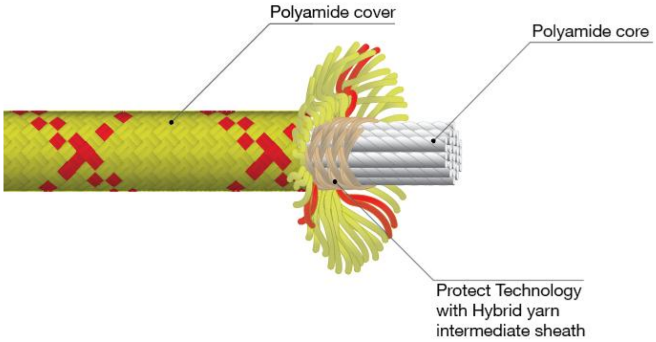

Figure 1: patented Core Protect Construction

As displayed in **Figure 2**, the polyamide filaments (1) act as a carrier yarn, ensuring elasticity, while the aramid (2) is wound around them with an intentional overlength. This overlength design allows the aramid fibres to structurally elongate in synchronicity with the rope under load, effectively allowing the core to absorb the fall energy without creating sudden peak forces. Once the rope is relaxed, the aramid filaments return to their original position, maintaining the protective function while preserving the rope's shock-absorbing properties.

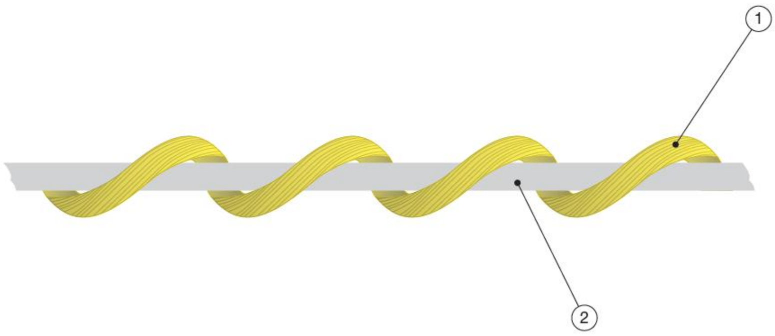

Figure 2: Hybrid Yarn, 1: Aramid filaments with overlength 2: polyamide carrier yarn

2.1 Force-Elongation Behaviour of Hybrid Yarns

Based on our data base a standardized fall test with a fall factor of 1.77, climbing ropes experience impact forces of approximately 8 – 9 kN while elongating around 30 %. A fall factor of 1.77 represents an extreme loading scenario, designed to simulate worst-case conditions. In contrast, typical climbing falls generate significantly lower forces, usually around 3 – 4 kN [7], with max. elongation of approximately 16 %.

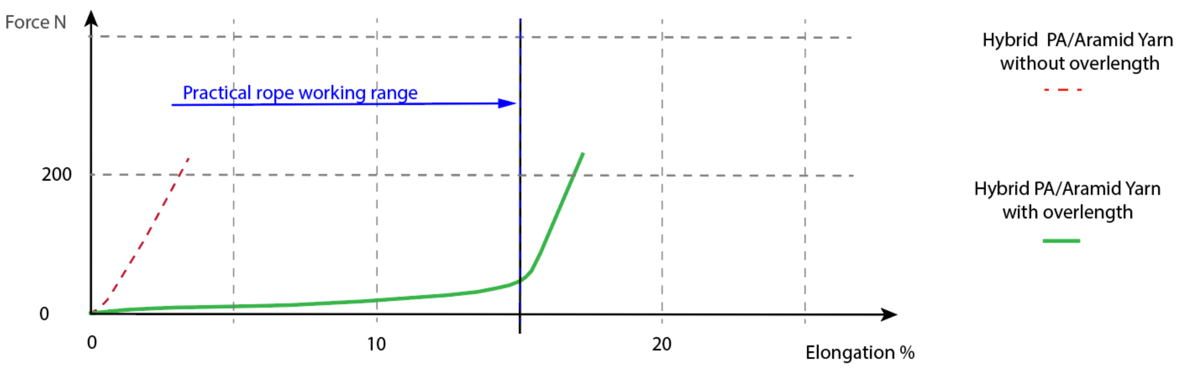

Figure 3: Force-Elongation Characteristics of Hybrid Yarns

Figure 3 compares the force-elongation behaviour of two different hybrid PA/Aramid yarn constructions, one without overlength of Aramid (red curve) and one with overlength of Aramid (green curve).

The x-axis represents elongation (%), indicating the strain experienced by the yarn under tensile loading. The y-axis represents force (N), corresponding to the tensile load applied during deformation.

The red curve (hybrid PA/Aramid yarn without overlength) exhibits a steep initial force increase with minimal elongation, characteristic of a highly rigid structure. This behaviour suggests premature stress localization and a lack of extensibility, making it unsuitable for dynamic applications where controlled energy dissipation is required.

The green curve (hybrid PA/Aramid yarn with overlength) demonstrates a gradual force buildup, allowing higher strain accommodation before significant load development. This response aligns with practical rope working range of climbing falls (up to 16%), indicating improved compliance under dynamic loading.

Figure 4 displays the mechanical behaviour during static loading. When subjected to rapid shock loading, as occurring during a climbing fall, the differences in mechanical behaviour of the presented hybrid yarns become even more significant. The aramid fibres of hybrid yarn without overlength engage immediately, leading to a stiff response with minimal energy absorption. This causes sudden peak forces, increasing the risk of brittle failure or excessive impact transmission.

On the other hand, in the yarn with overlength the polyamide carrier yarn elongates simultaneously with rope elongation under low-stress, while the aramid remains tension-free. As elongation progresses, the aramid engages gradually and smoothly, preventing abrupt stiffness transitions and improving impact resistance. This can be seen in the following experiment.

2.1 Interaction Between Rope Structure and Hybrid Yarns

Two different rope constructions, a standard PA 6 kernmantle rope (9.5 Crag Dry Rope) and a kernmantle rope featuring an intermediate sheath with hybrid yarn containing overlength aramid filaments (9.5 Alpine Core Protect Dry Rope), were subjected to falls acc. to EN 892 [8] but with varying fall factors. This was done to study the influence of the hybrid yarn on the impact force progression.

The x-axis in Figure 4 represents the fall factor, a measure of fall severity, while the y-axis indicates the impact force (kN) experienced by the rope.

Both rope constructions exhibit a progressive increase in impact force with rising fall factor. For low fall factors (≤ 0.5), which correspond to typical impacts in climbing falls, the two ropes show almost identical impact forces. This indicates that the addition of overlength aramid filaments does not impede with the rope's ability to absorb and dissipate energy under moderate loading conditions. This suggests that the integration of a hybrid yarn in the Alpine Core Protect Dry Rope maintains the fundamental dynamic performance of a standard polyamide rope.

However, as the fall factor increases beyond 0.5, a small but consistent divergence emerges, with the Alpine Core Protect Dry Rope exhibiting slightly higher impact forces compared to the standard Crag Dry Rope. At a fall factor of 1.77, the Alpine Core Protect Dry Rope reaches just above 8 kN, whereas the Crag Dry Rope remains slightly below 8 kN. This difference can be attributed to the gradual engagement of the Aramid filaments in the hybrid yarn construction.

As mentioned earlier, a common climbing fall generates impact forces around 3 – 4 kN. According to the tests conducted, those forces are already reached between fall factor of 0.25 to 0.5, see Figure 4. At fall factor of 0.5 a maximum rope elongation of 16% was recorded. During elongation levels up to 16 % of the rope the aramid component proves to remain inactive since no increased impact forces were recorded. Looking at Figure 3, one could deduce that the yarn elongation during such a fall should be significantly lower than 15 % considering that the curve tends steepen drastically after that point. This argument can be further supported by the visual analysis of rope samples exposed to a factor 1 fall. During a factor 1 fall, the 9.5 Core Protect rope recorded an elongation of 23 %. If the aramid fibres had exceeded their full structural elongation range, sudden peak forces would have been recorded, and most likely, there would have been noticeable damage to the fibres due to the extremely high strain rate. The samples were cut open, and no damage to the aramid fibres was found; therefore, the elongation of the hybrid yarn must be below 15 %.

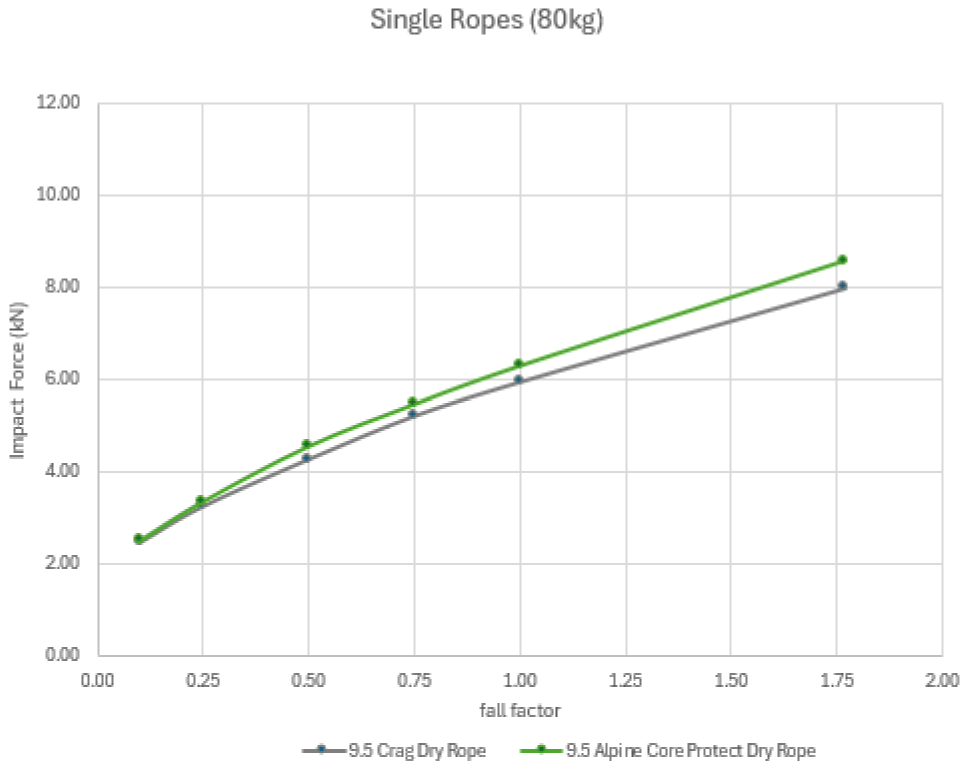

Figure 4: Impact force development with realistic fall factors up to standardized fall factor (1.77)

This can be explained by two mechanisms. One being the helical fibre arrangement in the intermediate sheath, the other being the overlength of the Aramid in the hybrid yarn.

Constructional elongation plays a crucial role of both mechanisms. When force is applied, the helically arranged intermediate sheath is straightened in the linear direction of the rope before the yarn is experiencing direct tensile strain. Once the helix structure reaches its full elongated capacity, the overlength of the hybrid yarn comes into play. Upon loading, the polyamide elongates structurally while the Aramid mirrors this behaviour thanks to its overlength construction. The aramid filaments remain tension-free during initial elongation and only engage progressively as elongation exceeds 15 % of the yarn itself, see Figure 3. This staged activation distributes stress more effectively and prevents sudden load spikes. Once the load is removed, the system recovers its original state due to the elastic properties of polyamide.

This engineered yarn architecture optimizes both impact absorption and mechanical durability, addressing the inherent trade-off between cut resistance and elasticity in climbing rope design.

3 Test methodology

Sharp edges present a serious hazard in climbing accidents, with the majority occurring during dynamic falls. According to publicly available accident reports, 25 % of accidents involving sharp objects happen in static situations, such as when a climber is hanging motionless or slowly weighting the rope. In contrast, 75 % of incidents occur dynamically, meaning they take place during a fall or sudden movement. The risk becomes even more critical when considering fatal accidents. A staggering 94 % of deadly incidents are linked to dynamic falls, while only 6% result from static scenarios. This highlights the heightened danger of sharp edges when combined with high-impact forces, as a rope under tension is far more vulnerable to cutting.

Over the years, various laboratory tests and field simulations have been developed to assess rope cut resistance. While these methods provide valuable insights into rope behaviour under sharp edge loading, none fully replicates the complex failure mechanisms observed in real climbing falls, as observed by Sedláček. [3]

UIAA 101 (2014) test measures a rope's ability to absorb energy before rupture by subjecting it to impact forces of approximately 9.7 ± 1.5 kN, simulating a standardized extreme fall condition. The failure mechanism in this test is shear, where the rope is primarily stressed by high tensile forces rather than direct cutting. [9] While it provides useful information about energy absorption, it does not realistically replicate sharp edge interaction, as real-world rope failures often result from a combination of tensile forces and localized cutting effects, which this test does not fully capture.

Edelrid Static Cutting Test applies a constant force of 1.0 kN on a sharp edge, making it comparable to the forces experienced when statically sitting in a rope. [3] As a result, the applied force remains relatively low, failing to replicate the high-impact, dynamic forces that occur during an actual fall. The failure mechanism in this test is pure cutting, which differs significantly from real-world climbing falls, where sharp edge failure is often triggered by a combination of tensile loading and sudden force peaks.

Despite their limitations, both UIAA 101 and the Edelrid test were taken into consideration when evaluating the novel Core Protect Construction, as they reflect single aspects of sharp edge performance. However, the impact forces applied in these tests differ significantly from those occurring in real climbing falls as well as a lack in dynamics, as shown in **Table 2**.

Table 2: Comparison of test methods vs accident simulation

Test method	**Maximum Tensile Force (kN)**	**Cut failure mechanism**	**Type of Impact**	**Measure**
UIAA 101 Test	9.7 ± 1.5 kN	Shear	Dynamic	Energy absorbed
EDELRID Test	1.0 kN (constant)	Cut	Static	Cutting distance
Granite Edge / Accident simulation	2- 3.5 kN	Cut + Shear	Dynamic	Rupture or not

The Granite Edge Test was specifically designed to better replicate the real-world scenario of a rope encountering a sharp edge during a dynamic fall. The test setup is depicted in the images of **Figure 5**.

This test combines cutting and shearing forces, making it a more realistic accident simulation than previous methods. The measured tensile forces range between 2 – 3.5 kN, which is significantly lower than UIAA 101 but within a range representative of real climbing falls.

Unlike the UIAA and Edelrid tests, this method does not focus on energy absorption or cutting length but instead assesses whether the rope ruptures or not. However, due to the natural variability of the granite edge, the test is not standardized, limiting its use to development and validation purposes. Despite this, it serves as an effective way to confirm rope performance improvements in cut resistance, particularly for innovative materials and constructions.

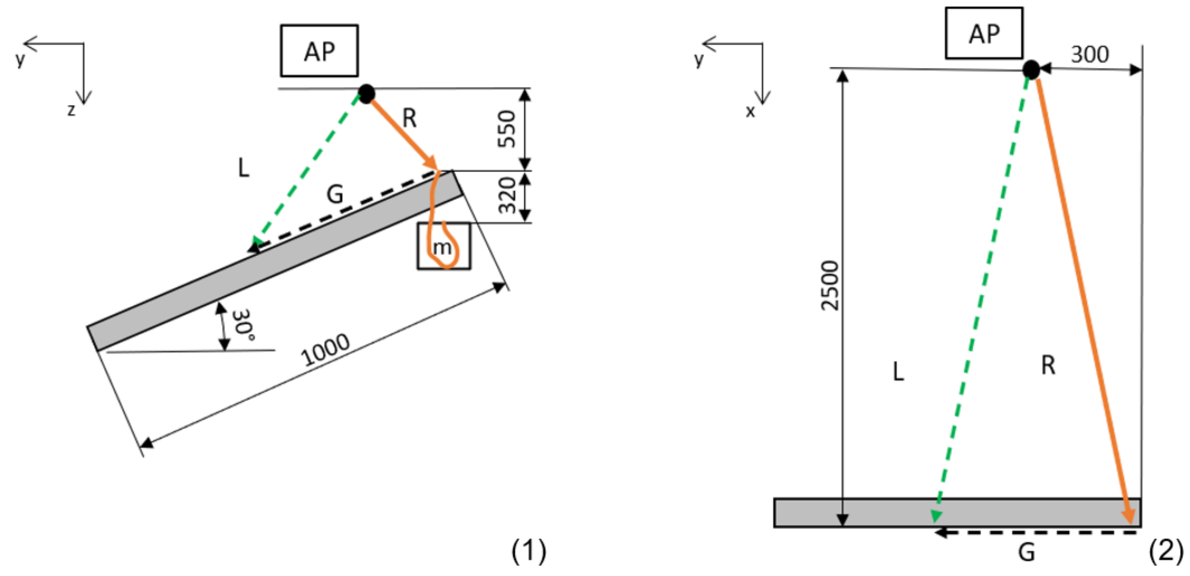

Figure 5: Test set-up: Granite Edge by Teufelberger/Mammut

Illustration (1) shows frontal view of test setup, illustration (2) provides a top-down perspective. G: cutting length (contact with granite edge, positioned at 30° angle, which acts as the cutting and shearing surface); R: distance of anchor point AP to edge (rope in start position); L: distance from AP to edge (rope during cutting process); m: 80 kg mass; AP: anchor point

			Edelrid Test @100daN	**Granite Edge 80kg**		**UIAA 101 100kg**
			Cut value (m)	ropes withstand edge fall (%)		Absorped energy (J/m)
Dynamic climbing Rope (EN892)	**Weight (g/m)**	**Textiles**	*n=5*		*n*	*n=3*
9.0 Alpine Sender Dry	55	PA 6	0,15	0	*n=3*	1713
9.5 Alpine Dry	[illegible]	PA 6	0,16	0	*n=10*	1799
9.9 Crag Dry		PA 6	0,17	20	*n=5*	1868
10.2 Crag Classic	[illegible]	PA 6	0,19	40	*n=5*	-
9.5 Core Protect (Proto)	59	PA 6, Aramid (3g/m)	0,39	93	*n=14*	1772
			Edelrid Test @120daN	**Granite Edge 100kg**		
			Cut value (m)	ropes withstand edge fall (%)		
Low Stretch Ropes (EN1891A)	**Weight (g/m)**	**Textiles**	*n=5*		*n*	
11.0 Patron	75	PA 6	0,51	0	*n=6*	
11.0 Core Protect (Rescue Assault)	77	PA 6 + Aramid (4,5g/m)	1,40	100	*n=5*	
10.5 Vulcanus	74	PA 6 + Aramid (27g/m)	1,85	17	*n=6*	

Figure 6: Test result comparison between various cut resistance evaluations

3.1 Dynamic Rope Behaviour

The performance of climbing ropes under sharp edge conditions varies significantly depending on their material composition and construction.

As seen in **Figure 6**, a clear behaviour emerges for PA6 ropes in the Edelrid static cutting test. An increase in material quantity leads to improved cut resistance. The Core Protect construction, which incorporates an Aramid additive of approximately 3 g/m (5 % of the rope's weight), demonstrates exceptional cut resistance. Compared to the 9.0 mm rope, the Core Protect nearly doubles the cut resistance, despite both ropes containing comparable amounts of PA6.

A similar trend is observed in the Granite Edge Test, which simulates real-world sharp edge falls. Thinner PA6 ropes (9.0 mm or 9.5 mm) fail every time, while thicker ropes (9.9 mm) rarely survive (1 out of 5 falls), and the thickest single rope (10.2 mm) succeeds in 2 out of 5 falls. In stark contrast, the Core Protect rope survives 13 out of 14 falls, highlighting its superior sharp edge resistance.

The results from the UIAA 101 test further confirm the relationship between absorbed energy and PA6 content. Ropes with a higher PA6 mass absorb more energy before rupture, whereas Core Protect exhibits lower energy absorption, as its reduced PA6 content does not allow for more energy absorption before failure. Additionally, the peak forces recorded in the UIAA 101 test are unrealistically high, exceeding what typically occurs in real climbing falls.

3.2 Low-Stretch Rope Behaviour

In the Edelrid test, the Core Protect rope achieves a cut value of 1.4, making it 2.7 times more resistant than the 11.0 Patron reference rope made purely from PA6. The Vulcanus rope performs even better, with a cut value 3.6 times higher than the reference rope. However, despite its much higher Aramid content, the expected extreme cut resistance does not fully materialize. This is due to the lack of extra-length Aramid fibres in Vulcanus, unlike Core Protect, where the fibres are strategically positioned for enhanced performance.

In the Granite Edge Test, Core Protect significantly outperforms Vulcanus, which's main application focuses on work near heat sources. The forces acting on Core Protect remain at the level of a standard PA6 rope, as its Aramid fibres do not reach their elongation limit, preventing a sudden increase in rope tension. Conversely, the Vulcanus rope experiences higher force peaks due to its sheath being made of tightly braided Aramid yarns without extra length. During a fall, these fibres stretch abruptly, leading to a rapid force spike within the rope. This results in higher pre-tension and stronger contact forces between the rope and the sharp edge, increasing the likelihood of failure.

These findings highlight the importance of rope construction in determining cut resistance. While material quantity plays a crucial role, fibre arrangement and the ability to control force distribution are equally important for maximizing rope durability in sharp edge scenarios.

4 Conclusions

Modern climbing ropes aim to balance tensile strength, elasticity, impact absorption, and cut resistance. While polyamide fibres provide elongation and energy absorption, they have moderate cut resistance, making them vulnerable to sharp edges. Hybrid constructions combining polyamide with aramid fibres, which offer superior cut resistance but low elasticity, are one way for improving rope performance.

The Core Protect Construction addresses this challenge by incorporating an aramid-reinforced intermediate sheath with an overlength yarn design. This configuration allows the aramid fibres to remain inactive during low-stress elongation while progressively engaging under higher loads. Experimental cut resistance testing, including standardized fall tests and the Granite Edge simulation, demonstrates that this hybrid yarn construction enhances cut resistance without compromising the rope’s dynamic performance. Compared to conventional polyamide ropes, the Core Protect ropes maintain impact absorption during typical climbing falls while significantly improving resistance against sharp edge failure.

These findings highlight the potential of hybrid textile engineering in climbing safety, offering a viable solution to enhance both fall protection and durability. Future research should further optimize the interaction between hybrid yarn structures and rope construction to refine performance characteristics, particularly in extreme conditions.

Regarding available test methods for the evaluation of cut resistance, it can be said that although both the Edelrid test and the UIAA 101 test provide reproducible data and quantifiable values, neither test represents real-world conditions. The Edelrid test falls short due to its purely static assessment of cut resistance and does not sufficiently produce the same results as those observed in the realistic Granite Edge Test. The UIAA 101 test is problematic for two reasons, the forces in the system are far too high and the test focuses purely on shear stress, while the more critical factor, cut stress, is not considered at all.

The Edelrid test could be significantly improved by considering the varying dynamic behaviour of ropes. This could be achieved by introducing variable preloads equal to the tested impact force of a fall at fall factor 0.3. Since ropes with varying impact forces are also preloaded differently in tests, this would provide a more accurate representation of dynamic rope failure due to cutting stress in a test setup that is otherwise only meaningful for static applications.

A modified UIAA 108 test (80 kg) with an abrasive edge similar to stone—but with a lower fall factor—would be ideal. The goal would be to ensure that rope failure (or a successfully held fall for cut-resistant ropes) occurs under forces that are more realistic. The maximum fall factor the rope can withstand without breaking could serve as a measure of the shear resistance of the rope.

5 References

[1] H. A. McKenna, J. W. S. Hearle, and N. O'Hear, *Handbook of Fibre Rope Technology*. Cambridge, UK: Woodhead Publishing, 2004, p. 375

[2] C. Hummel and F. Hellberg, “Seilrisse,” *Deutscher Alpenverein*, Sep. 13, 2016. [Online]. Available: https://www.alpenverein.de/artikel/seilrisse_0cb75bd9-7869-4555-8425-49f1001fab4b. [Accessed: Feb. 22, 2025]

[3] D. Sedláček and A. Stöhr, “Cut resistance of climbing ropes – A comparative analysis of existing measurement methods and a simulated accident,” *Engineering Failure Analysis*, vol. 157, p. 107906, Mar. 2024, doi: 10.1016/j.engfailanal.2023.107906.

[4] H. A. McKenna, J. W. S. Hearle, and N. O'Hear, *Handbook of Fibre Rope Technology. Cambridge*, UK: Woodhead Publishing, 2004, pp. 41-53.

[5] Y. Zhai, L. Mao, Y. Shen, and X. Yan, “Research progress of cut-resistant textile materials,” *Frontiers in Chemistry*, vol. 9, Art. no. 745647, Sep. 2021. [Online]. Available: https://doi.org/10.3389/fchem.2021.745647. [Accessed: Feb. 26, 2025].

[6] A. Reiter, “Rope made of textile fiber material, comprising a twine of excess length,” U.S. Patent, US 11,802,372 B2, Oct. 31, 2023.

[7] Petzl, "Forces at work in a real fall," *Petzl*, 2025. [Online]. Available: https://www.petzl.com/US/en/Sport/Forces-at-work-in-a-real-fall. [Accessed: Mar. 01, 2025]

[8] EN 892:2012+A3:2023, "Mountaineering equipment - Dynamic mountaineering ropes - Safety requirements and test methods; German version," *European Committee for Standardization (CEN)*, 2023

[9] UIAA, "101_V9 Dynamic Ropes," *International Climbing and Mountaineering Association*, Bern, 2019. [Online]. Available: https://theuiaa.org/documents/safety-standards/101_UIAA_Ropes_V9_2019.pdf. [Accessed: Feb. 22, 2025]

6 Authors' Introductions

Ms Adriana Stöhr earned her MSc in Textile Engineering from the University of Borås, Sweden, in 2019. She began her professional career interning at Adidas AG (2014), gaining hands-on experience in footwear product development. She then spent 1.5 years at Wearable Life Science GmbH, where she developed textile electrodes for wearable smart textiles. During her master's studies she deepened her expertise in polymer chemistry and smart textiles. Since 2019, she works as a Textile Engineer at Mammut Sports Group, where she applies her diverse background in textiles to improve the sustainability and performance of fibre ropes and narrow textiles for climbing applications.

Mr Arno Reiter received his MSc (DI) degree in Mechanical Engineering from University of Technology Graz, Austria 2015. He started his professional career as a Rope Design Engineer at Teufelberger Fibre Rope in 2016. As a passionate climber, professional IFMGA Mountain Guide (since 2011) and member and trainer of the Austrian Mountain Rescue (2010), he brings in-depth expertise in development, testing and application of climbing equipment.

Braided Endless Synthetic Structures from DYNEEMA®

Dr. Dietrich Wienke

AVIENT Protective Materials B.V., Geleen, The Netherlands

Karel Wetzels, Rope Technician

AVIENT Protective Materials B.V., Geleen, The Netherlands

Robert Cohnen, M.Eng.Sc.

AVIENT Protective Materials B.V., Geleen, The Netherlands

Summary

In various industries - from plant manufacturing to transport and from offshore to defence – round-shaped, heavy-weight, dangerous steel elements are still widely used such as, e.g., steel rings in connectors, grummets for heavy duty lifting and steel chains for sub-sea mooring.

For their replacement by a lightweight, safer alternative, we propose a circular braided soft rope with UHMWPE fibre. It adds to the existing laid synthetic grommets, fibre rope-slings and round-slings.

Technically, this has been achieved by round-braiding of a single strand rope of precise length by its own. By ISO-rules, we named it **B**raided **E**ndless **S**ynthetic **S**tructure with D**Y**NEEMA® (B.E.S.S.Y.).

Although the round-braided strand rope has two loose ends, their end-connection is not really required from the view point of strength and of load sharing. This, because the circular braided rope length is identical with a sufficiently overlong circular splice length. At any point of circumvention, B.E.S.S.Y. has equal strength. Hence, a B.E.S.S.Y. fibre chain or -ring is intrinsically safe, which is a prerequisite for demanding industrial use.

We compared the fibre strength efficiency of B.E.S.S.Y. fibre rings against rope-slings. Also, we describe a possible manufacturing route.

In conclusion we found, that various existing heavy round-shaped industrial steel applications can be replaced by significant lighter B.E.S.S.Y. fiber chains and -rings. That will provide better ergonomics, improved work safety, higher handling productivity and less damage costs.

Keywords: UHMWPE fibre rope, Synthetic fibre chain, Circular rope braid, Fibre ring

1 Introduction

In 2015, synthetic link chains were commercially launched for heavy load securing and in 2016 for overhead lifting (**Figure 1**). They are based on light weight super strong synthetic UHMWPE fibers, that are narrow woven into a belt and then wrapped with a Möbius twist [1] [2] [3].

Figure 1: Light weight high strength industrial synthetic fiber chain, made from UHMWPE fibre.

They are commercially mass manufactured for now up to 300 mTons minimum break load (MBL) and they are as prototype available already up to MBL ~ 1.000 mTons (**Figure 2**).

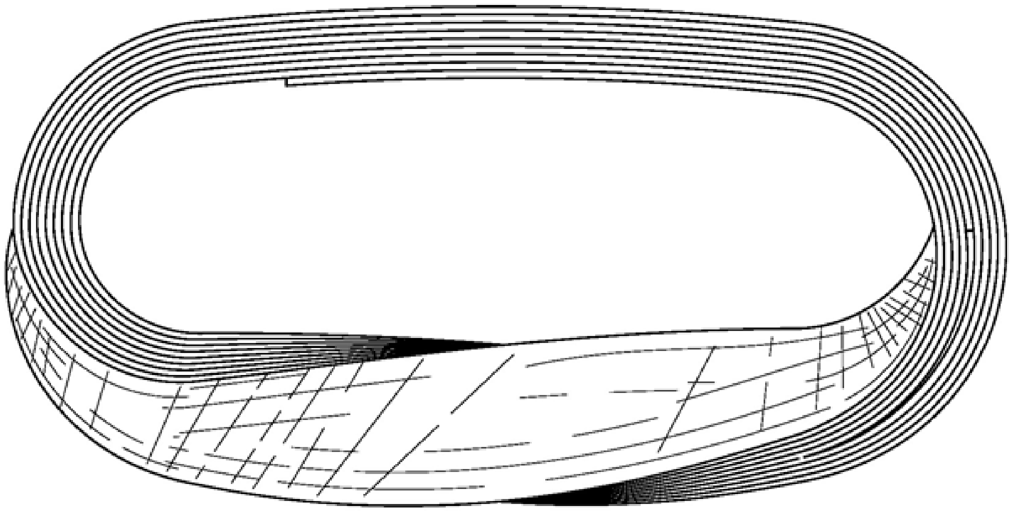

Figure 2: The minimum break load MBL of synthetic link chains is mainly controlled by four design parameters: Strength and amount of chosen UHMWPE synthetic fibre grade, number of webbing layers, width and thickness of each individual webbing layer.

2 Motivation

However, the latter three design parameters show upper technical manufacturing limits. In particular, when for belt weaving rapid needle looms are used rather than slow shuttle looms. Their maximum producable belt width is currently limited to 600 mm and the belt thickness is limited to 4 mm. And, the more belt layers are stacked, the more the layers tend to slide out. Hence, the more unstable the wrapped stack in Figures 1-2 becomes.

That limits the amount of UHMPE fibre, that can be put into such chain links, which finally limits the maximum achievable MBL of such a synthetic belt made chain.

Our motivation is market driven, since steel made offshore mooring chains of MBL > 2000 tons wait for their replacement by lighter alternative. Our ambition are synthetic fibre chains without a ceiling in MBL. Since braided ropes scale upwards in strength just by selected thicker rope diameters and by scaling the number of braids, we replaced the former building block of stacked webbing by the new building block of braided strand rope [4], (**Figure 3** a. – b.).

Figure 3 a. (above, in flash light) – 3.b. (below, filtered flash light): Example of the new chain link design obtained by five times round braiding just one Ø 5 mm strand rope with itself, made from black Dyneema® BK75 UHMWPE fiber. This endless circular structure has an inner diameter of Ø 200 mm, achieves an MBL = 20 mTons and is up to ten times lighter than a steel chain link (resp. steel wire rope grommet) of same size at equal MBL.

In line with ISO nomenclature we named the new design B.E.S.S.Y., derived from **B**raided **E**ndless **S**ynthetic **S**tructure with D**Y**NEEMA® fibre. In that way it distinguishes from laid steel wire rope grommets, from laid synthetic fiber grommets as well from rope slings and from round slings.

The new B.E.S.S.Y. design provides additional fibre strength efficiency over the former belt made synthetic chains and -rings. Woven belts have up to 15 % dead weight from their weft yarns. These weft yarns do not contribute to the tensile strength in longitudinal direction of the belt chain.

In the new rope based B.E.S.S.Y. chains and -rings all UHMWPE yarns form a longitudinal angle below 90 degrees, which lets them all share their load. The achieved gain in MBL for equal yarn quantity is significant [4].

3 Experimental & Methods

For our introductory study, three standard strand ropes were used, made on our inhouse ROBLON braider from Dyneema® fiber grade SK78 dtex1760 in diameters of Ø 5 mm, 10 mm and 20 mm. These ropes are standard available in our Technical Center Europe (Heerlen, NL) for many other experiments and therefore well characterized.

From these standard test ropes, various 5-strand, 7-strand and 12-strand B.E.S.S.Y. rings and - chains were manually made and tested. For gaining insights, we varied their construction, their dimensions and as a result their strength and fiber efficiency. (**Figures 3-5**).

Figure 4: Initial protoypes of B.E.S.S.Y.-rings. Left: dimension 1 meter, MBL = 400 mTons, 12 x Ø 20 mm strand rope. Right: dimension 0.4 meter, MBL = 100 tons, 12 x Ø 10 mm strand rope. All made from fiber SK78 dtex1760.

Figure 5: Initial protoypes of B.E.S.S.Y.-chain of three links after break test. Link dimension 1 meter, chain length 3 meters. Chain MBL = 200 mTons, link construction 12 x Ø 20 mm strand rope with fiber SK78 dtex1760.

That introductory study helped to improve the braiding tool (resp. mold). We started first with an inflated tyre with its toroidal shape and deflated after completed braid. The second generation braiding tool was a wooden tube, later followed by PVC-tubes as third generation braiding mold (**Figure 6**).

Figure 6: LEFT : Tubular braiding mold for a seven strand B.E.S.S.Y. ring. Ring diameter 30 cm from single 7 x Ø 10 mm strand rope braid from fiber 12 x 20 x SK78 dtex1760.

RIGHT: For the manufacturing of a five strand B.E.S.S.Y. chain, the chain mold can be opened and closed. Chain link diameter 30 cm from 5 x Ø 10 mm signle strand rope braid from fiber 12 x 20 x SK78 dtex1760.

With this third generation circular braiding tool, anybody can manually fabricate a B.E.S.S.Y. ring of any size with any rope between 15 – 30 minutes in a highly reproducible manner with a standard deviation of about +/- 3 % MBL.

3.1 Safe End-Termination

For proper fixation of both loose ends of the single strand rope, five types of end-terminations were studied: 1) Buried Chinese finger splice; 2) single knot / double knot; 3) tape / sticky coating ; 4) stitched seam ; 5) combinations thereof.

As example, the combination of taped and stitched end-connection is shown (**Figure 7**):

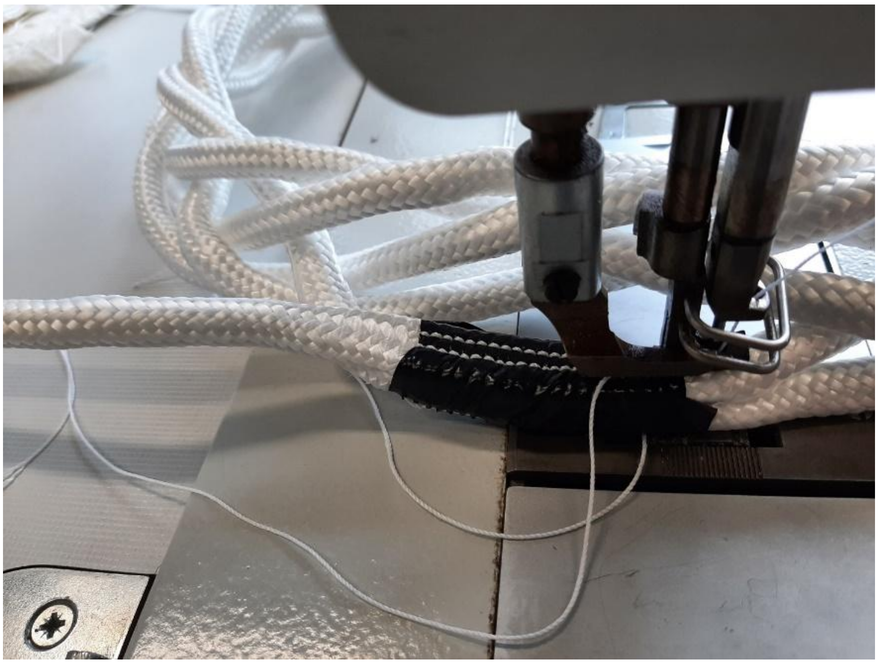

Figure 7: Fabrication of end-termination with tape and seam for booth loose ends of a five strand B.E.S.S.Y ring, made from Ø 10 mm strand rope from 12 x 20 x SK78 dtex1760 fiber.

The type of the end-termination has no significant impact on the final ring strength. This, because the B.E.S.S.Y. ring itself forms an overlong splice for the single strand rope. With that enormeous splice length, the loads and forces are safely distributed over the ring without any rope slip. Hence the type of end-termination is more a question of esthetics, comfort and productivity. Of course, they should not stick out of the ring for a safe industrial use.

3.2 Impact of the Strand Rope Design on Strength Efficiency

More fiber simply means more MBL for the rings and for the chains. That is achieved by a thicker strand rope and / or by more circular braid circumventions. However, that does not always mean an efficient use of the inherent fiber strength. Inefficient use of fiber increases costs without more MBL. For that, we studied the impact of five different strand rope constructions on MBL for identical amount of fiber.

For a constant amount of 240 yarns of grade SK78 dtex1760, the brading angle was varied as follows (**Table 1**):

Table 1: Five varied strand ropes with equal amount of yarn but different constructions for testing the yarn efficiency in B.E.S.S.Y. constructions.

# Number of yarns SK78 dtex1760	Ø Diameter strand rope (approx.)	Braiding angle	Remark 1	Remark 2
12 x 20 = 240 x	10 mm	62 mm	No cover	-
12 x 20 = 240 x	10 mm	62 mm	Jacketed	-
12 x 20 = 240 x	10 mm	100 mm	Jacketed	-
12 x 20 = 240 x	10 mm	140 mm	Jacketed	-
8 x 30 = 240 x	10 mm	0 mm	Jacketed	Twist 75 rpm

With each strand rope design in Table 1, five B.E.S.S.Y. rings of inner diameter of 200 mm were braided in a five strand design.

In that way, 25 B.E.S.S.Y. rings were fabricated and MBL tested, belonging to the five strand rope designs. From their individual MBL data, Tenacity of each ring as expression for yarn efficiency was calculated. As reference sample, a rope sling was added (**Figure 8**).

As end-termination the one in Figure 7 from tape and seam was applied to all 25 rings.

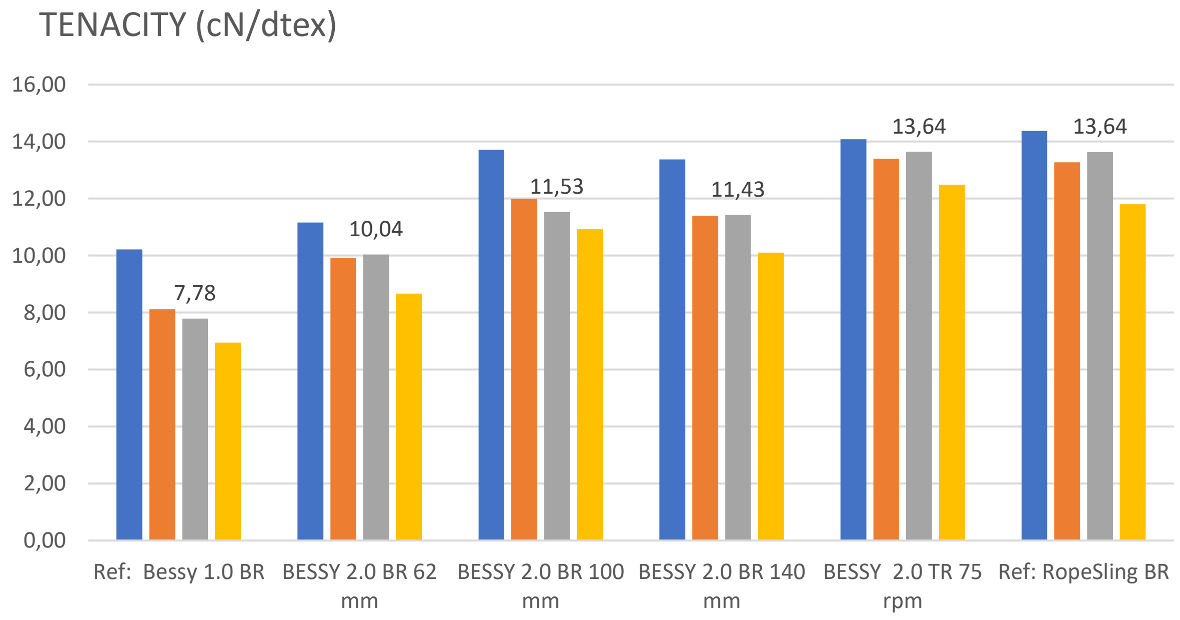

Figure 8: Bar chart of yarn efficiency, expressed by B.E.S.S.Y.-ring's Tenacity (cN/dtex) for the five different strand rope constructions according to Table 1. Since from each construction five parallel B.E.S.S.Y. rings were braided and their individual MBL tested, statistics of Tenacity was also obtained: Maximum tenacity (Blue bars), Minimum tenacity (Yellow bars), Average tenacity (Red bars), Median tenacity (Grey bars). A rope sling serves as reference sample (right hand bars). Number values for all six (grey) Median tenacities are given.

Looking at Figure 8 from left side to right side clearly shows a trend of improved yarn efficiency. Taking the Median tenacities (Grey bars) from 7,78 cN/dtex towards 13,64 cN/dtex, the improvement is nearly 6 cN/dtex ofwel 80 %. That is remarkable.

This improvement origins from three sources: First, from a cover that jackets the strand rope. The improvement is about 2,3 cN/dtex. The next improvement is the decreasing braiding angle, which adds an extra of ~ 1,5 cN/dtex. The more parallel and flat the yarns are, the more strength is obtained. The fifth sample with the mildly twisted strand rope ('tendon') provides another ~ 2 cN/dtex.

All three effects add up to the mentioned ~ 6 cN/dtex improvement in yarn efficiency.

As perfect independent proof of the result serve the bars on the very right hand for the reference sample of a parallel rope sling. They match the result of its left-handed fifth sample, made out of the jacketed parallel yarn tendon. This proof is valid, since both samples can be seen as a mirrored or inverted construction from each other.

4 Commercial Mass Manufacturing

So far, no automated mass manufacturing method exists for B.E.S.S. Y. chains or -rings. For the future, we see two routes. Route 1 could be the robotization of current circular manual braiding method around the proposed tubular mold. Such robotization of manual circular braiding will require a major investment.

The 2nd route is based on the time measurement of manual braiding of a small ring versus a large B.E.S.S.Y. ring. Since both take the same manual braiding time (between 15 – 30 minutes per ring, depending on the braiding expertise), the commercial focus will be on the largest - hence most profitable – application first.

In other words : Route 2 stays purely manual and priotizes in big applications – e.g. the mega sized synthetic chains resp. on oversized fiber rings for replacement of very large steel rings.

The following financial calculation illustrates this for a small B.E.S.S.Y. ring (MBL = 40 tons) versus a large B.E.S.S.Y. ring (MBL = 400 tons)

Table 2: Break down of the manufacturing costs for a small versus a large B.E.S.S.Y. ring.

Ø strand rope	B.E.S.S.Y. ring, design	Manual Braiding Time	Manual Labour Costs (80 Euro/h)	B.E.S.S.Y. ring, outer diameter / MBL (mTons)	B.E.S.S.Y. ring, weight	B.E.S.S.Y. ring, material costs (80 Euro/kg)	B.E.S.S.Y. ring, total costs added up
5 mm	12 x stranded braid	30 min	40 Euro	20 cm / 40 mT	400 grams	32 Euro	72 Euro
20 mm	12 x stranded braid	30 min	40 Euro	100 cm / 400 mT	10.000 grams	800 Euro	840 Euro

Due to identical manufacturing time of both samples, it can be concluded from Table 1, that the manual manufacturing of large B.E.S.S.Y. structures is more profitable, since material costs costs dominate over labour costs for large rings. In return it means, that small B.E.S.S.Y. structures only can be profitable made by automated manufacturing, e.g. by robotized circular braiding.

5 Conclusions

The newly developed and tested B.E.S.S.Y. chains and - rings with UHMWPE fiber may open up new business opportunities for replacement of a manifold of heavy and dangerous steel chains and steel rings (Figure 9).

Figure 9: Prototype photos of potential industrial applications for lighter and safer yet super-strong B.E.S.S.Y. : UP LEFT: Lifting masterlink under crane hook; UP CENTER: Cargo lifting connector; UP RIGHT: Versatile chain for mooring, lashing and lifting. DOWN BELOW: Light weight hybrid shackle (weight = 24 kg, height = 52 cm) versus tradional heavy steel shackle (weight = 55 kg)

By taking out the significant dead weight of the steel application, the weight saving by B.E.S.S.Y. will reach up to 85 %. That will improve handling safety, ergonomics and productivity and it will lower damage costs.

6 Acknowledgements

Authors thank following former and present colleagues of DSM Dyneema B.V., DSM Protective Materials B.V. and of AVIENT Protective Materials B.V. for their thoughts and contributions to the B.E.S.S.Y.- project:

Roel MARISSEN, Rigo BOSMAN, Rene HOMMINGA, Mihaela ZUIDEVELD, Saskia KRANENBURG, Judith BOSCH, Marc EIJSSEN, Jorn BOESTEN, Pieter Jan LEMSTRA, Masashi TORINOMI, Stewart LEE, Yong Le LIU, Bart TACKEN, Daan MEEWIS, Binay PATEL, Keith ROWSEY.

7 References

[1] WIENKE, Dietrich, DIRKS, Christiaan Henri Peter, JACOBS, Martinus Johannes Nicolaas: Chain Comprising a Plurality of Interconnected Links, International Patent Publication WO 2008/108 979 8 A1, July 31st , 2008

[2] WIENKE, Dietrich, MARISSEN Roelf, JACOBS Martinus Jojannes Nicolaas, DIRKS, Christiaan Henri Peter: Chain Comprising Links, International Patent Publication WO 2009/115249 A1, September 24th, 2009

[3] BOSMAN Rigobert, WIENKE, Dietrich, HOMMINGA, Jozef Siegfried Johannes: Endless Shaped Article, International Patent Publication WO 2014/ 14/40 59 908 A1, May 12st ,2014

[4] WETZELS, Karel Jozef, WIENKE, Dietrich, HOMMINGA Jozef Siegfried Johannes, MARISSEN Roelof, BOSMAN Rigobert, Chain with Endless Braided Chain Link, International Patent Publication WO 2017/077 141 A2, May 11th, 2017

8 Authors' Introduction

Dr. Dietrich Wienke started his profession with 16 as vessel engine mechanic / sailor. He got his M.Sc. and PhD in Physical & Process-Analytical Chemistry from Jena University (DE). After post-doc stays to University of Nijmegen (NL) and to Clarkson University (USA), he joined SONY Corp (JP) as Global Project Manager for electronic appliances recycling. He moved on to Dutch chemical corporation DSM as Head of Chemical Process Analysis and of Optical Spectroscopy Lab, while completing his business education in polymer science at Eindhoven University (NL), in finances and marketing. In 2004 je joined DSM Dyneema (NL) in business roles as Account Manager, Global Project Director and Manager New Business Development. He published more than 50 scientific papers and patents and regular presents at international conferencs . End of year 2025 he retires.

Robert Cohnen, M.Eng.Sc. graduated as Polymer Engineer. He started his career in Aerospace Industry in the design and manufacturing of composite parts for aircraft. After that, he joined the Technical Center Europe of DSM Dyneema in Heerlen (NL), where he works on projects with Dyneema® fibre for synthetic chains, synthetic ropes and composites. He is highly skilled in fiber testing, in yarn processing and in rope and chain design and testing.

Karel Wetzels, Textile Technician and Rope Expert, worked 45 years for DSM Dyneema and recently retired. He was highly skilled in textile and fiber processing methods ranging from yarn twisting, weaving and braiding. With is enormeous fiber and textile expertise, he was able to make and to study many new prototypes, test samples and commercial samples. As inventor and co-inventor, a number of patents carry his name.

Cost-effective replacement of steel wire hoisting ropes: the TechIce heat-resistant synthetic fibre rope

Bo Cornelissen

Teijin Aramid B.V., Arnhem, The Netherlands

Davíð Waage, Jón Atli Magnússon

Hampidjan, Reykjavík, Iceland

Summary

In hoisting applications, the bending fatigue performance of synthetic fibre ropes has been the key development topic for many years. To replace steel, it is of high importance to select a fit-for-purpose engineered fibre rope.

The TechIce® design combines the best properties of different synthetic fibres. The high temperature resistant load-bearing core of aramid co-polymer is combined with the abrasion resistance of a HMPE jacket.

Experimental studies were done to compare this novel solution to a classic design in a cyclic bending over sheaves (CBoS) test. Lab tests were done by the manufacturer and by NORCE, an independent testing institute based in Grimstad, Norway. User test experiences in the field are shared as well.

In this paper we present convincing evidence that proves the fit-for-purpose method in demanding hoisting applications. The TechIce® concept can replace steel wire as well as HMPE lightweight hoisting ropes in a safe and cost-effective way. The predictability of the rope's lifetime deserves more attention to come to the level of knowledge of SWR. Further evaluation is needed to grasp the full potential of this new rope solution.

Keywords: Fibre rope, Cyclic bending over sheaves, CBoS, TechIce, Technora, aramid, HMPE

1 Introduction

The increasing working depths in offshore hoisting demand novel synthetic fibre rope solutions. Steel wire rope (SWR) has a long standing track record, using established technology, and a quite well understood damage evolution during its lifetime [1, 2]. However, at increased water depths, typically beyond 1500 m, the self-weight of SWR becomes a limiting factor for cost-effective use. In any operation involving prolonged cycling of specific sections of hosting rope, like in active heave compensation (AHC), temperature can severely limit the operating window of SWR. The grease required for good lubrication melts and leaks from the rope, resulting in accelerated wear due to mainly internal abrasion in the rope [1, 3].

Synthetic fibre ropes (SFRs) offer several advantages compared to steel, like a higher strength-to-weight ratio, non-corrosiveness, and easy handling. On the other hand, SFR has its own challenges, mainly related to adequate prediction of the end-of-life [4]. Although the knowledge base grows rapidly, there are still limitations regarding condition monitoring [5, 6]. It is clear, however, that the dominant failure modes of different fibre types vary [7]. For example, for HMPE, creep is often the limiting factor in the rope's lifetime, whereas for aramids, the inter-strand abrasion is dominant [8]. Therefore, directly addressing those failure modes in its design can help to significantly improve a rope's lifetime.

In this work, we present a new rope construction, which reflects the best fit-for-purpose use of different synthetic fibres. The combination of aramid and HMPE fibres in one rope design allows to fully exploit the advantages of both materials, and at the same time avoid their limiting factors to become dominant in the rope's failure modes. This paper presents different experiments, among which a direct comparison of the cyclic bending over sheave (CBoS) lifetimes of DynIce® and TechIce® ropes, based on equal rope diameter. The measurements were done by the independent lab of NORCE Energy and Technology in Grimstad, Norway.

2 Literature – dominant failure modes in bending fatigue and lifetime assessment

2.1 Steel wire rope

A complete review of the extensive literature on steel wire rope applications does not fit in this paper. Without aiming to be exhaustive, an attempt was made to identify the most important failure modes and use conditions of SWR in offshore and onshore hoisting applications.

Vennemann et al. shared their insights from deep water subsea hoisting jobs [1]. One main finding was that temperature limits effective lubrication, leading to accelerated wear of rope. A specially designed CBoS machine was used on ø109 mm steel wire ropes on sheaves of 2.2 meter diameter. Measurements at loads ranging from 50 to 330 ton were performed. After measuring rope surface temperatures over 150 °C, the authors decided to apply water cooling to keep the lubricant in the rope. Another major risk which applies not only to offshore hoisting, is the occurrence of internal wire breakage. Let alone that these failures cannot be observed when using only (automated) visual inspection methods, the authors state that those defects are often not easily identified by non-destructive testing (NDT) methods like magnetic flux leakage (MFL), because they can be masked by other defects near the surface of the rope. It appears to be a difficult problem to tackle, with some illustrative examples of low rotation and rotation resistant ropes provided by Chaplin [9]. Mazurek et al. also mention this limitation of MFL in an extensive review of NDT to detect and if possible quantify SWR degradation [10].

In a totally different environment, poor lubrication plays a key role as well. Pal et al. investigated the premature failure of a SWR onshore hoisting application in a workshop handling hot steel [3]. The poor lubrication of a ladle crane rope led to premature failure due to excessive wear. A failure in a similar application but with a different failure mode was presented by Palit et al [11]. In this case, the build-up of torsion in the hoisting rope (8XK26 SW) of a crane in a steel plant led to a characteristic failure of wires under an angle of 45º to the wire axis.

Peng et al. reported in their study that lateral loads, twist angle, and lubrication can significantly affect the wear rate of steel wire rope in coal mines [12]. They conclude that the severity of wear marks in terms of depth and width increases in the case of dry friction conditions. Three wear mechanisms under dry friction are reported: abrasive, adhesive, and fatigue wear, whereas under (oil) lubricated conditions, abrasive and fatigue wear dominate. The recommended operating temperature of the lubricants ranges from -50 to 70 °C.

Katiyar et al [13] studied the failure of a 6X17 Seale rope (10 ton MBL) used for lifting in a mining application. The authors report that the rope failed earlier than expected (after 3 years in service when subjected to a 1 ton load). A detailed analysis of the failure showed that the main failure mode was most likely fatigue. Initiations of cracks occurred in individual wires that contained hardened regions (martensite formation at the wire surface), most likely induced during production of the rope and upon sliding contact with a hard surface. Microcracks and quenched cracks at the surface led to stress concentrations during bending. Also, the authors mention that hard inclusions can accelerate the wear rate and lead to faster rope deterioration. A detailed fractography study showed cracks growing from the steel wire surface (beach marks) and partly brittle and ductile failure patterns, typical for a cyclic fatigue failure mode. A poor lubrication regime can further accelerate wear.

Some hybrid rope developments took place over time, mainly limited to high D/d applications like in mine hoisting systems [14, 15]. The main advantage over full synthetic fibre rope is the higher robustness of the rope; it is expected to better resist impact from outside and perform better in multi-layer drum winding. Compared to full steel alternatives, hybrid ropes offer a higher strength-over-weight ratio and increased tension and bending fatigue life [15]. Furthermore, Ridge et al. mention that the steel part, which was on the outside, would fail first and its damage is detectable with established NDT, for example MFL [14].

Summarizing, it is essential for steel wire rope to have a good lubrication regime in place to reach the expected lifetime. Steel wire ropes can easily heat up during prolonged cycling and lose their lubricant, which in turn leads to excessive wear and early failure. Apart from being costly, this early failure can lead to unsafe situations, mainly because internal damage remains unnoticed.

2.2 Synthetic fibre rope

When focusing on high performance synthetic fibres, HMPE and co-polymer aramid are good candidates for hoisting applications. When it comes to the estimation of the remaining lifetime of SFRs, several approaches were proposed in literature. They often rely on a combination of non-destructive testing technologies with data-extraction supported by machine learning approaches and predictive models based on residual strength after pre-set CBoS exposure.

Davies et al. presented an approach which relates the residual strength of a HMPE-based SFR to its remaining CBoS lifetime [16]. The authors show that the CBoS lifetime as a function of the applied tension during cycling better fits a log-log relation than the commonly assumed semi-log relation. Further work is needed to confirm this relation for other synthetic fibres. They also present some interesting insights on the uneven distribution in loss of strength along the CBoS life of the rope. Tests were done on open 12-strand braided ropes, made of SK75-grade HMPE (Samson, nominal dia. 19 mm, nominal breaking strength 250 kN). Meuwissen et al. proposed a variation on this approach, they account for load variations during the rope's lifetime for an assessment of an adjusted safe working load to achieve the desired lifetime [17]. As a main motivation for this work, the authors mention that current prescriptive standards lack clear instructions and criteria for safe operation during the remaining lifetime. An acceptable empirical approach can help to lower the entry barriers of using SFR in mainly offshore hoisting applications. In order for the method to work at acceptable use conditions, the HMPE ropes have to be actively cooled. This adds cost and complexity to the offshore crane systems and heating of the core of the rope cannot be prevented. Therefore, a more temperature and creep resistant SFR can provide a less complicated and more cost-effective hoisting solution. The Technora® co-polymer aramid fibre combines these properties with a higher abrasion and fatigue resistance than other para-aramids on the market. Knoester and one of the present authors showed the advantage of aramids in terms of creep and temperature stability [18].

NDT technologies can help to lower entry barriers to replace SWR as well. About a decade ago, Schmieder et al. proposed a method to systematically assess the condition of SFRs in bending fatigue by using a combination of non-destructive inspection technologies [4]. The incentive for this work was the same as indicated by Meuwissen et al [17]. The increasing maturity of inspection methods and the rapid growth of machine learning possibilities will help to speed up the qualification of SFR in on- and offshore hoisting operations. In their research effort at the Technical University of Chemnitz, Schmieder et al. introduced a rope consisting of a load bearing core of Technora® with an electrically conductive thread for resistive measurements, an optical fibre sensor is used to monitor load and strain, and a rope jacket based on a distinct pattern of longitudinal marks in contrasting colors to identify torque. The research rope also contained a thread of bariumsulfate to provide contrast in X-ray tomography. All these features allowed for a very detailed study of changes of the rope's geometry and properties. Not only strength was a variable in the study, the changes in secant stiffness of the rope core compared to the jacket proved to be a good indicator of an approaching end of lifetime.

The review article from Oland et al. provides an overview of typical failure modes of SFR and discusses several methods to identify and even better, quantify damage [8]. Although SFR failure is often due to a combination of failure modes, the dominant failure mechanisms in CBoS are (temperature accelerated) creep for HMPE, and inter-strand abrasion for aramids respectively.

Falconer et al. presented an approach to use computer vision for advanced strain and thermal monitoring of, in this case, a 19 mm 12-strand braided HMPE DM20 rope [19]. They showed that accurate length change measurements can be done on specific rope sections in order to assess the local elongation of the rope during CBoS cycling. It was found to be temperature-dependent for this type of SFR. Perhaps not surprisingly, the highest elongation levels were found in the double bendig zone of the test rope. These measurements were done at the Mechatronics Innovation Lab (MIL) of the NORCE institute.

In their design process, van Wezel et al. looked at different parameters for the material selection of the tugging rope for an innovative tug boat design [20].They proposed a modelling and experimental approach to estimate the time to reach the fibre-specific critical temperature during cycling on the same rope section. Although the outside temperature of the aramid rope (without individual strand covers) increased more rapidly than that of its HMPE equivalent, the operating time window was twice as large, because of the material-specific maximum allowable temperature. Other aspects like multi-layer drum spooling behavior and friction on a metal drum surface were investigated as well.

Davies et al. compared 50 ton break load HMPE (SK75) and Technora® (T221) ropes for oceanographic applications [21]. They indicate that although the rope designs were dissimilar (HMPE 12-strand open braid, Technora® 16x2 braid with an extruded polyester elastomer cover and a light PET braid between core and cover), their nominal diameter (30 mm) and break load were comparable. So, equal D/d and life factor values apply during CBoS testing. The outcome of the study is that HMPE ropes have a higher dynamic stiffness and hysteresis, but about half of the CBoS lifetime compared to Technora®. A considerable factor is also the larger bedding-in effect on HMPE ropes. Permanent deformations are more than two times larger than those of the Technora® rope. Wet performance issues with the specific Technora® fibre type were expected, but not investigated. Teijin Aramid provides Technora® fibres with marine finish, which enable optimal performance in a marine environment.

Summarizing, the field of SFR in different hoisting applications is maturing rapidly. The increasing number of successful cases and the advancement of NDT technologies can accelerate the adoption of SFR in various CBoS applications like on- and offshore hoisting.

3 Experimental work

The experiment plan aimed to verify the hypothesis that addressing the inter-strand abrasion of aramid braided ropes can significantly improve their cyclic bending over sheaves lifetime. This section contains descriptions of different experiments, among which two lab experiments, and one field trial followed by lab experiments. Section 4 contains the aggregated results, together with results of steel wire rope and Technora® rope without individually covered strands. **Table 1** contains all the results of the experiments described in this section.

3.1 Synthetic fibre rope – Lab test – NORCE-MIL

Lab tests were done on request of the seismic services company Petroleum Geo-Services (PGS) by the NORCE Norwegian Research Centre AS on modified CBOS equipment at the Mechatronics Innovation Lab (MIL) in Grimstad, Norway [7]. Two rope types were evaluated in a simulated hot climate (43 ± 2 °C). This temperature range was chosen to check whether Technora® fibres offer an increased operational safety compared to HMPE. **Figure 1** shows some photographs of the actual setup and a schematic overview of the testing equipment. The measurements consisted of a direct comparison based on equal diameter between TechIce® and Dynice® (where Dynice® showed the best performance of in total 9 types of HMPE ropes). The comparison was based on one of the best performing HMPE warps in the market according to a test by TU Clausthal (multi-layer spooling behavior) [22].

(a) (b) (c)

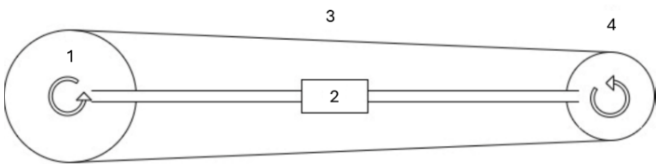

1) *Driving sheave ø1000 mm*
2) *Cylinder (keeps rope tension constant)*
3) *Test rope specimen*
4) *Testing sheave ø800 mm*

(d)

Figure 1: Pictures of the CBOS machine at the MIL lab (adopted from [7]). Before (a) and after (b) climate chamber application; test sheave and IR thermal camera (c). Schematic overview of the CBOS machine (adopted from [7])(d).

3.2 Synthetic fibre rope – Lab test – Hampidjan

Several CBoS tests were done at Hampidjan's lab in Lithuania. A first set of tests consisted of CBoS exposure to 30 mm TechIce® rope on two different sheave diameters as the only varying factor. The remaining strength was determined after a pre-determined number of CBOS cycles, as stated in Table 1. In a second series of tests, the same TechIce® rope as mentioned in the first test was compared to a commercially available rope fully based on HMPE as load-bearing fibre. The direct comparison of the two load-bearing fibre materials, Technora® and HMPE, respectively, resulted in a large difference in lifetime. Table 1 shows the results. The rope containing the Technora® fibres lasted for a rather long time. Therefore, it was decided to stop the test after 320000 cycles and determine the remaining breaking strength as a percentage of the initial minimum breaking load (MBL) of the rope prior to CBoS exposure. The remaining strength of the ropes was determined on a horizontal test bed in the same lab. This data convincingly shows the significant improvement in lifetime of Technora®-based rope compared to HMPE.

3.3 Synthetic fibre rope – Field test – Favelle Favco Malaysia

The crane company Favelle Favco from Australia supported a field trial on one of their onshore construction cranes in Malaysia. A ø16 mm TechIce® rope was evaluated as a direct replacement of SWR rope in regular hoisting jobs on a construction yard (reduced hoisting speed, but >100 mm/s, polymer sheaves, tropical climate). Two short rope specimens were sent for forensic analysis after the field test (**Figure 2**), and field tested specimens were shipped to the Institut für Fördertechnik und Logistik (IFT) in Stuttgart, Germany, for further CBoS testing (cycling to failure under pre-determined conditions, max. 100 mm/s). Table 1 shows the rope and hoist cycle properties. The annotation no bending in the table refers to the exposure of tension-tension only, that section of the rope was not bent over sheaves in the crane. Remaining strength tests of the in-field specimens were done at another test facility.

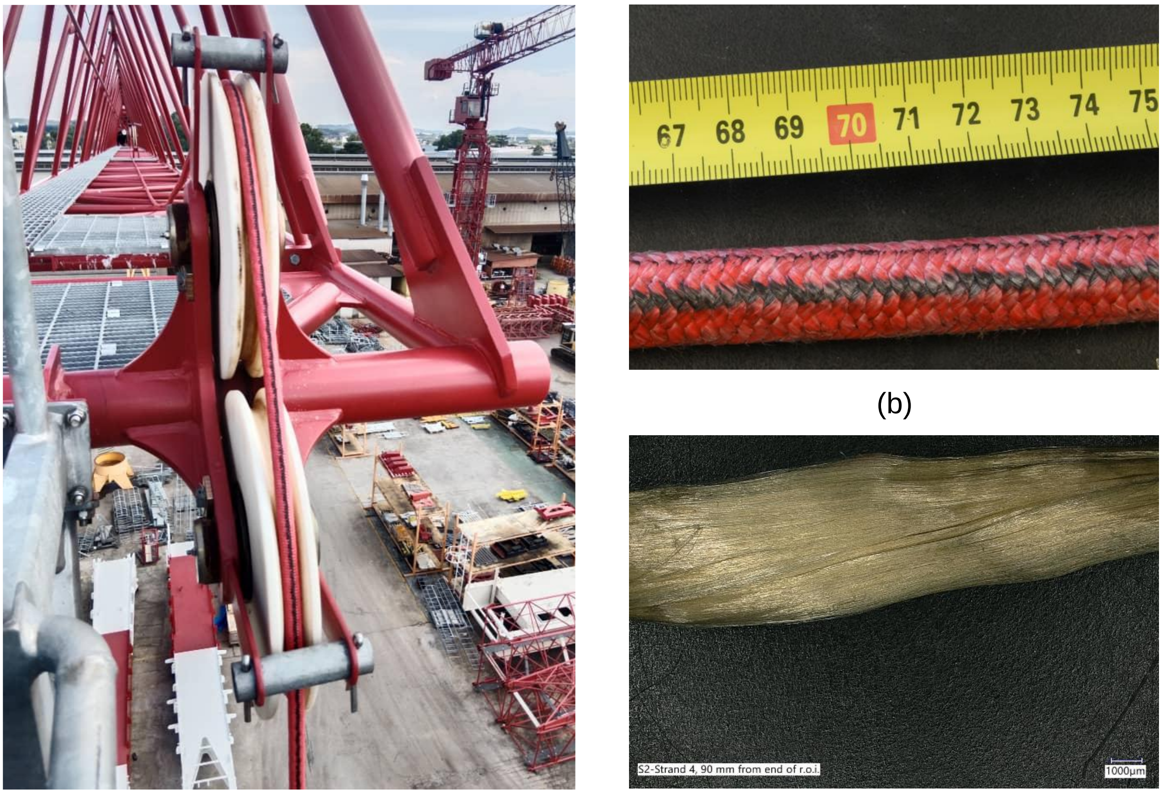

(b)

(a) (c)

Figure 2: Field test on Favelle Favco crane in Malaysia; rope in application (a); rope as-received for forensic analysis (rope #2 – bending)(b); close-up of an individual strand after removing the strand cover; the Technora® filaments are still intact (rope #2-bending), the scale bar at the bottom right of the picture is 1 mm long (c).

4 Results

Section 4.1 contains a representation of the experiments described in the previous in the context of other measurements. It is notoriously difficult to provide a real like-for-like comparison for different experiments. The proposed approach is to show the cycles to failure as a function of the applied life factors (LF) in a log-log plot. For clarity, different experimental results are combined in a single graph to facilitate comparison (Figure 3). The legend contains D/d values to enable an as fair as possible comparison of results from different labs and experiments. Note that the TechIce® datapoints represent measurements that were almost all stopped prior to failure. This is indicated by arrows pointing to the right next to the corresponding datapoint. The two dataseries of 13 mm Technora rope (without individual strand cover) originate from experiments done at the R&D lab of Teijin Aramid in Arnhem, the Netherlands (Lab 1), and the fibre rope testing lab of Royal IHC in Sliedrecht (currently Kinderdijk), the Netherlands (Lab 2), respectively. The 14 mm DynIce rope was tested by Royal IHC in Sliedrecht as well. The two meaurements at IFT Stuttgart on field-tested TechIce® ropes are shown in Figure 3 (Lab 3). Note that these datapoints fully overlap each other, only one is visible in the plot. The SWR data were adopted from the work by Onur and Imrak [23]. In their article, they report that different combinations of load and D/d (10 and 25) were applied.

4.1 Aggregated results

The graph in **Figure 3** clearly shows how the tested SFR ropes compare to a representative SWR construction. The results of TechIce® rope show the potential of the new design, despite the fact that only two out of six datapoints represent CBoS measurements to failure. Those two datapoints of approximately eighteen thousand cycles were evaluated on the CBoS tester in Stuttgart (IFT) after being exposed to almost 600 hoisting cycles in Malaysia (see Table 1 for details). Together with the four other datapoints and the remaining strength values of those rope specimens (Table 1), this clearly illustrates that TechIce® ropes outperform classic rope designs.

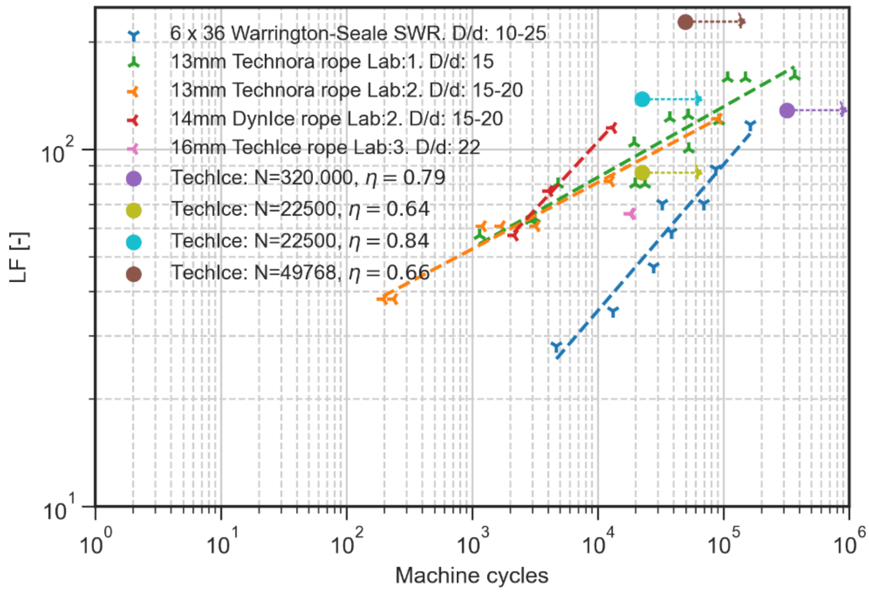

Figure 3: Log-log representation of different CBoS measurement results. The solid dots represent measurements which were stopped prior to failure, followed by a remaining strength measurement (denoted by η, the residual breaking strength relative to the MBL of the fresh rope). Note that no water cooling was applied in any of the presented measurements. Warrington Seale SWR data was adopted from [23].

4.2 Detailed test results – NORCE-MIL

In the test at the NORCE-MIL lab the elongation of the rope specimens was monitored on request of PGS. Apart from the absolute numbers, it is worthwhile to take a look at the elongation profiles as a function of time for the DynIce® and TechIce® rope, shown in **Figure 4**.

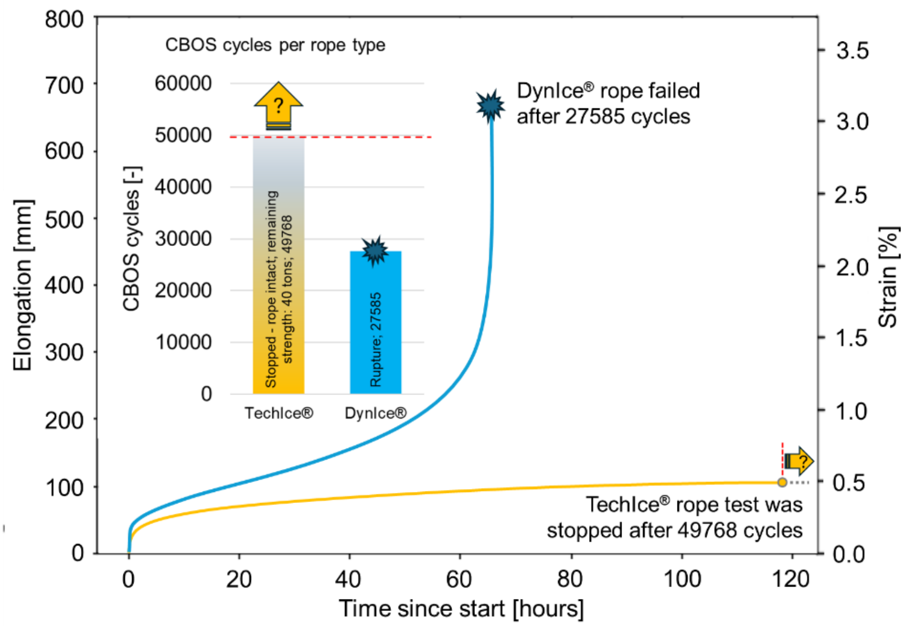

Figure 4: Elongation and strain evolution during CBoS tests on two rope specimens, the ambient temperature was controlled at 43 ± 2 °C, adopted from [7].

The full 3-regime creep curve of HMPE is visible, whereas for Technora® there is no sign of a transition from the second to the third regime. Knoester et al. provide more information on the background of these regimes [18]. Also, the rate of elongation due to creep is significantly lower. Section 5 elaborates on the temperatures observed in both ropes during CBoS cycling.

Table 1: Overview of test results per location.

Test and location	Rope type (Core / Strand cover material)	Breaking strength BS (Unspliced) [mt]	Rope dia. [mm]	Sheave dia. [mm]	D/d [-]	SF [-]	LF [-]	Cycle time [s]	Water Cooling ?	CBoS cycles to failure [-]	Stopped after # of cycles [-]	Breaking strength after CBoS [mt]	Remaining strength [%BS]
NORCE-MIL - Norway													
	TechIce® (Technora® / HMPE)	60.9	30	800	27	8.5	228	9	No		49768	40	66%
	DynIce® (HMPE-DM20 / n.a.)	53.6				7.5	200		No	27585	n/a		
Hampidjan - Material comparison - Lithuania													
	TechIce® (Technora® / HMPE)	48.5	33	1060	32	4	128	15	No	n/a	320000	38	~79%
	DynIce® (HMPE-SK75 / n.a.)	107.1	38	1060	28	4	112	60	Yes	3900-4200*	n/a		
Hampidjan - D/d comparison - Lithuania										*) n=3			
	TechIce® (Technora® / HMPE)	53.1	30	560	19	4.6	87	15	No	n/a	22500	34	64%
	TechIce® (Technora® / HMPE)			900	30		138		No	n/a		44.5	84%
Field test Favelle-Favco - Malaysia													
	TechIce® (Technora® / HMPE) - bending	13.5	16	352	22	3.1	66	n/a**	No	n/a	~600 hoists	11.78 / 11.80	87% / 87%
	TechIce® (Technora® / HMPE) - no bending	13.5	n/a	n/a	n/a	3.1	N/A	n/a**	No	n/a	~600 hoists	11.57 / 12.38	86% / 92%
Follow-up CBoS test on hoisting in Favelle Favco field test - Stuttgart								**) 27 m hoisting height				n=2	
	TechIce® (Technora® / HMPE)	13.5	16	352	22	3.1	66	10	No	18155	n/a		
	TechIce® (Technora® / HMPE)	13.5			22	3.1	66	10	No	18500	n/a		

5 Discussion

The previously mentioned hypothesis that addressing the inter-strand abrasion of aramid braided ropes can significantly improve their cyclic bending over sheaves lifetime can be confirmed, albeit qualitative. A quantitative answer requires more testing and evaluation work, including CBoS tests that run to failure. The inter-strand abrasion was significantly delayed, as shown by the test results in the previous section. The full potential of the TechIce® has to be explored further. In line with the approach of Davies et al., a relation between residual strength and rope lifetime is to be explored. At this moment, it is unclear whether the dominant failure mode is (delayed) fatigue or (delayed) abrasion.

There is no sign that temperature is a dominant factor in failure, which was also concluded earlier by van Wezel et al. (rope without individual strand cover) [20]. Interestingly, the surface temperatures of the ropes in the tests at NORCE (section 3.1) were rather high for the DynIce® rope, up to 70 °C during and up to 90 °C at the end of its lifetime. In contrast, the TechIce® rope surface remained between 60 and 64 °C until the test was stopped after close to 50,000 cycles. Note that the ambient temperature in the CBoS enclosure was kept at 42 °C.

6 Conclusions and future work

A novel rope concept was introduced that combines the best properties of synthetic fibres to provide a fit-for-purpose solution in onshore and offshore deep-sea hoisting applications. The concept of a braided rope with individually HMPE-covered Technora® strands enables a significant increase in bending fatigue lifetime.

Both in steel wire rope and synthetic rope bending fatigue applications the rope temperature is a key factor that influences the rope's lifetime. For steel wire rope, temperature is a critical factor in lubrication. For synthetic rope, temperature is critical to maintain the intrinsic material properties like strength, abrasion, or creep resistance. The individual strand covers in the braided rope design decrease the inter-strand friction. This concept limits the temperature increase during cyclic bending over sheaves and the wear of the aramid strands. It results in a longer lifetime, enabling cost-effective use of the hoisting rope. The TechIce® concept does not suffer from creep as a limiting factor in CBoS lifetime.

Furthermore, replacing steel wire rope in hoisting applications brings several benefits:

- No need for (re-)lubrication of the rope in use, nor corrosion prevention measures

- Smaller installation vessel design possible (crane capacity, power supply)
- Higher payload in deep-sea hoisting, lower energy use
- Easier handling of the rope on and below deck
- No cooling required during bending over sheaves, even for prolonged time.

Future work will focus on further gaining insights in the evolution of residual strength during the rope's lifetime in CBoS applications and the effect of loading history on the remaining lifetime. Furthermore, there is a high interest in performing cycling tests to failure and identifying the dominant failure modes as a function of the specific test conditions in more detail. At this point, we can confirm the qualitative aspect of the individual covered strands, the future tests will enable us to also quantify them.

7 Acknowledgements

The authors would like to acknowledge PGS Norway and the NORCE institute for sharing the results and details of the lab tests at their facilties. The authors are indebted to Royal IHC for sharing the rope test data done on Hampidjan ropes on their fibre rope tester. Furthermore, the support by John Dawson of Favelle Favco by sharing insights from an onshore hoisting crane field test case in Malaysia is highly appreciated. Teijin Aramid and Hampidjan are very grateful to be able to present the results obtained by these partners in this paper.

8 References

[1] O. Vennemann, I. Frazer, Installation of subsea structures in deep and ultra deep water using steel wire rope deployment systems, Proceedings of D.O.T. XXI Conference, Perth, 2008.

[2] K. Feyrer, Wire ropes, tension, endurance, reliability, Springer Verlag, 2007.

[3] U. Pal, G. Mukhopadhyay, A. Sharma, S. Bhattacharya, Failure analysis of wire rope of ladle crane in steel making shop, Intl. J. Fatigue, 116 (2018) pp 149-155.

[4] A. Schmieder, T. Heinze, M. Michael, Failure analysis of high-strength fibre ropes, Materials Science Forum, 825-826 (2015), pp 891-898.

[5] T. Jalonen, M. Al-Sa'd, R. Mellanen, S. Kiranyaz, M. Gabbouj, Real-time damage detection in fibre lifting ropes using lightweight convolutional neural networks, IEEE Sensors Journal, accepted for publication, 2024, DOI 10.1109/JSEN.2024.3521118.

[6] A. Rani, D. Ortiz-Arroyo, P. Durdevic, Defect detection in synthetic fibre ropes using Detectron2 framework, Applied Ocean Research, 150 (2024) 104109.

[7] E. Nordgård-Hansen, E. Hauge, Rope Testing at Elevated Temperatures – Test Results, NORCE 2024.

[8] E. Oland, R. Schlanbush, S. Falconer, Condition Monitoring Technologies for Synthetic Fibre Ropes – a Review, Int. J. Prognostics and Health Mgt, 2017, 014.

[9] R. Chaplin, Discard Criteria: A Review, OIPEEC Conference – Bardolino, 2024, pp 181-194.

[10] P. Mazurek, A Comprehensive Review of Steel Wire Rope Degradation Mechanisms and Recent Damage Detection Methods, Sustainability, 15 (2023) 5441.

[11] P. Palit, S. Kushwaha, J. Mathur, A. Chaturvadi, Life cycle assessment of wire rope used in crane application in a steel plant, J Fail. Anal. Preven., 19 (2019) pp 752-760.

[12] Y. Peng, K. Huang, C. Ma, Z. Zhu, X. Chang, H. Lu, Q. Zhang, C. Xu, Friction and wear of multiple steel wires in a wire rope, Friction, 11(5) (2023) pp 763-784.

[13] L. Katiyar, M. Khan, C. Sasikumar, The failure of a steel wire rope: A root cause analysis, J Fail. Anal. and Preven., 24 (2024) pp 1699–1706.

[14] I. Ridge, N. O'Hear, R. Verreet, O. Grabandt, C. Das, High strength fibre cored steel wire rope for deep hoisting, OIPEEC Conference – Johannesburg, 2007, pp 225-240.

[15] P. Wang, H. Schultheis, A. Eelbode, J. Karedan, Development of steel-fibre hybrid ropes and the application in mining hoist systems, OIPEEC Conference – Bardolino, 2024, pp 271-284.

[16] P. Davies, M. Fançois, N. Lacotte, T. Vu, D. Durville, An empirical model to predict the lifetime of braided HMPE handling ropes under cyclic bend over sheave (CBOS) loading, Ocean Engineering, 97 (2015) pp 74–81.

[17] M. Meuwissen, R. Bosman, M. Vlasblom, M. Eijssen, S. Leite, S. Bull, O. Haugland, V. Åhjem, Bending lifetime prediction method for HMPE rope solutions, OIPEEC Conference – Bardolino, 2024, pp 259-270.

[18] H. Knoester, B. Cornelissen, Assessing creep behavior of para-aramid fibres during their economic lifetime, OIPEEC Conference – Bardolino, 2024, pp111-126.

[19] S. Falconer, E. Nordgård-Hansen, G. Grasmo, Computer vision and thermal monitoring of HMPE rope condition during CBOS testing, Applied Ocean Research, 102 (2020) 102248.

[20] M. van Wezel, H. van den Heuvel, Rope lifetime estimation for the delta escort tug active constant tension winch, OIPEEC Conference – Stuttgart, 2022, pp 75-94.

[21] P. Davies, Y. Reaud, L. Dussud, P. Woerther, Mechanical behaviour of HMPE and aramid fibre ropes for deep sea handling operations, Ocean Engineering, 38 (17-18) (2011) pp 2208-2214.

[22] A. Lohrengel, M. Schulze, H. Erlendsson, J. Magnússon, P. Smeets, B. Tacken, The influence of high performance fibre rope designs on drum load and spooling performance in multi-layer drum equipment, OIPEEC Conference – La Rochelle, 2017, pp 95-116.

[23] Y. Onur, E. Imrak, Experimental and theoretical investigation of bending over sheave fatigue life of stranded steel wire rope, Indian Journal of Engineering & Material Science, 19 (2012) pp 189-195.

9 Authors' Introductions

Mr Bo Cornelissen received his PhD degree in Mechanical Engineering from the University of Twente in 2013. He started his industrial career as product and application development specialist at Teijin Aramid in 2013. He primarily works on the structural application of aramids in ropes and cables for marine and offshore use. The research topics of bending fatigue and long term behavior, as well as non-destructive inspection techniques have his specific interest.

Mr Davíð Waage received his M.Sc degree in Information Technology from University of Bournemouth in the UK. He started his professional career at Hampidjan Group in 2011, and has since worked on ropes, rope technology and rope development. His main interests are in the development of rope technology via material selection, rope design and application technologies to replace steel wire in areas where fibre ropes have a possibility of outperforming steel wire.

Mr Jón Atli Magnússon received his BSc degree in Mechanical Engineering from University of Iceland in 2007 and MPM in 2010 from same university. He directed research and development for Hampidjan from 2018 to 2022 and since 2022 as external consultant. He led the development of the TechIce rope and holds 3 patents on rope design.

New Rotary Bending Test Machine for Rope Wires

Professor Ulrich Briem

OTH Regensburg, Germany

Summary

Rotary bending tests are an excellent tool for evaluating the fatigue behavior of rope wires. There are four different types of testing machines. In order to avoid wire breaks at the terminal points, the first three types are designed so that the bending stress at the terminal points is zero. The disadvantage of these testing machines is that the usable test length of the wires is relatively short. In the fourth type, the bending stress at the terminal points is only 4% lower than in the middle of the free wire length. This small difference is enough to avoid wire breaks at the terminal points. The whole wire length can be regarded as loaded almost evenly. A testing machine for thick wires would be too large and for soft wires the testing length of the wires is too long. Based on the fourth type of testing machine, a new testing machine was developed to shorten the test length accordingly.

Keywords: Rotary bending tests, Rotary bending machines, Test lengths

1 Introduction

In 1933, Haigh and Robertson [1] introduced a rotary bending machine for rope wires. A straight wire, clamped at both ends with hinges, is subjected to a compressive force, causing it to buckle and rotate around its own axis. The bending stress is zero at the clamping points and maximum at the center of the free wire length. A free wire length of 150 times the wire diameter is recommended [2].

In 1942, Erlinger [3] introduced a rotary bending machine that essentially operates according to Haigh and Robertson's principle. By using a dial gauge for the compressive force, knowledge of the Young's modulus is no longer necessary. The testing machine is built and commercially distributed by Schenck AG. This testing machine has been incorporated into the DIN 50113 standard [5].

In 1948, the Hunter-Pressed-Steel Company Co. patented a rotary bending machine, which Votta [4] reported on. The clamping points are arranged in parallel. However, the wire length is so long that the bending stresses at the clamping points are zero.

In 1982, a testing machine was built at the IFT at the University of Stuttgart, based on the testing principle of the Hunter-Votta machine, Wolf [6]. It avoided the disadvantage of very uneven bending stresses across the wire length, which would result in almost maximum bending stress along the entire wire length.

For very thick wires, however, the testing machine would have to be very large, and for soft wires, such as copper, the stress length is too long. Based on the IFT Stuttgart machine, a new rotary bending machine was introduced, which allows the wire length to be appropriately reduced. This testing machine is referred to below as the OTH Regensburg machine. The setting parameters for the testing machine were derived.

2 Testing Priciple

The testing principle of the IFT Stuttgart machine is briefly explained here, which also makes the further development into the OTH Regensburg machine understandable.

2.1 Test bench principle IFT Stuttgart

The wire is clamped into the machine in a nearly semicircular configuration, **Figure 1**. The two clamping points are spaced at a distance of C. The free length of the wire is only slightly greater than $C\,\pi/2$, which means that the bending stress at the clamping points is only slightly lower than in the middle of the free wire length. Therefore, the bending stress is almost at its maximum over a large bending length, and wire breakage at the clamping points is largely avoided. **Figure 2** shows the basic bending stress curves along the free wire length for the IFT-Stuttgart and Schenck test bench types.

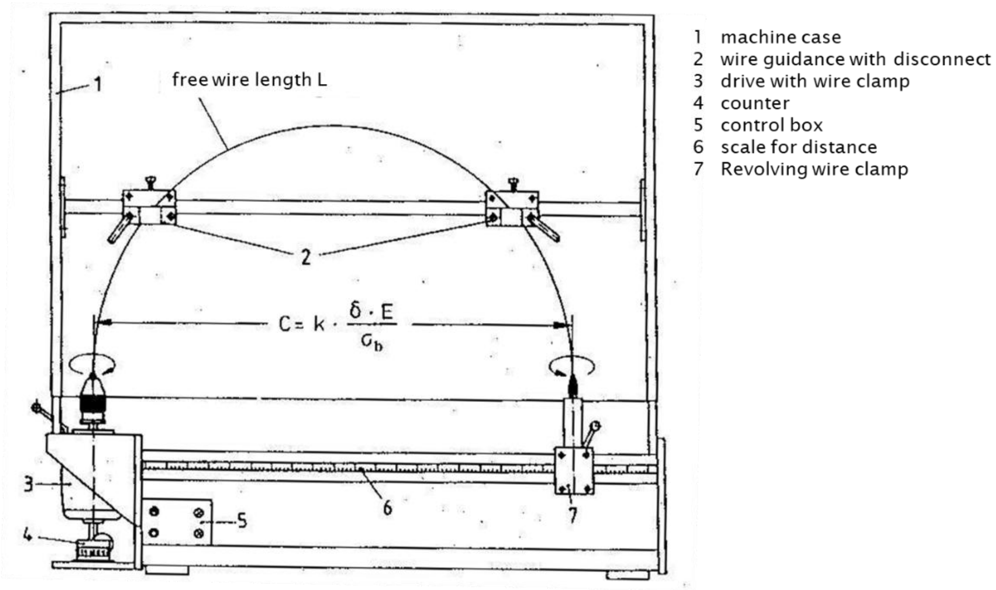

Figure 1: Rotary bending machine type IFT Stuttgart [7]

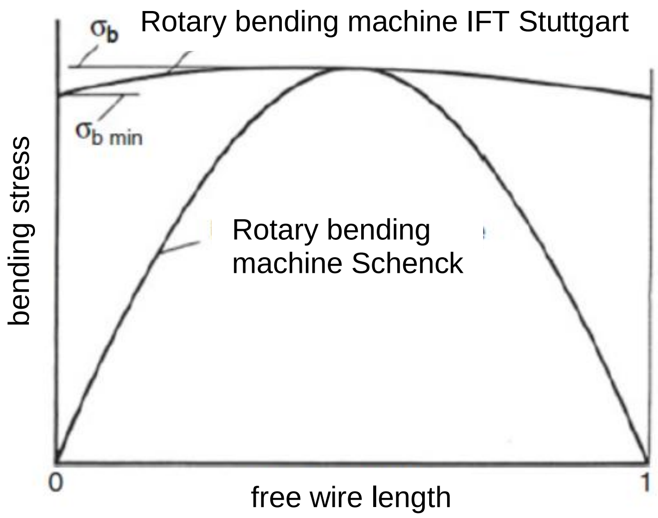

Figure 2: Bending stress along the wire bending length for test bench types IFT Stuttgart and Schenck [7]

2.2 Test bench principle OTH Regensburg

The IFT Stuttgart machine is designed for wire diameters up to approximately 2 mm. To test thicker wires, the testing machine would have to be much larger. For soft wires, e.g., made of copper, the free wire length is too long. The wire would be twisted. In the OTH machine, the free wire length is reduced by clamping the wire not in a semicircle, but in the form of a circular section with an opening angle of 2α. The clamping points are no longer parallel, but are rotated relative to each other by an angle α to the vertical, **Figure 3**. The two clamping points are spaced horizontally by a distance C. The free length of the wire is only slightly greater than C·α, so that the wire is again subjected to almost maximum bending stress and clamping fractures are largely avoided.

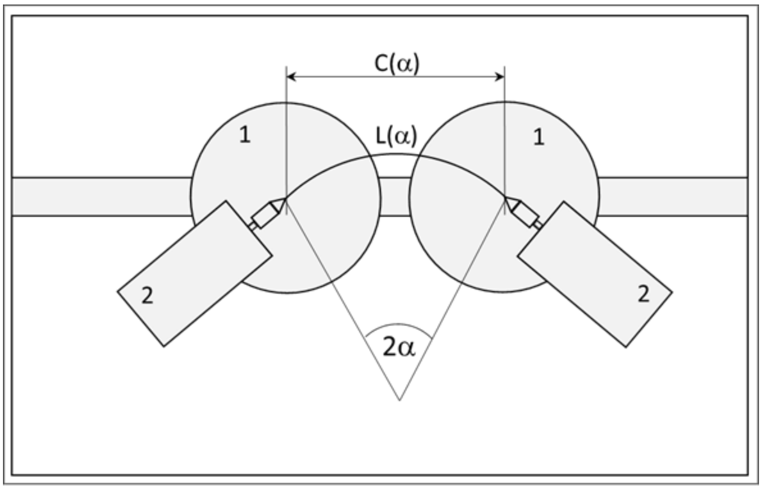

1 axially movable turntables
2 synchronized drive motors

Figure 3: Rotary bending machine type OTH Regensburg

3 Bending stress

Starting from the circular arc, a deformation occurs that is considered small. The bending stress σ_b occurring in the deformed circular arc is composed of the bending stress σ_K in the circular arc (Reuleaux bending stress).

$$\sigma_K = E\frac{\delta}{D} \tag{1}$$

with E … modulus of elasticity
δ … wire diameter
D … circular arc diameter

and an additional bending stress σ_{zus} due to the deformation of the circular arc

$$\sigma_{zus} = \frac{M}{I}\cdot\frac{\delta}{2} \tag{2}$$

with M … additional bending moment
I … moment of inertia of wire.

Due to the statically indeterminate nature of the problem, an exact determination of the bending stress is not possible. A solution is possible using energy methods and suitable approximations. Wolf [6] derived it for the test setup on the IFT Stuttgart test bench. He drew on calculation approaches by Föppl [8] and Müller-Breslau [9]. Wolf's approach is explained, including all the approximations introduced, and represented using slightly different formula symbols. His method is then applied to the new OTH Regensburg test bench type.

3.1 Test bench principle IFT Stuttgart

The circular ring is loaded with two oppositely directed forces of equal magnitude F, **Figure 4**. The distance between the force application points is reduced by e. The deformed circular ring remains symmetrical to the two axes, which forces a right angle between the deformed circular ring and the axes, i.e., the wire arch always enters the clamping fixture perpendicularly.

The upper left quarter of the deformed circular ring can be idealized as being firmly clamped at point B and loaded at point A by the external force $F/2$, **Figure 4.**

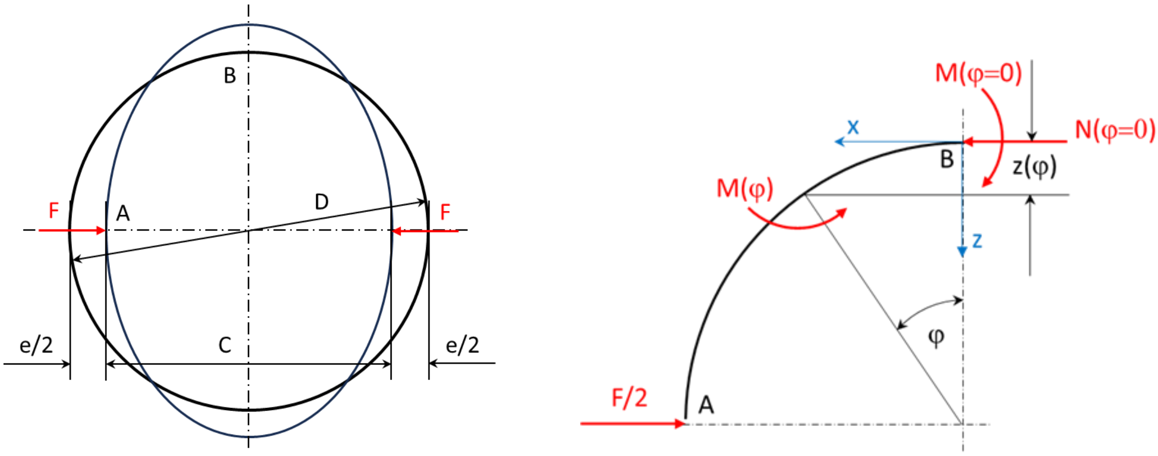

Figure 4: Circular ring loaded by force F and free cut of a quarter circle (enlarged) based on Wolf [6]

At point B, the normal cutting force $N = F/2$ and the cutting moment $M(\varphi = 0)$, which cannot be determined statically. Since point B does not experience any axial displacement, the deformation energy at this point is zero. According to [8], the bending stress component from the longitudinal wire force can be neglected. Due to the idealization of the deformed wire arch as a circular arc, the line center of gravity of the quarter arc can be used. The still unknown force F can be determined by considering the deformation energy at the point of force introduction of F and equating the deformation energy with the internal energy of the quarter arc. The length e is a control variable and results from the specimen length and the distance between the wire clamps. The sum of the Reuleaux bending stress and the additional bending stress at point $\varphi = 0$ results in

$$\sigma_b = \sigma_{b,max} = \sigma_K + \sigma_{zus}(\varphi = 0) = (0.994 + 0.014)\frac{E\delta}{C} = 1.008\frac{E\delta}{C} = k\frac{E\delta}{C} \qquad (3)$$

The coefficient 1.008 is called k b Feyrer [7]. For rotating bending tests, only the center distance C has to be set for the selected bending stress and the wire length L has to be selected with

$$C = 1{,}008\frac{E\delta}{\sigma_b} \quad und \quad L = 1{,}58 \cdot C \qquad (4), (5)$$

3.2 Test bench principle OTH Regensburg

The circular ring is loaded with four equal forces $F/2$, with the force application points arranged symmetrically to the axes, **Figure 5**. The distance between the force application points of the two upper forces is reduced by e. The wire arch must always enter the clamping fixture perpendicularly. Therefore, the angle of incidence of the clamping points must be specified separately.

The upper left part of the deformed circular arch can be idealized as being firmly clamped at point B and loaded at the beam end by the external force $F/2$.

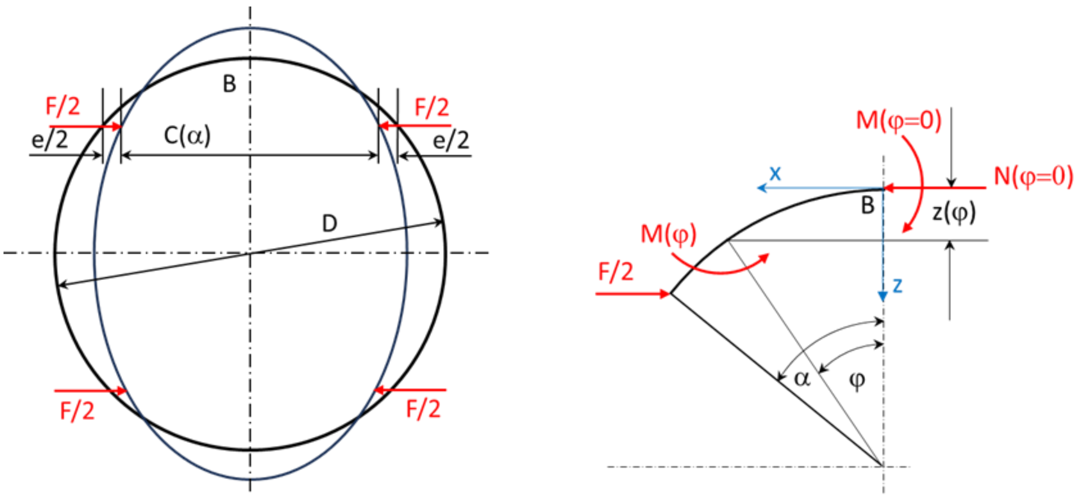

Figure 5: Circular ring loaded by force $F/2$
and free cut of a circle section (enlarged)

The calculation process is initially similar to that with the IFT machine. The additional bending stress at point φ=0 results in

$$\sigma_{zus}(\varphi=0)=\frac{\cos\alpha-\frac{\sin\alpha}{\alpha}}{\frac{\alpha}{2}-\frac{\sin\alpha}{\alpha}+\sin 2\alpha}\cdot\frac{\frac{\sin\alpha}{\alpha}\cdot\frac{L}{C}-1}{\frac{1}{\alpha^2}\left(\frac{L}{C}\right)^2}\cdot\frac{E\delta}{C}=f\left(\alpha,\frac{L}{C}\right)\cdot\frac{E\delta}{C} \tag{6}$$

For comparability with the test bench type IFT Stuttgart, the setting value could be selected as

$$\frac{L}{C}=\frac{1{,}58}{\pi/2}\cdot\alpha \tag{7}$$

However, at small angles α, the error becomes so large that another approach is necessary.

3.3 Approximation with an Ellipse

For angles $\alpha<45°$, the clamped wire arch in the IFT machine is approximated by an ellipse. The elliptical arc is shown with dimensions in **Figure 6**.

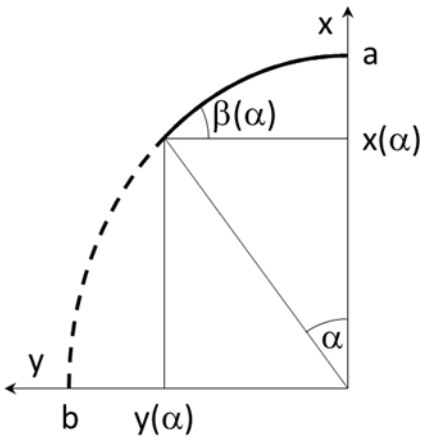

Figure 6: Elliptical arc with dimensions

The radii are determined from the test machine settings and the circumference of an ellipse. The small radius b is given by

$$b = C/2 \tag{8}$$

and from the equality of the circumference of the circle and the ellipse

$$U = \pi D \approx \pi \left[\frac{3}{2}(a+b) - \sqrt{ab}\right] \tag{9}$$

The big radius a is given by

$$a = 0.506\,C. \tag{10}$$

The freely selectable angle α leads to the coordinates

$$x(\alpha) = \frac{1}{\sqrt{\frac{\tan^2\alpha}{b^2} + \frac{1}{a^2}}} \quad und \quad y(\alpha) = \frac{\tan\alpha}{\sqrt{\frac{\tan^2\alpha}{b^2} + \frac{1}{a^2}}} \qquad (11), (12)$$

The pitch angles β(α) to be set on the turntables are then

$$\beta(\alpha) = \frac{\pi}{2} - \tan^{-1}\left(-\frac{b^2}{a^2} \cdot \frac{x(\alpha)}{y(\alpha)}\right) = \frac{\pi}{2} - \tan^{-1}\left(-\frac{0{,}976}{\tan\alpha}\right) \tag{13}$$

The length $L(\alpha)$ of the elliptical arc cannot be calculated analytically, but only numerically. **Figure 7** shows the free wire bending lengths in dependence of the angle α for two bending tensions 1000 and 600 N/mm².

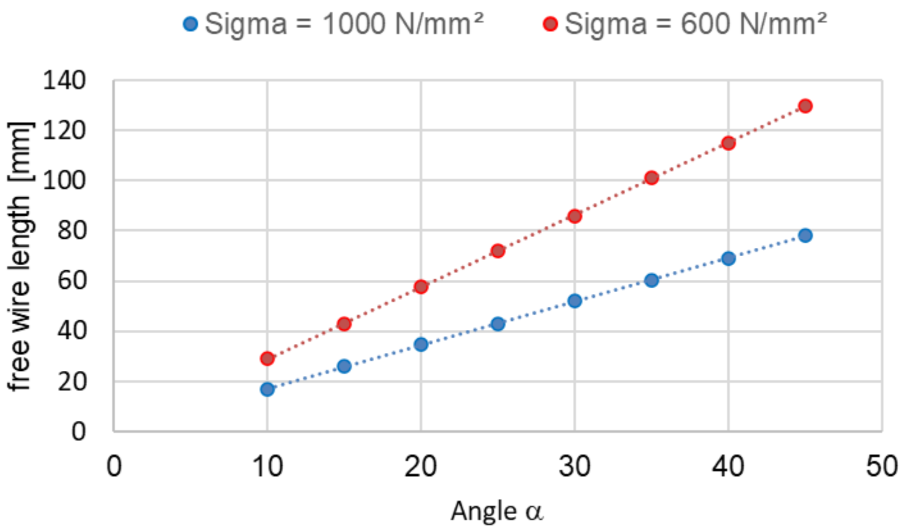

Figure 7: free wire bending lengths in dependence of the angle α for two bending tensions 1000 and 600 N/mm²

4 Conclusions

Based on the IFT Stuttgart machine, a new rotary bending machine is presented, which can be used to suitably reduce the wire length to be tested. The setting parameters for the IFT machine and the derivation by Wolf [6] are explained with all introduced approximations and represented using slightly different formula symbols. Wolf's approach cannot be applied to the OTH machine, as the error becomes too large at small angles α. Therefore, the wire arc is modeled with an ellipse instead of a circular arc. The setting parameters for selected angles are listed in a diagram.

5 References

[1] Anonym: A new form of fatigue testing machine for wires. Engineering (1933), S. 567

[2] Anonym: Fatigue testing machine for wire. Engineering (1934), S. 139-140

[3] Erlinger, E.: Umlaufbiegemaschine für Drahtproben. Fördertechnik 5/6 (1942) 3, S. 43-45

[4] Votta, A.: New wire fatigue testing. The Iron Age 12 (1948) 8, S. 78-80

[5] DIN 50113:2018-12 Umlaufbiegeversuch. Berlin: Beuth-Verlag

[6] Wolf, E.: Seilbedingte Einflüsse auf die Lebensdauer laufender Drahtseile. Diss. Universität Stuttgart 1987

[7] Feyrer, K.: Drahtseile, Bemessung, Betrieb, Sicherheit. Springer Verlag, 2017, ISBN 978-3-642-54295-4 und ISBN 978-3-642-54296-1 (eBook)

[8] Föppl, A.: Vorlesungen über Technische Mechanik, Band III, Festigkeitslehre. Druck und Verlag B. G. Teubner, Leipzig 1900

[9] Müller-Breslau, H.: Die neueren Methoden der Festigkeitslehre und der Statik der Baukonstruktion. Leipzig 1913

6 Author Introduction

Prof. Dr.-Ing. Ulrich Briem received his Doctorate degree in Mechanical Engineering from University of Stuttgart in 1996. He started his professional career as a Development Engineer at CASAR Company in 1996 and worked there for 9 years. In 2005 he went to OTH Regensburg, a university of applied sciences. He is member of OIPEEC and EWRIS and head of VDI working group “Cranes”. He is author of many papers about wire rope and rope wire technology as well as co-author of various VDI guide lines.

Influence of the positioning of plastic sheaves and steel sheaves on rope life and service life: Insights from extended bending fatigue analysis.

Marco Elig, M.Eng.

KV R&D Center GmbH, Germany

Dr.-Ing. Marc Fuhrmann

KV R&D Center GmbH, Germany

Summary

This study provides a comprehensive analysis of how the material composition and sheave arrangement affect the lifetime and safety of wire ropes. Using a special bending fatigue testing machine, the research evaluates the effect of different configurations of plastic and steel sheaves on rope durability.

The results indicate that the lifetime of wire ropes decreases significantly as the proportion of steel sheaves increases. Importantly, the study finds that, depending on the rope design, the presence of at least one steel sheave, in some cases at least two steel sheaves is critical in reliably signalling the imminent end of a rope's service life.

The research highlights the dual role of steel sheaves: while accelerating the wire breaks of the rope, they are essential in providing a timely indication of the need for rope replacement. This balance between durability and safety is critical to the design of reeving systems, providing essential guidance for improving both operational efficiency and safety protocols in industries that rely heavily on complex reeving configurations.

Keywords: rope life, service life, rope discard, wire ropes, steel sheaves, pulleys, plastic sheaves

1 Introduction

In the dynamic field of modern rope technologies, particularly within reeving systems, the use of lightweight materials such as plastic sheaves have increasingly been favoured for their notable cost and weight benefits. However, the need to integrate steel sheaves remains [1], serving a dual purpose of facilitating early detection of wire breaks and so the end of service life.

Previous research has highlighted that the inclusion of at least one steel sheave is crucial for enhancing safety by providing clear indicators for necessary rope replacement [2,3]:
The previous study investigated the effect of different configurations of plastic and steel sheaves on rope life and service life. Various sheave configurations were tested in a series of bending fatigue tests using an 8xK26WS - EPIWRC rope construction. These tests highlighted specific correlations between the service life achieved by each configuration and the time to reach rope´s discard state depending on these configurations.
It has been observed that the lifetime of the rope decreases by $\approx$17.50% for every additional 20% steel sheave in the reeving system. It has also been observed that the more steel sheaves are introduced into the system, the greater the safety margin between the service life and the failure of the rope if the steel sheaves are arranged consecutive.

In particular, the strategic placement of even a single steel sheave within the reeving system proved to be crucial in signalling when a rope was nearing the end of its service life. However, the underlying mechanisms driving this phenomenon remained elusive.

This study extends previous work by performing a comprehensive bending fatigue analysis to further investigate the effect of sheave materials and their positioning on service life and overall lifetime.
New experimental data is presented to evaluate the fatigue performance of different sheave configurations. The results show how specific configurations affect the bending fatigue behaviour of ropes and provide deeper insights into the optimum sheave positioning and the number of sheaves required for reliable end of service life detection.

2 Research Methodology & Experimental Design

In the study, an advanced machine concept was employed to test ropes under bending fatigue, markedly different from conventional testing methods. As it can be seen in **Figure 1**, at the core of this machine is a system comprising five sheaves, which can consist of varied materials. Unlike traditional testing machines that run the rope over a single sheave, this approach creates more realistic test conditions, especially regarding the influence of positioning different sheave materials in the reeving system

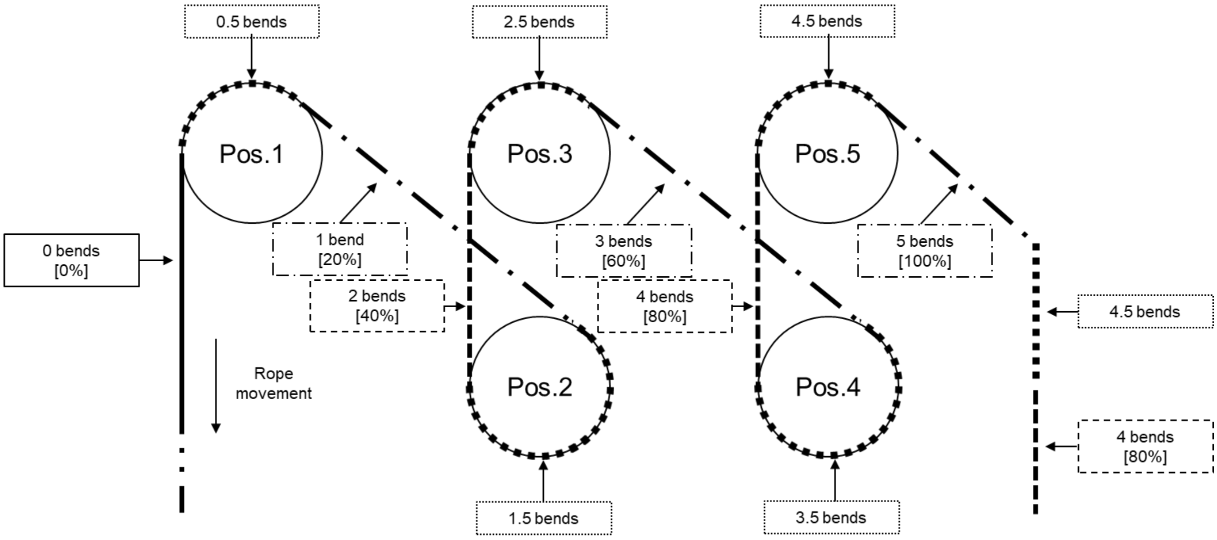

Figure 1: Bending Fatigue Test – Sheave Arrangement

This specialized bending fatigue machine allows for the testing of ropes in controlled conditions, with a focus on the most heavily stressed section of the rope. In this area, the rope is subjected to 10 bending cycles per machine cycles (100%), while adjacent areas experience decreasing bending cycles (80%, 60%, 40%, 20%), showed in **Figure 2**.

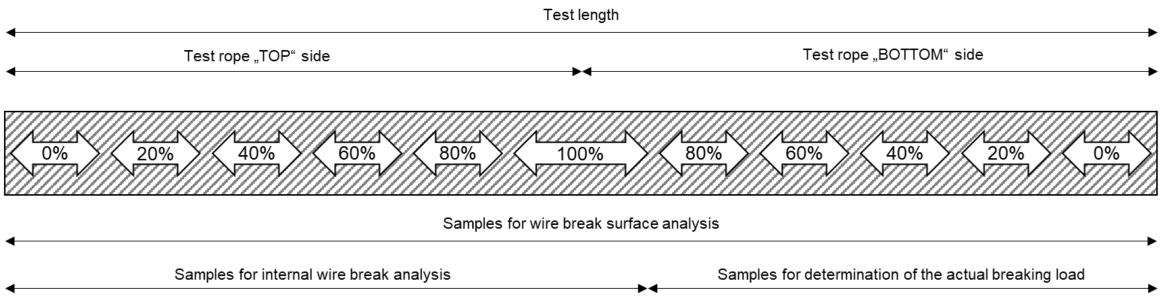

Figure 2: Bending Fatigue Test – Evaluation Scheme

Furthermore, the design allows for continuous measurement of various rope properties and a detailed analysis of both, external and internal rope damage as well as the actual breaking forces of the ropes at various stages of their lifecycle. A detailed description of the concept can be found in [4].

The specific test parameters, test sheaves used, and the rope construction that was investigated are shown in the tables below (**Table 1**,**Table 2**,**Table 3**):

Table 1: Rope construction & properties

	Rope 1	**Rope 2**
Construction	8 x K26WS EPIWRC	8 x K26WS EPIWRC
Rope diameter d	16 mm	16 mm
Lay direction	RHOL	RHOL
Surface	Galvanized	Galvanized
Nom. wire strength R_0	1960 N/mm²	1960 N/mm²
Rope Category Number (RCN)	09	09
Discard criteria ISO 4309		
Number of visible wire breaks on reference length of 6d	9	9
Number of visible wire breaks on reference length of 30d	18	18

Table 2: Sheave construction & properties

	Steel	**Plastic**
Material composition	42CrMo4	PA66
Hardness	53[1]	160/125[2]
D/d ratio	20	20
r/d ratio	0.53	0.53
Opening angle	60°	60°

Table 3: Test parameter

Safety Factor SF	8.33
Rope velocity v	1,15 m/s

To validate the hypothesis presented in the previous study [2,3], the former test series was extended to include configurations with three and four consecutive steel sheaves (configurations (4) and (5) in **Figure 3**).

In addition, configurations (1) to (7) were retested using the same rope construction, but sourced from a different manufacturer.

This approach was specifically designed to investigate the effect of sheave material and arrangement on the service life and lifetime of wire ropes.

Figure 3 shows all the configurations tested in this study.

[1] HRC

[2] $H_{358/30}$ according to ISO 2039-1

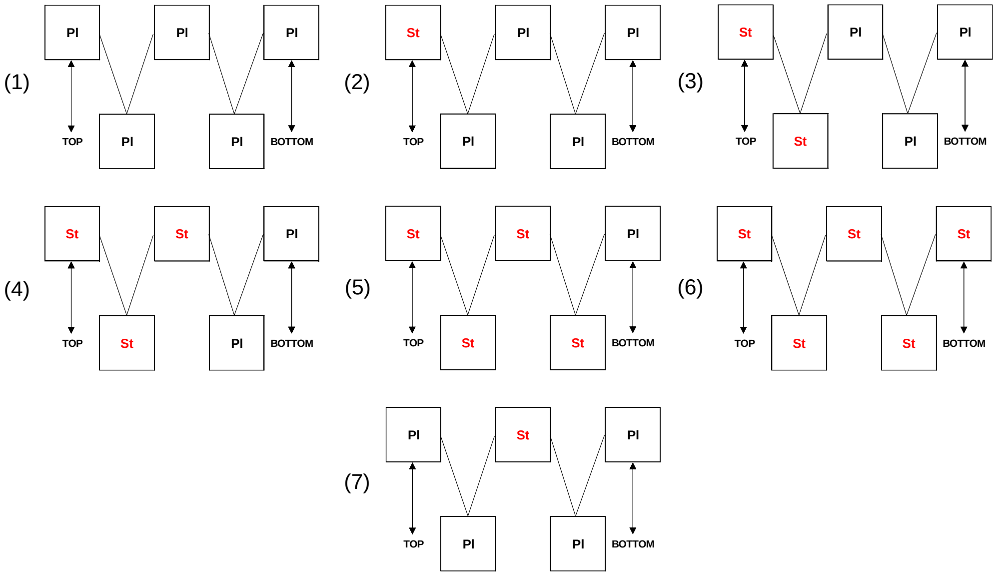

Figure 3: Bending Fatigue Test – Sheave Arrangement (1) – (7)

The general evaluation scheme is illustrated in **Figure 4** using the test configuration (7). This method makes it possible to associate the rope sections from the bending fatigue test and the identified wire breaks on the rope surface with a percentage of steel and plastic sheaves. This allows general statements to be made about the service life and lifetime of ropes in different reeving systems.

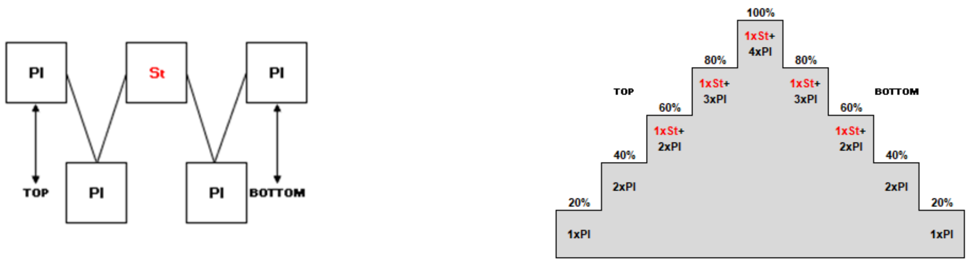

Number of St.[3]	% St.[3]	Number of Pl.[4]	% Pl.[4]	Lifetime	Sheave Order
0	0%	2	100%	20% -	PI PI
0	0%	4	100%	40% -	PI-PI PI-PI
2	33,33%	4	66,67%	60% -	PI-PI-St St-PI-PI
2	25%	6	75%	80% -	PI-PI-St-PI PI-St-PI-PI
2	20%	8	80%	100%-100%	PI-PI-St-PI-PI-PI-PI-St-PI-PI
2	25%	6	75%	- 80%	PI-PI-St-PI PI-St-PI-PI
2	33,33%	4	66,67%	- 60%	PI-PI-St St-PI-PI
0	0%	4	100%	- 40%	PI-PI PI-PI
0	0%	2	100%	- 20%	PI PI

Figure 4: Bending Fatigue Test – Evaluation Scheme

[3] St. = Steel Sheaves

[4] Pl. = Plastic Sheaves

3 Results

The approach described in the previous section was designed to ensure an accurate and reliable evaluation.

To this end, the rope was fatigued in the chosen sheave arrangement until either failure of an outer strand was detected or a significant increase in elongation occurred within a pre-defined period, indicating failure of the rope core.

On completion of the tests, a careful assessment of the wire breaks occurred, was made. This assessment was based on the examination of individual sections shown in **Figure 4** and was conducted in accordance with the guidelines of ISO 4309 [5].

The bending fatigue results from the different test configurations are presented in **Table 4**:

Table 4: Bending fatigue test results

Sheave Order		Lifetime N [-]	Discard N_{A30d}		Test Nr.	Rope Nr.
Pl-Pl-Pl-Pl-Pl	Pl-Pl-Pl-Pl-Pl	632290	619644	100%	2[5]	1
Pl-Pl-Pl-Pl-Pl	Pl-Pl-Pl-Pl-Pl	524502	514102	100%	10	2
St-Pl-Pl-Pl-Pl	Pl-Pl-Pl-Pl-St	511000	112420	22%	3[5]	1
St-Pl-Pl-Pl-Pl	Pl-Pl-Pl-Pl-St	379463	379463	100%	11	2
St-St-Pl-Pl-Pl	Pl-Pl-Pl-St-St	411500	102875	25%	4[5]	1
St-St-Pl-Pl-Pl	Pl-Pl-Pl-St-St	335697	99998	30%	12	2
St-St-St-Pl-Pl	Pl-Pl-St-St-St	328960	105267	32%	7	1
St-St-St-Pl-Pl	Pl-Pl-St-St-St	258974	98987	31%	13	2
St-St-St-St-Pl	Pl-St-St-St-St	275350	110140	40%	8	1
St-St-St-St-Pl	Pl-St-St-St-St	194410	105156	43%	14	2
St-St-St-St-St	St-St-St-St-St	242590	127164	52%	1[5]	1
St-St-St-St-St	St-St-St-St-St	149840	92582	62%	9	2
Pl-Pl-St-Pl-Pl	Pl-Pl-St-Pl-Pl	433750	433750	100%	5[5]	1
Pl-Pl-St-Pl-Pl	Pl-Pl-St-Pl-Pl	414930	402482	97%	6[5]	1
Pl-Pl-St-Pl-Pl	Pl-Pl-St-Pl-Pl	333520	333520	100%	15	2

[5] Tests conducted in the previous study

3.1 Consideration as a 5-Sheave-Reeving-System

In the following section, each test arrangement is considered as a dependent system, equipped with the same number of sheaves and materials as described in the previous chapters.

Figure 5 shows the influence of the number of steel sheaves to discard and failure of **Rope 1** based on the data of **Table 4**.

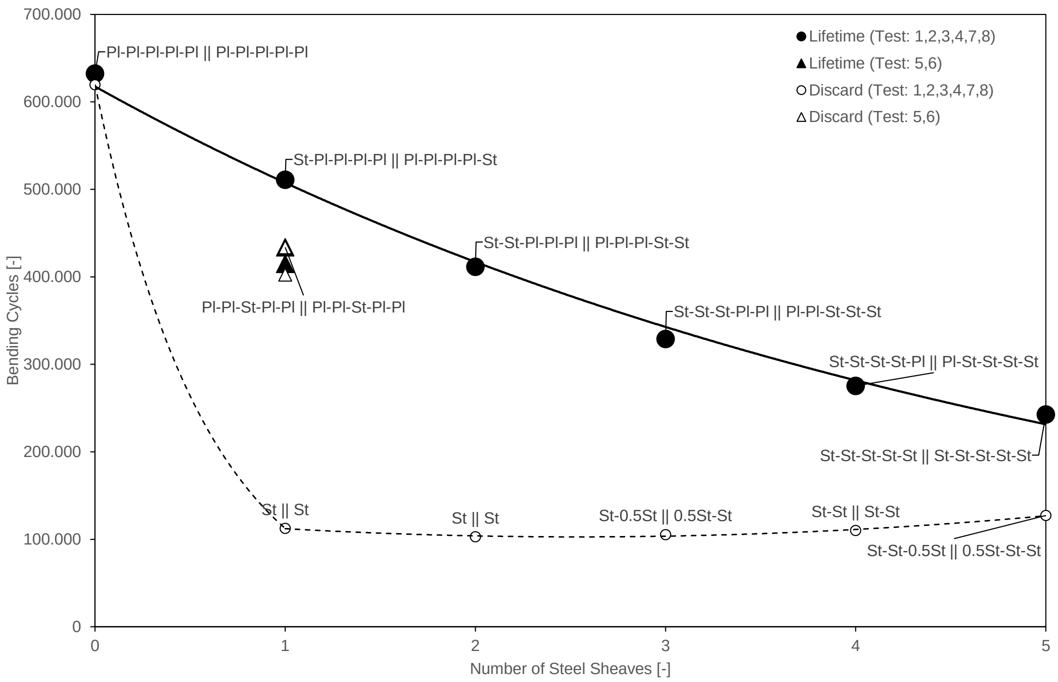

Figure 5: Lifetime and Discard depending on the Number of Steel Sheaves (Rope 1)

Figure 6 shows the influence of the number of steel sheaves to discard and failure of **Rope 2** based on the data of **Table 4**.

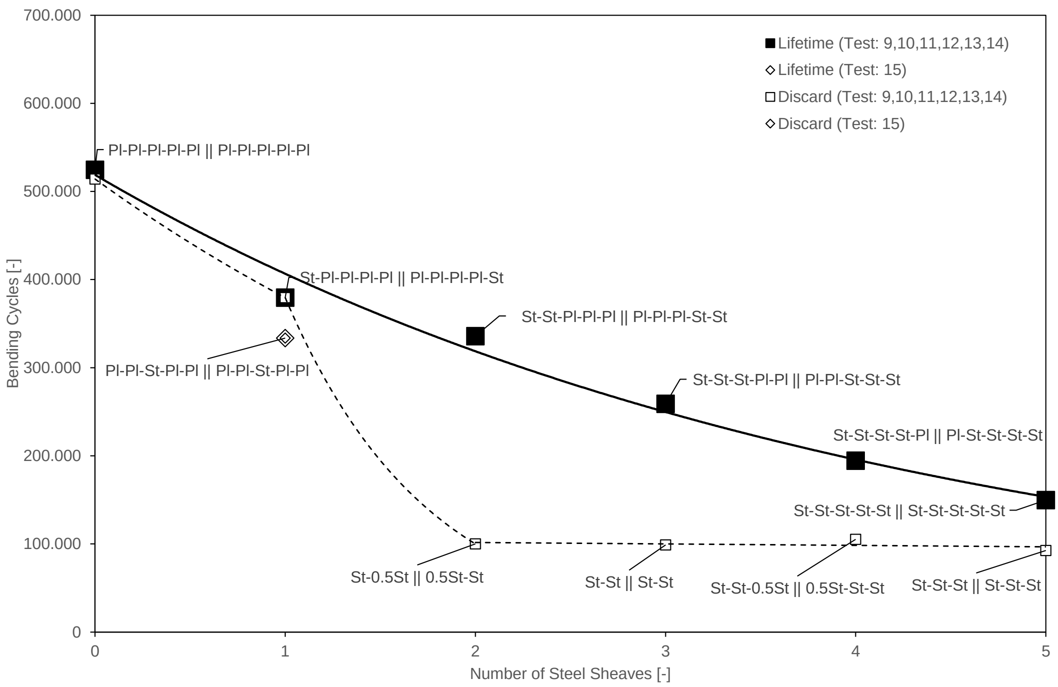

Figure 6: Lifetime and Discard depending on the Number of Steel Sheaves (Rope 2)

The following **conclusions** can be drawn from these data for Test **Rope 1**:

- The rope lifetime on **plastic sheaves only**, is increased by a factor of 2.61 compared to steel sheaves only, and the service life is increased by a factor of 5.40.
- If the **steel sheaves are arranged consecutive**,
    - the rope life will be reduced continuously as the number of steel sheaves increases.
    - for all tested configurations, the end of service life is reliably indicated on a steel sheave with sufficient residual lifetime, **if at least one steel sheave is installed in the reeving system**.
- If there is **no steel sheave** in the system, the service life of the rope ends short before end of rope life.
- If only **one sheave is positioned in the centre** of the arrangement, the lifetime is reduced to 83% compared to the lifetime with the sheave at the first position. The service life increases by a factor of 3.72 without having enough residual life.

The following **conclusions** can be drawn from these data for Test **Rope 2**:

- The rope lifetime on **plastic sheaves only** is increased by a factor of 3.50 compared to steel sheaves only, and the service life is increased by a factor of 5.55.
- If the **steel sheaves are arranged consecutive**,
    - the rope life will be reduced continuously as the number of steel sheaves increases.
    - for all tested configurations, the end of service life is reliably indicated on a steel sheave with sufficient residual lifetime, **if at least two steel sheave is installed in the reeving system**.
- If there is **no or only one steel sheave** in the system, the service life of the rope ends short before end of rope life.
- If only **one sheave is positioned in the centre** of the arrangement, the lifetime and the service life are reduced to 88% of the tests with the sheave at the first position. In both arrangements, there is no residual lifetime available.

It can be concluded that in both test series the position of the steel sheave has an influence on the service life and lifetime of the rope, especially when the sheave is placed in the middle of the reeving system.

Furthermore, it can be concluded that the rope type affects the minimum number of steel sheaves required within a reeving system, to ensure the detection of rope´s end of service life.

A possible conclusion for this dependency could be that ropes with lower residual lifetime, in steel sheave only reeving systems, require multiple steel sheaves to ensure safe and timely discard indication. However, this behaviour could also be due to the general scatter in fatigue tests.

3.2 Consideration as a General-Sheave-Reeving-System

In the following section, each test arrangement is considered as an independent system, equipped with a percentage amount of plastic and steel sheaves.

Figure 7 shows the influence of the percentage of steel sheaves to discard and failure of **Rope 1** based on the data of **Table 4**.

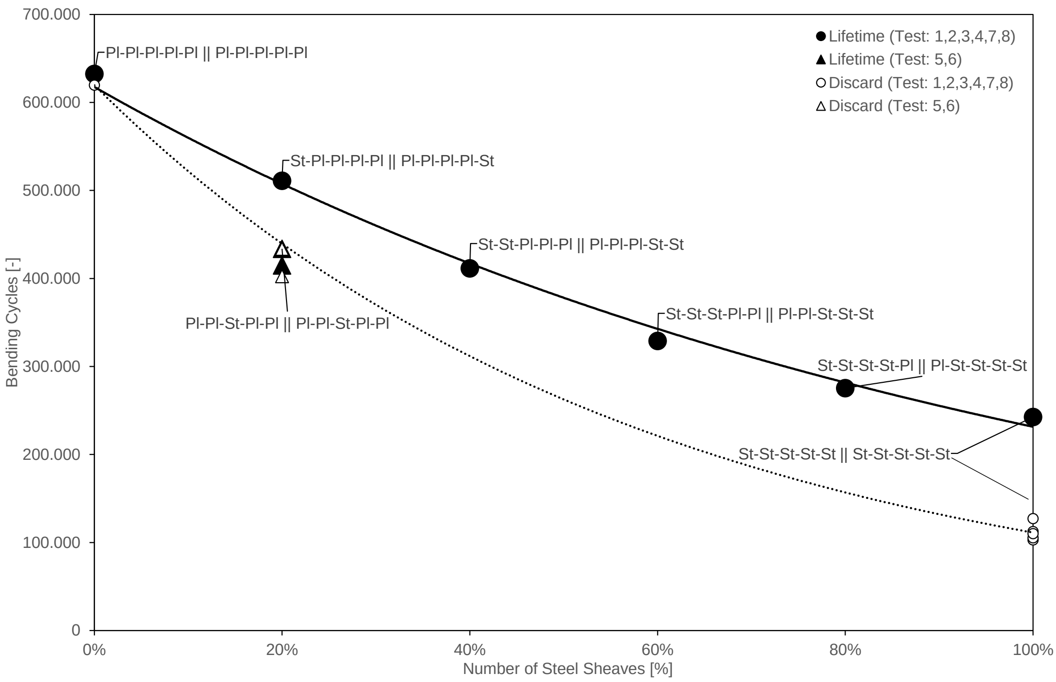

Figure 7: Lifetime and Discard depending on the Percentage of Steel Sheaves (Rope 1)

Figure 8 shows the influence of the percentage of steel sheaves to discard and failure of **Rope 2** based on the data of **Table 4**.

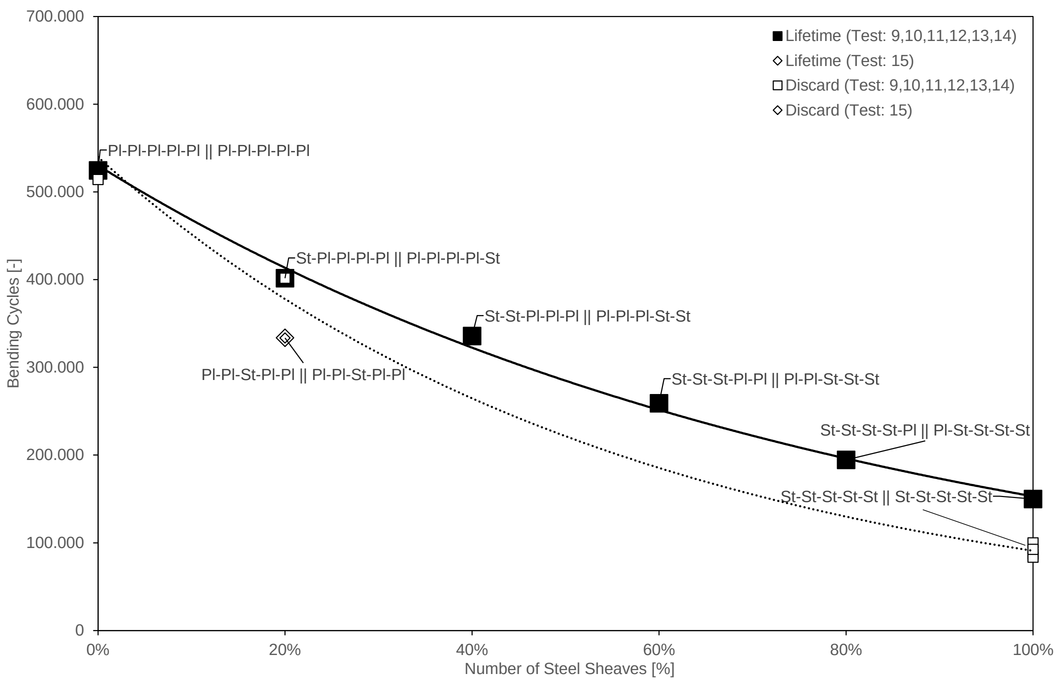

Figure 8: Lifetime and Discard depending on the Percentage of Steel Sheaves (Rope 2)

Several **conclusions** can be made from these data:

- As the number of steel sheaves increases, the lifetime of the rope decreases, if the steel sheaves are arranged consecutively.
- As the percentage of steel sheaves in the system increases, the service life of the rope decreases.
- Correlations can be found between the individual reached lifetime and the time to discard of the rope in dependence of different sheave arrangements.
- **Even a single steel sheave / two steel sheaves** in the system, correctly placed, can make the rope operation considerably safer by increasing the residual lifetime.

For **Rope 1**, it can be noted that the lifetime of the rope **decreases by ≈17.82%** for every additional 20% of steel sheave in the system Therefore, if the steel sheaves are arranged consecutive, the following relationship emerges:

$$Reduction\ factor\ rope\ life = e^{-0.981 * \frac{number\ of\ steel\ sheaves}{total\ number\ of\ sheaves}} \quad (1)$$

It can be also noted that the residual lifetime of the rope increases proportional for every additional 20% of steel sheave in the system. Therefore, if the steel sheaves are arranged consecutive the following relationship emerges:

$$Residual\ life = N * \left(1 - \left(1{,}00 * e^{-0.736 * \frac{number\ of\ steel\ sheaves}{total\ number\ of\ sheaves}}\right)\right) \quad (2)$$

For **Rope 2**, it can be noted that the lifetime of the rope **decreases by ≈22.01%** for every additional 20% of steel sheave in the system Therefore, if the steel sheaves are arranged consecutive, the following relationship emerges:

$$Reduction\ factor\ rope\ life = e^{-1.243 * \frac{number\ of\ steel\ sheaves}{total\ number\ of\ sheaves}} \quad (3)$$

It can be also noted that the residual lifetime of the rope increases proportional for every additional 20% of steel sheave in the system. Therefore, if the steel sheaves are arranged consecutive, the following relationship emerges:

$$Residual\ life = N * \left(1 - \left(1{,}01 * e^{-0.441 * \frac{number\ of\ steel\ sheaves}{total\ number\ of\ sheaves}}\right)\right) \quad (4)$$

The authors' assumption from the previous test series that the service life of **Rope 1** is reduced by approximately 17.50% for each additional sheave in the system can therefore be confirmed.

The positional dependence of the sheave, which can be seen from the results for **Rope 1** and **Rope 2**, can also be confirmed (see **Figure 7**, **Figure 8**).

There is also a difference in the reduction in rope life between **Rope 1** and **Rope 2**. This is probably due to the general behaviour of the different ropes during cyclic bending fatigue tests, as known from tests with different forces or D/d-ratios.[6].

3.2.1 Wire break distribution

Figure 9 shows the wire break distribution from the individual sections of the **Rope 1** on the data of **Table 4**.

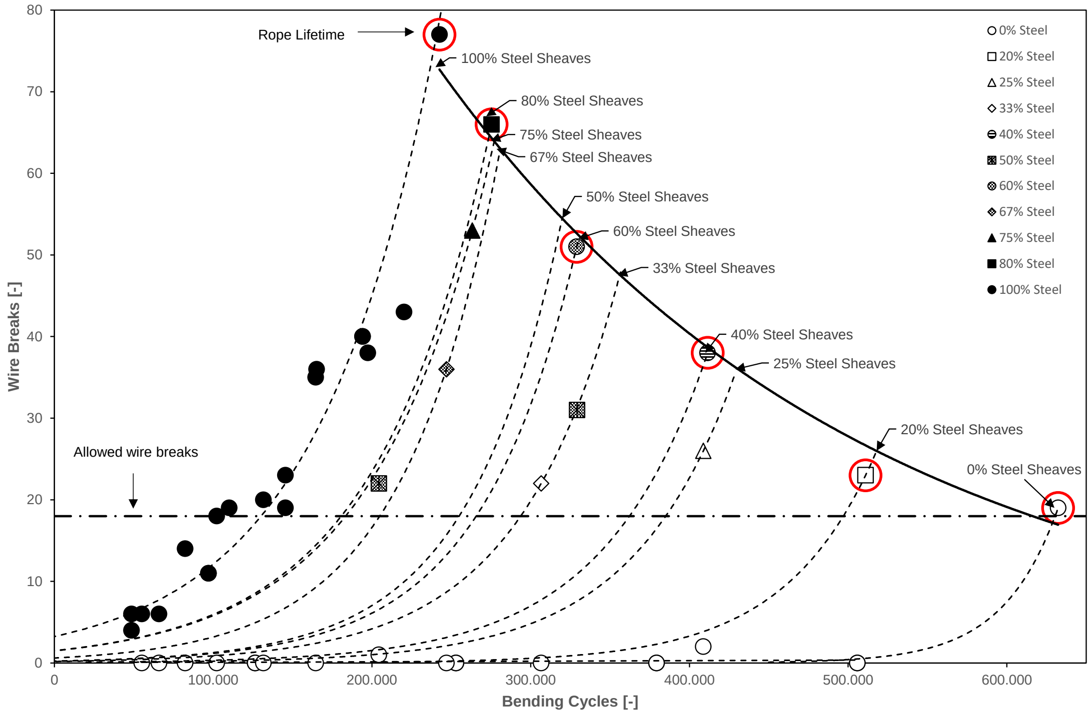

Figure 9: Wire Break Distribution (Rope 1)

Figure 10 shows the wire break distribution from the individual sections of the second tested rope based on the data of **Table 4**.

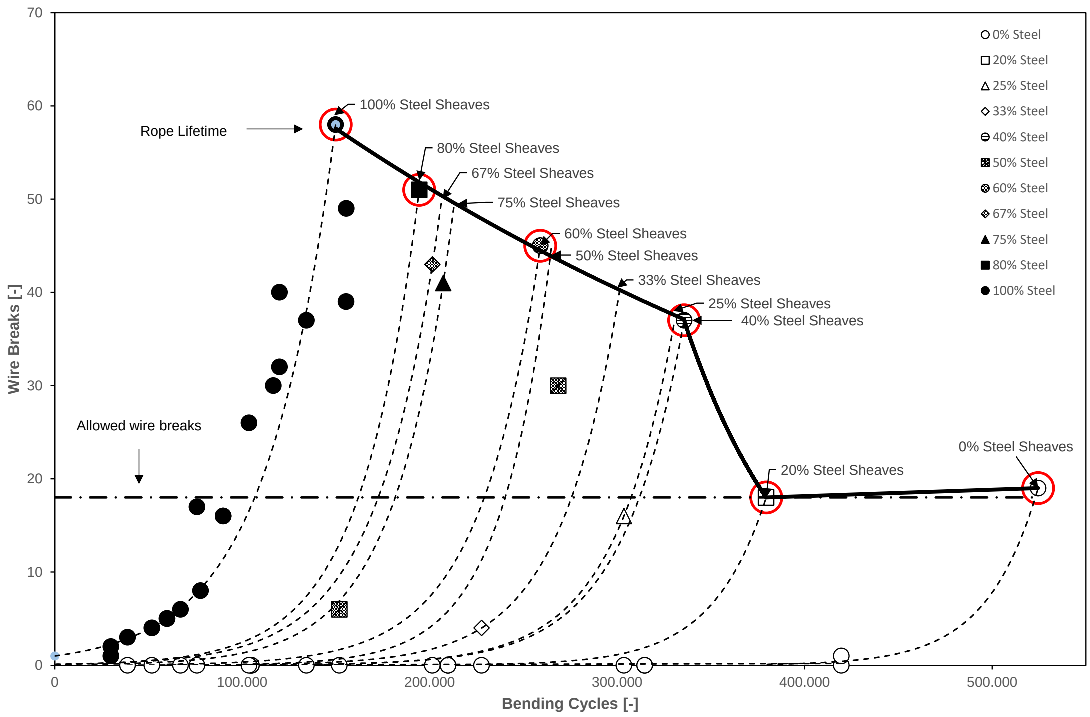

Figure 10: Wire Break Distribution (Rope 2)

For both ropes, the wire break distribution of different steel sheave proportions in a reeving system were determined using an exponential approach for the wire break distribution of the all-steel sheave configuration, as known from the literature [6].

As can be seen out of the two figures, there are some inconsistencies in the order to the distribution of total rope life and service life achieved. This approach represents a first attempt to represent the wire break distribution and the service life of the rope under the influence of different sheave materials and arrangements.

The authors are aware that this estimation is very limited due to the small amount of data available. Furthermore, the authors assume that for a combination of plastic and steel sheaves, the wire break distribution will only be subject to a limited exponential relationship.

4 Conclusions

The interaction between sheave materials—specifically plastic and steel—and their arrangement in a reeving system, significantly influences the lifetime, service life, and reliability of wire ropes. Results from extensive bending fatigue tests show that the presence and positioning of steel sheaves has a significant impact on the wire break and fatigue behavior of wire ropes, determining both their lifetime and the safety indications for rope replacement.

This study validates the previously established relationship between sheave material composition and wire rope service life [2,3,7]. Through systematic bending fatigue tests across a range of steel-plastic sheave configurations, clear trends regarding the impact of sheave materials and their arrangements on rope durability, discard indication reliability, and residual lifetime were identified.

The results indicate that the lifetime of wire ropes decreases significantly as the proportion of steel sheaves increases. Importantly, the study reveals that the presence of at least one steel sheave, in some cases depending on the rope design, at least two steel sheaves are critical in reliably signaling the imminent end of a rope's service life.

However, the strategic placement of steel sheaves within the system is critical to ensure reliable detection of the impending end of service life.

In addition, the evolution of wire breaks was estimated to assess the service life and wire break distribution of certain configurations. Further validation testing is necessary to refine the accuracy of this model and applicability across a broader range of configurations.

Overall, these insights underscore the importance of carefully selecting sheave configurations tailored to specific rope characteristics and application requirements. By understanding these boundary conditions, operators and system designers can optimize reeving systems to reliably detect discard conditions, thus minimizing risks and enhancing rope failure safety in accordance with ISO 4309 standards.

5 Acknowledgements

The authors would like to thank all contributors within the verope Group for their valuable comments and review of the paper, especially the team of the KV R&D Center GmbH.

6 References

[1] ISO 16625, Cranes and hoists – Selection of wire ropes, drums and sheaves, First edition 2013-07-01 (2013)

[2] Elig M.; Bae Y.: The influence of the position and number of steel and plastic sheaves on the service life and lifetime of wire ropes: A comparative bending fatigue study. Proceedings of the OIPEEC Conference 2024. (2024)

[3] Elig M. et al: Der Einfluss der Kombination von Stahl- und Kunststoffseilscheiben auf die Betriebs- und Lebensdauer von Stahlseilen: Eine vergleichende Biegeermüdungsstudie. Vol. 3 (2024): innoTRAC Journal. (2024)

[4] Verreet R.; Teissier J.M.: A new innovative wire rope bending fatigue machine. Proceedings of the OIPEEC Conference 2011. (2011)

[5] ISO 4309, Cranes – Wire ropes – Care and maintenance, inspection and discard, Fifth edition 2017-11. (2017)

[6] Feyrer K.: Wire Ropes – Tension, Endurance, Reliability. Springer edition, 2. Edition, Heidelberg (2015)

[7] Zhang D. et al.: Bending fatigue behaviour of bearing ropes working around pulleys of different materials. Engineering Failure Analysis, 2013;33: 37-47. (2013)

7 Authors' Introductions

Mr. Marco Elig received his Bachelor of Engineering degree in Mechanical Engineering from the University of Applied Science Kaiserslautern in 2015, followed by a Master of Engineering degree in the same field in 2023.

He began his professional journey as the Head of Testing at the verope Service Center GmbH in 2015. In 2018, he transitioned to a role as a Research Engineer at KV R&D Center GmbH.

Since 2021, Mr. Elig has been serving as the Managing Director at KV R&D Center GmbH.

Mr. Elig's professional interests primarily focus on the estimation and monitoring of rope lifetime. His work in this area includes both theoretical research and practical applications.

Dr.-Ing. Marc Fuhrmann received his Bachelor and Master of Engineering degrees in Microsystems and Nanotechnologies from Kaiserslautern University of Applied Sciences.

He completed his PhD in Engineering Technology at University Hasselt, Belgium, in 2024, specializing in surface science.

Since 2024, he serves as the Head of Research & Development at KV R&D Center GmbH.

His research focuses on the numerical analysis of structural degradation on rope surfaces and material enhancements in rope systems based on data science to enhance rope lifetime prediction accuracy.

ISO 16625 – revised – a 9 year journey to create a standard for the proof of competence of a steel wire rope in crane applications

Judith Reinl, M.Sc.

Convenor, ISO/TC 96 SC3 WG3

Summary

In 2015, a standardization project was launched to revise ISO 16625:2013 Cranes and hoists – Selection of wire ropes, drums and sheaves and a working group with experts from various crane and hoist manufacturers, rope manufacturers and scientist from universities has been established. Along the way to determine the scope and objectives of this standardization project, EN 13001-3-2:2014 was considered as a starting point. The evaluation of EN 13001-3-2 and especially the major shortcomings gave significant impetus to study the method Stuttgart and the method Leipzig and the scientific results thereof. As an outcome, an innovative approach was considered to reframe ISO 16625 that would eliminate the known shortcomings and would meet the objectives set. A revised edition of ISO 16625 shall adopt a cycle-based approach and incorporate proofs of competence based on the limit state method for fatigue strength and static strength as well as multilayer spooling. Also, different aspects of running ropes and stationary ropes need to be addressed. The innovative approach underlying the new edition of ISO 16625 has its foundation on a new mathematical approach to verify the fatigue strength of running steel wire ropes. As an outcome, a new reference point is introduced as a characteristic value for the fatigue strength from which the S-N curves at different D/d ratios are described.

Keywords: ISO 16625, wire rope, fatigue strength, static strength, bending, proof of competence, running rope, stationary rope.

1 Introduction

In 2015, the sub-committee SC3 of ISO/TC 96 took a resolution during its annual meeting in Sydney, Australia to establish a new working group to revise ISO 16625:2013 and to register the revision of the standard in the work programm at the preliminary stage. [1] The journey of the revision of ISO 16625 was kicked-off and back in 2015 it was not foreseeable that 9 years later, during the Annual Meetings of ISO/TC 96 - by accident again in Sydney, Australia - the revision of ISO 16625 was close to be approved and to be registered as FDIS (Final Draft International Standard), the last step prior to publication. [2] To set the framework of this standardization project, it has been essential to clarify the scope of the to be revised ISO 16625 first. Obviously, latest standardization activities in ISO/TC 96 and also related Technical Committees at that time took already into account that past standards have been established on outlining selection criteria rather than providing requirements on a proof of competence. The acknowledgement of this change in the standardization work, triggered in the year 2016 the foundational discussion to identify objectives for the revision of ISO 16625 and thus, set the path for this long lasting journey. [3] [4]

2 Objectives and key milestones of the revision of ISO 16625

2.1.1 As-is state ISO 16625:2013

The international standard ISO 16625:2013 Cranes and hoists – Selection of wire ropes, drums and sheaves (Edition 1) specifies a minimum design factor Z_p taking into account the classification of mechanism, the rope type and the application. [5] Furthermore, the group classification of mechanism is in accordance with ISO 4301-1:1986 and thus follows a time-based approach. [6] Considering the maximum rope tension S and selecting a specified value of the minimum design factor Z_p, the minimum breaking force of the rope F_{min} is determined by a simple calculation [5]:

$$F_{min} \geq S \times Z_p \tag{1}$$

Nowadays, modern standards apply the proof of competence method to prove that a design force does not exceed a certain limit to ensure a certain safety level. The (limit) design force itself is not determined by specified values, it is rather calculated considering influencing factors. Furthermore, standards elaborated during the last years applying a cycle-based approach instead of a time-based approach. [7]

The shortcomings of ISO 16625:2013 are obvious: a time-based approach, i.e. the total duration of use of the classification of mechanism forms the foundation to select a minimum design factor Z_p although components of a mechanism are worn by stress cycles. Furthermore, the first edition of ISO 16625 misses a link to scientific-based results on impacts from bending stress or tensile loads during operation.

2.1.2 Objectives of the standard revision

The conclusions based on evaluating the as-is state of ISO 16625:2013 outlined the objectives for the revision of the standard. A new revision of ISO 16625 shall adopt a cycle-based approach, e.g. as outlined in ISO 4301-1:2016. [8] Also, modern methods need to be incorporated to provide a proof that the limits of fatigue strength and static strength of a wire rope – in relation to the drum and sheave geometry of load bearing structure – are met. Regarding the introduction of proofs of competence based on the limit state method to a revised ISO 16625 standard, it is of particular importance to focus on proof of static strength and fatigue strength. Along with that, the difference of running ropes that are under bending stress permanently in contact with drums and sheaves and stationary ropes that are primarily under tensile load having no contact with drums or sheaves must be considered. Furthermore, a revision of ISO 16625 shall be enhanced to address the requirements of wire ropes in multi-layer spooling.

Another objective is to implement modern, well-known methods and to incorporate scientific proven input from wire rope tests like bending tests or tension-tension tests as a foundation of a revision of ISO 16625.

2.1.3 Key milestones along the journey

A very first milestone reached on this journey of the revision of ISO 16625 was the establishment of a working group and in particular to get commitment of experts from different areas like representatives from universities, research institutes, wire rope manufacturers and crane and hoist manufacturers joining the working group. In retrospective, the collaboration of these experts with their different background over so many years and the dedication to contribute has been an essential factor to successfully achieve the revision of ISO 16625 that set a benchmark.

Developing an ISO standard follows a clear stage process with associated timeline and usually takes - from first proposal to publication – 3 years. [9] [10] In many cases this 3-years timeline is ambitious to meet. To address this challenge, in ISO standardization there is the possibility to start working under a so-called preliminary work item (PWI). Objective is to outline a working draft (WD) that is mature enough to then start the proposal phase without yet tight to follow a dedicated timeline during that preliminary phase. For the revision of ISO 16625, utilizing PWI was a key factor as it enabled spending enough time on agreeing the foundational approach and content clarification during the first years. In 2018, a resolution was taken to even re-register the PWI as the working draft was not yet on a sufficient maturity level. [11]

Finally, another major milestone was reached in November 2021 when the working group WG3 of ISO/TC 96 SC3 concluded that the ISO/WD 16625 was ready and mature enough to initiate the new project (NP) and to continue now following the 36-months standards development track. [9] [12]

In early 2020, the world was hit by the Covid-19 pandemic and also impacted the work on the revision of ISO 16625. Traditionaly, the working group meetings – as well as all (sub-) committee meetings - were held face-to-face. Despite the fact that face-to-face meetings were not possible and travelling during the pandemic years was limited, changing the meeting routine to remote work turned out to be another success factor. Especially, after the new project was approved in late 2021, the frequent remote meetings of the working group WG3 have contributed to efficient work progress during the years 2022 to 2024 and to meet the key milestones of further ballots, comments work and enhancement of the new revision of ISO 16625 itself.

Further key milestone was reached in regards to the approach and content of ISO 16625 revision. Referring to the objectives, the adoption of a cycle-based approach, the introduction of proofs of competence and to incorporate scientific proven inputs set yet another benchmark for this revised ISO standard.

During the initial scope alignment discussions of the future ISO 16625, any potential input available was reviewed and the European standard EN 13001-3-2:2014 was considered as starting point. [13] Although EN 13001-3-2 applies the limit state method and outlines proofs of competence for static strength and fatigue strength, there have been major shortcomings in this standard identified and discussed at length. [14] [15] [16] It became obvious that the approach defined in EN 13001-3-2 cannot be taken as-is into account as a baseline input for a revised ISO 16625. This learning was another key element and triggered the foundational work to revisit scientific studies and to define a new approach based on them.

3 Scientific foundation

3.1.1 Overview

Reviewing the state of research and scientific studies, the work undertaken by the University of Stuttgart and the Technical University of Dresden (in continuation of the work undertaken by the “Institut für Bergbausicherheit Leipzig”) is of high interest and of particular importance for the revision work of ISO 16625. Both universities have a strong presence with their research about steel wire ropes.

3.1.2 Method Leipzig

The method Leipzig lays down a mathematical estimate in line with the Wöhler-line-system based on endurance tests with known statistical variances of the failure probability to calculate the attainable number of bending cycles of a wire rope in a rope drive system.

In the event of strain due to the rope tension force and bending and compression of rope drive elements, there are stress combinations acting in the wires of a wire rope that could lead to fatigue cracks. To calculate the stresses, certain parameters like the D/d-ratio of the rope drive system, the rope force or load spectrum, the nominal strength of the wires as well as the rope design itself must be considered. The method Leipzig summarizes these stresses to a strain y formula and sets up a single-parameter Wöhler-line-system with strain y over bending cycles N. Thus, the attainable number of bending cycles N can be determined under consideration of the failure probability. To calculate the compressive stress, the contact conditions of the outer wires of the outer strands to the sheaves and wire rope core are considered which is a notably feature of the method Leipzig. That enables to assess the inner rope deterioration without yet visible wire break development. [17] [15]

$$y = \frac{1}{R} \times \left(1{,}04 \times \frac{R}{v} + \frac{0{,}6 \times E}{KL^2 \times \frac{D_G}{d}} + KL \times L \times B \times \sqrt{\frac{\pi}{4} \times \frac{f \times R}{v \times \frac{D_G}{d}}} \right) \tag{2}$$

$$N^{PA\%} = \frac{H^{PA\%}}{y^{CL}} \tag{3}$$

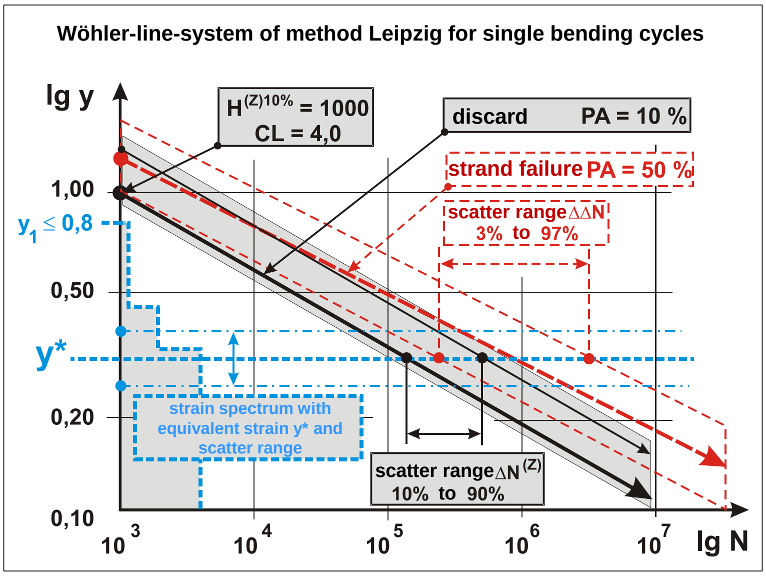

Figure 1: Wöhler-line-system method Leipzig [15]

3.1.3 Method Stuttgart

The method Stuttgart goes back to Feyrer under whose leadership thousands of bending tests have been conducted and evaluated since the 1980s. The empirical findings have been transferred into lifetime diagrams of different wire ropes and utilized to develop a linear regression model to determine the number of bending cycles N of a wire rope, expressed by the well-known Feyrer formula.

$$\lg N = b_0 + \left(b_1 + b_3 \times \lg\frac{D}{d}\right) \times (\lg\frac{S}{d^2} - 0.4 \times \lg\frac{R_0}{1770}) + b_2 \times \lg\frac{D}{d} + \lg f_d + \lg f_L + \lg f_C \tag{4}$$

The method Stuttgart considers the most important influences on the number of bending cycles like the rope tensile force S and the D/d-ratio of a rope drive system. Furthermore, different endurance factors f_j and regression coefficients b_i have been derived from the empirical findings and incorporated to the Feyrer formula.

A lifetime diagram of a wire rope drawn in a logarithm scale is typically represented by straight lines for constant D/d-ratios. The lifetime diagram shows that at a certain high tensile force, the number of bending cycles declines suddenly. This limit of the tensile force where the number of bending cycles starts to decline is called the Donandt force and the kink in the lifetime diagram is called Donandt point respectively. [18]

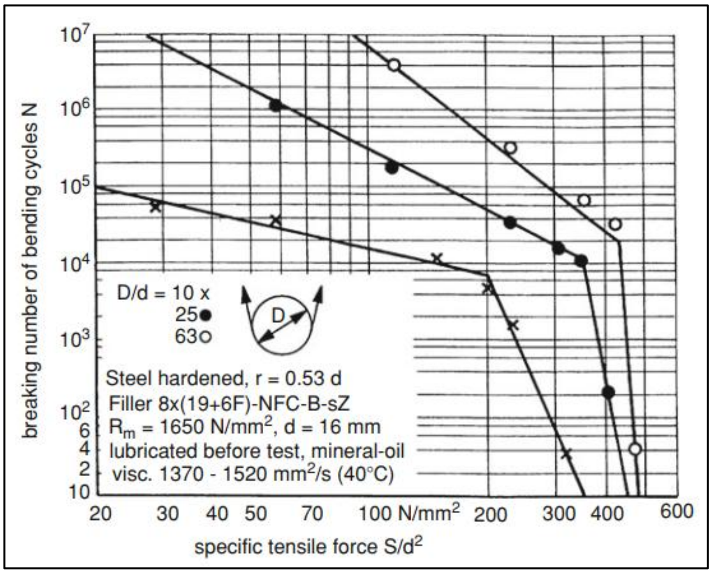

Figure 2: Lifetime diagram of a Filler rope [18], p. 220

4 Innovative approach to reframe ISO 16625

The significant change to reframe ISO 16625 lies in the determination of the limit design rope force $F_{Rd,f}$ for the proof of fatigue strength for running ropes.

The innovative approach of ISO 16625:2025 has its foundation on a newly defined reference point that could be determined by assuming that a regression calculation by the method Stuttgart could be done for forces exceeding the Donandt force. [19] From a mathematical standpoint such a regression calculation is defined, although a wire rope in a rope drive system exposed to such high forces will fail. The graphical representation of this mathematical approach is simple: the straight lines of different D/d-ratio in a Wöhler diagram of one wire rope type will extend until they intersect at a common point. This reference point proposed as the Golder-Point is defined by a specific reference force F_{ref} and a reference number of bending cycles w_{ref}.[14] [20]

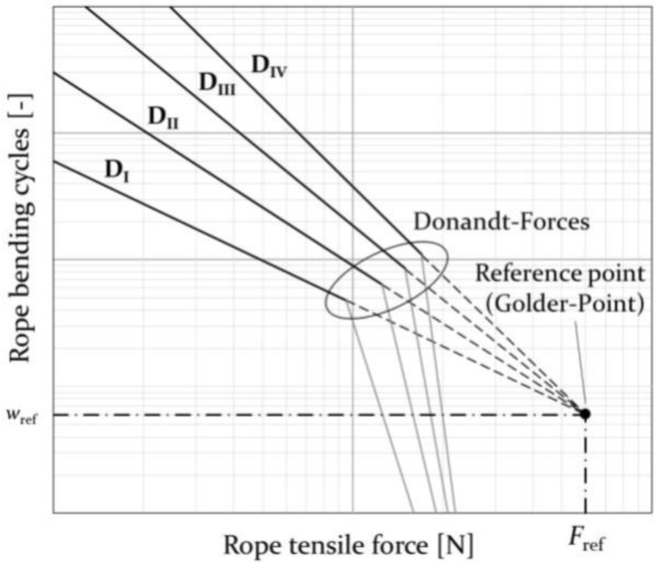

Figure 3: Schematic diagram from ISO 16625:2025 to illustrate the new reference point – Golder-Point - as an extension of Wöhler-curves for individual D/d-ratio [20], p. 24

The originator of this idea – the project lead of ISO/TC 96 SC3 WG3 Prof. Golder – formulated this innovative approach during a discussion in a small group that took place in late September 2017 in Tokyo on the sidelines of the ISO/TC 96 Annual Meetings. Prof. Golder stated the hypothesis that the intersection of the Wöhler curve lines of a wire rope type in one point exceeding the Donandt force could be considered as a reference to a virtual limit, because this intersection point is characterized by a lower amount of bending cycles with simultaneously very high rope force. Although for example the author of this paper challenged this unconvential assumption, the project lead insisted to pursue this idea and so, the innovative idea of the reference point – proposed to be called Golder-Point – was born.

Consequently, to proof this idea, experts from the University of Stuttgart (Dr.-Ing. Novak), the University of Dresden (Dr.-Ing. Anders) and expert from company Liebherr (Ch. Eiwan) have given major contribution to determine respective value of this reference point based on data available from past bending tests and to support in elaborating this innovative approach further. [14] [15]

The mathematical approach proves that the reference point would exist if a wire rope could withstand forces higher than the Donandt force. In conclusion the reference point could be utilized to determine the total number of bending cycles N by a simplified calculation, less complex than the regression calculations of the method Stuttgart or the method Leipzig, but comparable to scientific results. [15] [17] [18]

$$lg(N_1) = lg(N_2)\, with\ \left(\frac{D_1}{d}\right); \left(\frac{D_2}{d}\right) \tag{5}$$

$$\frac{S_{ref}}{d^2} = 10^{\frac{\left(b_3 \times 0{,}4 \times \log\left(\frac{R_0}{1770}\right) - b_2\right)}{b_3}} \tag{6}$$

$$w_{ref} = 10^{b_0 + b_1 \times \left(\frac{-b_2}{b_3}\right) + (\lg(f_d) + \lg(f_L) + \lg(f_C))} \tag{7}$$

$$N = w = \left(\frac{F_{ref}}{F}\right)^m \times w_{ref} \tag{8}$$

Utilizing formula (6) and (7), it could further be proven that formula (8) and formula (4) are equivalent and that the slope of the Wöhler-curve (S-N curve) m can be derived as follows:

$$m = -(\lg\frac{D}{d} \times b_3 + b_1) \tag{9}$$

The parameters of interest can be calculated by simply inserting values of the regression coefficients b_i that have been empirically determined by bending tests conducted by Feyrer. [18] Those empirical findings of Feyrer can be utilized to further simplify the formula to calculate m which in turn is more feasible from a standardization work point of view and in particular if the regression coefficients b_i of a specific wire rope construction are not known. [15]

$$m = 2{,}6 \times log_{10}\left(\frac{D}{d}\right) - 1{,}6 \tag{10}$$

Based on the Golder-Point, formula (8) can be utilized to determine the respective bending cycles w for any rope tension force F. The number of bending cyles at the Golder-Point w_{ref} and the reference rope tension force F_{ref} enable a uniform description of the different fatigue strength lines of the fatigue bending strength at different D/d-ratios of a steel wire rope.

5 Basic principles of ISO 16625:2025

5.1.1 Proof of competence for static strength of running ropes

For the proof of static strength of running ropes, formula (11) shall be proven

$$F_{Sd,s} \leq F_{Rd,s} \tag{11}$$

To calculate the design rope force $F_{Sd,s}$ it is relevant to consider applicable rope force increasing factors f_{Si} on vertical hoisting and general rope drive respectively. In general, the determination of the limit design rope force $F_{Rd,s}$ applies the limit state method.

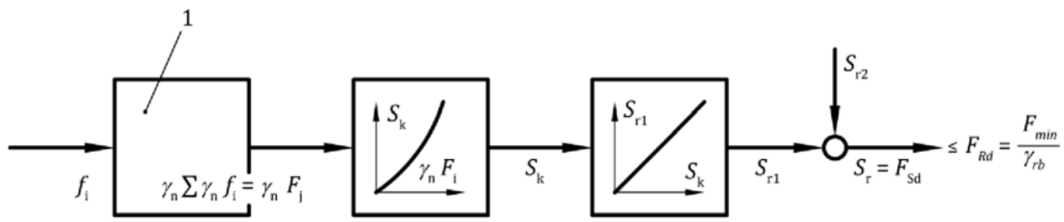

Key

1	see ISO 8686-1:2012, Table 3 and Table 2
f_i	characteristic load action *i* acting on the component including dynamic factors ϕ_i
F_j	combined load actions from load combination j

Figure 4: Flow chart of limit state method for the proof of competence of wire ropes [19], p. 13

To calculate the limit design rope force $F_{Rd,s}$, a reduction factor due to the type of the rope termination f_{S4} and a reduction factor due to D/d-ratio f_{S5} are considered. The rope resistance factor γ_{rb} is calculated according formula (15) and results from the product of the general resistance factor γ_m and the specific resistance coefficient γ_s.

$$\text{Vertical hoisting: } F_{Sd,s} = \frac{m_{Hr} \times g}{n_m} \times \phi \times f_{S1} \times f_{S2} \times f_{S3} \times \gamma_p \times \gamma_n \tag{12}$$

$$\text{General rope drive: } F_{Sd,s} = S_r = S_{r1} + S_{r2} = \frac{S_k}{n_m} \times f_{S1} \times f_{S2} + S_{r2} \tag{13}$$

$$F_{Rd,s} = \frac{F_{min}}{\gamma_{rb}} \times min\{f_{S4}; f_{S5}\} \tag{14}$$

$$\gamma_{rb} = \gamma_m \times \gamma_s \tag{15}$$

5.1.2 Proof of competence for fatigue strength of running ropes

For the proof of fatigue strength of running ropes, formula (16) shall be proven

$$F_{Sd,f} \leq F_{Rd,f} \tag{16}$$

To calculate the design rope force $F_{Sd,f}$ it is relevant to consider applicable rope force increasing factors f_{Si}^{*} on vertical hoisting and general rope drive respectively. To calculate the limit design rope force $F_{Rd,f}$ the innovative approach as outlined in chapter 4 is implemented.

According to the Golder-Point, the maximum number of bending cycles w for any rope tension force F can be calculated, refer to formula (8). The fact that the D/d-ratio increases w is now incorporated in the calculation and expressed by the exponent m. The slope of the Wöhler-curve (S-N curve) m is calculated according formula (10) and is in dependency of the D/d-ratio instead of a constant number. The number of bending cycles at the reference point w_{ref} are calculated according formula (21) considering the factor of influences f_w to w_{ref} like the rope type factor and the rope diameter factor. The reference rope tension force F_{ref} is calculated according formula (20) considering the different factors of influences f_F like the influences from the tensile strength of the wire, the fleet angle, the rope lubrication and the groove radius. The factor γ_{ref} adapts the minimum breaking force F_{min} to the reference rope tension force F_{ref} and by that achieves a survival probability of 97.7%.

Vertical hoisting: $$F_{Sd,f} = \frac{m_{Hr} \times g}{n_m} \times \phi^{*} \times f_{S2}^{*} \times f_{S3}^{*} \times \gamma_n \quad (17)$$

General rope drive: $$F_{Sd,f} = S_r = S_{r1} + S_{r2} = \frac{S_k}{n_m} \times f_{S2}^{*} + S_{r2} \quad (18)$$

$$F_{Rd,f} = min\left\{\frac{F_{ref}}{\gamma_{rf} \times \sqrt[m]{s_r}}; \frac{F_{min}}{\gamma_{rfD}}\right\} \quad (19)$$

$$F_{ref} = \frac{F_{min}}{\gamma_{ref}} \times f_F \quad \text{with } \gamma_{ref} = 0{,}5 \quad (20)$$

$$w_{ref} = 600 \times f_w \quad (21)$$

$$\gamma_{rf} = 1{,}25 \quad (22)$$

$$\gamma_{rfD} = 1{,}1 \times \left(\frac{1}{0{,}65 - 3{,}80 \times \frac{d}{D}}\right) \quad (23)$$

$$s_r = k_r \times v_r \quad (24)$$

$$k_r = \sum_i \left(\frac{F_{Sd,f,i}}{F_{Sd,f}}\right)^m \times \frac{w_i}{w_{tot}} \quad (25)$$

$$v_r = \frac{w_{tot}}{w_{ref}} \quad (26)$$

5.1.3 Proof of competence for multilayer spooling

To address the characteristics of multilayer spooling of running ropes, a separate proof of competence is introduced, following the structure of the proof of competence for fatigue strength of running ropes in single layer spooling.

For the proof of multilayer spooling, formula (27) shall be proven

$$F_{Sd,m} \leq F_{Rd,m} \tag{27}$$

To calculate the design rope force $F_{Sd,m}$ it is relevant to consider applicable rope force increasing factors f_{Si} on vertical hoisting and general rope drive respectively. To calculate the limit design rope force $F_{Rd,m}$, formula (30) is applied. It has to be noted that y_{rb} is empirically defined, depending on the type of crane, the type of wire rope and the mechanism and respective values can be found from **Table 9** in ISO 16625:2025. [19] Also, the proof of competence for multilayer spooling is carried out with design loads and not with nominal loads.

$$\text{Vertical hoisting: } F_{Sd,m} = F_{Sd,s} = \frac{m_{Hr} \times g}{n_m} \times \phi \times f_{S1} \times f_{S2} \times f_{S3} \times \gamma_p \times \gamma_n \tag{28}$$

$$\text{General rope drive: } F_{Sd,m} = F_{Sd,s} = S_r = S_{r1} + S_{r2} = \frac{S_k}{n_m} \times f_{S1} \times f_{S2} + S_{r2} \tag{29}$$

$$F_{Rd,m} = \frac{F_{min}}{\gamma_{rb}} \times \sqrt[4]{\left(\frac{\frac{D}{d}}{\left(\frac{D}{d}\right)_{ref}} \right)} \tag{30}$$

5.1.4 Proof of competence for static strength of stationary ropes

For the proof of static strength for stationary ropes, formula (31) shall be proven

$$F_{Sd,s} \leq F_{Rd,s} \tag{31}$$

For stationary ropes, the static proof of competence follows the same approach as given for running ropes. Stationary ropes can be subject to non-linear effects due to elasticity of surrounding structure. The design rope force $F_{Sd,s}$ for stationary ropes shall be calculated according to ISO 8686 series of standards as applicable. [21]

To calculate the limit design rope force $F_{Rd,s}$, a reduction factor due to the type of the rope termination f_{S4} is considered. The rope resistance factor $\gamma_{rb}$is calculated according formula (15) and results from the product of the general resistance factor γ_m and the specific resistance coefficient γ_s.

$$F_{Rd,s} = \frac{F_{min}}{\gamma_{rb}} \times f_{S4} \tag{32}$$

5.1.5 Proof of competence for fatigue strength of stationary ropes

For the proof of fatigue strength for stationary ropes, formula (33) shall be proven

$$F_{Sd,f} \leq F_{Rd,f} \tag{33}$$

The design rope force $F_{Sd,f}$ shall be calculated considering the rope as a beam with one degree of freedom for regular loads only, with partial safety factor γ_p set to 1. The number of stress cycles N shall be derived from the number of working cycles C of the crane. The limit design rope force $F_{Rd,f}$ is calculated as follows

$$F_{Rd,f} = \frac{F_{ref}}{\gamma_{rf} \times \sqrt[m]{s_r}} \tag{34}$$

$$F_{ref} = \frac{F_{min}}{\gamma_{ref}} \times f_{S4} \tag{35}$$

The fatigue proof of competence has been revised to incorporate scientific findings of the method Stuttgart and the method Leipzig and to reflect empirical verified results from tension-tension tests conducted by the University of Stuttgart.

6 Conclusions

The journey to revise ISO 16625 took a bit more than 9 years and turned out to be a completely new development of a standard rather than just a revision of an existing standard. In many aspects, the several years lasting study of well-established scientific methods like the method Leipzig and the method Stuttgart facilitated the development of an in-depth understanding of underlying physics and characteristics of wire ropes considering the limiting forces and influcences relevant for fatigue strength and static strength. Thus, to determine a substantial, innovative approach to reframe ISO 16625 became a challenging, but game changing aspect. Along this journey, various calculations elicited and proved not only the shortcomings of EN 13001-3-2, rather verified the appropriate safety level of a rope reeving system determined by this new approach. Lately, publications in this subject area provide further calculations on application examples and focus on the use of the revised ISO 16625 as well as comparing the standard with EN 13001-3-2. [20] [22]

Although this 9-years journey came to an successful end with the publication of the edition 2 of ISO 16625:2025 in February 2025, a subsequent objective is about to start: the journey to revise EN 13001-3-2:2014 and to transfer ISO 16625 into an European standard.

7 Acknowledgements

The author would like to thank the expert members of the working group WG3 of ISO/TC 96 SC3 for their lasting support and contribution throughout the years to revise the standard ISO 16625. The work efforts of the standardization project were successfully concluded by the publication of ISO 16625:2025 (Edition 2) in February 2025.

8 List of symbols

Symbol	Description
B	Wire contact factor
b_i	Constants, regression coefficients
C	Total number of working cycles during the design life of a crane
CL	Strain exponent

D	Sheave diameter (method Stuttgart) Rope bending diameter
D_G	Bending diameter at bottom of groove
d	Nominal diameter of the wire (method Leipzig) Nominal rope diameter (method Stuttgart)
E	Modulus of elasticity of the rope wire
F, S	Rope tension force
F_{min}	Minimum breaking force of the rope
$F_{Rd,f}$	Limit design rope force for the proof of fatigue strength
$F_{Rd,m}$	Limit design rope force for multilayer spooling
$F_{Rd,s}$	Limit design rope force for the proof of static strength
F_{ref}	Reference value of rope tensile force to describe the reference point of the Wöhler-curve (S-N curve) at the proof of fatigue strength
$F_{Sd,f}$	Design rope force for the proof of fatigue strength
$F_{Sd,m}$	Design rope force for multilayer spooling
$F_{Sd,s}$	Design rope force for the proof of static strength
f	Fill factor
f_d	Endurance factor rope diameter
f_C	Endurance factor rope core
f_F	Factor of further influences to the rope tension force F_{ref}
f_L	Endurance factor bending length
f_{Si}	Rope force increasing factors to be used at the proof of static strength
f_{S1}	Rope force increasing factor from rope reeving efficiency to be used at the proof of static strength
f_{S2}	Rope force increasing factor from non-parallel falls to be used at the proof of static strength
f_{S3}	Rope force increasing factor from horizontal forces to be used at the proof of static strength
f_{S4}	Rope force reduction factor due to the type of rope termination
f_{S5}	Rope force reduction factor due to D/d-ratio of drum or sheave and rope
f_{Si}^*	Rope force increasing factors to be used at the proof of fatigue strength
f_{S2}^*	Rope force increasing factor from non-parallel falls to be used at the proof of fatigue strength
f_{S3}^*	Rope force increasing factor from horizontal forces to be used at the proof of fatigue strength
g	Acceleration due to gravity
H	Constant operation period
KL	Construction factor wire rope
k_r	Rope force spectrum factor
L	Wire factor
m	Exponent, slope of the Wöhler-curve (S-N curve)
m_{Hr}	Mass of the hoist load or that part of the mass of the hoist load that is acting on the rope falls under consideration
N	(Attainable) Number of bending cycles
n_m	Mechanical advantage
$PA\%$	Occurrence probability respectively failure probability
R	Nominal tensile strength of the rope wire
R_0	Nominal tensile strength

S_k	Design load effect in rope drive k of rope falls, as an inner force, resulting from load combination F_j
S_r	Resulting design force in particular rope
S_{r1}	Design load effect in particular rope
S_{r2}	Design load effect in particular rope arising from local effects
S_{ref}	Reference rope tension force
s_r	Rope force history parameter
w	Number of bending cycles
w_{ref}	Reference number of bending cycles of the Wöhler-curve (S-N curve) for the proof of fatigue strength
w_{tot}	Total number of bending cycles during the design life of a rope under the rope section under investigation
y	Strain
Z_p	Minimum design factor
γ_m	General resistance factor
γ_n	Risk coefficient
γ_p	Partial safety factor
γ_{rb}	Rope resistance factor to be used at the proof of static strength and multilayer spooling
γ_{ref}	Factor to adapt the minimum breaking force F_{min} to the reference rope tension force F_{ref} at the proof of fatigue strength
γ_{rf}	Rope resistance factor to be used at the proof of fatigue strength; a combined safety factor taking into account the accessibility of the rope and the possible consequences of fatigue damage
γ_{rfD}	Minimum rope resistance factor to prevent from exceeding the Donandt force
γ_s	Specific resistance factor for a proof of competence against breaking strength of a wire rope taking into account the decrease of the minimum breaking load over the operating time as well as the exceeding of the yield point of individual wires in the rope
ν	Safety factor
ν_r	Relative number of cycles
ϕ	Dynamic factor for interial and gravity effects

9 References

[1] ISO/TC 96 SC3: N375 – SC3 Resolutions taken during the meeting held on 2015-09-08 (Sydney)

[2] ISO 16625:2025: Cranes and hoists – Selection of wire ropes, drums and sheaves, Life cycle [Online]. Available: https://www.iso.org/standard/77889.html?browse=tc#lifecycle

[3] ISO/TC 96 SC3: N387 – Report of SC3 Meeting held on 2016-09-07 (Changsha)

[4] ISO/TC 96 SC3: N383 – SC3 Resolutions taken during the meeting held on 2016-09-07 (Changsha)

[5] ISO 16625:2013: Cranes and hoists – Selection of wire ropes, drums and sheaves

[6] ISO 4301-1:1986: Cranes and lifting appliances – Classification – Part 1: General

[7] Golder, M., Wagner, G.: As time goes by: classification of hoists, cranes and lifting equipment [Online]. Available: (PDF) As time goes by… classification of hoists, cranes and lifting equipment

[8] ISO 4301-1:2016: Cranes – Classification – Part 1: General

[9] ISO. Stages and resources for standards development [Online]. Available: https://www.iso.org/stages-and-resources-for-standards-development.html

[10] ISO. International harmonized stage codes [Online]. Available: https://www.iso.org/stage-codes.html

[11] ISO/TC 96 SC3: N410 – SC3 Resolutions taken during the meeting held on 2018-06-29 in Helsinki

[12] ISO. Timeframe of the different standards development track [Online]. Available:https://www.iso.org/files/live/sites/isoorg/files/developing_standards/resources/docs/std%20dev%20target%20date%20planner.pdf

[13] EN 13001-3-2:2014: Cranes – General Design – Part 3-2: Limit states and proof of competence of wire ropes in reeving systems

[14] Reinl, J., Golder, M.: Wire ropes in Crane Applications – Current state of the Standardization Work of ISO/WD 16625. innoTRAC Journal. Volume 1 (2020), pp. 37-46. Available: https://doi.org/10.14464/innotrac.v1i0.456

[15] Golder, M. et al: New Approach for ISO 16625. Proceedings of the XXIII International Conference on Material Handling, Construction and Logistics, MHCL 2019, Vienna, Austria

[16] Steinbach, G., Anders, M., Ryk, D.: Drahtseile in Seiltrieben nach DIN EN 13001-3-2:2014-12 – Bemessungsbiegewechselzahl und Realbiegewechselzahl, Exklusivbeitrag, Hebezeuge Fördermittel, no. 1 (2016), pp. 1-23.

[17] Steinbach, G., Anders, M., Ryk, D.: Betriebsdauer in Seiltrieben – Berechnung der Biegewechselzahl – Methode Leipzig, Exklusivbeitrag, Hebezeuge Fördermittel, no. 5 (2018), pp. 34-35.

[18] Feyrer, K.: Wire Ropes, 2nd ed. Heidelberg, Springer Verlag, 2015.

[19] ISO 16625:2025: Cranes and hoists – Selection of wire ropes, drums and sheaves

[20] Schöneck, T. et al : Theoretical comparison of ISO/WD 16625:2023 with DIN EN 13001-3-2:2015 for the selection and verification of wire ropes for cranes and hoists. innoTRAC Journal. Volume 3 (2024), pp. 19-38.
Available: https://doi.org/10.14464/innotrac.v3i1.801

[21] ISO 8686 series of standards: Cranes – Design Principles for loads and load combinations
Part 1: General (2012); Part 2: Mobile cranes (2018); Part 3: Tower cranes (2018); Part 4: Jib cranes (2005); Part 5: Overhead travelling and portal bridge cranes (2017)

[22] Schöneck, T., Maximov, I.: Anwendung der neuen ISO/DIS 16625:2024 bei der Auslegung und Nachweisführung von Seiltrieben in Kranen und Hebezeugen. 33. Internationale Kranfachtagung 2025, Magdeburg, Germany.

10 Author Introduction

Judith Reinl received her MSc degree in Industrial Engineering from Karlsruhe Institute of Technology in 2020. She holds a BA degree in International Business and Management from Hogeschool Zeeland Vlissingen (2003) and a diploma degree in Management in Industry from Berufsakademie Mosbach (2004). She started her professional career in 2004 and worked in several roles in logistics, production planning and control, global business process harmonization, master data management, patent management and product lifecyle management. Her current role at Konecranes is Manager, Product Lifecycle Process. Since 2017, she is engaged in ISO standardization work of ISO/TC 96 Cranes and since 2019 Convenor of ISO/TC 96 SC3 WG3.

Connect: linkedin.com/in/judith-reinl-8aa87921a

Renaissance of twisted fibre rope constructions for arts, architecture and ski-lifts

Dr.-Ing. Konstantin Kuehner

Jakob Rope Systems, Goeppingen / Germany

Summary

High-tensile fibre ropes are usually braided designs as they show no torque and, if compactly jacketed, a low initial settlement and high Young's modulus. But they may provide disadvantages in bending lifetime, haptics or appearance and coloring. In recent projects of Jakob Rope Systems, twisted designs experienced a renaissance as they could be implemented in surprisingly different applications:

- a new 16mm twisted rope was certified according to the European Ropeway Directive for low level ski-tows with a special monofil-multifil strand-jacket. Bending tests of rope and splice lifetime were carried out within development.
- a red-and-white striped 28mm polypropylene rope was manufactured and long-spliced for a moving arts object of the German artist Boris Petrovsky. Traditional splice techniques had to be carried out to make the moving loop build up a shimmering visual impression.
- over 1 million meters of hawser laid fibre ropes were installed for cladding in the façades of a luxury hotel in Saudi Arabia. The management, especially of in-time manufacturing and installation, was challenging.

Twisted ropes revealed their potential in price and performance of material and end connections. The following paper will present processes of development, technical data and test results as well as experience about handling and installation.

Keywords: twisted fibre ropes, synthetic fibres, skilift, arts, architecture

1 Fibre ropes – braided and twisted designs

First evidence of natural fibre ropes – or rope-like designs – was recently dated about 8'000 years back to the period of Aurignacian, 35'000 years before Christ [1], see **Figure 1**. Since then, natural fibre ropes were handmade both as twisted and braided construction. In the 18th century, beyond the classic ropewalks, the industrial production of fibre ropes started [2]. While, as we all know, the wire rope soon overshadowed the fibre rope with its invention in 1834 [3].

Figure 1: Prehistoric rope maker's ivory top – note twisted grooves close to the holes

With the development of endless technical fibres, a first renaissance for fibre ropes took place. The initiator was the successful launch of nylon by DuPont in the 1930s [4]. But these ropes primarily entered marine technics, not yet a broad use in industrial applications. Polyester turned out to be a robust and popular fibre for slings, sports and let's say simpler rope drives until high tensile fibres like LCPs (*1965) and HMPEs (*1980 – 1990) came to market [5],[6].

Today, modern fibres replace more and more applications of wire ropes due to their advantageous properties in own weight, bending flexibility and lifetime.

For various reasons, braided rope constructions seem to dominate the choice of ropes. They do not develop torque, they are usually easy to knot and to bend and spliced eyes can be carried out more comfortably and faster than with twisted ropes.

But single braided ropes have a weak transverse stiffness. If one needs a stable rope shape, an additional braid is manufactured onto the core rope, forming a “Kernmantle” or double braided rope.

The additional braid is usually communicated as an advantage: the load bearing fibre in the core can be protected e.g. from abrasion, UV-radiation or heat. But it may also cause a lack of load bearing capacity, referring to its diameter and cross-section. Especially, in thinner diameters, the jacket-braid takes a huge portion of the ropes cross section, see **Figure 2**.

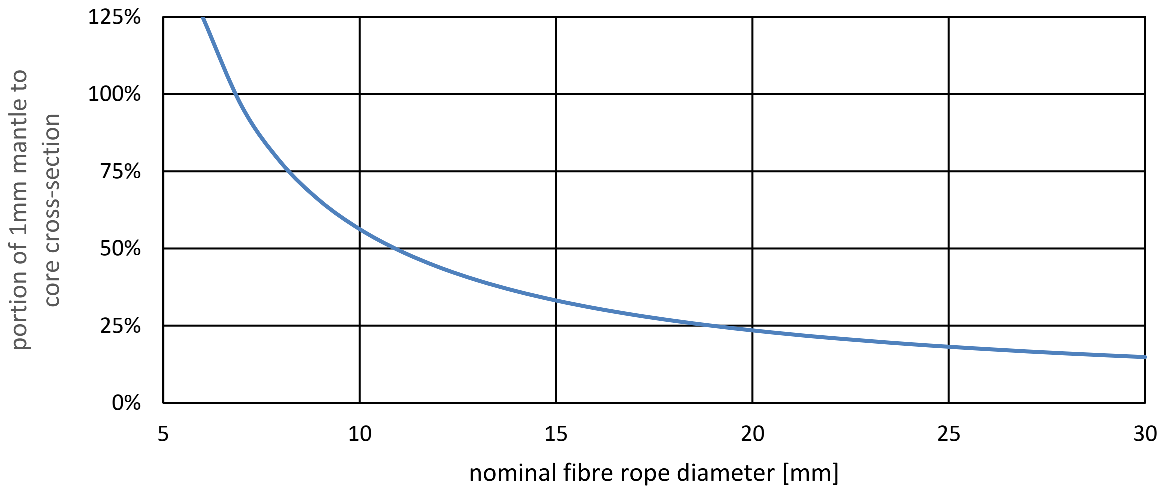

Figure 2: diagram of portion of mantle to core area with assumed jacket thickness of 1 mm

Another disadvantage of jacketed ropes is that end connections may cause a high effort in manufacturing or, if clamped, the jacket may affect the maximum applicable load as it could slip or tear apart first, see **Figure 3**. These properties are often counteracted by the mechanical coupling of the rope core and jacket.

Figure 3: Ripped jacket in a tensile test of a customer project

In summary, it gives the impression that there is a certain reluctance to use twisted fibre ropes. It is possible that they are perceived as old-fashioned and no longer meet the modern requirements of industrial applications. With the following three examples, we would like to show that there can be reasons to choose the classic fibre rope design.

2 A twisted high-tensile fibre rope for low-level ski-tows

Since the 1950s, low-level ski-tows as shown in **Figure 4** have been installed in children's ski areas as well as for cheap and simple connections between a lower end of a slope and ropeway station located a little higher up [7]. Without the need of intermediate support-structures, a spliced rope loop is tensioned between dismantlable drive and counter stations which are usually garaged in summer season. Producers like Staedeli (CH), Borer (CH), Bruckschloegl (AT) and later Multerer (DE), at first, offered both systems with thin simple 6x7 wire ropes and grips as well as natural fibre ropes to hold on to it directly. Later, the common carrying-hauling rope to be held directly was made of synthetic fibres. Small rubber or plastic grips can add comfort to using the lift and to easily identify the intended distance of passengers.

Since decades, a 16mm Atlas® rope containing Polyamide monofils has been installed on these lifts as a kind of standard. It proved to be feasible and robust, but it showed a high elongation of more than 6% after installation and initial operation. Its minimum breaking load was limited. And with increased wear, broken monofils tended to protrude from the rope and catch users' gloves or poke a passenger's hand – with the risk of injuries. The rope is classically long-spliced and needs wrapping of the tucked tails to enlarge the diameter. This causes mounting effort. On systems with multiple bendings in the stations, like the French “Télecorde” or the “Swisscord”, the lifetime of the rope and splice was rather poor.

Another occurrence was, as low-level ski tows usually run in the periphery of ski resorts and technical surveillance, often any type of simple and cheap fibre rope was installed for replacement in case the original rope reached its end of life. Also, in former times, Jakob Rope Systems provided cheap replacement ropes which did not ask for special ropeway certificates.

Figure 4: Fibre ropes on low-level ski-tows

With modern structures of the European Ropeway Regulation, its safety components and certificates, new attention was also paid to the conformity of both existing and newly installed small lift-systems [8].

This initial situation as well as feedback from customers and mounting personnel made the Jakob Rope Systems team think about setting up a new rope design with the following properties [9]:

- Higher breaking force
- Same or lower weight
- Better gripping-by-hand properties
- Less risk of injuries caused by wear
- Less effort and more comfort in splicing
- Better lifetime performance

After some intermediate steps of prototype designs which did not fulfil the expectations, the ideal design was found by a five stranded twisted rope made of jacketed strands. A braided

HMPE-core takes the load, while a mixed jacket of both thin monofils and multifils made of Polyester provide very good manual grip conditions. This technique was adopted from fibre ropes which are attached to helicopters for load-transport. The five stranded design is supported by a classic and economic Polypropylene fibre core, which can be replaced in the long-splice area by the strands without the need of additional wrapping.

The rope properties of the existing design and the new Hybrid 5 are compared in the following **Table 1**:

Table 1: Comparison of existing and new fibre rope designs for low level ski-tows

Rope Type	**Atlas® Rope**	**Hybrid 5**
Cross section	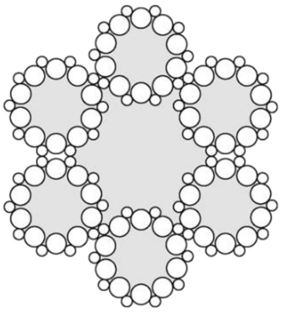 [source: drahtseilwerk.de]	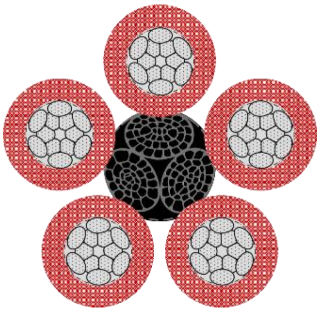
Specific weight	179 g / m	170 g / m
MBL	49.50 kN	51.00 kN
certified safety-factor	5	4
WLL	9.90 kN	12.75 kN
Initial elongation	6 %	2 %

A comparative bending test of the rope designs on a real lift system showed that the new Hybrid 5 offers a longer bending performance. The counter station was adapted to a sharper reverse-bending situation to simulate the use in a Swisscord lift system. In addition, the tests were used to extract pictures for the operation and maintenance manual to give examples for different degradation states of the rope. An example is given in **Table 2**.

Within the bending test, diameter development and elongation of the rope (see **Figure 5**) was monitored.

For the existing Atlas® rope, the elongation rapidly grows to 6 % with the first 200 Operation hours. Later on, it keeps elongating constantly with about 1 % per 390 hrs.

The new Hybrid 5 rope shows a lower initial elongation, it reaches 2 % after 300 hrs. Afterwards, it keeps elongating constantly with about 1 % per 650 hrs.

The diameter development of the Hybrid 5 both on free rope length as well as in the splice knots showed a significant decrease at the beginning of operation. But over continuing operation, the diameter decrease turned to be very slow and can be neglected up to putting out of service by visible damage of the strand jackets, especially the monofils.

After launching the product in 2022, today, already about 15 km of the new rope Hybrid 5 are in operation. The development of a modern twisted 5-stranded rope design was a successful project of Jakob Rope Systems, making us confident to work with twisted designs in further future projects.

Table 2: Graphic support of the condition assessment in the maintenance manual [10]

Bending cycles	Free rope length	Splice knot
50’000 cycles		
500’000 cycles		
1’000’000 cycles		

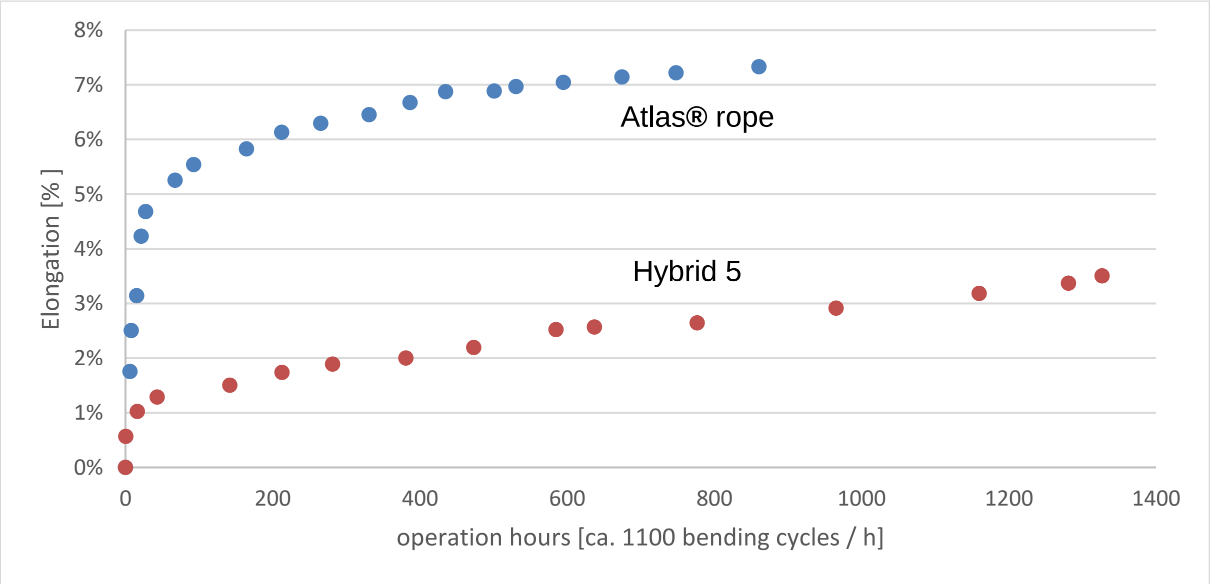

Figure 5: Elongation in relation to operation hours

3 Filament Momentum – a performative Installation or “built movie”

The German artist Boris Petrovsky is known for larger scale installations combining textwork, lighting objects, interpassive or active media and kinetic room installations. His works are often characterized by a noticeable technical fascination for the viewer [11], [12]. Boris himself talks about his personal connection to cable car technology, which he has felt since his youth and now interprets in his work. Visiting Jakob Rope Systems, he showed a portable model of a hall-sized installation. He asked for manufacturing a fibre rope in larger scale, referring to the demonstrator model, which can be moved continuously over numerous sheaves. In fact, the prototype in the model was a classic "sausage yarn", see **Figure 7**. The basic idea of the arts installation was to generate a silent, complex and interfering moving pattern of the red- and white striped rope in a deep space. Therefore, the rope should cross the room in various planes, (running) directions and inclinations, being deflected by means of visible and individually alignable sheaves. A box-like, observable friction drive station was placed on the ground, running a random pattern of movements in alternating directions.

Elastic behavior, delays and damping in the movement were even welcomed and explicitly desired to make the movement more fluid and unpredictable.

Figure 6: Artist Boris Petrovsky and splicer Marcel Habegger

The artist's main recommendations for the rope were a cheap, long-splice-able fibre rope which could be installed as a continuously running rope. The diameter should be as large as possible and feasible, showing a clear appearance of the desired red and white stripes on the rope surface. The pulley diameter was already set at this point.

As solution, a 28 mm red-&-white 6-stranded Polypropylene rope was designed and manufactured in Switzerland. The strands were made of 16 PP-yarns of Nm 0.450 titer, with 5 yarns wrapped around the core and ten outer yarns. To achieve the desired pattern, the first three strands are white while the following three strands are made of red yarn, RAL 3020. A classic 12mm PP-rope, form B was used as fibre core as it is usually applied in wire ropes.

Figure 7: Working model of "Filament Momentum" by Boris Petrovsky

For long splicing, common wrapping materials for the tucked tails like braided sleeving or tape could not be used due to the softness of the rope yarns. Instead, as shown in **Figure 6**, classic hemp wrapping was applied to make the end connection bear the multiple bending cycles in the arts installation. Within the exhibition from 8th to 29th July 2022, the rope proved its function in the halls of Greenbox Konstanz [13], see **Figure 8**. Right now, the installation is stored and ready for possible new projects and re-installation in a new location.

Figure 8 Finalized installation “Filament Momentum” by Boris Petrovsky

4 Rope Cladding for Nujuma Resort in Saudi Arabia

Foster + Partners Architects realized the luxury Nujuma Resort of Ritz Carlton Hotels on the Ummahat AlShaykh Island in Saudi Arabia at the coast of the red sea. The project is characterized by single wooden cabins, some of them resting on stilts directly above the sea water [14]. The houses are covered by rope claddings to create a natural, shell-like appearance, see **Figure 9**. Due to the curved shape of the individual buildings, the ropes act as both the façade and the roof. The ventilation provided by the design creates a layer of insulation and shading to cool the building envelope. Some ropes are also used for purely decorative purposes.

Figure 9: Impression of the cabins at Nujuma Resort [source: ritzcarlton.com]

The contact was established by the Swiss timber construction company Blumer-Lehmann AG who were looking for suitable ropes within the first stages of mockups.

At the beginning of the project, it was planned to cover the houses with natural fibre ropes made of Manila, but it turned out that the material would not be sufficiently long-lasting and too heavy, especially in wet state.

Therefore, a special mixture of fibrillated Polypropylene yarns in four different color-shadings of beige was set-up to form mostly 30 mm and 36 mm diameter 4-stranded hawser laid ropes, form B according to ISO 1346. The yarns contained special additives to enlarge UV resistance.

The total length was calculated to be more than 1’000 km of rope respectively 500 tons of fibre material. The special yarns were manufactured at Bächi-Cord AG, Switzerland, while the tight plan for rope production was successfully fulfilled by the manufacturers Lippmann German Ropes, Hölscher Ropes and Seilfabrik Ullmann AG.

Jakob Rope Systems planned and delivered both ropes and spacers of the support structure. The wooden framework of the single nutshell houses was already finalized when the outer design was detailed to a deviating shape. This required the parametric planning, production and clear marking of approx. 1800 different spacers per house to attach the rope structure to the substructure and realized the desired outer shape, see **Figure 10** and **Figure 11**.

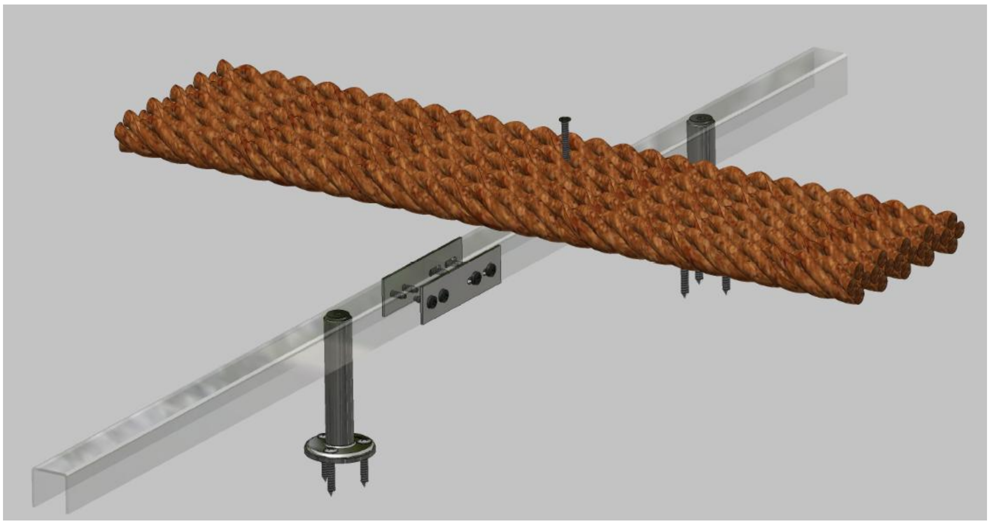

Figure 10: Example CAD model of ropes and support structure

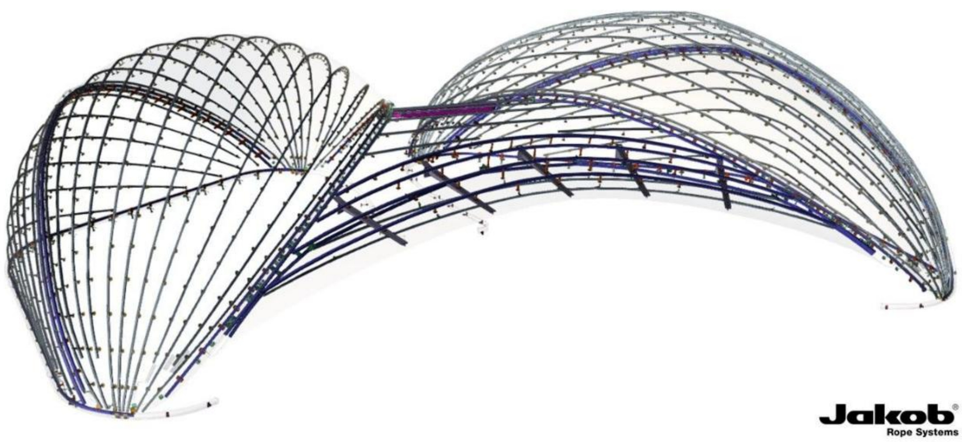

Figure 11: CAD model of a shell with rope support structure for one cabin

The ropes were screwed-through directly into an aluminum support structure by self-cutting screws. The 4-stranded design allows fixing the rope at the lower strands, while the upper strands can cover the screws heads after mounting. The ropes themselves were cut to length on site as there was doubt that the real length from end to end would meet the calculated geometry due to tolerances within construction. Therefore, the ropes were coiled off from the laying reel and twist was released by hands if necessary. One cut-end was directly attached to the structure, while the final length was cut by cut-off grinders and secured with stainless steel cable ties. The cut ends are covered by sheet metal screens.

The total structure of spacers, aluminum rails and ropes were installed with the help of 500 to 600 workers over 1.5 years between Nov. 2022 until Feb 2024. Our Swiss personnel started with four fitters to instruct local foremen. Later on, only one Swiss fitter was present on-site.

The project was successfully completed, and the resort is in operation, now [15].

5 Conclusions

The described projects show that twisted fibre rope designs can provide convincing properties for moving applications, architecture and arts. Although they often stay behind modern braided ropes made of high-tensile fibres, it may be profitable to investigate solutions with the classic constructions. They provide efficiency in production, handling and mechanical properties, and they may offer better possibilities to meet high visual appearance requirements. We hope that this paper encourages other participants of our rope community to think about using twisted fibre rope designs and to take part in the – as we have named it – “renaissance” of their implementation.

6 Acknowledgements

I would like to express my sincere thanks to my colleagues for their support in the projects shown, but also in writing and proofreading this publication: Elzbieta Bortkevic, Alfred Beer, Fabian Graber, Marcel Habegger and Urs Schneider. My special thanks go to Boris Petrovsky for the good cooperation and for coming to us with his exciting idea. Finally, many thanks to Dr.-Ing. Bjoern Ernst and Christoph Schoefberger of Teufelberger Fiber Rope GmbH for the technical exchange on fibre rope constructions and their support in the preparatory tests for the presentation.

7 References

[1] Conard, Nicholas J.; Rots, Veerle: Rope making in the Aurignacian of Central Europe more than 35,000 years ago, Science Advances 10, eadh5217, published 31.01.2024, downloaded on 2024/11/27 at: https://www.science.org/doi/10.1126/sciadv.adh5217#tab-contributors

[2] Lepperhoff, Bernhard: Die Flechterei, 2.Auflage, Bibliothek der gesamten Technik; Bd. 208, Dr. Max Jänecke Verlagsbuchhandlung, Leipzig 1922

[3] Benoit, G.: Zum Gedächtnis an W.A. Julius Albert und die Erfindung seines Drahtseiles, Schriftenreihe der Fachgruppe für Geschichte der Technik beim Verein Deutscher Ingenieure, VDI-Verlag Berlin 1935

[4] Weber, Wolfang: Seilerlexikon Band 2, Aegis Verlag, Ulm 2004

[5] der Spiegel / mxw/Reuters/AFP: Chemikerin Kwolek gestorben - Ihre wichtigste Erfindung ist stärker als Stahl. online-report published 21.06.2014, downloaded on 2024/11/27 at: https://www.spiegel.de/wissenschaft/technik/stephanie-kwolek-erfinderung-der-superfaser-kevlar-ist-tot-a-976595.html

[6] The Society of Fibre Science and Technology Japan: High-Performance and Specialty Fibres. Springer Japan 2016

[7] Schmoll, Hans-Dieter: Weltseilbahngeschichte 2, Ottmar F. Steidl Verlag, Eugendorf/Salzburg 2000

[8] European Union: REGULATION (EU) 2016/424 OF THE EUROPEAN PARLIAMENT AND OF THE COUNCIL of 9 March 2016 on cableway installations and repealing Directive 2000/9/EC, downloaded on 2024/11/27 at: https://eur-lex.europa.eu/legal-content/EN/TXT/PDF/?uri=CELEX:32016R0424

[9] Jakob Rope Systems: Ein Seil, das leicht zu spleissen ist und gut in der Hand liegt, news on www.jakob.com, downloaded on December 21st 2024 at https://www.jakob.com/ch/de/news/jakob-entwickelt-neues-skiliftseil/ein-seil-das-leicht-zu-spleissen-ist

[10] Jakob Rope Systems: Operation and maintenance manual, Hybrid 5 Fibre Rope for low-level Ski Tows, Jakob AG Trubschachen, 09/2023, downloaded on 2025/01/24 at: https://www.jakob.com/files/6_downloads/technical-information-sheets/EN/jakob-rope-systems-operation_and_maintenance_manual_Hybrid_5_2023_A5_EN.pdf

[11] Petrovsky, Boris: Biografie C.V., downloaded on 2025/02/13 at: https://petrovsky.de/BIOGRAFIE%20%20C.V.-36

[12] Petrovsky, Boris and Wagner, Velten (publisher): Buzzerworld, Catalogue of Städtisches Museum Engen + Galerie, Engen (DE) 2022

[13] Lünstroth, Michael: Im Netzwerk verheddert, thurgau kultur ag, Bottighofen, 25.07.2022, downloaded on 2024/12/02 at: https://www.thurgaukultur.ch/magazin/im-netzwerk-verheddert-5225?fbclid=IwAR3KhzOsvlc3ZSGr5jIsW00bVj6wZBWhEbYWgjULQR5THVsS9yri3FdiJCI

[14] Harrouk, Christele: Foster + Partners Designs Hotel 12, part of the Red Sea Project in Saudi Arabia, report on archdaily.com dated 05th March 2021, downloaded on March 3rd https://www.archdaily.com/957797/foster-plus-partners-designs-hotel-12-part-of-the-red-sea-project-in-saudi-arabia

[15] Movie “The Making of Nujuma, a Ritz-Carlton Reserve”, Red Sea Global, youtube.com viewed on 2025/03/03 at: https://www.youtube.com/watch?v=yi-M383bkNw

8 Author Introduction

Dr.-Ing. Konstantin Kuehner worked at IFT University of Stuttgart in the rope technology department from 2009 to 2017. He received his PhD degree in Mechanical Engineering in 2017, the research topic deals with the twist behaviour of cable car wire-ropes within operation. Since September 2017, he is working for the Swiss rope manufacturer Jakob Rope Systems in the technical and the rope & lifting technology department. In 2024, he became Head of Research and Development.

Reliability of fibre ropes in crane application

Piia Koskenjoki, M.Sc.

Konecranes Global Corporation, Finland

Kirsi Saarinen-Pulli, D. Sc. (Tech)

Konecranes Global Corporation, Finland

Summary

Rope is a safety critical component in crane applications. Failure of the rope can cause a load drop with critical consequences. Typically steel wire ropes have been used as load carrying elements in hoists and cranes. Since 2019 Konecranes product offering has included a rope hoist with a synthetic fibre rope. Material change from well-known solution to synthetic requires design changes and comprehensive reliability and safety verifications.

This paper summarizes the issues to be considered when fibre rope is taken into use in crane application. Rope selection, use, maintenance, inspection and discard needs to be rethinked. In addition, the whole reeving system (including rope drum, sheaves, and rope end terminations) needs to be optimized for fibre rope. There are limited number of standards and instructions related to this topic. Testing can be used to verify the reliability of the rope and the whole reeving system. Good practices and lessons learned are shared with practical examples.

Keywords: Fibre rope, Reliability, Safety, Crane application

1 Introduction

Main function of a crane is lifting and moving a load in three directions. Hoist is the part of the crane which is responsible for lifting and lowering action with a hook or other load handling device. [1] In rope hoist, the hoisting medium between the hoisting machinery and the hook is a rope. Typically, steel wire ropes have been used as hoisting medium in hoists and cranes. Their functionality and wearing behaviours are well-known. In addition, steel wire rope selection guidelines and inspections criteria are standardized. Recently also high performance fibre ropes (HPFR) have been started to use in material handling applications. Advantages of using fibre ropes are for example light weight, no need for re-lubrication and easy handling. There are some standards also for fibre ropes but very little experience-based information about their behavior in lifting applications compared to steel wire ropes. [2]

In 2019 Konecranes launched a fibre rope hoist as a part of its product offering, see **Figure 1**. The hoist uses fibre rope with 12-strand single-braid construction as a lifting medium.

Figure 1: Fibre rope hoist by Konecranes

Transition from steel wire rope to fibre rope requires comprehensive understanding of the fibre ropes and their requirements to the application as well as reliability verification through testing for the rope and the whole reeving system. This paper summarizes the lessons learned in the process.

2 Reliability and safety

Reliability of a component is the probability that it will perform its defined function under defined conditions and time without failure. Safety of a component is the probability that the component does not fail in a way that it would cause immediate safety hazard. [3] Rope is safety critical component and needs both of these. Failure of the rope can cause a load drop and possibly cause injury to persons or damage to materials.

High reliability with rope requires visible wearing to be able to recognize the discard criteria in inspections. Rope lifetime should be known in normal usage so that it is possible to inspections intervals. [4] In addition to normal fatigue wearing, it is important to understand what can cause local wearing to the rope and how different environments or misusage cases should be taken into account. With steel wire rope, the knowledge has been accumulated over a long period of time but to achieve same level of confidence with fibre rope requires comprehensive reliability verification and testing.

Reliability testing can be lifetime testing. When component is lifetime tested separately from the system, it is called component lifetime testing. System lifetime testing can be used to verify component lifetime in its real system, for rope it means testing with a hoist. Functional testing can be used to test functionality of the component with different loadings or in different environments. [3]

3 Requirements for the rope

Requirements for the rope come from the application. In practice from the hoist design, how it is used and in what kind of environment. Rope is attached to the hoist from both ends. Rope is in contact with other reeving components such as drum, rope sheaves and rope guide. Materials and rope groove profiles are know to have an effect on rope lifetime. In addition, the ratio, between sheave diameter and nominal diameter of the rope (D/d ratio), is important factor from rope lifetime perspective. The more severe the bend, the more rapidly the rope will wear. In case of the multiple reevings, rope is also subjected fleet angels. Meaning that rope comes to the rope groove with some angle which causes wear to the rope. [5]

Rope strength must be suitable for the application. Minimum breaking load (MBL) of the rope should not just cover working load but also provide the required safety factor [6]. In addition, rope must have good bending lifetime and be suitable for reverse bending to enable multiple reevings. **Figure 2** shows an example of a reeving with four rope falls. The rope is attached to the drum, goes through three rope sheaves and ends up to fixed rope end termination. Different parts of the rope see different amount of bendings when hook is lifted and lowered. Coefficient of friction is needed to be able to attach the rope. Holding a rope at end termination requires friction, but on the other hand, low friction is beneficial in terms of internal and external abrasion. [6]

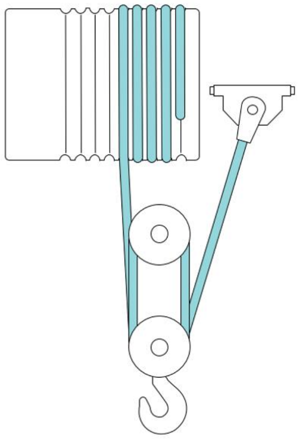

Figure 2: Reeving with four rope falls

Usage environment also affects to the behavior and service life of the rope. Usage conditions of a crane may include different temperatures, humidity, UV and abrasive particles or chemicals. These environmental factors can expose the rope to for example corrosion, abrasion wearing and ageing. The effect on the physical properties of the rope can be for example reduced strength, increased elongation or changes in friction coefficient.

4 Differences between steel wire rope and fibre rope

What are the key differences between steel wire rope and high performance fibre ropes? Steel wire ropes are varying by material, construction and core type but if simplified steel wire rope is a bunch of small steel wires. Then again HPFR are made from polymer fibres, e.g. from high modulus polyethylene (HMPE), aramid or liquid crystal polymer (LCP) [6]. Strenght of HPFR is from molecules which are highly oriented along the fibre axis [7]. These fibre ropes have comparable strength to steel wire rope [2], but other properties may differ significantly depending on the fibre.

Table 1 has a summary of the rope properties that are relevant in crane application and the differences between steel wire rope and fibre rope. In addition, reliability verification needs are listed when steel wire rope is replaced by fibre rope.

Table 1: Differences in rope properties and their effect on reliability verification

Property	**Steel wire rope** 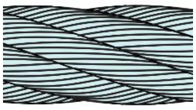	**Fibre rope** 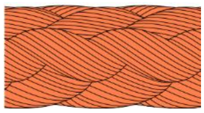	**Reliability verification** 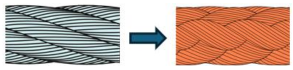
Stength	Strength depends on the strength of the steel wires and rope structure [8].	Strenght from highly oriented molecules along the fibre axis [7]. Comparable strength to same sized steel wire rope [2].	Tensile testing to verify that rope fulfils MBL requirement.
Bending lifetime	Depends on the strength of the steel wires and rope structure.	Depends on the fibre type, rope construction and coating. [6]	Component lifetime testing to get an indication of lifetime and wearing mode or to compare different ropes to each other. System lifetime testing to verify rope lifetime and safe failure in real system. Rope residual testing to verify rope strength at discard condition.
Wearing in cyclic bending	Broken wires on the surface and inside the rope [9]	Broken fibres on the surface and inside the rope [2].	
Inspection methods	Visual inspection for surface wire breaks and magnetic rope testing (MRT) [9]	External and internal condition can be inspected visually [2].	
Discard criteria	Based on visible surface wire breaks, quantitative, based on ISO 4309 [9].	Based on external and internal wearing, quantitative, based on ISO/TS 23624 and crane manual [2].	
Rotation resistance	Tendency to open with high lifting hights, rotation resistant ropes can be used in special applications [10]	12-strand braided rope has six S-twist strands and six Z-twist strands arranged so that rope is naturally balanced [11].	Functional testing with hoist.
Coefficient of friction	Depending on the lubrication but typically suitable for easy rope attachment with clamps and wedge socket.	May be close to zero [6]. → End terminations (splices or mechanical hardware) require greater attention than with steel wire rope.	Friction coefficient determination, component testing for splicings and end terminations.
Elongation	Low elongation	Elongates under tension, can be elastic or permanent elongation. May require pre-stretching to remove structural elongation. [2]	Component and system testing
Weight	Heavy in relation to fibre ropes.	Light in relation to steel wire rope [2].	No need for testing.
Coating	Uncoated or coated with zinc or other protective coating [8]. Used to enhance corrosion resistance.	Applied to enhance rope properties: for example decrease abrasive wearing and improve UV resistance [6].	Component testing, lifetime testing with hoist and environmental testing.
Lubrication	Needed to reduce friction wearing and provide protection against corrosion [8].	Coating may have lubricating properties but no need for other lubrication.	
Handling	Rigid structure in relation to fibre rope, sharp wire cuts.	Easy to handle due to flexible structure and light weight. Wearing does not produce sharp fibres.	No need for testing.
Contact damage	Loss of material on the surface wires or deformations [9].	Broken fibres or strands on the surface of the rope [2].	Functional testing and rope residual testing.
Deformations like flattening or crushing	Deformations are permanent and lead to uneven stress distribution on that area [9].	Does not affect to load bearing cabability if it is removable by flexing the rope.	Functional testing and rope residual testing.

Cut resistance	Not that prone to cutting as fibre rope.	Susceptible to cutting when under tension. Need to be considered in hoist design.[2]	Functional testing and rope residual testing.

Environmental factors may have different effect on steel wire rope and fibre rope. **Table 2** has summary of environmental factors that are relevant in crane application and the differences between steel wire rope and fibre rope. In addition, reliability verification needs are listed.

Table 2: Differences in rope environmental resistance and the effect on reliability verification

Environmental factor	**Steel wire rope** 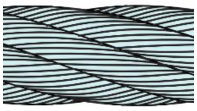	**Fibre rope** 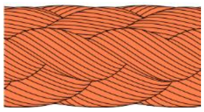	**Reliability verification** 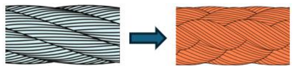
High temperature	Depends on the exposure time. Stranded ropes with steel core can be used up to 200 °C but working load limit reduction needed. High temperatures may weaken lubrication.[12]	Change in material properties, (decreased strength, increased creep etc.), when operating over limiting temperature for long period of time. Limiting temperature depends on fibre. For example for HMPE fibre long term exposure should not exceed 50 °C. [6] Short term high temperature exposure may cause melting of the fibres and decrease in strength [2].	Environmental testing
Low temperature	Service conditions as low as -40 °C possible without working load limit reduction. May weaken lubrication. [12]	Good performance if the fibre does not absorb water. Aramids do absorb water but HMPE and LCP fibres do not. [6]	Environmental testing
Humidity	Causes corrosion [9].	Good corrosion resistance. May absorb water depending on the fibre. [6]	Environmental testing
Exposure to UV	No effect	May damage fibres. Strength reduction is more critical with small ropes since UV penetrates only small depths. UV resistance can be improved by coating. [6]	Environmental testing
Chemicals	Chemicals which accelerate corrosion are harmful [9].	Chemicals used in cranes can have harmful effect on fibre rope [2].	Environmental testing
Abrasive particles	Increase wearing. Wearing depends on the nature and size of abrasive particles. [9]	Increase wearing. Wearing depends on the nature and size of abrasive particles and may be different between wet or dry conditions. Abrasive wearing can be decreased by coating. [6]	Functional testing

5 Conclusions

Usage of any kind of a rope subjects it to wear by bending, torque, tension and environmental factors. The type of damage that leads to failure is dependent on the fibres, rope construction, usage and environmetal conditions. Failure mechanisms and modes of fibre ropes should be known when they are considered as a substitutional for steel wire ropes.

Hoist design needs to be suitable for fibre rope. Materials of the reeving components, quality of surface finishing, rope groove profiles and fleet angles caused by the reeving have an effect to the rope lifetime. In addition, attaching of the rope requires special attention.

Knowing the properties, wearing mechanisms and the lifetime of the rope are essential factors when selecting the rope. Knowledge can be gained to some extend by material study. It helps to understand the differences between steel wire ropes and fibre ropes, and focus testing to the right things. Testing is needed to verify how the rope actually works in some specific application or conditions.

6 References

[1] ISO 4306-1, 2007. Cranes — Vocabulary — Part 1: General, SFS Finnish Standards, Helsinki, Finland.

[2] ISO/TS 23624, 2021. Cranes — Safe use of high-performance fibre ropes in crane applications, SFS Finnish Standards, Helsinki, Finland.

[3] O'Connor, P. and Kleyner, A., 2012. Practical Reliability Engineering, 5th Edition. Chichester, United Kingdom: John Wiley & Sons.

[4] EN 14492-2, 2019. Cranes. Power driven winches and hoists. Part 2 : Power driven hoists, SFS Finnish Standards, Helsinki, Finland.

[5] SFS-EN 13135:2013 + A1, 2018. Cranes. Safety. Design. Requirements for equipment, SFS Finnish Standards, Helsinki, Finland.

[6] McKenna, H. A., Hearle, J. W. S. and O'Hear, N., 2004. Handbook of fibre rope technology. Cambridge, England: Woodhead Publishing Limited in association with The Textile Institute.

[7] William D. and Callister, Jr., 2007. Materials science and engineering: an introduction, 7th Edition. New York, United States of America: John Wiley & Sons.

[8] EN 12385-2 +A1, 2008. Steel wire ropes. Safety. Part 2: Definitions, designation and classification, SFS Finnish Standards, Helsinki, Finland.

[9] ISO 4309, 2021. Cranes — Wire ropes — Care and maintenance, inspection and discard, SFS Finnish Standards, Helsinki, Finland.

[10] Verreet R., 2018. The rotation characteristics of steel wire ropes. Wire Rope Technology Aachen, Germany.

[11] ISO 9554, 2019. Fibre ropes — General specifications, SFS Finnish Standards, Helsinki, Finland.

[12] EN 12385-3 +A1, 2020. Steel wire ropes. Safety. Part 3: Information for use and maintenance, SFS Finnish Standards, Helsinki, Finland.

7 Authors' Introductions

Mrs Piia Koskenjoki received her M.Sc. degree in Materials Engineering from Tampere University of Technology, Finland in 2014. She started her professional career as a Reliability Engineer at Konecranes Global corporation in 2014, and has worked with testing and reliability verification of different materials and ropes. Her research interests are in reliability of steel wire ropes and fibre ropes.

Mrs Kirsi Saarinen-Pulli received her M.Sc. and Ph.D. degrees in Electronics from Tampere University of Technology, Finland in 2007 and 2012, respectively. She worked as a researcher in the field of electronics reliability in Tampere University of Technology for 5 years. Currently she is Head of Reliability Engineering in Konecranes Global corporation where she has worked for the last 12 years. Her research interests include Design for Reliability, reliability analytics and reliability verification. She has authored more than 30 papers in peer-reviewed scientific journals and conferences

Fiber-reinforced steel wires for rope applications in the high-performance sector

Stefan Hecht, Wendel Frick

University of Stuttgart, IFT, Germany

Jan Ferino, Andrea Meleddu

Astarte Strategies SRL, Italy

Muhammad Najih Amin

Teufelberger Redaelli, Italy

Summary

The development and verification testing of an innovative type of carbon fibers reinforced steel wire rope was the objective of the consortium of research and industry in the Framework of the FIRST-WIRE project. The project was co-funded by the Research Fund for Coal and Steel, an EU programme supporting research projects in the coal and steel industries. The aim was to design a lightweight yet resistant structural rope/cable element for demanding onshore/offshore application such as mooring lines for offshore platforms or cable stayed bridges. In the present paper the hybrid concept is discussed and results from a dedicated full-scale test program presented. Results suggest that hybrid exhibits a good resistance and strength-to-weight ratio, when compared to traditional full steel solutions. On the other hand, cable terminations appear to be critical regions to exploit the full potential of the hybrid solutions.

Keywords: hybrid rope, carbon fiber hybrid wire, rope, testing

1 Introduction

In the wire ropes market, the high performance-to-weight ratio of steel ropes presents significant challenges for onshore/offshore applications such as mooring lines for offshore platforms, lifting equipment for deep sea mining operations or cable stayed bridges/large-scale guyed structures. Conventional steel wire ropes are successfully adopted in those scenarios. As mooring lines (e.g.: for floating platforms) steel ropes demonstrate robust strength properties and superior elastic rigidity, while extension and hysteresis do not pose significant issues. However, they are prone to corrosion, and their inherent mass presents constraints for extended spans in deep-sea applications. Currently the self-weight of conventional high-performance steel ropes represents a limitation in the achievement of deep-sea levels for lifting offshore application. For most of the world leading operators, this limit is of ~2,000 m and the resulting payload reduction may easily achieve a half of the initial load.

In civil applications, steel ropes and cables are mainly used for suspension bridges, cable stayed bridges, arch bridges, roof structures, and Ferris wheels. For these applications in addition to the cable sag effect which can be dominant and can significantly reduce the stiffness of the cable, the dynamic interaction with the structure is of paramount importance given the earthquake resistance requirements. Also, corrosion issues due to marine exposure and fatigue due to repeated service loading can be a limitation. This has led to a surge in the use of fiber-reinforced plastics (FRP), carbon-reinforced polymers (CFRP), and synthetic fibers across various applications, traditionally dominated by steel. While FRP and CFRP offer excellent mechanical properties like tensile strength and stiffness and fatigue, synthetic fibers struggle with wear, heat resistance [1] and UV/weather exposure [2], sometimes limiting their use.

Tentative of hybridization of steel and CFRP materials can be found in the works [3] and [4], where the hybridization consists in the simultaneous adoption of steel wires and CFRP wires to form lighter rope structures.

In the frame of the EU RFCS founding programme, the FIRST-WIRE project [5] aimed at developing a steel & carbon fiber hybrid wire for ropes and cables with improved performances and reduced weight. This paper describes the hybrid wire concept developed and results from the testing campaign performed to characterize the product. Results obtained have shown that high performance lightweight wire and ropes can be obtained, fully validating the hybrid concept, while some further research should be performed to improve terminations and socketing.

2 Application use-cases and corresponding selection of full-scale test setups

As exemplary use-cases, three applications were chosen in the scope of the FIRST-WIRE project. The three assessed use-cases are shown in **Figure 1**.

Figure 1: Exemplary use-case applications assessed in the FIRST-WIRE project, Offshore wind (left), bridge construction (center), deep-sea lifting (right)

Each of the exemplary applications would benefit of a hybrid rope design with decreased net mass by e.g.

- smaller rope diameters due to lower net mass and/or longer ropes with same diameter at same design factor (in relation to MBL) **for offshore wind**,
- lighter structures, longer rope span at same reaction force to the structure or smaller diameter ropes and lower reaction force to the structures for same rope span **for cable-stayed bridges,**
- higher payload when working in deep-sea, higher operation range into the deep see, less inertia in heave compensation, less total mass on the winch **for deep-sea lifting**.

As a typical example, one rope geometry has been manufactured and tested for each use-case: A 19x7 low-rotating rope typically used as running rope on cranes or e.g. deep off-shore applications, an open strand spiral (OSS) typically adopted as mooring lines in offshore platforms, and fully locked coil (FLC) typical used in static applications, such as cable-stayed bridges and as track rope in cableways. The three types are shown in **Figure 2**. The FLC rope features the same OSS geometry for its core and includes two additional layers of Z-shaped wires. The OSS rope consists of 61 hybrid (steel+carbon fibers) wires, while Z shaped C82 steel wires have been obtained from rolling process preceded by cold drawing.

Figure 2: Hybrid rope geometries: Open spiral strand rope OSS (left), Fully locked coil rope FLC (center), 19x7 rotation resistant rope (right)

Each rope type was additionally as reference also manufactured as conventional rope featuring only steel wires in the same diameters.

For each of the above-mentioned rope type, a specific test plan for full-scale testing was established depending on the expected applications and its certain characteristics. The conducted types of test for each rope type can be found in **Table 1**.

Table 1: Tests per each rope type

Test Type	**Rope Type**
Breaking load	all rope types
Bending fatigue	non-rotating ropes
E-modulus / Diameter vs. load	all rope types
Torque / rotation	all rope types
Axial fatigue (tension tension)	spiral and full-locked coil
Long term (relaxation)	full-locked coil

3 Manufacturing and testing of hybrid wires

The novel idea involves a stainless-steel mantel (with a diameter ranging from 3-5 mm and a thickness of 0.3-1.0 mm) that encases a core made of high-performance fibers. A diagram illustrating this new steel-fiber hybrid wire concept can be found in **Figure 3** [6]. The ultimate effectiveness of the wire is determined by both the steel and the fiber components, impacting not just the cross-sectional area but also heavily depending on the materials' specific attributes. Through careful choice of both the mantle and the core fiber materials, optimal mechanical strength and corrosion resistance is ensured.

Figure 3: Hybrid wire samples

The hybrid wires were by the company Cunova GmbH (Germany) manufactured by means of rolling process to form the outer tube with a longitudinal seam weld by means of by both TIG and laser technique. The fiber cores were introduced inside the U-shaped stainless strip during rolling and before the final tube closing by means of the longitudinal welding. A final calibration step was applied after welding to roll the tube diameter down to the target size, thus ensuring a tight interaction and a high grip between the outer tube and the fibrous core.

The hybrid wires were tested on their mechanical and galvanic corrosion properties by the University of Padua in Italy (Università degli Studi Di Padova, Departimento di Ingegneria Industriale). Static tensile tests were performed on empty tubes, fiber bundles and hybrid wires to determine mechanical properties of the base materials and of the composite wire. **Figure 4** shows an exemplary tensile test on a hybrid wire in a specially optimized clamp holder to ensure equal loading of the stainless-steel tube and the fibre bundle.

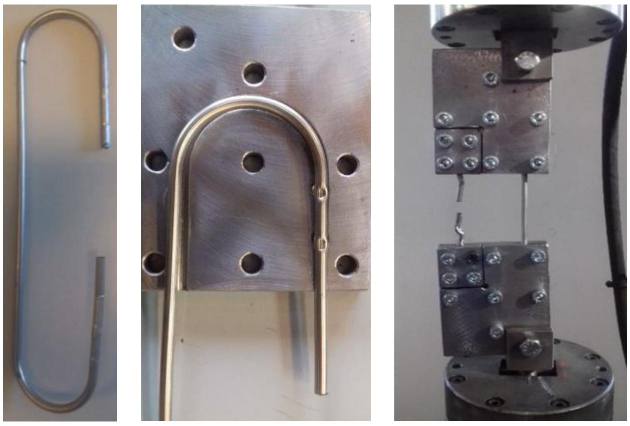

Figure 4: Hybrid wire specimen (left), clamping system for the hybrid wire (middle), tensile test setup (right)

The results of the tensile tests, performed on Ø 5.16 mm wires of diameter are reported in **Figure 5**. The initial length of the samples was 250 mm for the hybrid wires. The tests were performed at 1 mm/min rate. From the reported results the combination of the fibers and of the stainless-steel tube allows obtaining a hybrid wire characterized by high tensile strength and good elongation. The tensile strength calculated on the wire external area is about 1,200-1,400 MPa.

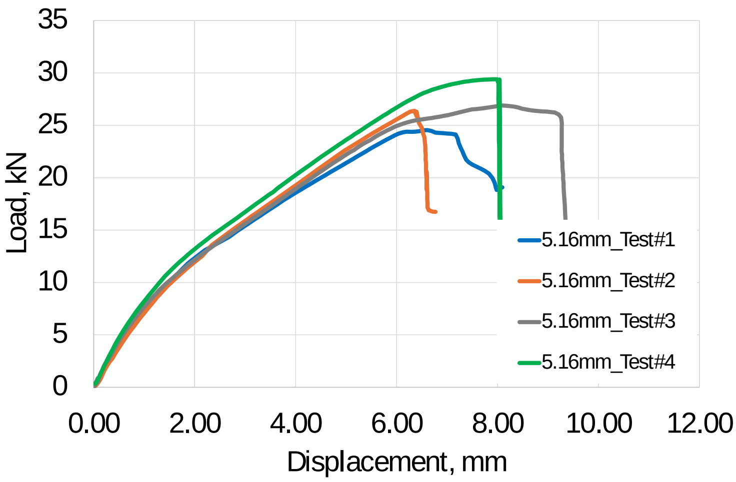

Figure 5: Tensile test results on hybrid wires

The mechanical interaction between the bundle and the stainless-steel tube was investigated to evaluate the adhesion strength between the tube and the fibers. Pull-out tests were performed on hybrid wires with 5.16 mm of diameter. A 50 mm specimen was circumferentially etched for the full depth of the steel cladding so that the two half-tubes are pulled apart by sliding over the carbon fiber core. The test showed that, after a first ramp, shear stress approaches a plateau of about 4 MPa, which then decays at the end of the test as the residual length of fiber-tube interaction becomes negligible. The result is very interesting because it shows that although no specific treatment was applied to the fiber-pipe interface, the frictional force required to extract the fibers is high enough to ensure good synergy of both components within the composite wire.

The interaction between the fibers and the stainless-steel tube was studied both from the corrosion point of view, to study the possible occurrence of galvanic corrosion, and from the mechanical point of view. The value of stabilization of the circulating current density resulted $4{,}26 \cdot 10^{-7}$ A/cm^2, thus indicating very low corrosion rates and excluding possible technological problems related to galvanic corrosion. This is related to the presence of a polymer layer that impregnates the fibers bundle, preventing the direct electrical contact between the tube and the carbon fibers.

4 Full-scale testing of hybrid ropes vs. conventional ropes

<u>Breaking load tests</u>

The breaking load tests were conducted directly after rope production on a tensile testing machine with a maximum load capacity of 3,000 kN by Redaelli. The breaking load tests on the FLC type rope were expected to exceed 3,000 kN and therefore were conducted under the authority of Redaelli at an external laboratory LATIF (Laboratorio Tecnologico Impianti a Fune) based in Ravina di Trento, Italy. The tests were conducted following the standard EN 12385-1.

The test setup for the breaking load tests can be seen in **Figure 6**.

Figure 6: Test setup for tensile tests at Redaelli (left), 19x7 before and after breaking load test (right)

The aim for the tensile properties of the hybrid ropes was to rank about equal in tensile strength as the conventional full steel wire ropes. **Table 2** shows the results of the breaking load tests.

The MBL of the hybrid rope types as shown in Table 2 was calculated based on the single wire tensile properties. The deviation shown between different test could come from mainly the different condition of the end terminations. To be considered as well that during the manufacturing of the hybrid wires (and ropes successively), some welding defects are found on the wires. This defect can lead to the decrease of the breaking load of single wires, and successively on the rope. In the tests not only the actual value is recorded, also the load-displacement curve is generated and the final rope condition is assessed.

Table 2: Calculated MBL and determined ABL for all rope types

Rope Type	Conventional Rope			Hybrid Rope		
	MBL (kN)	Actual Breaking Load (kN)	Test Result	MBL (kN)	Actual Breaking Load (kN)	Test Result
19 x 7	1,632	1,830	OK	1,648	1,020	Core failure
		1,830	OK		1,070	Core failure
		1,830	OK		930	Failure close to socket
OSS	1,191	1,180	Early rupture inside resin	1,024	334	Wire slippage out
		1,310	OK		830	Break of tubes near the resin end
		1,280	OK		824	
FLC	3,675	3,875	OK	3,508	3,626	Break of tubes inside resin end, not visible externally
		3,845	OK		3,537	
		3,854	OK		3,498	

<u>Bending fatigue tests</u>

The Cyclic Bending Over Sheave tests (CBOS) were carried out by University of Stuttgart at the Institute of Mechanical Handling and Logistics (IFT) according to OIPEEC recommendation No. 4 OIPEEC Bulletin 56 (1988). The tests were performed at the bending fatigue machine No. 5 of IFT, shown in **Figure 7**. The bending fatigue machine consists of a driven steel made test sheave and a steel made deflection sheave. In the bending machine, the rope runs over the in relation to the desired rope force S loaded test sheave and performs an oscillating movement with a predetermined stroke. Consequently, during one bending cycle the rope at the bending zone changes from straight to bent and back to straight state, as illustrated in the sketch. The test is completed when the rope or at least one strand is broken.

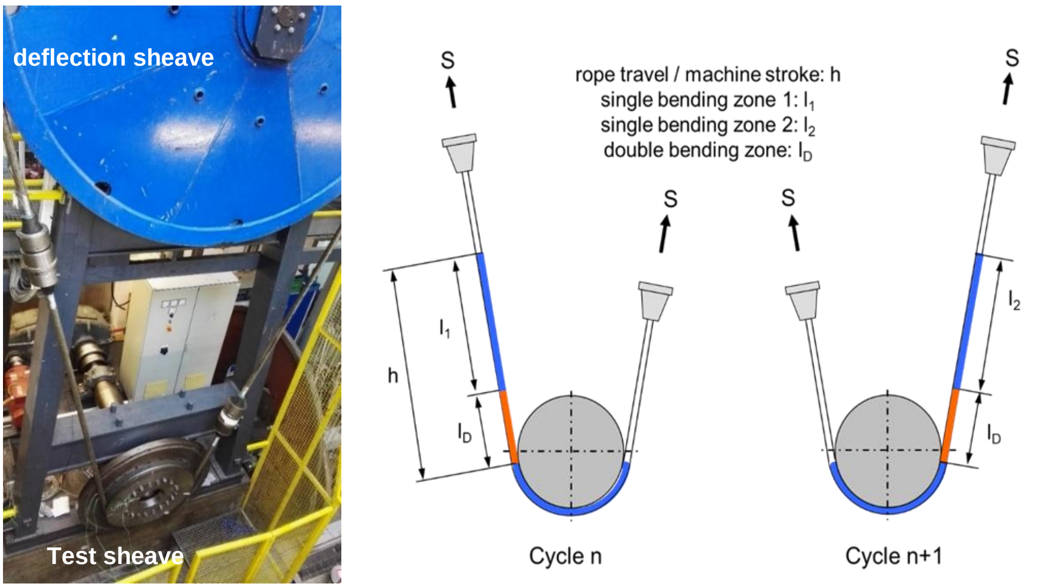

Figure 7: Test setup in bending fatigue machine No. 5 at IFT (left) and illustration of bending zone (right)

The non-rotating rope was tested in CBOS with the parameters listed in **Table 3**. The results in absolute mean number of bending cycles until rope failure is also given in Table 3.

Table 3: Test parameters for CBOS testing and achieved bending cycles

Characteristics	Unit	Conventional rope	Hybrid rope
CBOS test force S	[kN]	451	451
Sheave Diameter D	[mm]	1,040	1,040
Diameter ratio D/d	[-]	20.2	20.2
Sheave material and hardness	[-]	42CrMo4 (HRC60)	42CrMo4 (HRC60)
Type of groove	[-]	round	round
Opening angle γ	[°]	60	60
Groove radius relation r/d	[-]	0.53	0.53
Number of bending cycles reached until discard (ISO 4309)	[-]	12,500	(not covered by standard)
Number of bending cycles reached until rope break	[-]	21,913	9,396

The 19x7 hybrid rope was tested under the same conditions as the conventional steel wire rope. The hybrid rope achieved a total of 9,396 bending cycles until the complete rope break. This means that the hybrid rope has approximately half the lifetime of the conventional rope. It must be taken into account that the hybrid rope was also subjected to a tensile load of 451 kN in the bending test, which corresponds to a percentage actual breaking load of approx. 50 % instead of 28 % compared to the conventional 19x7 rope, as the actual breaking load of the hybrid rope is lower. In this respect, a lower lifetime is not unexpected. This could be explained with the already mentioned welding defects from wire manufacturing which lead the welded tubes to opening in stranding process. The thereby resulting sharp edges inside of the rope could potentially lead to cut damages to the carbon fibre bundles in bending fatigue testing.

<u>E-modulus measurements and diameter vs. load</u>

The rope modulus test was carried out by the IFT according to ISO 12076. The tests were performed on a horizontal tensile testing machine with maximum force of 2,500 kN and calibrated according to ISO 7500-1 Class 1. To record the rope elongation, two wire draw encoders were used. The sensor wire ends were attached to the test rope in the distance of the measuring length *L*, shown in **Figure 8**.

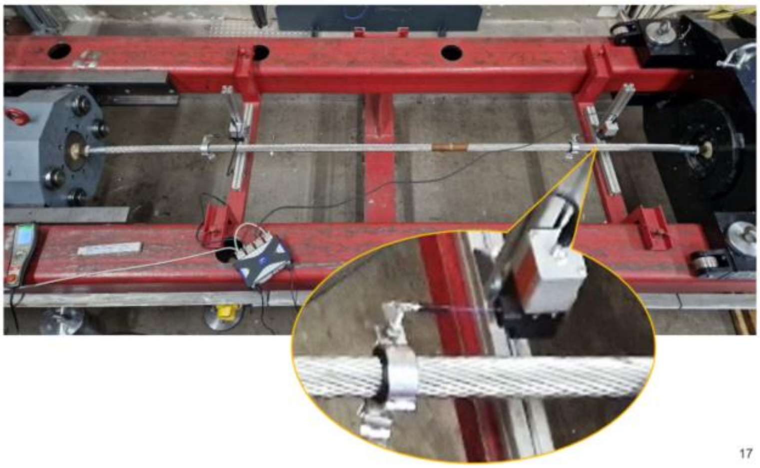

Figure 8: Test setup for rope-modulus and diameter vs. load measurement

The rope modulus was determined as secant modulus between 10 % and 30 % of MBL at the 10th loading. **Table 4** lists the parameters used for measurement of E-Modulus.

Table 4: Test parameters for rope modulus tests and result as secant modulus between 10 % and 30 % of MBL at the 10th loading

Characteristics	Unit	Non rotating		Spiral		Full locked	
Rope construction	-	**FIRST**	**Conv.**	**FIRST**	**Conv.**	**FIRST**	**Conv.**
Nominal diameter d	[mm]	54		41		61	
Minimum breaking load (MBL)	[kN]	1,904		1,405		3,366	
Lower rope force (10 % of MBL) S_{lower}	[kN]	190.4		140.5		336.6	
Upper rope force S_{upper} (30 % of MBL)	[kN]	571.2		421.5		1,009.8	
Loading rate v (0,5 % of MBL / sec)	[kN/sec]	9.52		7.03		16.83	
Rope condition	-	Fully bedded					
Free rope length l	[mm]	2,000		2,000		6,000	
Gauge length L	[mm]	>1,000					
Rope modulus $E_{10\%-30\%}$	[N/mm²]	71,032	93,814	113,667	141,250	144,658	145,351

The rope modulus is not a constant for the rope but is largely dependent on the tensile stresses. The results obtained are shown in **Figure 9** for the respective rope types. The curves have been shifted by 0.2 % each for a better overview.

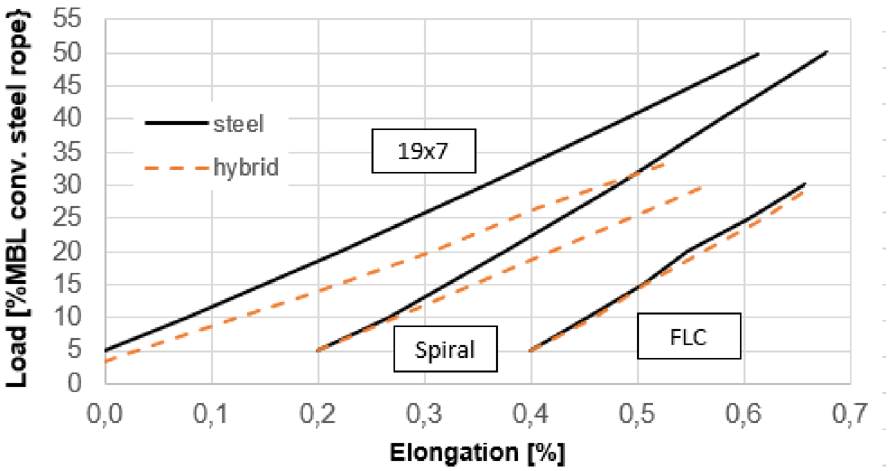

Figure 9: Load-elongation curve for the conventional and the hybrid ropes

The load-elongation behavior differs depending on the rope type. The non-rotating 19x7 shows the greatest elongation. The comparison between hybrid rope and conventional shows similar behavior, especially for the FLC rope construction where the curves are almost congruent. With the spiral rope, the hybrid rope appears to be softer and has a slightly lower modulus.

To determine the behavior of the diameter against the applied load the diameter was measured at two different positions on the rope that are 1,000 mm apart and on each of them in two planes in 90° offset to each other. The obtained results concerning the change in diameter depending on the tensile load are shown in **Figure 10**.

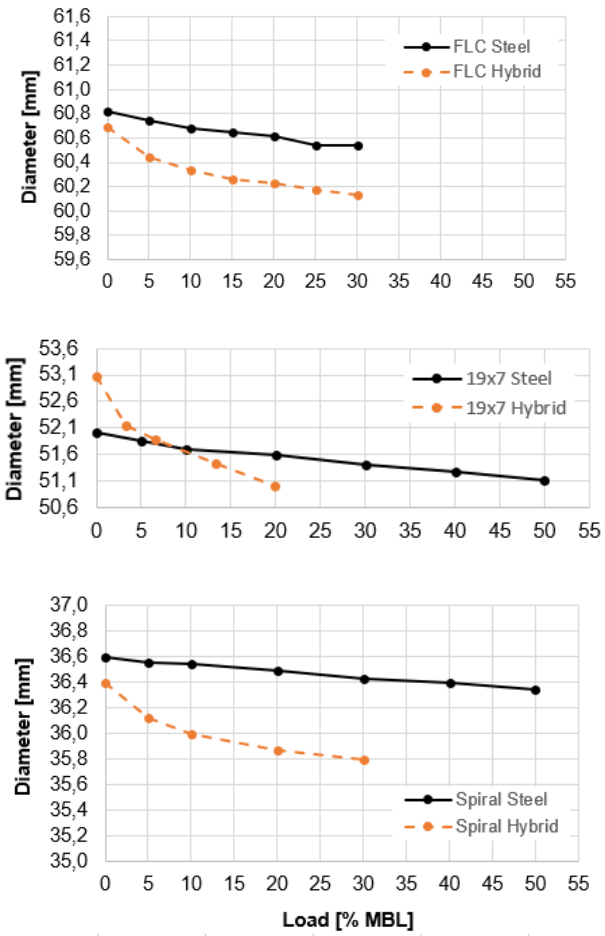

Figure 10: Change in diameter depending on the tensile load for conventional and hybrid rope

It can be found by the diameter measurement results, that the diameters of the hybrid ropes is in general for all three types showing a higher decrease over increasing tensile load.

5 Conclusions

In the framework of the FIRST-WIRE project a hybrid wire was manufactured, tested and included into three different hybrid rope constructions related to three use-case application studies. A test plan was developed for each type of rope and the hybrid ropes were comparatively tested with conventional wire rope of the same construction as a reference.

As an outcome, it could be shown that it is in general possible to manufacture the three ropes reaching very promising results in wire testing and in full scale testing of the corresponding ropes. Challenges arose with slight occasionally occurring defects on the welding seam of the wires which could lead to tear open of the wires under torque in the rope making process. This potentially as one factor lead to lower results in actual breaking load, especially for the OSS and the 19x7 rope type and to lower performance of the 19x7 in bending fatigue testing. An additional factor were challenges to manufacture an end termination for the ropes which sufficiently transfers the tensile loads to the carbon fibre bundle inside of the stainless-steel tube, especially the OSS and the 19x7 with 100 % hybrid wires. Opening of the welding seams of the hybrid wires in the 19x7 potentially lead to the significant lower lifetime in bending fatigue testing due to sharp edges inside of the rope and cutting effects to the carbon fibre bundles. Also, here it has to be kept in mind that the 19x7 rope was comparatively tested to the conventional steel wire rope under the same tensile load. Not considering the lower actual tensile strength in testing.

In general, it could be shown that manufacturing and usage of the new hybrid rope concept is possible and has potential for the assessed use-case scenarios. Further investigation has to be done on the manufacturing process of the wire and the rope and on an optimized end termination which can be expected to allow significantly better performance of the ropes, especially OSS and 19x7 in tensile testing.

6 Acknowledgements

This research was co-funded by European Union in the frame of the Research Fund for Coal and Steel - RFCS programme. Project-number 899299.

7 References

[1] López, C., Firmo, J.P., Correia, J.R., Tiago, (2013), C. Fire protection systems for reinforced concrete slabs strengthened with CFRP laminates. Constr. Build. Mater., 47, 324–333

[2] Shi, Z.; Zou, C.; Zhou, F.; Zhao, J., (2022), Analysis of the Mechanical Properties and Damage Mechanism of Carbon Fiber/Epoxy Composites under UV Aging. Materials 2022, 15, 2919. https://doi.org/10.3390/ma15082919

[3] Xiong, W, Cai, C.S., Xiao, R., Deng, L. (2011). Concept and analysis of stay cables with a CFRP and steel composite section. KSCE Journal of Civil Engineering. 16. 10.1007/s12205-012-1152-1.

[4] Cai, H., Aref A.J., (2015), On the design and optimization of hybrid carbon fiber reinforced polymer-steel cable system for cable-stayed bridges. Composites Part B: Engineering, Volume 68,2015, Pages 146-152, ISSN 1359-8368

[5] https://firstwire.eu/

[6] Redaelli Patent WO 2013/065074 A1: Composite Wire with Protective External Metallic Mantle and Internal Fiber

8 Authors' Introductions

Dipl.-Ing. Stefan Hecht is a mechanical engineer and head of the department "Rope Technology" of the Institute of Mechanical Handling and Logistics (IFT) of the University of Stuttgart. He is active in testing, research and standardization of fibre ropes, steel wire ropes and PPE against fall from height. He is Member of the OIPEEC Management Committee and member of EUROCORD, EWRIS and several national and international standardization committees in different fields of rope application.

Wendel Frick M.Sc. is a mechanical engineer specializing in production and materials engineering. He completed his Master's degree in 2015 and subsequently joined the Institute of Mechanical Handling and Logistics (IFT) of University of Stuttgart as a research assistant and doctoral student. He has been Head of Destructive Rope Testing there since 2022. His research primarily focuses on two key areas: the fatigue behavior of high-strength steel and fiber ropes, and the development of appropriate discard criteria.

Ing. Jan Ferino is a mechanical engineer specializing in Finite Element Analysis (FEA), industrial plant modeling, machining processes, and structural dynamics. From 2005 to 2015, he worked at RINA Consulting SpA (formerly Centro Sviluppo Materiali SpA) as a researcher in the Oil & Gas sector. In 2015, he co-founded Astarte Strategies Srl, an engineering consultancy focused on R&D for industrial innovation. He contributed to European projects on steel industry innovation and participated in coordinating First Wire, a co-funded by RFCS, a EU programme supporting research projects in the coal and steel sectors.

Ing. Andrea Meleddu is a mechanical engineer with expertise in structural integrity, fluid dynamics, materials science, and experimental testing. From 2004 to 2015, he worked at RINA Consulting SpA (formerly Centro Sviluppo Materiali SpA), focusing on engineering research and development for Oil&Gas. In 2015, he co-founded Astarte Strategies Srl, where he now serves as Technical Manager, overseeing technical planning and coordination. He has contributed to several European research initiatives and coordinated of the First Wire project, co-funded by RFCS, a EU programme supporting research in the coal and steel sectors.

Muhammad Najih Amin received his MSc degree in Materials Engineering and Nanotechnology from Politecnico di Milano (Italy) in 2018. He began his professional journey as an intern with the R&D team at Redaelli Tecna SPA in 2018. A year later, he transitioned to the role of R&D Engineer, and in 2025, he was promoted to R&D Team Lead, a position he currently holds. His research interests primarily focus on technological advancements in continuous rope monitoring and product development for applications in people transportation.

Finite Element simulation for investigating the performance of standard and hybrid steel-carbon wire ropes

Jan Ferino, Andrea Meleddu

Astarte Strategies SRL, Italy

Stefan Hecht, Wendel Frick

University of Stuttgart, IFT, Germany

Muhammad Najih Amin

Teufelberger-Redaelli, Italy

Summary

This paper presents an innovative carbon fiber-reinforced steel wire rope developed within the FIRST-WIRE project, funded by the EU Research Fund for Coal and Steel. The objective is to design lightweight/highly resistant structural cables suitable for demanding applications, including mooring lines for offshore platforms and cable-stayed bridges. This study introduces the hybrid rope concept, combining high-performance carbon fibers within a stainless-steel outer mantle to achieve enhanced mechanical properties and reduced weight. Two rope configurations were analyzed: Ø 36mm Open Strand Spiral rope (OSS) and Ø 60mm Fully Locked Coil rope (FLC). Both conventional steel and hybrid ropes were subjected to extensive full-scale testing to assess their tensile performance. Experimental results indicate that hybrid ropes demonstrate favorable strength and stiffness-to-weight ratios compared to traditional full-steel ropes. The hybrid wires exhibited a characteristic nonlinear stress-strain behavior, resulting from the combined mechanical properties of the carbon fiber core and stainless-steel sheath. Elastic moduli measured ranged between 110-155 GPa, confirming efficient structural performance. Finite element (FE) simulations conducted showed strong correlation with experimental findings, validating the numerical approach and material modeling choices. The analyses identified a nonlinear stress-strain response for the hybrid wires attributed to interactions between the steel tube and carbon fiber bundle. In summary, the developed hybrid ropes offer enhanced performance, including increased strength-to-weight efficiency, essential for advanced onshore and offshore structural applications. However, additional research is necessary to optimize cable-end connections to maximize the potential of these hybrid solutions.

Keywords: Steel-carbon fiber hybrid wire, Steel Wire Rope, Full-Scale Testing, Numerical Simulations.

1 Introduction

In the wire rope industry, the high performance-to-weight ratio of steel ropes presents critical challenges in demanding applications such as offshore platform mooring lines, deep-sea lifting operations, and structural elements of cable-stayed bridges. Traditional steel ropes are extensively utilized due to their high strength and stiffness, low extension, and minimal hysteresis. However, limitations including susceptibility to corrosion and significant self-weight restrict their effectiveness, especially in deep-sea operations exceeding 2,000 meters, where payload capacity can be substantially reduced. In civil engineering applications, steel ropes are integral to suspension and cable-stayed bridges, arch structures and others. These applications face additional concerns, notably cable sag effects significantly affecting stiffness and dynamic interactions with structural frameworks, particularly under seismic conditions. Corrosion from marine exposure and fatigue resulting from cyclic loading further limit steel rope performance. Consequently, there has been increasing adoption of alternative materials such as fiber-reinforced plastics (FRP), carbon fiber-reinforced polymers (CFRP), and synthetic fibers. While FRP and CFRP exhibit superior tensile strength, stiffness, and fatigue resistance, synthetic fibers often display limitations related to abrasion, thermal stability, and environmental degradation under UV exposure [1] [2]. Recent research explores hybrid ropes combining steel and CFRP wires to achieve reduced weight with preserved structural integrity [3] [4]. Within the EU Research Fund for Coal and Steel (RFCS) funded FIRST-WIRE project [5]. This hybridization concept has been further developed to create an advanced steel-carbon fiber composite wire rope, demonstrating improved performance and weight efficiency. The current paper outlines the hybrid rope concept and presents results from comprehensive experimental characterization. Findings validate the potential of these innovative hybrid ropes, as the demonstrated performance-to-weight ratios make them competitive to traditional full-steel solutions. Nonetheless, further optimization of cable terminations and connection systems remains necessary for fully realizing the advantages of hybrid rope technologies.

2 Hybrid wire concept and manufacturing process

The innovative hybrid wire concept discussed herein involves a stainless-steel outer tube, ranging in diameter from 3 to 5 mm and wall thickness from 0.3 to 1.0 mm, encapsulating a high-performance fiber core, as illustrated in **Figure 1**. This novel concept, currently under patent consideration by Redaelli [6] integrates steel and fiber materials to optimize mechanical strength, stiffness, and corrosion resistance.

Figure 1: Hybrid wire concept (left) carbon fibre core bundles (right)

The manufacturing process employed a rolling method to form an outer stainless-steel tube with a longitudinal seam weld, executed using both TIG and laser welding techniques. The fiber cores were placed inside the steel tube during the rolling phase, preceding the final closure and welding steps. A subsequent calibration stage reduced the tube diameter to the desired dimensions, enhancing the mechanical bond between the steel mantle and the fiber core. The tube was fabricated from a corrosion-resistant stainless steel (VDM ALLOY 926, 1.4529/UNS N0896), specifically chosen to protect the enclosed fiber core from environmental degradation. A significant challenge in the production phase was selecting an optimal fiber core material and supply form. Carbon fibers were ultimately selected due to their superior modulus and tensile strength relative to glass or aramid fibers. High-strength Hyosung carbon fiber tows H2550 (12k/24k) [7] were chosen owing to their favorable balance between mechanical properties and the flexibility required for reeling, stranding, and rope closing processes. Initially considered pultruded carbon bars exhibited good mechanical stability but insufficient flexibility for practical manufacturing needs involving spool handling, stranding, and rope assembly. Additionally, the higher cost of pultruded bars limited their practical application. Conversely, untwisted fiber tows presented insertion and welding interference issues during tube rolling. To address these challenges, carbon fiber tows were lightly twisted (28 turns per meter) to form cohesive bundles, maintaining stiffness (~140 GPa modulus) and achieving tensile strength around 2000 MPa. Additionally, these fiber bundles were coated with a polymer layer serving as a dielectric barrier to mitigate galvanic corrosion risks at the carbon-steel interface.

Two rope types were produced and analysed: open strand spiral (OSS) and fully locked coil (FLC). Both standard and hybrid configurations were tested (**Figure 2**). Standard ropes were made from steel wires drawn from 9.5 mm rods to diameters of Ø 5.47 mm and Ø 5.16 mm, achieving tensile strengths of 1,703 MPa and 1,798 MPa, respectively. FLC ropes included two outer layers of 6 mm Z-shaped wires, achieving a strength of 1,694 MPa. Hybrid ropes differed by utilizing 0.4 mm thick steel tubes internally reinforced with carbon fiber bundles, replacing standard core wires.

Figure 2: Samples of ropes produced for testing. From left to right: OSS, FLC and detail of Z-shaped wires

3 Laboratory testing

3.1 Testing of hybrid wires

Tensile tests conducted on carbon fiber bundles revealed a tensile strength of approximately 1,600 MPa. Cyclic loading experiments, depicted in **Figure 3** (left), confirmed a stable elastic modulus of 140 GPa for longitudinal deformations up to 1 %, following an initial fiber settlement phase. Additionally, Figure 3 (right) illustrates the tensile response of a hollow 6 Mo stainless-steel tube (5.16 mm × 0.4 mm), utilized in hybrid wire manufacturing. Hybrid wires with diameters of Ø 5.16 mm and Ø 3.51 mm exhibited tensile strengths of approximately 1,430 MPa and 1,650 MPa, respectively. A distinct nonlinear stress-strain behavior emerged, characterized by dual elastic moduli: approximately 150 GPa and 75 GPa. This nonlinearity results from the combined mechanical contributions of the stainless-steel outer tube, exhibiting nonlinear behavior, and the carbon fiber core, which has a quasi-linear response.

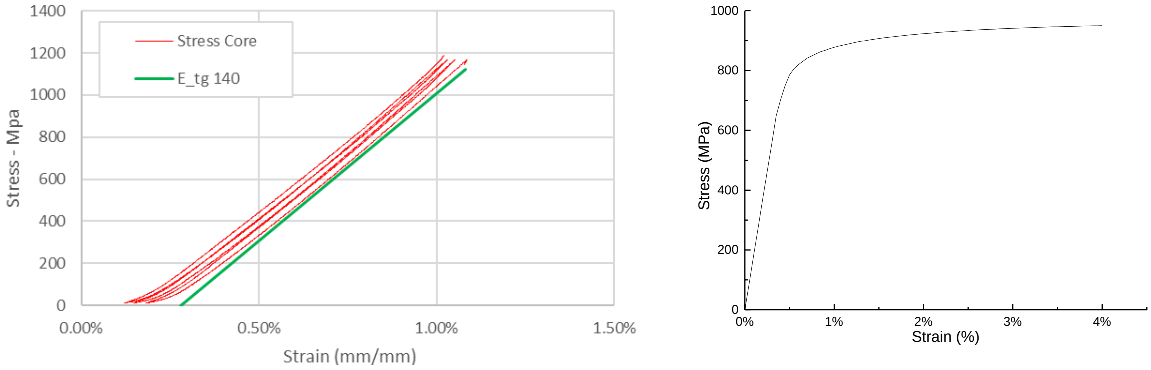

Figure 3: Carbon bundle stress-strain response under cyclic loading (left), 6Mo stainless steel tube Ø 5.16 mm x 0.4 mm tensile response (right).

The carbon fiber core, constructed from lightly twisted fiber bundles, was coated with a polymer layer serving as a dielectric barrier against galvanic corrosion. The carbon fiber bundle configuration yielded a tensile strength of around 2,000 MPa and an elastic modulus of approximately 140 GPa. Pull-out tests further demonstrated substantial adhesion between steel and fiber cores, achieving tangential frictional stress around 8 MPa. This frictional interaction ensured a coherent deformation response between both materials, effectively allowing the hybrid wire to behave as a homogeneous structural component after initial settlement.

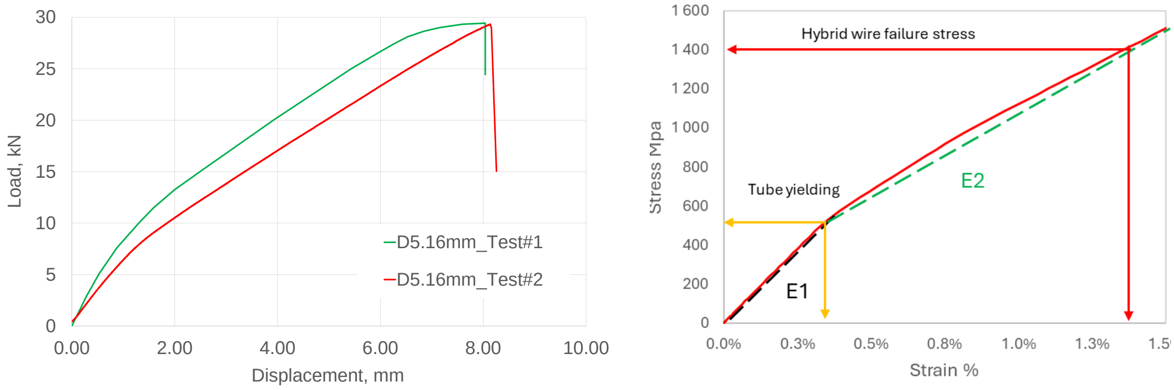

Figure 4: Hybrid wires: tensile tests results(left), Typical stress strain diagram (right).

3.2 Full scale testing of ropes

Experiments were conducted by Redaelli-Teufelberger and by the Institute of Mechanical Handling and Logistics, University of Stuttgart. **Figure 5** illustrates a horizontal frame tensile testing apparatus employed.

Figure 5: Tensile test apparatus in Redaelli (left) and in University of Stuttgart (right).

Rope elongation measurements utilized wire drawing encoders, while torque evaluation involved a twisting device adjustable in 1-degree increments and strain gauges mounted on a shaft for torque measurement. Three main characteristics are tested and compared: tensile strength, E-modulus, torque-rotation. Tensile breaking force results are summarized in **Table 1**, confirming that all specimens successfully exceed the minimum required qualification tensile loads, more details of the test results will be presented in the next sections.

Table 1: Full-steel and hybrid ropes tensile properties resulting from tensile testing

Rope Design	Conventional Rope				Hybrid Rope			
	MBL (kN)	**ABL (kN)**	**E (GPa)**	**Linear mass (kg/m)**	**MBL (kN)**	**ABL (kN)**	**E (GPa)**	**Linear mass (kg/m)**
Open Spiral Strands (OSS)	1,191	1,180	140	6.5	1,024	334	114	3.0
		1,310				830		
		1,280				824		
Full Locked Coil (FLC)	3,675	3,875	145	20.2	3,508	3,626	136	16.7
		3,845				3,537		
		3,854				3,498		

**Note: MBL: Minimum Breaking Load, ABL: Actual Breaking Load*

4 FE modeling: development and comparison with experimental results

Numerical simulations of the OSS and hybrid FLC ropes were performed using the commercial software Abaqus [11]. The finite element model consisted of a rope segment with a length equal to six rope diameters, as depicted in **Figure 6.** Both hybrid and full-steel configurations were modelled using identical geometries, differing uniquely in material properties. Wires were represented using 3D solid elements (type C3D8) and described through experimentally derived elastic-plastic stress-strain curves. Each hybrid wire comprised distinct regions to simulate the fiber bundle core and stainless-steel outer tube, ensuring accurate representation of the observed integral deformation behavior due to strong frictional bonding. Inter-wire frictional contact was modelled using a Coulomb friction coefficient of 0.1. To efficiently handle complex contact interactions, an explicit solution scheme was adopted. Mass scaling was applied to maintain computational feasibility, validated through sensitivity analysis to minimize kinetic energy disturbance effect. Boundary conditions, applied through kinematic constraints at strand ends connected to reference points, are summarized in **Table 2**.

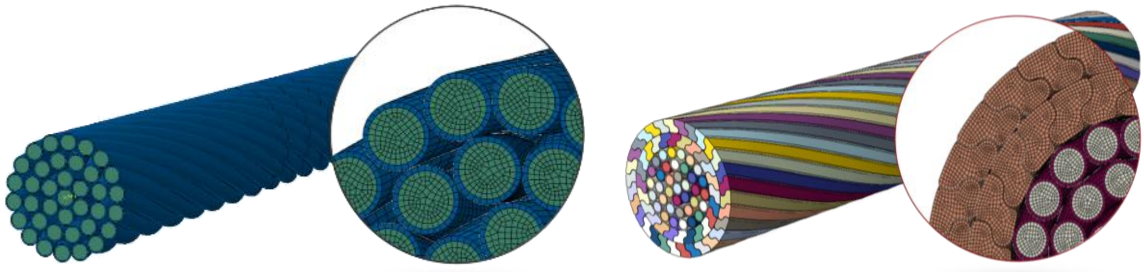

Figure 6: Finite element model mesh for the hybrid ropes: OSS (left), FLC (right)

Table 2 Applied boundary conditions in the simulations.

Test configuration	End #1	End #2
Tensile	fixed rotations + applied displacements (monotonical)	fixed rotations + fixed displacements
E modulus	fixed rotations + applied cyclic displacements (monotonical)	fixed rotations + fixed displacements
Torque rotation	1-aplied rotations 2- applied displacement	fixed rotations + fixed displacements

4.1 FEA modeling of hybrid wire strands

Finite Element (FE) model validation for ropes was conducted through two stages: initial benchmarking against literature data and subsequent comparison with experimental results from this study. The preliminary validation involved modeling a single 1x7 steel strand subjected to tensile loading with fixed rotational constraints at its ends. Under these conditions, the strand exhibited axial displacement and generated torque at the fixed end. Numerical simulations were compared with established analytical models, specifically the Costello model [8] and the Foti and Martinelli model [9]. Figure 7 demonstrates that simulated force and torque stiffness closely matched analytical predictions. Since analytical models were limited to elastic responses, an additional elastic-plastic FE model was developed and compared with experimental data from Jang [10], again demonstrating strong agreement, confirming the accuracy of the FE modeling approach across both elastic and plastic deformation regimes.

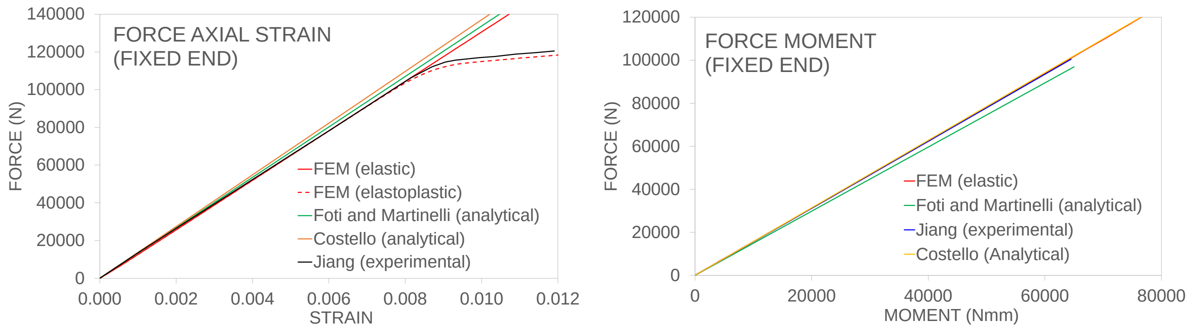

Figure 7: Experimental, analytical and numerical predictions of strand behaviour under axial and torsional loading.

4.2 FEA modeling of standard steel and hybrid ropes

Once applied and validated to the single strand, the upgraded FE model is adopted to simulate the full-scale tests conducted under different loading conditions. A comparison of the experimental and numerical results for both standard steel and hybrid ropes is shown in **Figure 8**. It has been observed that steel ropes typically exhibit a failure mechanism involving the plastic collapse of individual strands (necking), which subsequently leads to a reduction in load following the onset of necking. This phenomenon is evident in the diagrams for OSS and FLC ropes depicted in Figure 8. In the case of hybrid material ropes, the OSS rope, Figure 8 (left) demonstrates linear behavior up to failure, attributable to the plasticity-free behavior of the carbon fibers. The contribution of the steel tube is nonlinear elastic-plastic, accounting for approximately 28 % of the total resistant section. Past yielding contributes marginally to strength increase. Furthermore, it is observed that the failure of the hybrid ropes is influenced to some extent by the gripping system in the terminations. This is a matter of concern, as it has not yet been fully resolved and has hindered the full potential of the rope from being realized. Hybrid and steel FLC ropes are compared in Figure 8 (right), showing that similar tensile properties are achieved. The breaking stress is not significantly compromised by the hybrid design, and stiffness is only slightly reduced. This highlights that, under conditions allowing better load distribution between hybrid and steel wires, the hybrid wires withstand greater stress and deformations. Hybrid FLC ropes can endure deformations exceeding 2 %, compared to 1.5 for hybrid OSS ropes with grip failures. Steel FLC ropes can tolerate breakage deformations of around 4 % due to the ductility of steel. Shown results indicated a good correlation between experimental and FEA results up to the point of failure. For steel ropes, both experimental and numerical analyses predicted load decay due to necking of steel wires immediately prior to the rupture.

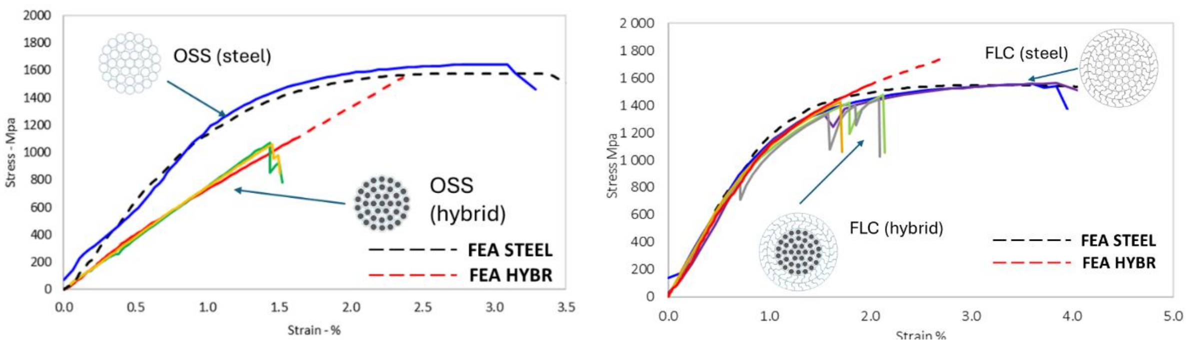

Figure 8: Tensile test results: full-steel vs hybrid. OSS (left). FLC (right)

As illustrated in **Figure 9**, the von Mises stress distribution is observed to vary during different stages of axial load application to the rope. At the onset of the nonlinear section of the stress-strain diagram (left), the distribution of stress is depicted. Additionally, the moment of buckling is indicated. The collapse of the strands initiates in the outer layers, leading to a redistribution of the load to the innermost layers of the rope.

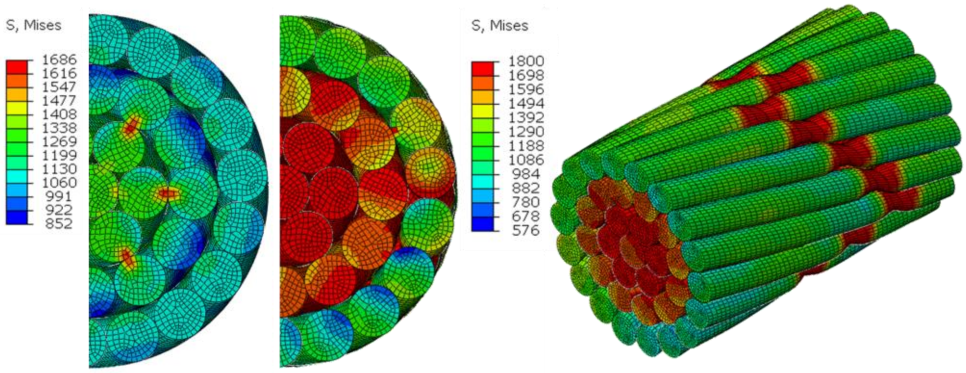

Figure 9: stress distribution at the end of elastic range (left), and at plastic instability onset (center and right).

Stabilized elastic moduli obtained from load-elongation cyclic curves were approximately 145 GPa for OSS steel ropes and 115 GPa for hybrid ropes, while 150 GPa and 145 GPa have been measured for FLC Steel and hybrid counterparts respectively. The comparison of E-modulus tests with corresponding numerical simulations shows good agreement, particularly after the first load cycles where all the gaps and slacks on wires are recovered. This is observed also in the FE model but to a minor extent, due to the more precise helical geometry compared to real case.

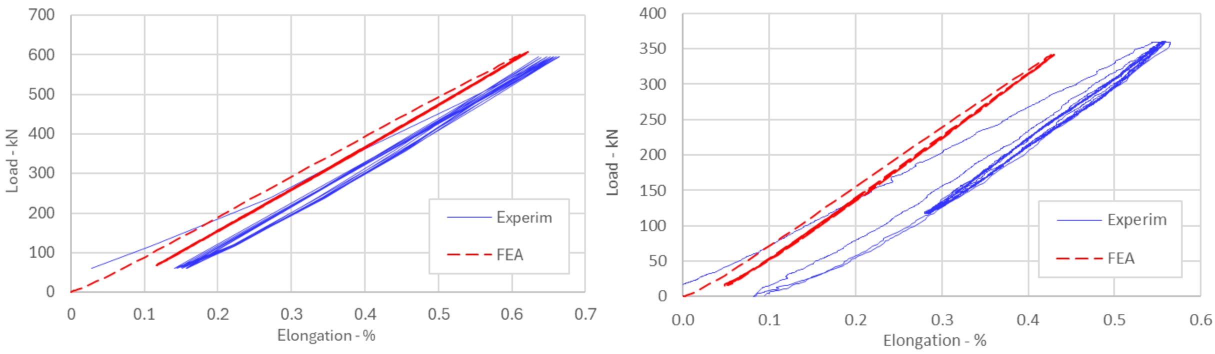

Figure 10: OSS: experimental vs FEA - cyclic test: steel rope (left), hybrid (right).

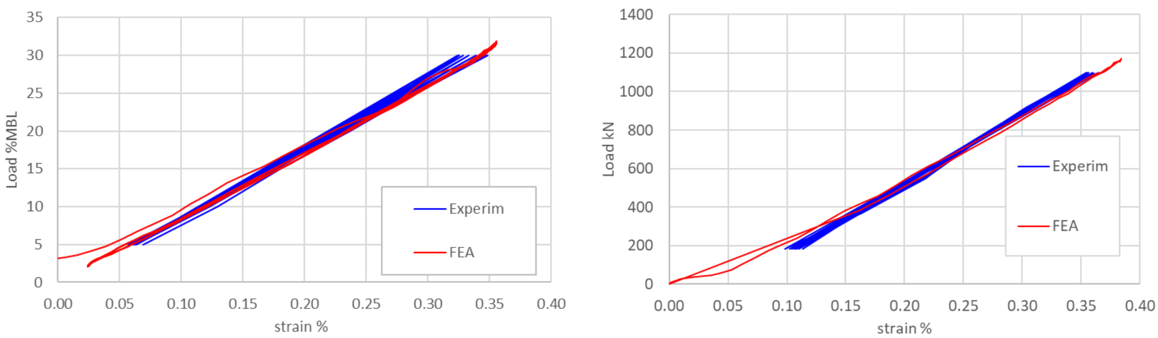

Figure 11: FLC: experimental vs FEA - cyclic test: steel rope (left), hybrid (right).

4.2.1 Torsional response

The torque-rotation response under tensile load depends significantly on rotational boundary constraints at rope ends. Testing was performed by applying an initial rotation and subsequently imposing axial tensile loads keeping rotation fixed, resulting in torque-load relationships depicted in **Figure 12**. Axial loads are presented as percentages of minimum breaking load (MBL %), with positive rotation angles indicating tightening and negative angles representing strand opening. Available experimental data focused on OSS steel ropes (Figure **12** left), while for OSS hybrid ropes only FEA results are available (Figure 12 right). Results demonstrated torque increasing with tensile load for rotation angles ≥ 0, whereas torque initially decreased at negative angles due to limited wire contact and boundary conditions before rising similarly at higher loads. Simulations accurately matched experimental data, effectively capturing rope rotational stiffness, with slight discrepancies attributed to minor geometric differences enhancing stiffness in the numerical model. Although tests on hybrid ropes were not available. FEA showed that a similar behaviour to steel ropes can be observed. Slightly lower torsional stiffness is observed on hybrid rope, which is consistent with slightly lower E-modulus for hybrid wires.

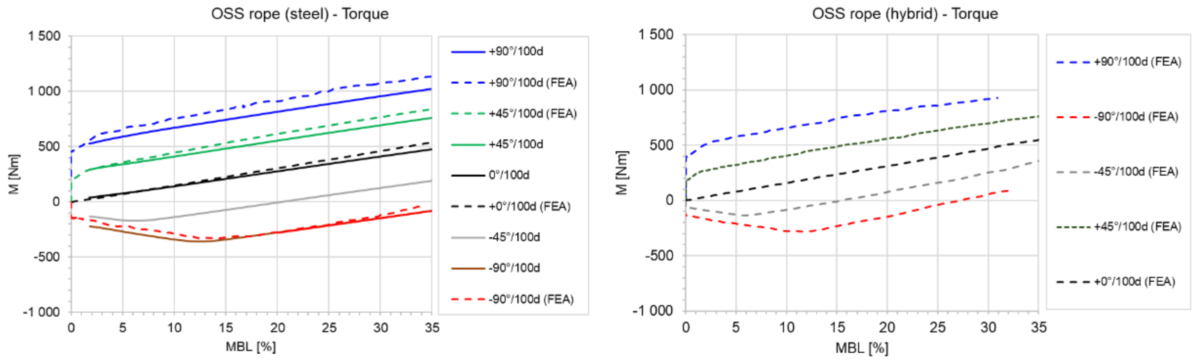

Figure 12: Experimental vs FEA of OSS steel rope torsional response (left) FEA OSS hybrid rope (right).

5 Conclusions

This study, conducted within the FIRST-WIRE project, investigates the mechanical properties of innovative hybrid ropes featuring a high-performance carbon fiber bundle enclosed within a stainless-steel mantle. Specifically, the research examined Ø 36 mm Open Strand Spiral (OSS) ropes and Ø 60 mm Fully Locked Coil (FLC) ropes through extensive full-scale experimental testing and finite element (FE) modeling. The hybrid wires were produced using a strip rolling process combined with longitudinal seam welding (TIG or Laser), confirming the feasibility of large-scale manufacturing across various dimensions. Experimental results showed good agreement with FE analyses, validating the accuracy and reliability of the modeling approach for predicting mechanical behavior under diverse loading scenarios. Hybrid ropes demonstrated significant advantages compared to conventional steel ropes, including enhanced tensile strength, elastic modulus, and optimal elongation capabilities, particularly beneficial for applications demanding high strength, stiffness, and weight reduction. These properties offer notable improvements in structural efficiency, design flexibility, and weight savings. Results confirm the effectiveness and practicality of hybrid wire ropes, though further research remains necessary, particularly addressing challenges associated with rope terminations and connections to structural components. The successful implementation of hybrid wire technology outlined in this study represents a substantial advancement in rope and cable design, indicating significant potential for enhancing performance, sustainability, and cost-efficiency in both industrial and commercial sectors.

6 Acknowledgements

This research was co-funded by European Union in the frame of the Research Fund for Coal and Steel - RFCS programme. More info about the project are available at the website www.firstwire.eu.

7 References

[1] López, C., Firmo, J.P., Correia, J.R., Tiago, (2013), C. Fire protection systems for reinforced concrete slabs strengthened with CFRP laminates. Constr. Build. Mater., 47, 324–333.

[2] Shi, Z.; Zou, C.; Zhou, F.; Zhao, J., (2022), Analysis of the Mechanical Properties and Damage Mechanism of Carbon Fiber/Epoxy Composites under UV Aging. Materials 2022, 15, 2919. https://doi.org/10.3390/ma15082919.

[3] Xiong, W, Cai, C.S., Xiao, R., Deng, L. (2011). Concept and analysis of stay cables with a CFRP and steel composite section. KSCE Journal of Civil Engineering. 16. 10.1007/s12205-012-1152-1.

[4] Cai, H., Aref A.J., (2015), On the design and optimization of hybrid carbon fiber reinforced polymer-steel cable system for cable-stayed bridges. Composites Part B: Engineering, Volume 68,2015, Pages 146-152, ISSN 1359-8368.

[5] https://firstwire.eu/

[6] Redaelli Patent WO 2013/065074 A1: Composite Wire with Protective External Metallic Mantle and Internal Fiber

[7] https://www.hyosung.co.jp/en/production/industrial/carbon/

[8] (Costello, 1990) GA Costello, Theory of wire ropes, Springer-Verlag, New York USA, 1990.

[9] Foti, Francesco & Martinelli, Luca. (2016). Mechanical modeling of metallic strands subjected to tension, torsion and bending. International Journal of Solids and Structures. 91. 10.1016/j.ijsolstr.2016.04.034.

[10] (Jiang et al., 1999) WG Jiang, MS Yao, JM Walton, A concise finite element model for simple straight wire rope strand, International Journal of Mechanical Sciences 41, 143-161, 1999.

[11] https://www.3ds.com/products/simulia/abaqus

8 Authors' Introductions

Ing. Jan Ferino is a mechanical engineer specializing in Finite Element Analysis (FEA), industrial plant modeling, machining processes, and structural dynamics. From 2005 to 2015, he worked at RINA Consulting SpA (formerly Centro Sviluppo Materiali SpA) as a researcher in the Oil & Gas sector. In 2015, he co-founded Astarte Strategies Srl, an engineering consultancy focused on R&D for industrial innovation. He contributed to European projects on steel industry innovation and participated in coordinating First Wire, a co-funded by RFCS, a EU programme supporting research projects in the coal and steel sectors.

Ing. Andrea Meleddu is a mechanical engineer with expertise in structural integrity, fluid dynamics, materials science, and experimental testing. From 2004 to 2015, he worked at RINA Consulting SpA (formerly Centro Sviluppo Materiali SpA), focusing on engineering research and development for Oil&Gas. In 2015, he co-founded Astarte Strategies Srl, where he now serves as Technical Manager, overseeing technical planning and coordination. He has contributed to several European research initiatives and coordinated of the First Wire project, co-funded by RFCS, a EU programme supporting research in the coal and steel sectors.

Dipl.-Ing. Stefan Hecht is head of the department "Rope Technology" of the Institute of Mechanical Handling and Logistics (IFT) of the University of Stuttgart. He is active in testing, research and standardization of fibre ropes, steel wire ropes and PPE against fall from height. He is Member of the OIPEEC Management Committee and member of EUROCORD, EWRIS and several national and international standardization committees in different fields of rope application.

Wendel Frick, M.Sc. is a mechanical engineer specializing in production and materials engineering. He completed his Master's degree in 2015 and subsequently joined the Institute of Mechanical Handling and Logistics (IFT) of University of Stuttgart as a research assistant and doctoral student. He has been Head of Destructive Rope Testing there since 2022. His research primarily focuses on two key areas: the fatigue behavior of high-strength steel and fiber ropes, and the development of appropriate discard criteria.

Mr Muhammad Najih Amin received his MSc degree in Materials Engineering and Nanotechnology from Politecnico di Milano (Italy) in 2018. He began his professional journey as an intern with the R&D team at Redaelli Tecna SPA in 2018. A year later, he transitioned to the role of R&D Engineer, and in 2025, he was promoted to R&D Team Lead, a position he currently holds. His research interests primarily focus on technological advancements in continuous rope monitoring and product development for applications in people transportation.

Impact of outside Plastic-Coated Ropes on Drum Stress in Multilayer Applications

Max Stök M. Sc.

Clausthal University of Technology, Institute of Mechanical Engineering (IMW), Germany

Prof. Dr.-Ing. Armin Lohrengel

Clausthal University of Technology, Institute of Mechanical Engineering (IMW), Germany

Summary

Wire ropes have a limited service life due to fatigue, with outer strands experiencing high mechanical stresses that leads to wire breakage. A plastic coating is supposed to distribute contact forces over a larger area, reducing individual wire stress and extending the rope's lifespan. The load on a rope drum is significantly influenced by the properties of the wound rope. In multilayer spooling, load relief effects occur, reducing hoop stresses within the drum shell. The rope's lateral stiffness plays a crucial role, as deformation under pressure alters its diameter, lowering tension and stress. Additionally, friction coefficients between rope-rope and rope-drum contacts impact flange loads.

Experimental studies examined two plastic-coated wire ropes with different constructions, focusing on winding height, lateral stiffness, and drum stresses. A comparison between measured and calculated stress values revealed discrepancies between the ropes and the calculation methods. The findings emphasise the importance of ascertaining the unknown friction values for the plastics, with a view to increasing the accuracy of the stress calculations.

Keywords: wire rope, outside plastic coated ropes, drum stress, multilayer spooling

1 Introduction

Due to wear and tear, ropes do not have an endurance life, but only a fatigue life [1]. To conserve resources and increase the sustainability of the rope as a machine element, its service life must be maximised. The outer strands of wire ropes are subjected to high mechanical stresses. The wires are subjected to both compression and bending. In the long run, this leads to wire breaks in the outer strands, which mark the discard point of the rope with a limit value defined in the standards e.g. [2]. The contact between the outer wires of the rope and the sheaves or drums varies from short line contact to surface contact in compacted ropes, depending on the ropes design. The resulting Hertzian pressures are correspondingly high. With a plastic sheath around the outside of the wire rope, the forces acting on the contact are distributed over several wires and thus over a larger area. This reduces the stress in the individual wires and results in later wire breakage and prolonged rope life.

The load that is applied to a winch is predominantly dependent on the properties of the rope with which it is wound. In the multi-layer spooling application, load relief effects occur which increasees the stresses non proportional to the number of layers. The initial relief effect is initiated by the subsequent winding, which also deforms the drum shell in the area of the previous windings, see **Figure 1**, left. This process relieves the already wound rope, leading to a reduction in the ropes pretention, resulting in a lower pressure on the drum shell and consequently a lower hoop stresses within the shell. The second effect is related to the rope's lateral stiffness. The pressure exerted by the upper layers causes the rope cross-section to deform from a circle to an oval shape, cf. Figure 1 right. This deformation corresponds to a decrease in the mean winding diameter of the rope, leading towards a lower tension, which in turn leads to a reduction in the hoop stresses within the drum shell. The extent of the relief effects is largely dependent on the transverse and longitudinal modulus of the rope. [3]

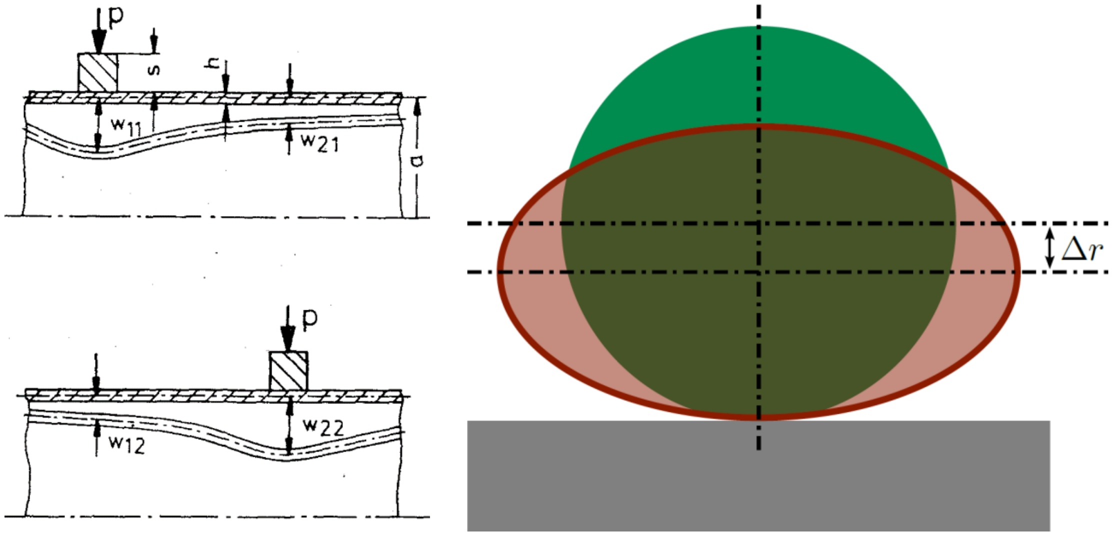

Figure 1: Visualisation of the relief effects due to the drum deformation (left,[3]) and the rope deformation (right)

In addition to these factors, the load on the drum flanges is influenced by the coefficients of friction that exist within the rope-rope contact and the contact between the ropes and the drum. In the event of a low coefficient of friction in the rope-rope contact, the rope package is more likely to slide in width and the forces on the Flanges increase. [4]

Ovalisation of fibre ropes is considerably more distinct than for steel ropes, which is why it has to be taken into account not only in the winding radii for the force application on the flanges, but also in the calculation of the pressure on the drum shell. Due to the smaller winding radii, the area to be taken into account for the winding pressure, on which the radial force acts, is smaller and the winding pressure increases compared to wire ropes. [5]

The present paper aims to compare the actual stresses occurring in a drum with those expected from conventional calculations. For this purpose, two plastic coated wire ropes were spooled on the IMW spooling test rig and the drum calculated according to [4] and [5].

2 Testing rig, ropes and measuring equipment

In this paper two different rope constructions coated with two different plastics are compare in multilayer spooling. Rope 1 is a 6x36WS coated with a high density Polyethylene, while Rope 2 is a rotation resistant 39(W)xK7-WSC covered in Polypropylene. Both ropes are spooled back and forth between two rope drums with a D/d-ratio of 18 on the IMW spooling test rig. In order to maintain a compact test configuration, the rope drums are positioned in a vertical arrangement with the rope being returned by a deflection sheave. The test rig is illustrated in **Figure 2**, left. The upper rope drum is equipped with measuring equipment. Strain gauges are attached to the outside of the flange to measure the bending, see Figure 2, right. Further strain gauges are applied in the drum shell to record the tangential and axial strain so that the hoop and axial stress can be calculated.

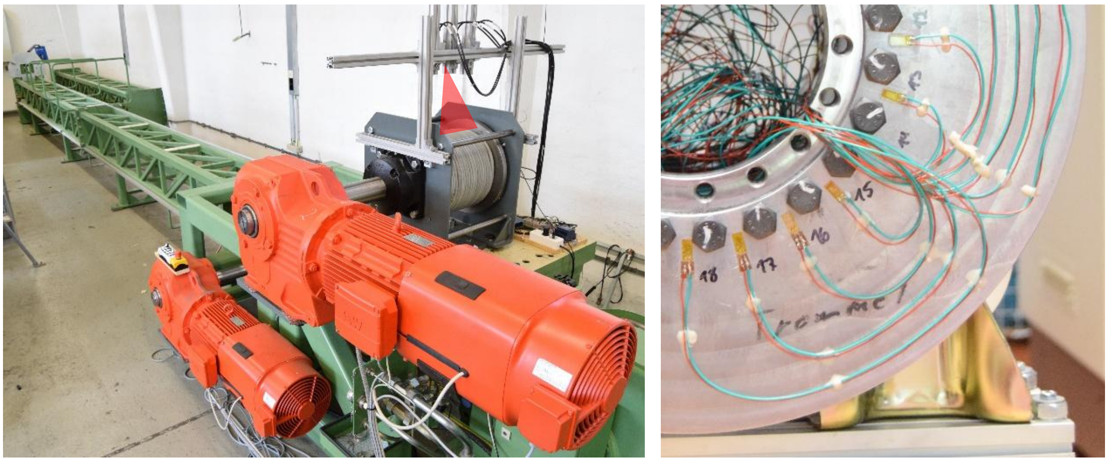

Figure 2: The spooling test rig (left) and attached strain gauges on the out side of the drums flange (right)

3 Experimental results

To calculate the loads on the drum shell and the flanges in accordance with [4], it is necessary to take into account the longitudinal and lateral moduli of elasticity, the geometric dimensions of the drum, the rope pull per layer, the material properties of the drum and the coefficients of friction in the rope-rope contact and in the rope-drum contact. For the calculation according to [5], the deformation of the rope is also taken into account.

3.1 Rope deformation

The winding heights of the two ropes analysed, each with a line pull of 30 kN, were recorded using laser scanners. The results for Rope 1 correspond to the values measured in [6], taking into account the slightly higher load.

Table 1: Winding heights of the two analysed ropes at 30 kN line pull for the parallel and crossing sections

	Rope 1		Rope 2	
	Parallel section	Crossing section	Parallel section	Crossing section
1. layer	13.7	13.7	13.5	13.5
2. layer	11.1	12.7	10.5	11.9
3. layer	11	12.3	10.6	11.9
4. layer	10.9	12.0	10.5	11.0
5. layer	10.9	12.3	10.5	11.7

In [7], the theoretical analysis of the deformation of the plastic coating was conducted. In the event of complete deformation of the plastic, a winding height of 10.47 mm is to be expected in the parallel section. This phenomenon is evident in Rope 2, while Rope 1 exhibits a lower deformation of 11 mm on average. In the crossing section, the winding heights correspond to the 12 mm diameter of the wire rope, indicating complete displacement of the plastic from the rope-rope contact. For Rope 2, a smaller increase in height than the wire rope diameter is observable in the crossing section of the fourth layer. This phenomenon can be explained by a shift of the crossing section to the drum circumference, which is now in the actual parallel section. This is due to a permanent deformation of the plastic, resulting in the rope diameter no longer matching the system groove of the drum perfectly. Consequently, the rope is shifted at a later position than anticipated. The shift of the crossing section can also be seen in the bending stress of the flanges in **Figure 3**. The minimum stress shifts from the end of the crossing section at 240° into the parallel section at 255°.

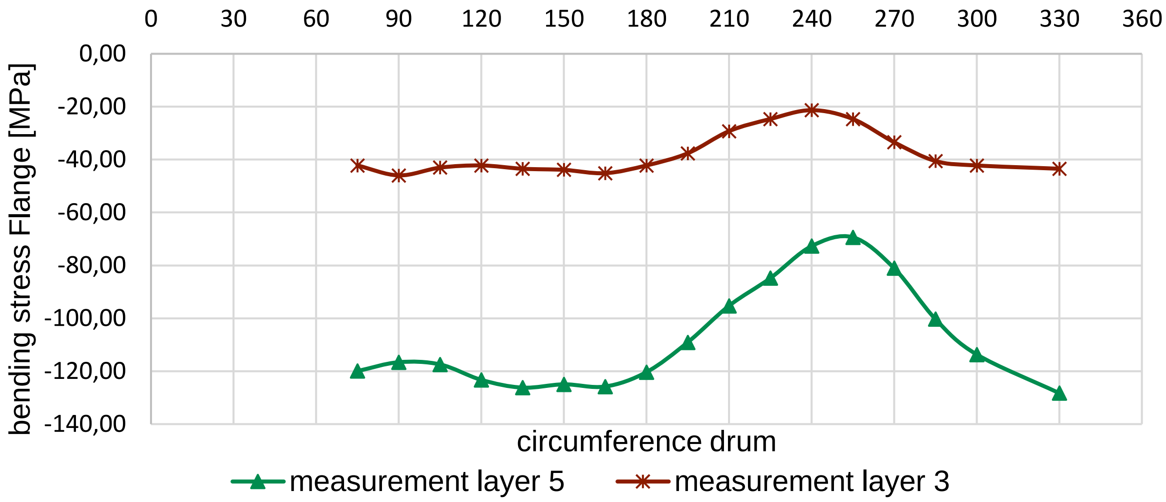

Figure 3: Bending stress of the drums flange

3.2 Lateral stiffness

The lateral stiffness of ropes is measured using the institute's own test rig. For this purpose, a round groove according to [8] is generally used on one side and a flat punch on the other side, as illustrated in **Figure 4** on the left. The lateral elasticity of ropes is influenced by the longitudinal and lateral forces applied, so that the lateral stiffness is determined for different longitudinal and lateral force combinations.

The elasticity of the plastic-coated Rope 1 has previously been determined in [9] and then set in relation to the elasticity of the non-coated wire rope.The lateral stiffness of Rope 2 was determined using two different test geometries: firstly, the geometry already described and, secondly, the shape of the maximum deformed plastic according to [9]. The underlying hypothesis is that plastic with a Poisson's ratio of almost 0.5 [10] is incompressible and thr coated ropes stiffness should therefore become stiffer after complete deformation. For this purpose, test pieces were produced that represent the final shape of the completely deformed plastic coating in the parallel section (see Figure 4, right).

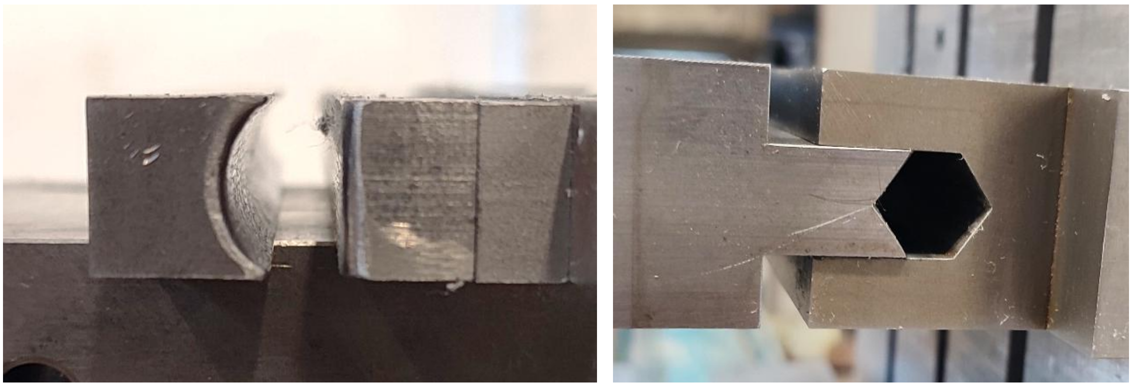

Figure 4: The different test geometries, round groove with flat counterpart (left) and hexagon (right) [11]

The stiffness of the plastic coated Rope 2 compared to the uncoated rope differs only slightly in the median depending on the test geometry, as shown in **Figure 5**. However, the scatter of the ratio is less for the hexagonal test geometry than for the round groove. For the two ropes analysed in [9] and for Rope 2 analysed here, the stiffness of the plastic-coated wire rope is on average approximately 62 % of the stiffness of the non-coated wire rope. In absolute terms, however, Rope 2 as a rotation-resistant crane rope is slightly stiffer than Rope 1 (6x36WS).

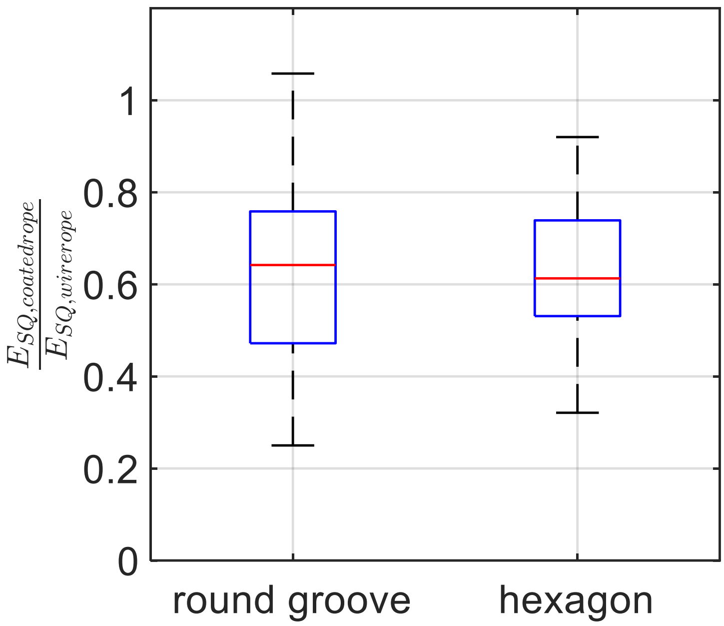

Figure 5: Boxplots of ropes 2 stiffness for the round groove (left) and the hexagon (right)

4 Comparison between calculated and measured stresses

A comparison of the stress data reveals discrepancies between the two ropes, as well as between the measured and calculated values. Forces on the flanges and pressure on the drum shell are calculated analytically and subsequently entered into a finite element model (FEM) of the rope drum. The measuring grids of the strain gauges are cut out of the rope drum model as surfaces, thereby enabling a direct comparison of the stresses.

As depicted in **Figure 6**, the bending stresses for the flanges of the rope drum vary between both ropes. The crossing sections are between 0° and 60°, as well as 180° and 240°. The minimum stress for Rope 1 is recorded directly at the beginning of the crossing section, in contrast to Rope 2, whose minimum stress is recorded within the parallel section. This outcome can be attributed to inadequate sizing of the plastic material employed, which compromises the effectiveness of the system grooving of the drum. A comparison of the calculated stresses between the two ropes reveals minimal discrepancies. Significant disparities emerge, however, when comparing the two calculation methods with respect to their predicted stresses. The calculation method proposed by [4] appears to provide more precise results in terms of stress levels up to the minimum stress point, yet neither calculation method successfully anticipates the increase in stress observed in the following parallel section.

The deviations in the positions of the crossing sections, as determined on the flanges, can also be detected in the hoop stress of the rope drum. The stresses determined by both methods show such a minor deviation for both ropes that a differentiation of the curves in Figure 7 is not possible. The predicted stresses correspond to the stresses of Rope 2, while the approximate 20% lower hoop stresses of Rope 1 are not predicted. However, it should be noted that the calculation is on the conservative side.

The coefficients of friction between the plastic coatings are unknown for the materials used and are to be determined by experiments yet to be carried out. Thus far, the coefficients of friction for steel wire ropes have been used, which has had an influence on the calculated stress values. For the method [4], it should also be noted that the deformation of the rope was only taken into account for the winding height, not for other factors which could have an influence on the calculated loads on the flanges.

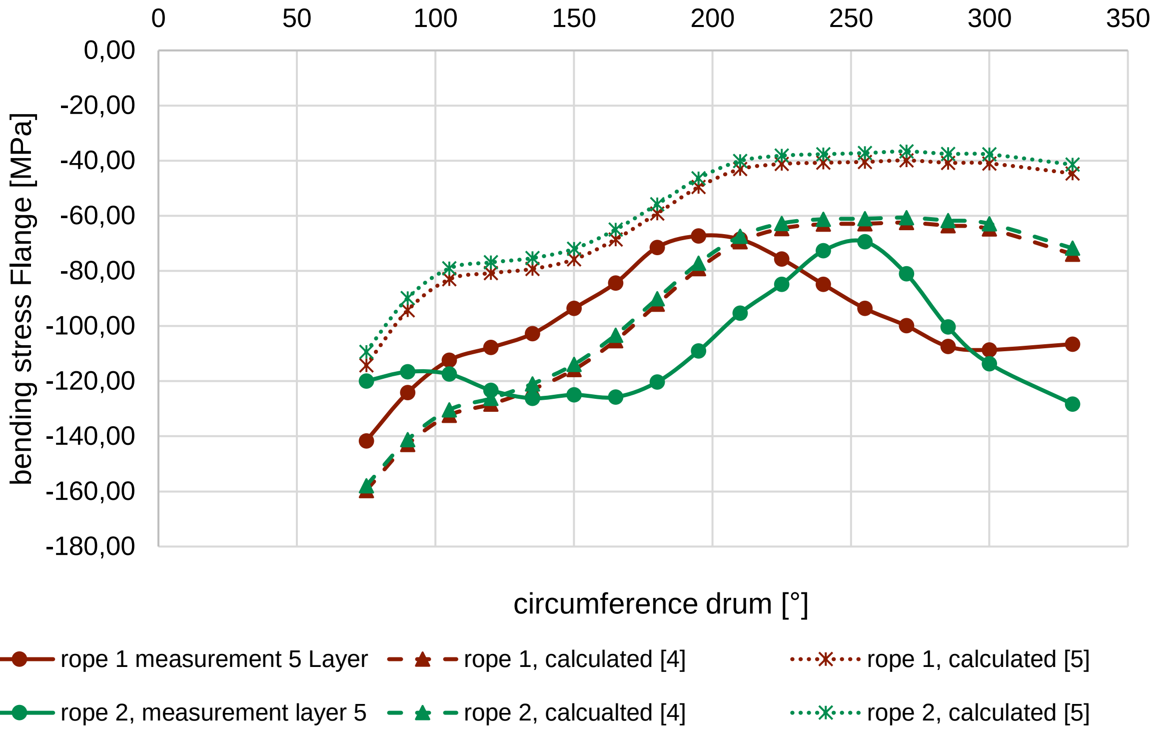

Figure 6: the measured and calculated stresses for the drum flanges

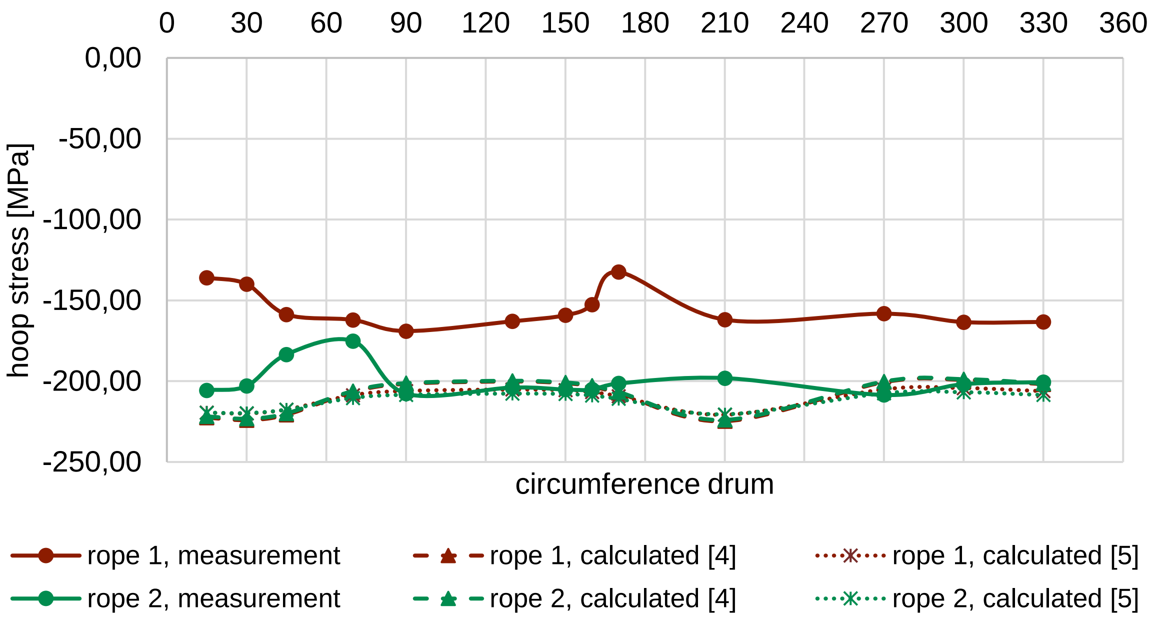

Figure 7: comparison of the measured and calculated hoop stress in the drum

5 Conclusions

The present study deals with the loads on rope drums, whereby the properties of the ropes with which the drums are wound must be considered a significant factor; the hoop stresses in the drum shell are determined conservatively by both calculation methods. The determination of the flange loads for the investigated ropes is carried out using method [4] with a higher precision, but the specific friction values for the plastics used are unknown in the calculations carried out here, so that further research is required, In addition, it must be examined to what extent the properties of the plastics can be included in the calculation.

6 Acknowledgements

The authors would like to thank the German Federal Ministry of Economics and Climate Protection for funding the research project "Design and size influence on service life and multi-layer winding applicability of plastic-coated wire ropes " (IGF project no.: 22663 BG) on the basis of a decision by the German Bundestag and the German Federation of Industrial Research Associations "Otto von Guericke" e.V. (AiF). The research project is being carried out jointly with the Institute of Material Handling and Industrial Engineering (headed by Prof. Dr.-Ing. habil. Thorsten Schmidt) at TU Dresden.

7 References

[1] Wehking, K.; Hecht, S.; Moll, D.; Novak, G.; Verreet, R.: Laufende Seile - Bemessung und Überwachung. 5. Renningen: Expert Verlag, 2018. – ISBN 978–3–8385–5191–3

[2] DIN ISO 4309 Cranes – Wire ropes – Care and maintenance, inspection and discard (ISO 4309:2017)

[3] Dietz, P.: Ein Verfahren zur Berechnung ein- und mehrlagig bewickelter Seiltrommeln; Dissertation, Technische Hochschule Darmstadt, Darmstadt, 1971.

[4] Mupende, I.: Beanspruchungs- und Verformungsverhalten des Systems Trommelmantel – Bordscheiben bei mehrlagig bewickelten Seiltrommeln unter elastischem und plastischem Werkstoffverhalten; Dissertation, TU Clausthal, Curvillier Verlag Göttingen, 2001.

[5] Stahr, K.: Beitrag zur Gestaltung und Dimensionierung von Windentrommeln bei mehrlagiger Bewicklung mit Faserseilen. 1. Auflage. Clausthal-Zellerfeld : Papierflieger Verlag, 2020. – ISBN 978–3–86948–775–5

[6] Stök, M.; Schulze, M.; Rechnagel, T; Lohrengel, A., Schmidt, T.: final report Lebensdauer und Wickelverhalten kunststoffummantelter Drahtseile, AIF, 2020, https://tu-dresden.de/ing/maschinenwesen/itla/tl/ressourcen/dateien/projekte/lifetimecoatedrope/19598_BG_Schlussbericht.pdf?lang=en

[7] Stök, M.; Chen, Y.; Lohrengel, A.: Geometrical and mechanical considerations for the outer plastic coating of wire ropes on multilayer spooling. Bardolino, Italy: Proceedings of the OIPEEC Conference, Pengzhu Wang, 2024. – ISBN 978–1–7336004–3–9

[8] DIN 15020 Lifting appliances — basic principles for rope reeving components, Beuth Verlag GmbH, 1974

[9] Stök, M.; Recknagel, T.; Wächter, M.; Lohrengel, A.; Schmidt, T.: Lifetime and suitability for multi-layer spooling of running wire ropes with plastic coating. Stuttgart, Germany: Proceedings of the OIPEEC Conference, Pengzhu Wang, 2022. – ISBN 978–1–7336004–1–5

[10] Erhard, G.: Konstruieren mit Kunststoffen. München: Hanser, 2008.

[11] Lontsi, B.: Experimentelle Bestimmung der Quersteifigkeit von Faserseilen mit unterschiedlichen Prüfaufbauten, nicht veröffentlichte Bachelorarbeit, Clausthal-Zellerfeld, 2025

8 Authors' Introductions

Max Stök M. Sc., research assistant at the Chair of Machine Elements and Design, Institute of Mechanical Engineering, Clausthal University of Technology.

Since 2019, Max Stök has been a research assistant at the Institute of Mechanical Engineering. Prior to this, from 2013 to 2019, he studied 'General Mechanical Engineering' at the Clausthal University of Technology. Currently, Max Stök is assigned to a research project that examines the multilayer spooling of plastic-coated ropes. Additionally, he is researching the lateral stiffness of ropes and the interaction between the rope and drum in rope drives.

Prof. Dr.-Ing. Armin Lohrengel, Head of the chair of Machine Elements and Design Theory, Institute of Mechanical Engineering, Clausthal University of Technology.

Armin Lohrengel became a professor at Clausthal University of Technology in 2007. He studied at TU Clausthal and RWTH Aachen mechanical engineering. Since 1995 he was a research assistant at RWTH Aachen and received his doctor's degree in 2001. From 1999, Mr. Lohrengel worked as head of machine development at Paul Hartmann AG in Heidenheim. In 2007, he was appointed to the professorship for machine elements and design theory. His field of research are the following machine elements: rope drives, couplings, shaft-hub connections and thrust collar. Furthermore process engineering machines, especially for production and recycling processes and Design theory, especially for the field of acoustics and circular economy.

From deformation behavior to fatigue life: A new way to predict the lifetime of wire ropes more precisely

Wendel Frick

University of Stuttgart, IFT, Germany

Summary

This study investigates how the rope-specific deformation behavior influences the lifetime under tension-tension load. In fatigue tests, the lifetime was determined experimentally at different load amplitudes. The quasi-static tensile test makes it possible to determine and characterize the load-dependent deformation behavior of ropes. The comparison between the dynamic lifetime at a load level and the load-dependent deformation, derived from the static stress-strain curve, shows a direct correlation. A small load-induced deformation leads to a longer lifetime and vice versa. The results indicate that the quasi-static tensile test is sufficient as a quick test for predicting the lifetime of nominally identical ropes of different qualities.

Based on these findings, a new approach for predicting the lifetime of wire ropes under tension-tension loading is presented, which systematically considers rope-specific deformation for the first time. In addition, it is explained how this approach can be transferred to other rope qualities and how generalization can be achieved. By taking the individual deformation behavior into account, differences in lifetime between nominally identical ropes can be precisely recorded. The deformation characteristic of a rope determined in a time-saving tensile test, combined with the working load, allows the resulting deformation to be determined precisely. On this basis, a specific lifetime prediction can be made for each individual rope.

Keywords: Rope lifetime, tension-tension fatigue, deformation behavior, prediction method

1 Introduction

Ropes are often essential in numerous technical applications due to their unique combination of flexibility, tensile strength and load-bearing capacity. Modern architecture uses ropes as essential structural elements [1]. These are permanently installed in a fixed position and are therefore known as “standing ropes” or “guy ropes” [2]. Such permanently installed ropes play an important role in the structural integrity and load-bearing capacity of various structures. Impressive examples include prestressed roof structures and suspension bridges, where the guy ropes are key components for stability and load-bearing capacity.

During operation, ropes are subjected to recurring mechanical loads. In the case of standing ropes, e.g. on bridges, this load results from traffic and environmental influences such as wind and snow loads. The recurring loads on the ropes lead to gradual fatigue, which negatively affects the load-bearing capacity and safety and can ultimately lead to mechanical failure of the ropes [3], [4]. As a result of the time-dependent onset of fatigue, the service life is limited, i.e. ropes have a finite lifetime and must be replaced before it expires. Sudden rope failure during operation must be avoided by means of a appropriate and operationally safe design.

For standing wire ropes under tension-tension fatigue, the method according to Feyrer [4], equation (1), is used for the mathematical estimation of the lifetime N. The empirically determined equation takes into account the load amplitude S_a, the lower rope tensile load S_{low}, the nominal rope diameter d and empirically determined constants a_i depending on the rope construction and strength.

$$lgN = a_0 + a_1 lg\frac{2S_a}{d^2} + a_2\frac{S_{low}}{d^2} + a_3\left(\frac{S_{low}}{d^2}\right)^2 + a_4 lgd \quad (1)$$

The fatigue behavior of standing ropes under recurring tensile load was investigated by KLÖPFER [5]. **Figure 1** shows the lifetime of two nominally identical ropes which are characterized by the same diameter, the same strength and the same construction, but which come from different manufacturers. The lifetime prediction according to equation (1) is shown as a dashed curve.

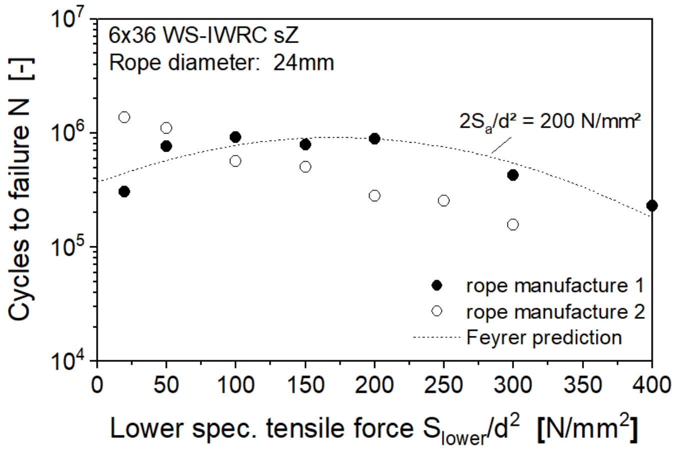

Figure 1: Scatter of the lifetime of nominally identical ropes of type 24-6x36WS-IWRC sZ under tension-tension load according to [5] compared to the predicted rope lifetime according to equation (1) as a dashed curve

As can be seen, the currently available prediction of the lifetime regularly shows a curved curve. This means that the number of fatigue cycles initially rises with increasing lower rope tensile load and then falls again. However, other curves can also be observed, as the comparison of the nominally identical ropes shown here demonstrates. This means that ropes do not necessarily have a curved curve and that the number of fatigue cycles that can be achieved, for example, decreases continuously with increasing lower related rope tensile load. Consequently, the currently available method cannot cover the listed lifetime differences of nominally identical ropes. Only the loads on the rope are currently taken into account. The deformation capacity of the material and the load-induced deformation are not taken into account.

This study presents an innovative approach to predicting the lifetime of wire ropes, which is based on the use of deformation parameters and leads to a more precise prediction. By taking into account rope-specific deformation behavior, differences in lifetime between nominally identical ropes can be detected. The focus here is on the behavior of wire ropes under recurring tensile load - standing ropes. In particular, a direct comparison and correlation between the load-dependent fatigue lifetime and the load-dependent rope deformation is presented. This approach enables an individual and therefore more precise prediction of the lifetime and thus contributes to the improvement of safety and efficiency in applications with wire ropes.

2 Investigated wire ropes and methods

Four strand ropes with common nominal strengths were examined and evaluated. Three of the ropes are ropes of the same construction with different strengths. The findings on fatigue behavior and fundamental dependencies obtained in [6], which were investigated on individual rope wires of the same and different strengths, served as the basis. Table 1 shows the investigated ropes, their nominal diameter and strength data and the actual values determined.

Table 1: Examined wire ropes with their properties

Sample designation	Construction	Nominal diameter d_0 [mm]	Nominal strength R_0 [MPa]	Actual breaking load [kN]	Tensile strength R_m [MPa]
8x19W	8x19W – IWRC U sZ	6.0	1,770	28.08	1,518
18x7_1570	18x7 – WSC U sZ	16.0	1,570	164.54	1,484
18x7_1960	18x7 – WSC U sZ	16.0	1,960	184.50	1,661
18x7_2360	18x7 – WSC U sZ	16.0	2,360	209.01	1,890

The dependence of the lifetime on the rope-specific deformation was examined and analyzed in detail, particularly on the 8x19W rope. To determine the lifetime, dynamic fatigue tests were carried out under various tension-tension loads. In contrast, the rope-specific deformation was determined by means of quasi-static tensile tests. The 18x7 ropes were primarily used for a detailed investigation of the specific deformation behavior. The focus here is on ropes with an identical construction, but which differ in terms of their material properties.

3 Experimental results

A series of tests were carried out to investigate two main aspects: firstly, the deformation behavior of ropes under quasi-static loading and secondly, its correlation with the fatigue life under dynamic loading. The main objective of these experiments was to confirm the hypothesis that rope fatigue depends primarily on the specific load-induced deformation. The various experiments are described below.

3.1 Quasi-static tensile tests

Tensile tests were carried out to characterize the deformation behavior and a stress-strain curve was drawn up for the wire ropes tested. **Figure 2** shows the characteristic curves determined for the ropes. The symbols used in the curves are for visual differentiation only.

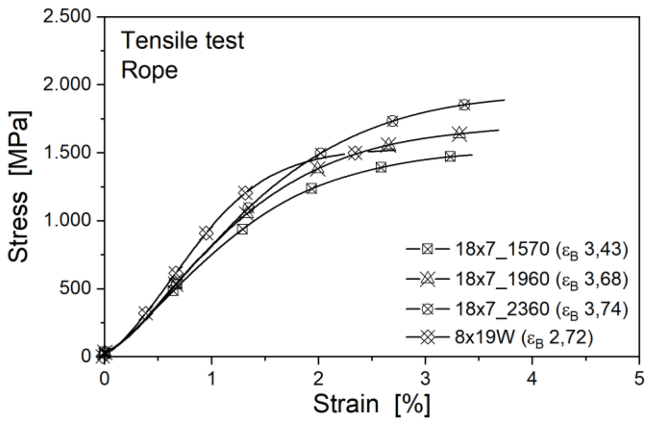

Figure 2: Determined stress-strain curves of the tested wire ropes

The measured stress-strain curves are all non-linear. This means that there is no proportionality between the applied stress and the resulting elongation. In addition, the ropes differ not only in their breaking stress R_m, which corresponds to the respective nominal strength, but also in their elongation at break ε_B.

In order to evaluate the deformation capacity of ropes and to interpret the fatigue behavior, several possibilities have been researched. An effective approach for the comparative analysis of the overall deformation behavior of ropes is the normalized representation of the stress-strain curves, **Figure 3**. This innovative way of representing the relationships between stress and strain enables a clear evaluation of the deformation behavior up to break and provides a sound basis for further analyses and interpretations, especially if different strengths are present. The stress is related to the breaking stress R_m and the strain to the elongation at break ε_B. A material that is elastic up to rupture corresponds to a normalized 45° straight line in the diagram and has a normalized strain energy density of 0.5, which corresponds to the area below the straight line. In contrast, the tested ropes show curved curves that deviate from this 45° straight line. This deviation results in higher normalized strain energy densities.The more the value exceeds that of an ideal elastic material, the higher the specific plastic deformation capacity up to rupture. This transformation of the axes, which initially appears minor, provides significant added value for the comparative analysis. For a given load, it illustrates the associated specific deformation and the remaining specific deformation capacity of the different ropes. In other words, the safety against breaking stress and against elongation at break resulting from a given load.

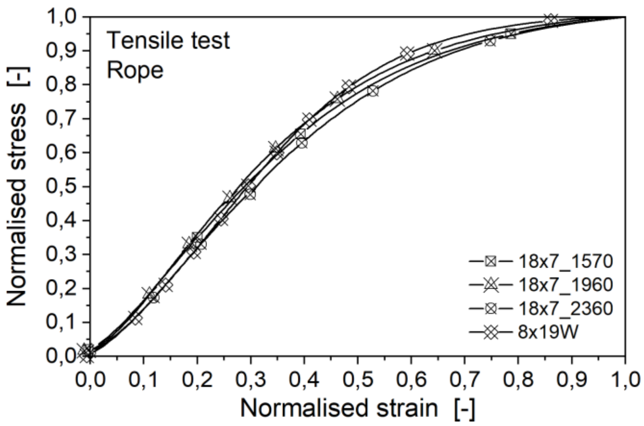

Figure 3: Normalized stress-strain curve of the tested wire ropes

The normalized representation clearly shows that all ropes of the 18x7 type exhibit an almost congruent normalized curve. Consequently, under the same percentage load, the strain capacity is utilized to the same extent, i.e. the same distance to the breaking elongation (strain safety). Whereby the high-strength rope (18x7_2360) is slightly lower.

In order to analyze the relationship between tension and elongation, a multi-stage test was carried out on the 8x19W rope. It should be emphasized that the load always remained below the breaking stress during the entire test. **Figure 4** shows the deformation of the tested rope sample under a recurring load, which was gradually increased and then reduced in six stages. At each load level, 20 cycles were performed. While the upper load level varied between 15 % and 90 % of the breaking stress, the lower load level was a constant 4 % of the breaking stress. Although the load did not exceed the breaking stress of the rope at any time during the entire test, failure still occurred. Which proves that failure is independent of stress.

It can be seen that the higher the load, the greater the viscous deformation. The stress-strain cycles at the lowest load of 227 MPa are quite narrow, while the cycles at the highest load of 1,366 MPa expand significantly. The test demonstrates the viscous deformation behavior of wire ropes and supports the underlying hypothesis that the total accumulated viscous deformation plays an important role in the fatigue of a wire rope.

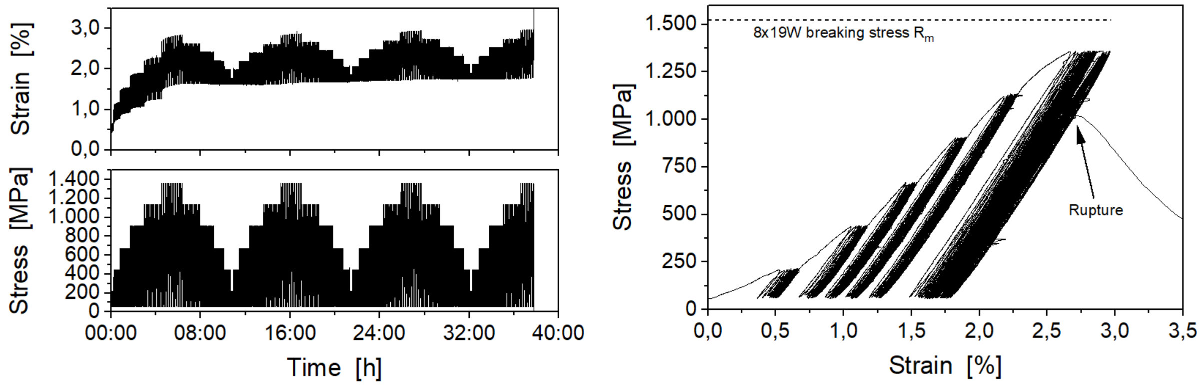

Figure 4: Multi-stage test with 20 cycles each with varying upper load between 15 % and 90 % R_m, with constant lower load of 4 % R_m on the 8x19W type rope, left: stress and strain against time, right: stress against strain

During a rope operation, the load level is generally constant, which means that the safety against breaking stress is also constant. As long as there is no overloading above the breaking stress, no stress-related failure will occur. Also, a recurrently applied load does not accumulate, so that the stress decreases completely after relief. However, it is known from the previous multi-stage test that ropes exhibit a viscous deformation behavior. This means that the strain accumulates over time. In this respect, the distance between the operating point and elongation at break (strain safety) is particularly important. The greater this distance, the longer the accumulation time and therefore the longer the fatigue lifetime must be.

3.2 Dynamic tension-tension tests

To investigate the influence of the deformation behavior on the fatigue life, systematic tests were carried out under tension-tension loading at various load levels. **Figure 5** shows the number of cycles to failure determined in the test as a function of the lower diameter-related rope tensile load S_{low}/d^2 and the respective double amplitude $2S_a/d^2$. Furthermore, the predicted lifetime behavior according to equation (1) is shown as a dashed curve. For the tests at the respective loads, the predicted number of cycles corresponds to the intersection point underneath between the additionally drawn straight line and the dashed curve.

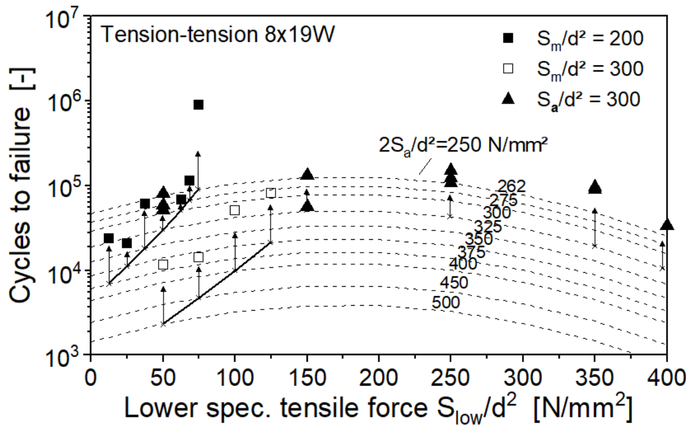

Figure 5: Number of cycles to failure of the 8x19W stranded rope as a function of the lower diameter-related rope tensile load S_{low}/d^2 and the respective double amplitude $2S_a/d^2$

The test results largely show the expected behavior, a curved curve, corresponding to the currently available method for predicting the lifetime of ropes subjected to tension-tension, albeit with a certain degree of uncertainty in the prediction. It is worth noting that the lifetime initially increases for the same amplitude up to a certain mean stress value and then decreases. The basic assumption that an increasing stress safety inevitably results in an increased lifetime of dynamically stressed ropes is therefore incorrect. This is in contradiction to the existing stress-related safety concept in rope design.

4 Methodological investigation and prognosis approach

Based on the previously collected experimental data, a newly developed approach for predicting the lifetime of standing ropes is presented below, taking into account rope-specific deformation characteristics.

In order to analyze and correlate the relationship between fatigue life and deformation height, the load values were converted into strain values. According to equation (2), the normalized strain amount $\Delta\varepsilon_{nor}$ was determined for each test, resulting from the respective upper load S_{up} and lower load S_{low}.

$$\Delta\,\varepsilon_{nor.} = \frac{\varepsilon_{up} - \varepsilon_{low}}{\varepsilon_B} = \frac{f(S_{up}) - f(S_{low})}{\varepsilon_B} \tag{2}$$

The experimentally determined lifetime as a function of the rope-specific normalized strain amount is shown in **Figure 6**.

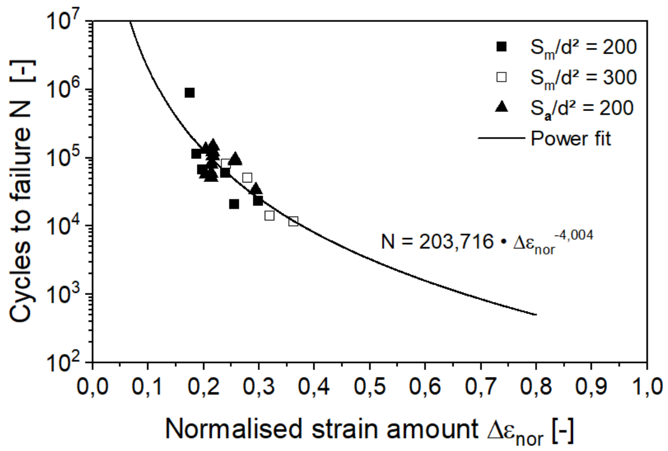

Figure 6: Number of cycles to failure as a function of the normalized strain amount and associated power function for the investigated rope of type 6-8x19W-IWRC U sZ 1770

For standing ropes, there is a clear correlation between the number of cycles to failure N and the normalized strain amount $\Delta\varepsilon_{nor}$, which can be precisely described by the power function shown, Figure 6. This power function can be used as an analytical approach for lifetime prediction. The lifetime can be determined by entering the normalized strain amount resulting from the upper load and lower load, acc. equation (2).

An application-oriented approach to strain-based lifetime prediction is made possible by the newly developed operating diagram, shown in **Figure 7**. This innovative diagram combines two essential relationships. Namely, the relationship between load and the resulting normalized strain amount, as well as the correlation between normalized strain amount and the lifetime dependent on it. Based on the stress-strain curve determined experimentally on the rope, the resulting normalized strain amount for predefined lower loads S_{low} and upper loads S_{up} (0 %, 10 %, 30 % and 60 % of the actual breaking load ABL) were plotted. The operating diagram is to be run through step by step from left to right. The starting point is the breaking load-related upper load S_{up}/ABL prevailing during operation in the left-hand section of the abscissa. Using this and the associated related lower load S_{low}/ABL, the resulting normalized strain amount can be determined on the ordinate. This strain amount can be used to determine further the respective lifetime in the right-hand section of the abscissa according to the intersection point on the power curve. For example, a lifetime of 33,000 cycles is achieved if the rope is subjected to an upper load of 60 % of its breaking load and an lower load of 10 %.

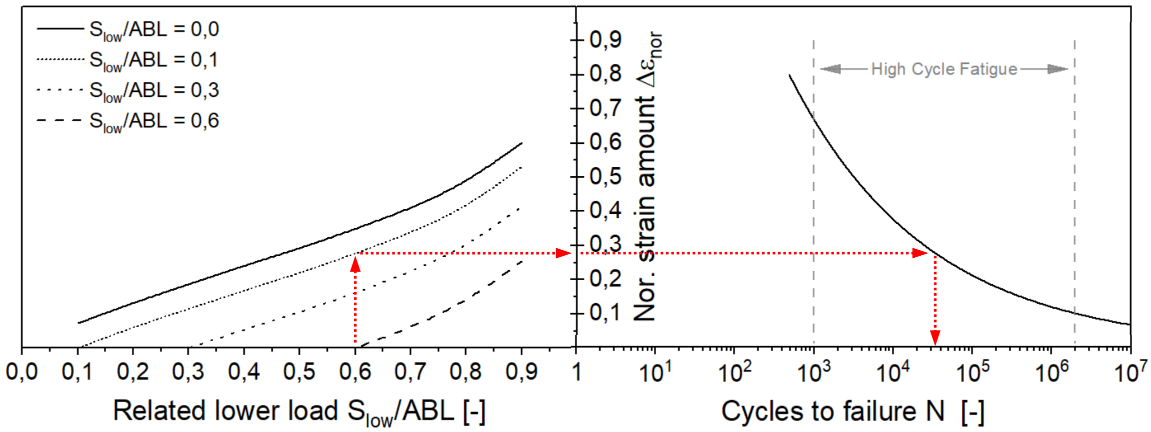

Figure 7: Operating diagram for determining the number of cycles to failure for a given breaking load-related upper and lower load

The operating diagram and the power function contained therein are only valid for the 8x19W rope used here and its specific stress-strain characteristics. To take other possible deformation characteristics into account, the experimentally determined stress-strain curves of the ropes were examined analytically. For the analytical description of rope curves, the use of a sigmoid function [7] has proven to be particularly suitable as a first approximation, according to equation (3). This enables an accurate mathematical representation of the non-linear behavior of the rope under load.

$$\sigma = \left(\frac{\dfrac{1}{1+e^{-k\cdot(\varepsilon - C)}} - \dfrac{1}{1+e^{-k\cdot(-C)}}}{\dfrac{1}{1+e^{-k\cdot(\varepsilon_B - C)}} - \dfrac{1}{1+e^{-k\cdot(-C)}}} \right) \cdot R_m \qquad (3)$$

The parameter k describes the slope of the curve, while the parameter c defines the inflection point of the curve. Using these parameters and the known elongation at break ε_B and breaking strength R_m, the corresponding stress σ can be calculated for any given strain value ε. **Figure 8** shows a comparison of the experimentally determined and analytically calculated stress-strain curves for the tested ropes according to equation (3).

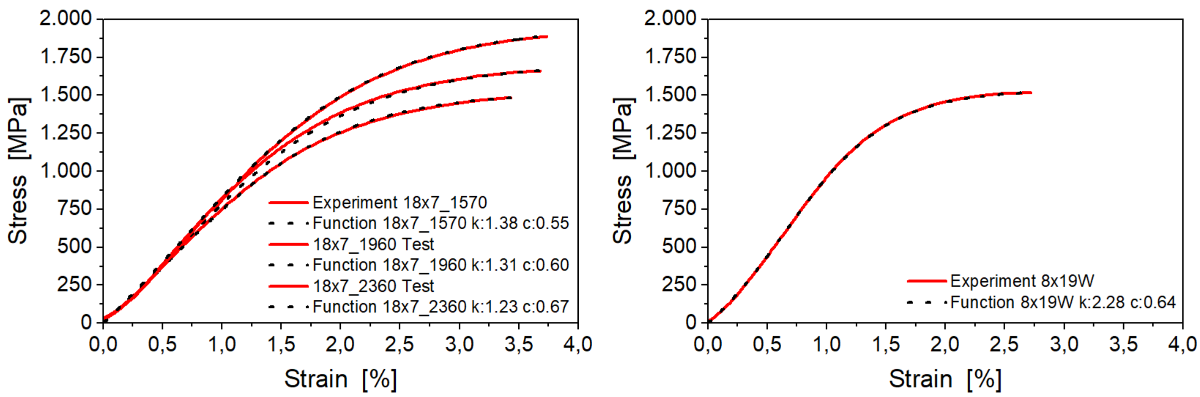

Figure 8: Comparison of experimentally and analytically determined stress-strain curves according to equation (3), left: ropes of type 18x7, right: rope of type 8x19W

Using the determined stress-strain curves of ropes of the same type 18x7 with different strengths, it was possible to analyze the change in the curve characteristics as a function of the increase in strength. As a result, a dependency on the breaking strength R_m was identified for each of the two parameters:

$$k_{8x19W} = 2{,}29 \cdot 0{,}97^{\frac{R_m - 1500}{100}} \tag{4}$$

$$c_{8x19W} = 0{,}63 \cdot 1{,}05^{\frac{R_m - 1500}{100}} \tag{5}$$

Based on these findings, further curves were modeled using the experimentally determined stress-strain curve of the 8x19W rope. Both the elongation at break ε_B and the breaking strength R_m were varied. **Figure 9** shows the modeled curves in comparison to the experimentally determined curve, in both absolute and normalized representation.

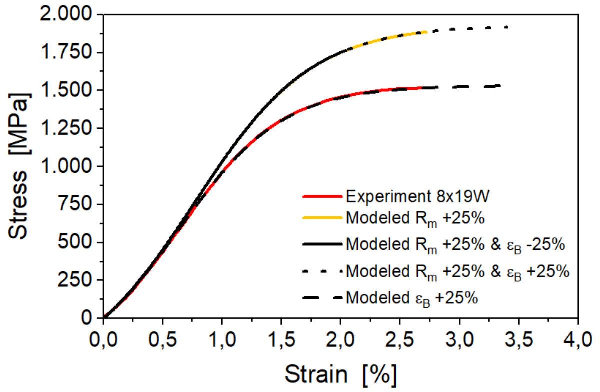

Figure 9: Modeled stress-strain curves with variation of elongation at break and breaking strength, deviating from the experimentally determined curve on rope 8x19W, left: absolute representation, right: normalized representation

The resulting normalized strain amount was determined for the modeled curves based on the load from the experimental tension-tension tests on the 8x19W rope. The corresponding lifetime values were then calculated for the respective strain amount using the previously experimentally determined power function. **Figure 10** shows these analytically determined lifetime values together with the experimental test results on the 8x19W rope. The lifetime values of the modeled curves were plotted against the respective values of the strain amount of the 8x19W rope. This representation enables an evaluation of the variation of elongation at break and breaking strength of the differently modeled curves on the lifetime.

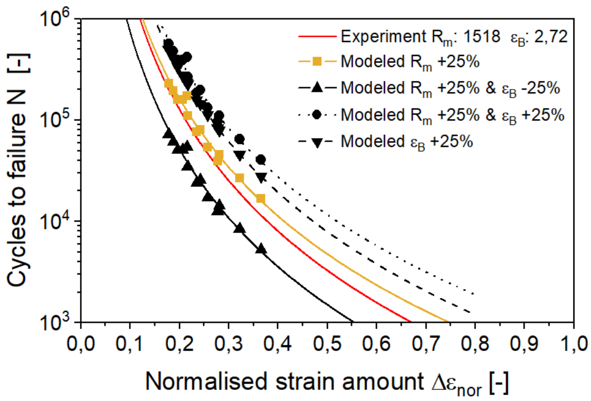

Figure 10: Deviation of the lifetime curve as a function of the rope breaking elongation and rope breaking strength, deviating from the experimentally determined curve on rope 8x19W

The effects of elongation at break and breaking strength on lifetime vary. An increase in strength by 25 % with the same elongation at break results in an increase in lifetime by a factor of 1.14. In contrast, an increase in elongation at break, also by 25 %, with the same breaking strength, leads to a much more significant increase in lifetime, namely by a factor of 2.14. The integration of these analytically determined relationships makes it possible to take into account the comprehensive deformation characteristics of 8x19W ropes in the operating diagram, as shown in **Figure 11**.

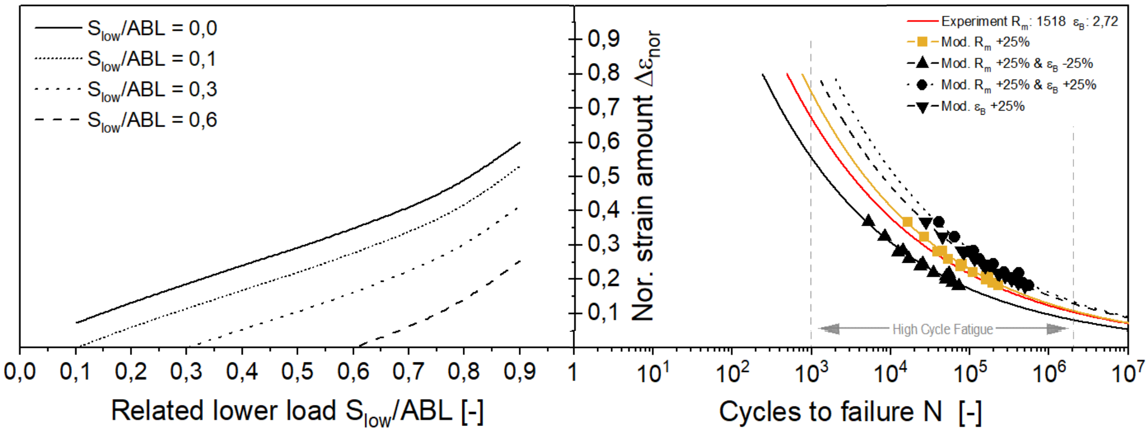

Figure 11: Operating diagram for 8x19W ropes to determine the number of cycles to failure for a given breaking load-related lower and upper load including variation of elongation at break and breaking strength

The newly developed approach enables a precise lifetime prediction for wire ropes under tension-tension load by taking into account the specific deformation properties of ropes. This enables a differentiated assessment of different rope qualities, so that even differences in lifetime between nominally identical ropes can be recorded and the prediction significantly improved. At the same time, the approach is designed to be practical and user-friendly and offers an intuitive way of assessing lifetime. All that is required for the application is the maximum and minimum rope load in operation in relation to the rope breaking load - values that are generally already available during design and operation. Based on this data, the lifetime can then either be read off directly or determined by interpolation, taking into account the specific breaking strength and elongation at break of the rope used.

In addition, this approach opens up the possibility of using the tensile test as an efficient quick test for the first time. This means that rope-specific predictions of the expected lifetime can be made in a time-saving manner and without the need for time-consuming endurance tests.

5 Conclusions

An innovative approach to predicting the lifetime of standing ropes was presented, which combines intuitive applicability with high prediction accuracy to provide a practical and reliable solution.

Tensile tests and tension-tension tests were carried out to analyze both the quasi-static deformation behavior and the fatigue behavior of ropes. The results highlight the central role of rope deformation in relation to fatigue life. In particular, the load-induced deformation of the rope in relation to the total deformation capacity has a decisive influence on the lifetime under cyclic loading. However, a direct correlation between the fatigue life and the rope strength could be ruled out. Against this background, it appears necessary to critically scrutinize the previous safety-related design of dynamically loaded ropes, which is primarily focused on strength, and to adapt it if necessary.

The amount of rope deformation generated is neither linear nor constant, but is determined by the specific deformation characteristics of the rope. Depending on the material and construction, differences can occur which can be characterized and comparatively analysed in normalized form using the stress-strain curve from a quasi-static tensile test.

For the first time, a prediction approach has been developed that takes into account the rope-specific deformation - initially for standing ropes under recurring tensile load. Particularly noteworthy is the graphical operating diagram, which enables a practical and intuitive determination of the lifetime. Only the maximum and minimum rope load in operation in relation to the breaking load are required for the prediction. In addition, individual deformation characteristics can be included through rope-specific breaking strengths and elongations at break.

The systematic combination of the innovative, normalized stress-strain diagram and the newly developed operating diagram makes it possible to specifically take into account rope-specific deformations. Thus, for the first time, a deformation-related design with dynamic safety ($\Delta\varepsilon/\varepsilon_B$) can be realized, which relates directly to the lifetime - instead of a purely strength-related, static safety consideration against overload ($\Delta S_a/R_m$). This leads to a considerable increase in prediction accuracy, especially for nominally identical ropes, and contributes to improving safety and reliability in applications with wire ropes.

6 References

[1] E. Cueto and D. González, An Introduction to Structural Mechanics for Architects, Cham, Switzerland: Springer, 2018.

[2] VDI 2358, Drahtseile für Fördermittel, Düsseldorf: Verein Deutscher Ingenieure e.V., 2012.

[3] K.-H. Wehking, K. Feyrer, A. Klöpfer, D. Moll, R. Vereet, W. Vogel and S. Winter, Laufende Seile - Bemessung und Überwachung, vol. 3. Auflage, Renningen: expert Verlag, 2005.

[4] K. Feyrer and K.-H. Wehking, FEYRER: Drahtseile - Bemessung, Betrieb, Sicherheit, vol. 3. Auflage, Berlin: Springer-Verlag, 2018.

[5] A. Klöpfer, Untersuchung zur Lebensdauer von zugschwellbeanspruchten Drahtseilen, Stuttgart: Universität Stuttgart, 2002.

[6] W. Frick, A new method for evaluating the service life of steel wire ropes of different wire strength, Vols. Proceedings of OIPEEC Conference 2022 and 7th International Stuttgart Ropedays, p. 1-21, 2022.

[7] D. Langemann and C. Reisch, So einfach ist Mathematik – Mathematische Modellierung, Berlin: Springer-Verlag GmbH, 2025.

7 Author Introduction

Wendel Frick, M.Sc. is a mechanical engineer specializing in production and materials engineering. He completed his Master's degree in 2015 and subsequently joined the Institute of Mechanical Handling and Logistics (IFT) of University of Stuttgart as a research assistant and doctoral student. He has been Head of Destructive Rope Testing there since 2022. His research primarily focuses on two key areas: the fatigue behavior of high-strength steel and fiber ropes, and the development of appropriate discard criteria.

AI technologies for rope manufacturing: optimisation of the wire drawing process.

Marco Bertoli, Marco Pintus, Andrea Meleddu, Jan Ferino

Astarte Strategies Srl, Italy

Maurizio Meleddu

Teufelberger-Redaelli, Austria

Summary

This paper presents an application of AI technology for the rope manufacturing industry. A tool is designed to provide fast and reliable predictions of key outcomes in steel wire drawing processes. The AI model is developed using data derived from validated Finite Element models which simulates the wire drawing process and incorporates all main process parameters. The integration of AI enables real-time predictions of ultimate tensile stress, elongation at failure and the damage index, an indicator of the residual strain-ability of the wire. The methodology includes full-scale testing, Finite Element modelling, AI model training, and data comparison. Results indicate that the AI model effectively captures the key trends in wire behaviour with high accuracy, offering a powerful tool for process optimization in industrial applications. The significance of this approach lies in the reduction of computational costs associated with high fidelity Finite Element simulations while maintaining a high level of predictive accuracy.

Keywords: Drawing process, steel wires, AI, FEA, numerical simulation, ultimate tensile stress, failure at strain, ductile damage.

1 Introduction

The wire drawing process is essential for manufacturing high-performance steel wires used in offshore mooring lines, structural cables, and mechanical components subjected to high stress. It involves reducing a wire's diameter by pulling it through a converging die, inducing plastic deformation to enhance mechanical properties. Despite its widespread application, the process remains complex due to the interplay of material properties, lubrication, and process kinematics.

Early investigations by Wiestreich in the 1950s analysed deformation mechanics, deriving relationships between pulling force, reduction ratio, and die pressure distribution [1]. Siebel proposed optimal die angles to minimize energy consumption [2], while Avitzur explored velocity fields and central bursting defect criteria through upper-bound limit analysis [3][4]. Though many studies have addressed single-step drawing, fewer have examined property evolution across multiple stages. Cao compared various damage models and multi-stage forming processes, proposing a methodology to define mechanical properties suitable for damage analysis, [5]. Research has also highlighted the need for kinematic hardening models to accurately assess residual stresses [6].

Given the complexity of the process, Finite Element Analysis (FEA) effectively models the process, providing insights into stress distribution and optimization. Since 2016, Astarte and Teufelberger-Redaelli undertook a project to develop a FE model to simulate multi-stage drawing, predicting key process parameters and failure risks. The model incorporates Bai and Wierzbicki's ductile damage formulation [7] to track material ductility. However, the computational cost of running detailed simulations limits real-time industrial applications.

Advancements in Artificial Intelligence (AI) now enable predictive tools for real-time performance forecasting, [8]. By integrating machine learning (ML) techniques, an AI-based model was developed to estimate key wire properties instantly. Since acquiring extensive experimental data is challenging, a high-fidelity FEA model was used to generate training datasets, ensuring accuracy. This hybrid approach leverages FEA's precision with AI's efficiency, making it viable for industrial-scale optimization.

This paper details the FEA approach used to simulate wire drawing and generate training data, comparing results with experimental testing. It also presents the methodology for developing the AI model, including dataset generation, model training, and validation.

2 Finite Element modelling

A finite-element model was developed to simulate drawing by using the software Dassault Systèmes Abaqus. The intrinsic circular symmetry of the wire-die system was exploited to realize a less expensive axisymmetric configuration based on CAX4RT and CAX3T element types, **Figure 1**. The model simulates drawing-induced changes in material state and predict the effect of the state of stress and strain applied to the material on its mechanical properties.

Thermal effects due to frictional heating and plastic dissipation work are also incorporated. The friction factor is calibrated through reverse engineering and applied to the model. Given the relative simplicity of the contact and the stability of the process, the FE calculations employ an implicit solution scheme. The simulation workflow includes up to 14 drawing steps. At the end of each drawing step, the numerical mesh may become highly deformed due to the plastic deformation undergone by the material. To avoid a computational expensive iterative remeshing procedure, a default mesh was generated for each drawing step. The results from each step are mapped onto the following one. At the end of the whole drawing simulation, the results are transferred to a model that performs a numerical tensile test, from which a virtual stress-strain curve is derived.

From the operative point of view, the model allows various plant options to be compared and prioritized, thus assisting operators in process optimization.

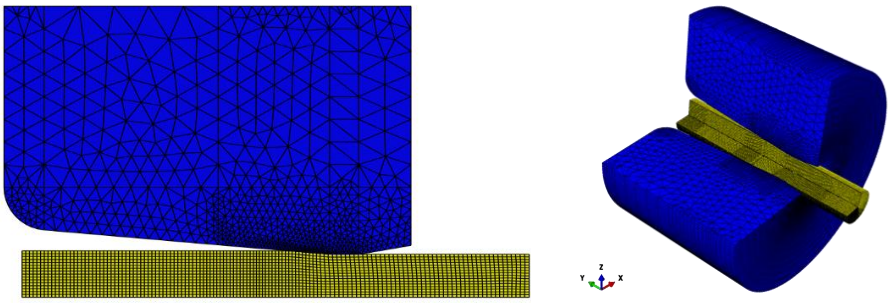

Figure 1: Finite element model of the drawing process (left) and swept visualization (right).

2.1 Damage prediction

A ductile damage criterion based on the Bai and Wierzbicki model was implemented to predict fracture initiation as a consequence of defects which are hidden in the material core, [7]. Although these defects do not cause an immediate failure, they may become critical in conjunction with fatigue or high tensile loads. According to its formulation, the ductile damage calculation was therefore implemented which results in the damage index (D) ranging from 0 to 1, that is from "virgin state" to 1 "fracture onset". D is calculated as a function of the critical equivalent plastic strain at rupture and it cumulates as plastic deformation increases according to the following:

$$D(\epsilon_p) = \int_0^{\epsilon_p} \frac{d\epsilon_p}{\epsilon_f(T,X)} \tag{1}$$

ε_P = plastic strain
ε_f = fracture strain
$T=(1/3)*(\sigma 1+ \sigma 2+ \sigma 3)/ \sigma_{VM}$
$X = \cos(3\theta)$
θ = Lode parameter, see [7]

where the fracture surface is expressed by:

$$\varepsilon_f(T,\theta) = \left[\frac{1}{2}\left(D_1e^{-D_2T} + D_5e^{-D_6T}\right) - D_3e^{-D_4T}\right]\theta^2 + \left[\frac{1}{2}\left(D_1e^{-D_2T} - D_5e^{-D_6T}\right)\right]\theta + D_3e^{-D_4T} \quad (2)$$

Coefficients D1-D6 are typical of each material and are determined by lab testing procedure on a set of samples, as described by Cao et al. [9]. The FEA-estimated damage distribution is consistent with typical observations of internal cracking, when occurring. In fact, D is higher in the centreline, and it expands upon exit from the die as in **Figure 2**.

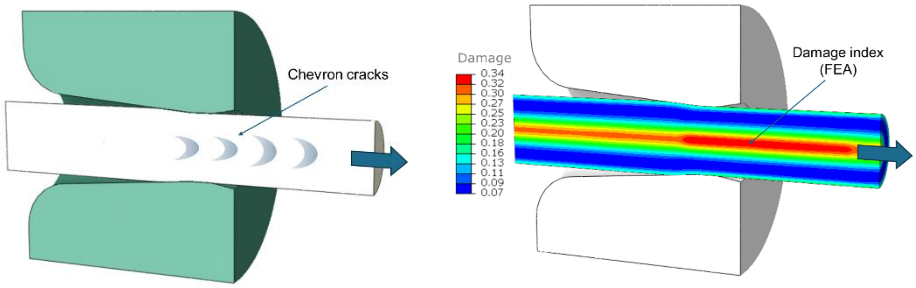

Figure 2: Chevron crack along wire centreline and D index as per FEA.

2.2 FEA validation

The effectiveness of the FEA model in simulating the drawing process and predicting the wire properties are given briefly in the pictures. A drawing process of a C82 grade wire rod was performed and simulated across the whole set of drawing dies from 6.50mm to 2.83mm diameter. At each intermediate step, the rod was sampled and subjected to tensile testing in laboratory. FEA vs. actual comparison is given the following and proves the effectiveness of the numerical model to catch the actual material performance across the process. **Figure 3** refers to the material ultimate tensile strength and the corresponding uniform elongation, while **Figure 4** shows the whole engineering stress-strain curve at two intermediate steps.

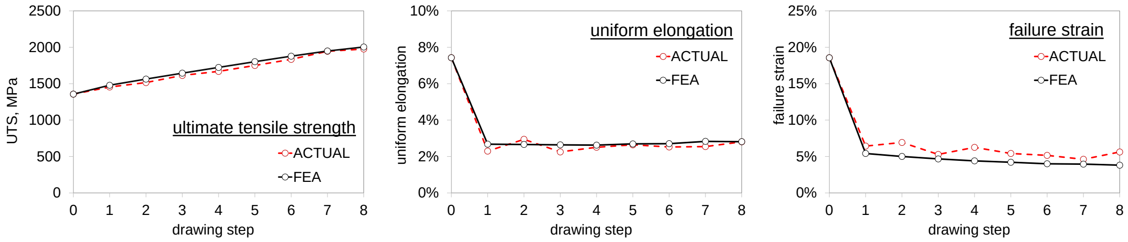

Figure 3: evolution of the UTS and uniform elongation of wire rod during drawing.

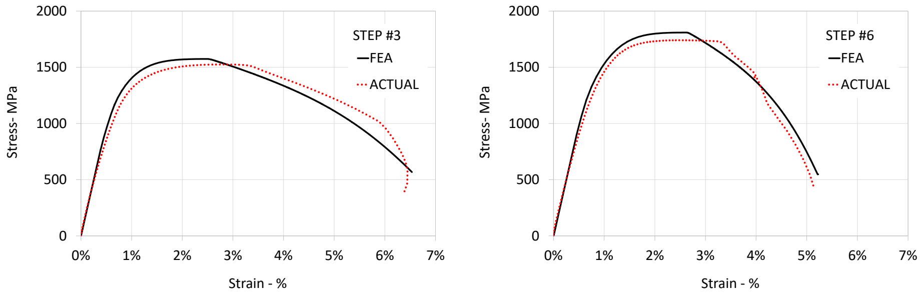

Figure 4: tensile curves of steel rods at intermediate steps.

However, the computational cost of running detailed simulations limits real-time industrial applications. Though FEA still is a reference technology for off-line investigation and R&D projects, it is not suitable for in-line purposes.

3 AI model development

The innovative AI tool for drawing process simulation is based on the most accredited machine learning regression algorithms. Their selection and setup were performed with the aim to provide a real time prediction of the synthetic indicators. These indicators characterise the manufactured wire, by taking as input the operating parameters of the drawing setup. For explanatory purposes, the training procedure is described below with reference to grade C82 steel wire rods but is intended to apply identically to other materials. The development of the model requires the execution of the following steps:

1. design space definition
2. Design of Experiments (DOE) implementation
3. AI model training.

3.1 Design space definition

The design space is defined by the set of operating parameters that control the drawing process and by the respective variation ranges selected to ensure the coverage of typical manufacturing conditions. Constraints were applied to specific operating parameters to avoid critical combinations that may lead to infeasible process configurations. **Table 1** summarizes the limits of the design space that have been defined.

Table 1: Limits of the design space for C82 steel grade wires

C82	
Operating parameters	
Initial diameter Di	5.50mm – 7.50mm
Final diameter Df	2.0mm – 3.5mm
Last step reduction	14% - 26%
Number of drawing steps	5 - 14
Die angle	6°, 8°, 10°, 12°, 14°
Additional constraints	
Single step reduction	10% - 26%
Maximum total reduction	89%

3.2 Design of Experiments (DOE)

Training AI models requires a dataset of features and labels representative of established manufacturing processes. The features consist of various combinations of the operating parameters, whose values are sampled within the design space, while the labels are the corresponding target outputs. Three parameters were selected as final output of the AI model:

- Ultimate tensile stress (UTS, MPa)
- Failure strain
- Damage index at the core

A Latin hypercube sampling technique was employed to generate 500 different manufacturing processes (design points), ensuring a uniform coverage of the parameter space. Each design point was then simulated with the FE model to determine the accurate estimation of the corresponding labels. **Figure 5** reports the statistical distribution of the operating parameters of the 500 design points. All the distributions show a nearly even trend, thus assuring the uniform coverage of the variation interval. The unique exception is the number of drawing steps, whose value was modified to comply with the constraints imposed by the process feasibility.

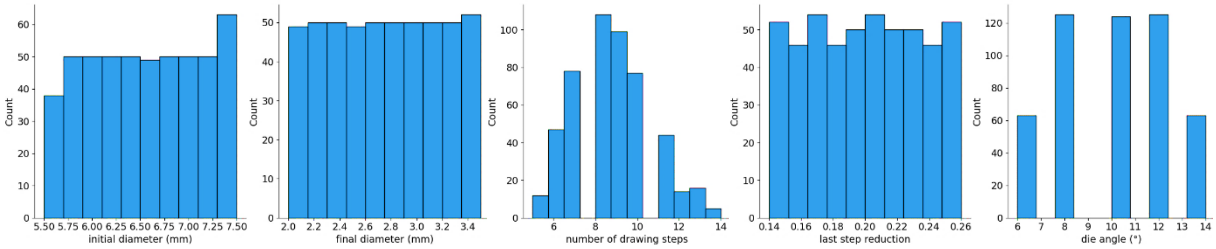

Figure 5: Statistical distribution of the DOE operating parameters sampled by the Latin hypercube algorithm.

3.3 Model training

A comparative analysis of different machine learning algorithms was carried out to determine the optimal combination of models that best replicated the FE estimations for the three key parameters under investigation. Tested algorithms included Random Forest (RF, [10]), Support Vector Machine (SVM, [11]), Logistic Regression (LR), and Deep Neural Networks (DNN). Each model was evaluated based on its ability to accurately approximate the numerical results obtained with the FE simulations.

The dataset was partitioned into training and validation sets, with 80% of the data allocated for training and the remaining 20% reserved for validation. To mitigate the risk of overfitting and ensure robust generalization, a five-fold cross-validation procedure was implemented. This technique involved randomly resampling the dataset five times. Each iteration produced a different split between training and validation data, thereby enhancing the reliability of the performance assessment.

To further refine the models and optimize their predictive capabilities, a grid search algorithm was employed for the hyperparameter tuning. This process systematically explored different hyperparameter configurations to identify the combination that yielded the highest prediction accuracy for each machine learning model.

The final step involved validating the trained models by comparing their predictions against FEA results. Based on the outcomes of this evaluation, the most accurate model configurations were established for each key parameter:

1. SVM for UTS and failure strain
2. Random Forest for the damage index.

4 Wire tensile testing

Tensile testing was conducted at Teufelberger-Redaelli's testing lab on specimens extracted from drawn steel wires, which were manufactured according to the drawing parameters detailed in **Table 2**. The starting material for all processes was a virgin C82 grade steel rod with an initial diameter of 6.5 mm. Experimental tensile test results exhibited minimal scatter, suggesting a high degree of uniformity in the material behaviour, thus confirming the repeatability of the manufacturing process.

To further investigate the influence of modelling approaches on the prediction accuracy, each drawing series was analysed using both FE models and ML regressors. Such approach allowed for a systematic comparison between numerical and data-driven models, facilitating the identification and quantification of error sources. Specifically, the study aimed at discriminating between discrepancies ascribable to the intrinsic approximations of the AI models and those stemming from potential inaccuracies in the original finite element simulations. By correlating experimental data with the predictions from both modelling techniques, a more comprehensive understanding of the reliability and limitations of AI-driven estimations in comparison to traditional FE simulations was achieved.

Table 2: Tensile test results and drawing parameters on round wires.

Test #	Rod diameter (mm)	Nominal wire diameter (mm)	# Reduction steps	Total reduction (%)	Average real UTS (MPa)	Standard deviation on UTS (%)
1	6.5	2.32	10	87.3	2149	0.76
2		2.36	10	86.8	2119	0.00
3		2.47	9	85.6	2096	1.85
4		2.16	9	89.0	2270	1.41
5		2.1	9	89.6	2261	2.12
6		2.29	9	87.7	2084	1.74

5 Data comparison and validation

Table 3 and **Table 4** shows a summary of the UTS, Failure Strain and Damage at core, after the final drawing step of each of the six reference process. Three sets of data are available for UTS, i.e. experimental, FEA-predicted and AI-predicted data. Experimental data are not available for Failure strain and Damage at core. The first refers to the very local measure of deformation at rupture and it is not easily measurable, while the second is calculated as in section §2.1 and it is not achieved by lab testing.

The comparison confirms the good agreement between AI and FEA predictions of the UTS, expressed via maximum and average errors equal to 1.3% and 0.7%, respectively. When comparing AI and experimental data, a slightly higher difference arises as a consequence of the inherent deviation of the FE results adopted to train the AI model. The maximum deviation amounts to 5.9% while the average is 2.9%.

The accuracy of the AI damages prediction can be evaluated only with respect to FEA data, as the corresponding index cannot be experimentally determined. The maximum error observed corresponds to 11.1%. Although, it is underlined that D is a qualitative parameter accounting for the damage state of the material and a larger tolerance with respect to mechanical properties can be reasonably accepted.

Finally, the estimation of the failure strain showed error levels comparable to the UTS predictions and characterized by a maximum value equal to 1.7% and an average deviation of 1.1%.

Table 3: Comparison of experimental, FEA and AI model data

Test #	Final UTS (MPa)			Failure strain (%)		Damage at wire core	
	Exp.	FEA	AI	FEA	AI	FEA	AI
1	2149	2080	2088	36.3	36.5	0.19	0.20
2	2119	2069	2088	36.1	36.5	0.20	0.20
3	2096	2042	2069	36.2	36.5	0.18	0.18
4	2270	2130	2135	36.6	36.2	0.18	0.20
5	2261	2148	2154	36.6	36.2	0.19	0.20
6	2084	2090	2113	35.7	36.3	0.19	0.20

Table 4: AI average errors

	Avg. error on final values (%)		Maximum error on final values (%)	
	AI-to-FEA	**AI-to-exp.**	**AI-to-FEA**	**AI-to-exp.**
UTS	0.7 ± 0.4	2.9 ± 1.8	1.3	5.9
Failure strain	1.1 ± 0.34	-	1.7	-
Damage at core	4.4 ± 3.8	-	11.1	-

Figure 6 shows the variation of the wire parameters under investigation — UTS, core damage, and failure strain of the produced wire — as a function of the sequential steps in the reference manufacturing process. Notably, the curves generated by the AI model exhibit a strong correspondence with those obtained with FE simulations. The deviation between AI and FE predictions observed in the last drawing steps is confirmed throughout the entire manufacturing procedures. The damage curves continue to show higher errors with respect to both UTS and failure strain.

It is important to stress that the FEA model grants an extensively in-depth study of the drawing procedure, encompassing a wider result set when compared to the developed AI tool: albeit at a significantly greater computational time and cost. A FEA high fidelity simulation can be performed in a varying number of hours, depending on the investigated drawing process. Conversely, the AI model predicts a concise result within a fraction of a second.

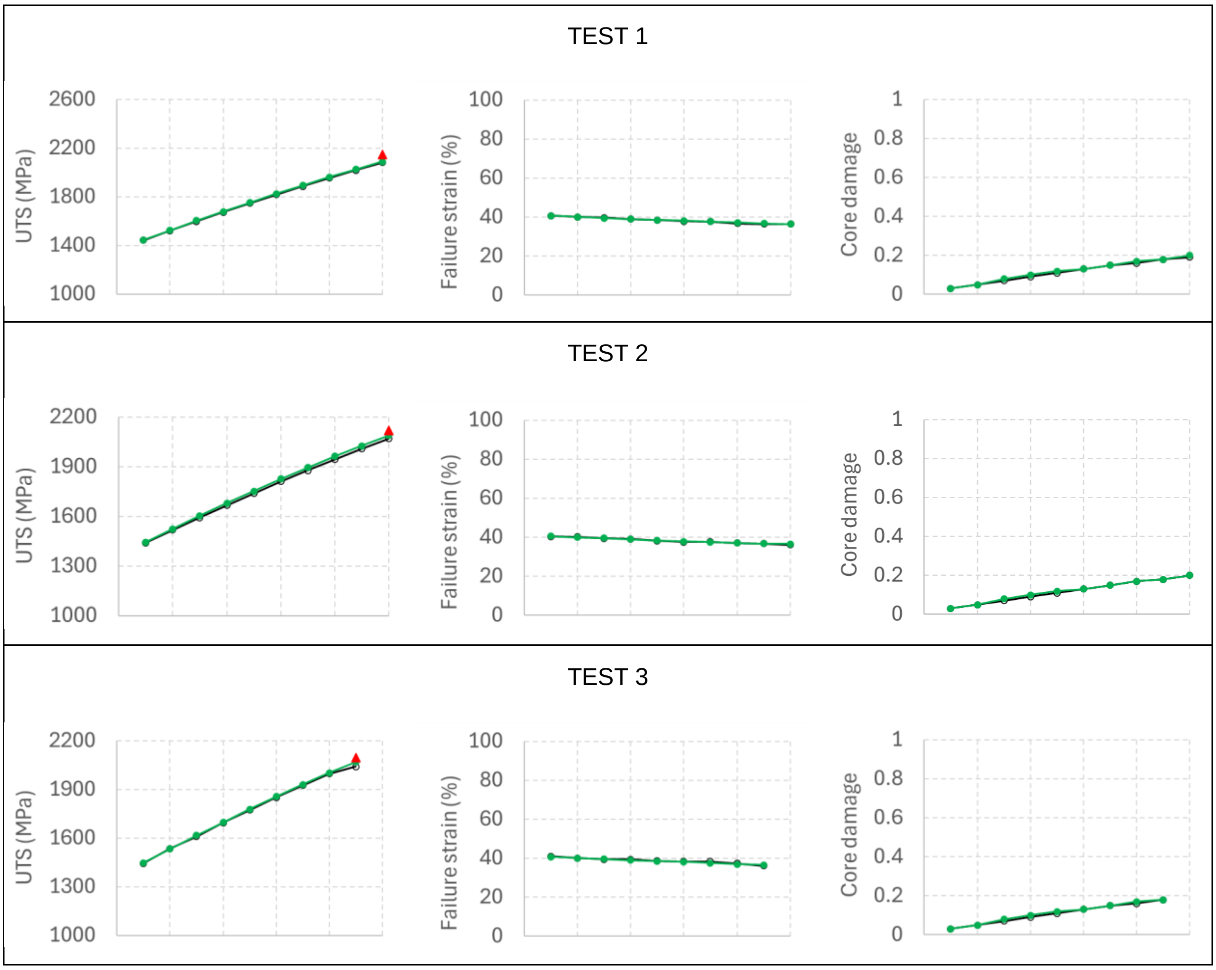

Figure 6: Drawing key parameters as a function of the drawing step for the reference manufacturing processes; comparison between measurements and numerical predictions of FE and AI.

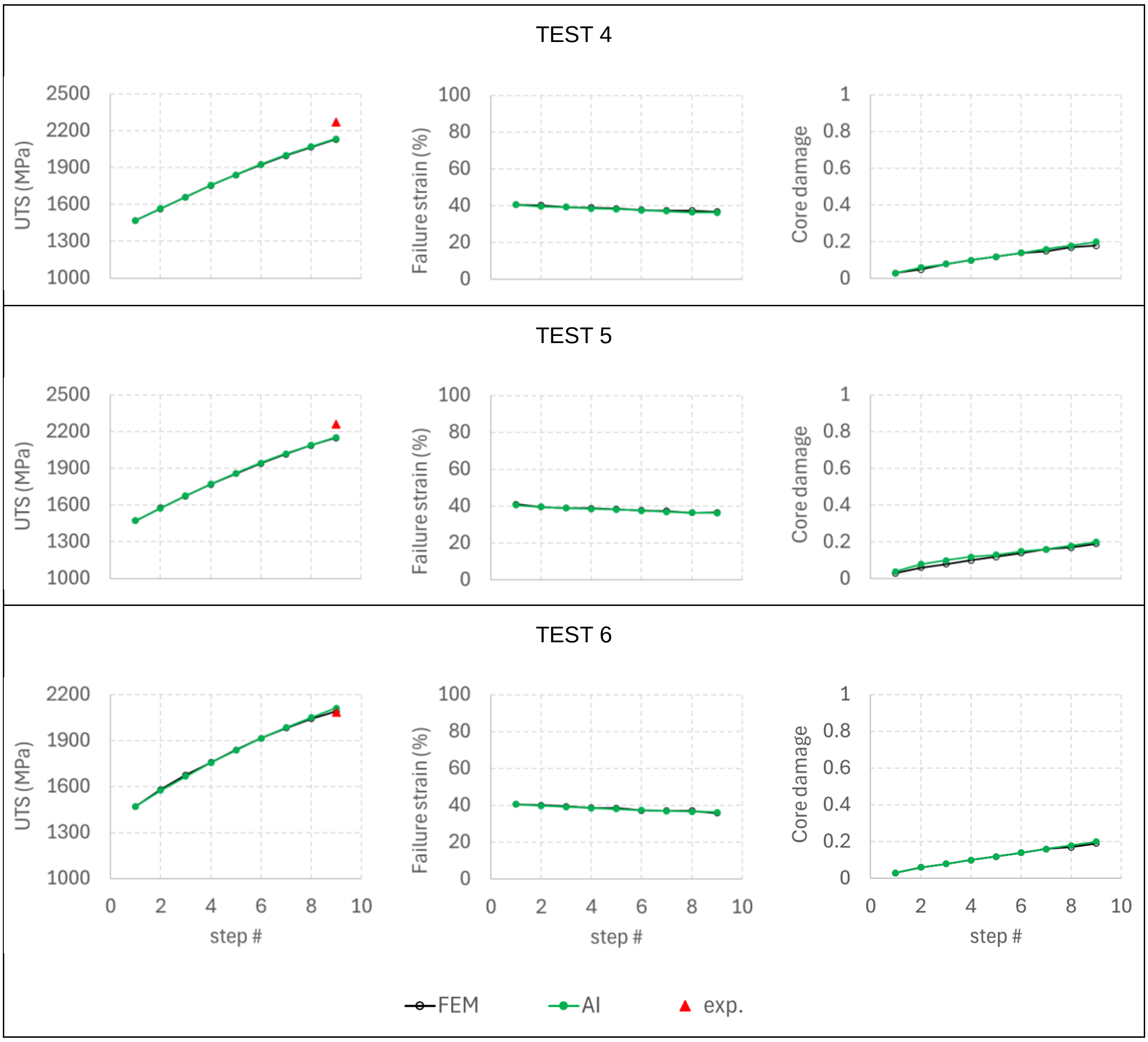

Figure 6 (Cont'd): Drawing key parameters as a function of the drawing step for the reference manufacturing processes; comparison between measurements and numerical predictions of FE and AI.

6 Conclusions

The development of a machine learning-based tool for the simulation of the steel wire drawing process has demonstrated its potential in providing fast and reliable predictions of key process outcomes. The AI model, trained on data obtained from validated Finite Element simulations, accurately replicates the behaviour of the drawing process while significantly reducing computational costs. The comparison between AI and FEA predictions of the Ultimate Tensile Strength (UTS) confirms an excellent agreement, with maximum and average errors of 1.3% and 0.7%, respectively. When compared to experimental data, slightly larger deviations were observed, with a maximum error of 5.9% and an average error of 2.9%. This discrepancy is attributed to the intrinsic variability of the FEA results used for AI training as well as the variability in the experimental testing of the wire. A good accuracy between FEA and AI was also obtained in the estimation of the failure strain, with maximum and average errors of 1.7% and 1.1%. The prediction of the core damage index, although only verifiable against FEA results, showed a maximum error of 11.1%.

The good agreement between AI-based and FEA predictions together with the validation on experimental data, prove the validity of the AI approach and show substantial promise to further invest in the application of AI-based technology in the drawing. The potential provided by AI to investigate a multitude of different technical solutions with a limited computational cost when compared to high fidelity simulations offers the opportunity to further invest in the application of AI-based technology in the drawing.

7 References

[1] Wistreich J. G.: “Investigation of the mechanics of wire drawing,” Proc. Institute of Mechanical Engineers, 169, 1955, pp. 654-665.

[2] Lange, Kurt (Ed.): “Handbook of Metal Forming,” McGraw-Hill, p. 13.20.

[3] B. Avitzur, W. C. hahn,JR. and S. ISCOVICI : Limit Analysis of Flow Through Conical, Converging Dies, Journal of The Franklin Institute, Vol. 299, No. 5, May 1975.

[4] B. Avitzur, J.C. Choi, Analysis of Central Bursting Defects in Plane Strain Drawing and Extrusion, Journal of Engineering for Industry NOVEMBER 1986, Vol. 108/317.

[5] T.-S. Cao, C. Vachey, P. Montmitonnet, P.-O. Bouchard, Comparison of reduction ability between multi-stage cold drawing and rolling of stainless steel wire – Experimental and numerical investigations of damage Journal of Materials Processing Technology 217 (2015) 30–47.

[6] A. Panteghini, F. Genna, Effects of the strain-hardening law in the numerical simulation of wire, drawing processes, Computational Materials Science 49 (2010) 236-242.

[7] Bai, Y., T. Wierzbicki, A New Model of Metal Plasticity and Fracture with Pressure and Lode Dependence. International Journal of Plasticity, vol. 24, no. 6, pp. 1071–1096, 2008.

[8] M.-K. Kazi, F. Eljack, E. Mahdi, Data-driven modeling to predict the load vs. displacement curves of targeted composite materials for industry 4.0 and smart manufacturing, Compos Struct, 258 (2021), p. 113207.

[9] T.-S. Cao, A. Gaillac, P. Montmitonnet, P.-O. Bouchard, Identification methodology and comparison of phenomenological ductile damage models via hybrid numerical–experimental analysis of fracture experiments conducted on a zirconium alloy, International Journal of Solids and Structures 50 (2013) 3984-3999.

[10] A. Liaw, M. Wiener, Classification and regression by random Forest, R N, 2 (3) (2002), pp. 18-22.

[11] J.C. Platt, Fast training of support vector machines using sequential minimal optimization. In Advances in kernel methods. MIT Press 1999; 185–208.

8 Authors' Introductions

Ing. Marco Bertoli earned his Bachelor's and Master's degrees in Mechanical Engineering from the University of Cagliari, Italy. Until 2015, he collaborated with Centro Sviluppo Materiali (CSM) on fluid dynamics related to Oil & Gas pipeline transportation. In 2015, he co-founded Astarte Strategies, a consultancy specializing in technological innovation for industrial products and processes. Marco specializes in fluid dynamics, heat exchange, combustion, internal flows, and aerodynamics. At Astarte, he is the expert and reference for AI processes applied to industry.

Ing. Jan Ferino is a mechanical engineer specializing in Finite Element Analysis (FEA), industrial plant modeling, machining processes, and structural dynamics. From 2005 to 2015, he worked at RINA Consulting SpA (formerly Centro Sviluppo Materiali SpA) as a researcher. In 2015, he co-founded Astarte Strategies Srl, an engineering consultancy focused on R&D for industrial innovation. He has contributed to European projects on steel industry innovation and participated in coordinating First Wire, a co-funded by RFCS, an EU programme supporting research projects in the coal and steel sectors.

Ing. Andrea Meleddu is a mechanical engineer with expertise in structural integrity, fluid dynamics, materials science, and experimental testing. From 2004 to 2015, he worked on research and development projects for Oil&Gas industry. In 2015, he co-founded Astarte Strategies Srl, where he now serves as Technical Manager, overseeing technical planning and coordination. He has contributed to several European research initiatives and coordinated of the First Wire project, co-funded by RFCS, an EU programme supporting research in the coal and steel sectors.

Ing. Marco Pintus earned his Master's degree in Mechanical Engineering from the University of Cagliari in 2022. In 2023, he joined Astarte Strategies, where he specializes in virtual prototyping and AI applications in industrial processes. His expertise includes structural and fluid dynamics modeling, combustion, heat transfer, and metalworking, using Computational Fluid Dynamics (CFD) and Finite Element Analysis (FEA). Proficient in programming languages, Marco plays a key role in developing innovative engineering solutions at Astarte

Ing. Maurizio Meleddu receives his master degree in Mechanical engineering in 2005. He starts his career at Centro Sviluppo Materiali specializing in process development and numerical simulation. After 4 years he takes over the role of R&D manager in Tesmec specializing in technology and product development for stringing equipment and digging&trenching machines. Starting in 2013 he joins Teufelberger-Redaelli as R&D manager of the group. Co-author with Politecnico of Milano of publication such as "Temperature on heave compensation rope - OIPEEC April 2017 "and "Analytical Model and its implementation in the Wire Rope industry -OIPEEC April 2024".

University of Stuttgart
Institute of Mechanical Handling
and Logistics

IFT

University of Stuttgart
Institute of Mechanical Handling and Logistics
Univ.-Prof. Dr.-Ing. Robert Schulz

Holzgartenstraße 15 B
70174 Stuttgart
Germany
www.ift.uni-stuttgart.de/en/

ISBN 978-3-00-081732-8